Microwave-shielded ultracold polar molecules

Xing-Yan Chen (陈兴炎)

München 2023

Microwave-shielded ultracold polar molecules

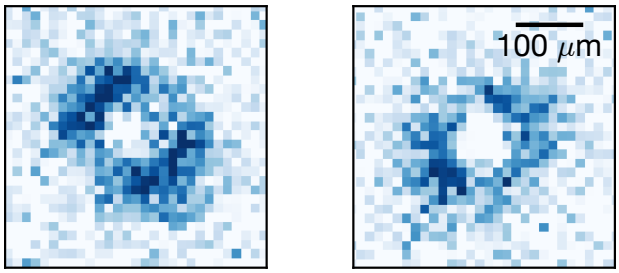

Dissertation an der Fakultät für Physik
der Ludwig–Maximilians–Universität München

vorgelegt von

Xing-Yan Chen (陈兴炎)

aus Wuhan, China

München, den 7. September 2023

Erstgutachter: Prof. Dr. Immanuel Bloch
Zweitgutachter: Prof. Dr. Simon Cornish
Tag der mündlichen Prüfung: 20. Oktober 2023

Zusammenfassung

Seit der Verwirklichung der Bose-Einstein-Kondensation und entarteter Fermi-Gase sind ultrakalte Atome mit verstimmbaren Wechselwirkungen zu einer wesentlichen Plattform für die Untersuchung von Quantenvielteilchenphänomenen geworden. Bemerkenswerte Beispiele sind die Realisierung des BCS-BEC-Übergangs und die Simulation des Bose-/Fermi-Hubbard-Modells. Ultrakalte polare Moleküle könnten mit ihrer langreichweitigen Dipol-Dipol-Wechselwirkung den Werkzeugkasten für Quantengase bereichern, was nicht nur neue Möglichkeiten in der Vielkörperphysik, wie die Realisierung des topologischen Suprafluid und des erweiterten Hubbard-Modells, eröffnet, sondern auch Anwendungen in der Quantenchemie, der Quantenberechnung und bei Präzisionsmessungen bietet. Die große Anzahl interner Freiheitsgrade der Moleküle stellt jedoch eine große Herausforderung dar, wenn es darum geht, sie bis zur Quantenentartung abzukühlen und ihre Wechselwirkungen zu kontrollieren. Im Gegensatz zu atomaren Gasen leidet eine dichte molekulare Probe unter schnellen Kollisionsverlusten, was die Anwendung von Verdunstungskühlung und die Beobachtung von Streuresonanzen verhindert. In dieser Dissertation beschreiben wir, wie wir das seit langem bestehende Problem der Kollisionsverluste durch Mikrowellenabschirmung gelöst, ein entartetes Fermi-Gas aus ^{23}Na^{40}K-Moleküle produziert und eine neue Art von Streuresonanz entdeckt haben, durch die wir die ersten ultrakalten tetratomischen Moleküle erzeugen konnten.

Indem wir die Rotation polarer Moleküle mit einem zirkular polarisierten elektrischen Mikrowellenfeld synchronisieren, statten wir die Molekülprobe mit einem hochgradig manipulierbaren intermolekularen Potenzial aus. Dies stabilisiert das Gas nicht nur gegen inelastische Kollisionen, sondern ermöglicht auch *feldinduzierte* Streuresonanzen zur präzisen Kontrolle der Streulängen. Im Fernbereich interagieren die Moleküle über ihre induzierten rotierenden Dipolmomente. Wenn sie sich einander nähern, richten sie sich neu aus, wodurch eine abstoßende Kraft erzeugt, durch die unelastische Kollisionen in geringer Entfernung abgeschwächt werden. Mit einem Verhältnis von elastischen zu unelastischen Stößen von 500 haben wir eine Verdunstungskühlung des Molekülgases bis auf 21 nK und das 0,36-fache der Fermi-Temperatur erreicht und damit einen neuen Rekord für das bisher kälteste polare Molekülgas aufgestellt.

Dank der Kollisionsstabilität mikrowellenabgeschirmter Moleküle können wir sie direkt in eine einzelne Schicht eines magischen optischen 3D-Gitters laden und so einen Spitzenfüllungsgrad von 24% erreichen. Diese ultrakalten Moleküle bieten aufgrund ihrer langen Lebensdauer im Grundzustand und ihrer weitreichenden dipolaren Kopplung eine einzigartige Plattform zur Untersuchung des Quantenmagnetismus. Mit dem erreichten hohen Füllungsgrad sind wir in der Lage, Nicht-Gleichgewichts-Spindynamik wie Rotationssynchronisation und Spin-Squeezing zu studieren.

Wir haben gezeigt, dass die Wechselwirkung zwischen mikrowellenabgeschirmten polaren Molekülen über die Mikrowellenleistung, die Verstimmung und die Polarisation manipulier-

bar ist. Wenn das Wechselwirkungspotenzial tief genug ist, um feldinduzierte gebundene Zustände an der Kollisionsschwelle zu erlauben, wird eine Formresonanz induziert, die es uns ermöglicht, die Streurate über drei Größenordnungen zu varieren. Die feldinduzierten Resonanzen ermöglichen eine Kontrolle der Streulänge in ähnlicher Weise wie die Feshbach-Resonanz für ultrakalte Atome und versprechen die Realisierung stark korrelierter Phasen, wie z. B. dipolarer p-Wellen-Suprafluide. Sie ebnet auch den Weg zur Untersuchung des Zusammenspiels zwischen Kurzstrecken- und Langstrecken-Wechselwirkungen in neuartigen Quantenmaterien, wie z. B. exotischen Superfestkörpern.

Darüber hinaus haben wir durch eine feldinduzierte Resonanz zum ersten Mal ultrakalte tetratomische Moleküle im 100 nK-Bereich mit einer Phasenraumdichte von 0,04 assoziiert. Der Übergang von einem Fermi-Gas aus zweiatomigen Molekülen zu einem Bose-Gas aus tetratomischen Molekülen ist ein erster Schritt hinzu einem dipolaren BCS-BEC Übergang.

Mit mikrowellenabgeschirmten polaren Molekülen haben wir ein Quantengas mit hochgradig manipulierbaren Langstreckenwechselwirkungen realisiert. Die Technik ist universell für polare Moleküle mit einem ausreichend großen Dipolmoment und bietet somit eine allgemeine Strategie zur Kühlung und Manipulation polarer Moleküle und zur Assoziation schwach gebundener ultrakalter polyatomarer Moleküle. Unter Verwendung des für ultrakalte Atome entwickelten Werkzeugkastens hat diese Plattform das Potenzial, einen völlig neuen Bereich der Quantensimulation der Vielteilchenphysik zu erschließen.

摘要

自实现玻色-爱因斯坦凝聚和简并费米气体以来, 具有可调相互作用的超冷原子已成为研究量子多体现象的重要平台, 包括实现 BCS–BEC 渡越和模拟玻色/费米哈伯德模型。超冷极性分子通过长程偶极-偶极相互作用进一步丰富了量子气体工具箱, 这不仅为多体物理 — 如拓扑超流体和扩展哈伯德模型 — 提供了新的机遇, 也为量子化学、量子计算和精密测量带来了广泛的应用前景。然而, 分子内部自由度的数量之大, 给分子冷却至量子简并和控制其相互作用带来了重大挑战。不同于原子气体，在致密分子气体系统中，碰撞损耗限制了系统寿命，从而阻碍了蒸发冷却和可调散射共振的有效实施。在本论文中，我们针对这一长期挑战，通过微波屏蔽技术成功解决了碰撞损耗问题，从而实现了费米简并 ^{23}Na^{40}K 分子气体的制备。进一步地，我们还发现了一种新型散射共振现象，并借助该共振成功制备了首个 100 nK 温区的超冷四原子分子气体。

在近圆偏微波驱动下, 分子与交流电场同步旋转, 从而诱导出可调的分子间相互作用。该相互作用不仅能稳定气体, 抑制非弹性碰撞, 同时还能实现场联散射共振, 控制散射长度。在远距离上, 分子通过诱导的旋转电偶极矩相互作用。当分子相互接近时, 它们的取向会重新调整以相互排斥, 从而阻止近距离非弹性碰撞的发生。在微波屏蔽下, 弹性碰撞与非弹性碰撞的比率为达到了 500, 使得我们可以将分子蒸发冷却至 21 nK, 仅为费米温度的 0.36 倍。这是迄今为止最冷的极性分子气体。

得益于微波屏蔽所带来的碰撞稳定性, 我们能够直接将大部分分子装载到一个魔术三维光学晶格的单层中, 实现了约 24% 的峰值填充率。由于这些超冷分子在基态下的长寿命及其长程偶极耦合, 它们为研究量子磁性提供了一个独特的平台。高填充率为研究非平衡自旋动力学, 如旋转同步和自旋压缩, 做好了准备。

我们展示了微波屏蔽相互作用可以通过微波功率、失谐和偏振进行精确调解。当相互作用势的深度足以在碰撞阈值处容纳场联 (field-linked) 束缚态时, 就会诱发形状共振, 从而使我们能够在三个量级内调节碰撞速率。场联共振能够以类似于超冷原子中 Feshbach 共振的方式控制散射长度, 促成强相关多体相的实现, 例如偶极 p 波超流体。这一机制还为研究新型量子材料中短程和长程相互作用的联合效应提供了实验基础, 比如实现奇异

超固体。

此外, 借助场联共振, 我们首次在 100 nK 温区缔合了相空间密度为 0.04 的弱束缚超冷四原子分子。从双原子分子的费米气体过渡到四原子分子的玻色气体, 为实现偶极 BCS-BEC 渡越铺平了道路。

通过微波屏蔽极性分子, 我们成功实现了一种具有高度可调长程相互作用的量子气体。该技术对具有足够大偶极矩的极性分子具有广泛适用性, 因此为冷却极性分子以及制备超冷多原子分子提供了一种通用策略。利用超冷原子–分子工具箱, 这一平台有望开启多体物理学量子模拟的全新篇章。

Abstract

Since the realization of Bose–Einstein condensates and degenerate Fermi gases, ultracold atoms with tunable interactions have become an essential platform for studying quantum many-body phenomena. Notable examples include the realization of BCS–BEC crossover and the simulation of the Bose/Fermi Hubbard model. Ultracold polar molecules could enrich the quantum gas toolbox with their long-range dipole-dipole interaction, which offers not only new opportunities in many-body physics, such as realizing the topological superfluid and the extended Hubbard model, but also applications in quantum chemistry, quantum computation, and precision measurements. However, the large number of internal degrees of freedom of molecules present a significant challenge in both cooling them to quantum degeneracy and controlling their interactions. Unlike atomic gases, a dense molecular sample suffers from fast collisional losses, preventing the implementation of evaporative cooling and the observation of scattering resonances. In this thesis, we describe how we solved the long-standing issue of collisional losses by microwave shielding, created a degenerate Fermi gas of $^{23}Na^{40}K$ molecules, and discovered a new type of scattering resonances via which we created the first ultracold tetratomic molecules in the 100-nK regime.

By synchronizing the rotation of polar molecules with a circularly polarized microwave electric field, we equip the molecular sample with a highly tunable intermolecular potential. This not only stabilizes the gas against inelastic collisions but also enables *field-linked* scattering resonances for precise control over scattering lengths. At long range, the molecules interact via their induced rotating dipole moments. As they approach each other, their orientations realign to produce a repulsive force, thereby mitigating inelastic collisions at close distances. With an elastic-to-inelastic collision ratio of 500, we have achieved evaporative cooling of the molecular gas down to 21 nK and 0.36 times the Fermi temperature, setting a new record for the coldest polar molecular gas to date.

Thanks to the collisional stability of microwave-shielded molecules, we can directly load them into predominantly a single layer of a magic 3D optical lattice, achieving a peak filling fraction of 24%. These ultracold molecules, owing to their long lifetimes in their ground state and their long-range dipolar coupling, provide a unique platform to study quantum magnetism. With the achieved high filling fraction, we are prepared to study non-equilibrium spin dynamics such as rotational synchronization and spin squeezing.

We demonstrated that the interaction between microwave-shielded polar molecules is highly tunable via the microwave power, detuning, and polarization. When the interaction potential is deep enough to host field-linked bound states at the collisional threshold, a shape resonance is induced, allowing us to tune the scattering rate by three orders of magnitude. The field-linked resonances enables controls over the scattering length in a similar fashion as Feshbach resonance for ultracold atoms, promising the realization of strongly correlated phases, such as dipolar p-wave superfluid. It also paves the way to

investigate the interplay between short-range and long-range interactions in novel quantum matters, such as exotic supersolid.

Moreover, through a field-linked resonance, we associated for the first time weakly bound tetratomic molecules in the 100-nK regime, with a phase space density of 0.04. The transition from a Fermi gas of diatomic molecules to a Bose gas of tetratomic molecules paves the way for dipolar BCS–BEC crossover.

With microwave-shielded polar molecules, we have realized a quantum gas featuring highly tunable long-range interactions. The technique is universal to polar molecules with a sufficiently large dipole moment, and thus offers a general strategy for cooling and manipulating polar molecules, and for associating weakly bound ultracold polyatomic molecules. Utilizing the toolbox developed in ultracold atoms, this platform possesses the potential to unlock an entirely new realm of quantum simulation of many-body physics.

Publications

The papers listed below were published during the course of this PhD thesis. Those most relevant to this thesis are highlighted in bold font.

- Roman Bause, Ming Li, Andreas Schindewolf, Xing-Yan Chen, Marcel Duda, Svetlana Kotochigova, Immanuel Bloch, and Xin-Yu Luo, *Tune-out and magic wavelengths for ground-state $^{23}Na^{40}K$ molecules*. Physical Review Letters 125, 023201 (2020).

- Roman Bause, Andreas Schindewolf, Renhao Tao, Marcel Duda, Xing-Yan Chen, Goulven Quéméner, Tijs Karman, Arthur Christianen, Immanuel Bloch, and Xin-Yu Luo, *Collisions of ultracold molecules in bright and dark optical dipole traps*. Physical Review Research 3, 033013 (2021).

- Roman Bause, Akira Kamijo, Xing-Yan Chen, Marcel Duda, Andreas Schindewolf, Immanuel Bloch, and Xin-Yu Luo, *Efficient conversion of closed-channel-dominated Feshbach molecules of $^{23}Na^{40}K$ to their absolute ground state*. Physical Review A 104, 043321 (2021).

- Xing-Yan Chen*, Marcel Duda*, Andreas Schindewolf, Roman Bause, Immanuel Bloch, and Xin-Yu Luo, *Suppression of unitary three-body loss in a degenerate Bose–Fermi mixture*. Physical Review Letters 128, 153401 (2022).

- Marcel Duda, Xing-Yan Chen, Andreas Schindewolf, Roman Bause, Jonas von Milczewski, Richard Schmidt, Immanuel Bloch, and Xin-Yu Luo, *Transition from a polaronic condensate to a degenerate Fermi gas of heteronuclear molecules*. Nature Physics 19, 720-725 (2023).

- Marcel Duda*, Xing-Yan Chen*, Roman Bause, Andreas Schindewolf, Immanuel Bloch, and Xin-Yu Luo, *Long-lived fermionic Feshbach molecules with tunable p-wave interactions*. Physical Review A 107, 053322 (2023).

- Andreas Schindewolf, Roman Bause, Xing-Yan Chen, Marcel Duda, Tijs Karman, Immanuel Bloch, and Xin-Yu Luo, ***Evaporation of microwave-shielded polar molecules to quantum degeneracy***. Nature 607, 677-681 (2022).

- Xing-Yan Chen*, Andreas Schindewolf*, Sebastian Eppelt, Roman Bause, Marcel Duda, Shrestha Biswas, Tijs Karman, Timon A. Hilker, Immanuel Bloch, and Xin-Yu Luo, ***Field-linked resonances of polar molecules***. Nature 614, 59-63 (2023).

- Fulin Deng, Xing-Yan Chen, Xin-Yu Luo, Wenxian Zhang, Su Yi, and Tao Shi, ***Effective potential and superfluidity of microwave-shielded polar molecules***. Physical Review Letters 130, 183001 (2023).

- Xing-Yan Chen, Shrestha Biswas, Sebastian Eppelt, Andreas Schindewolf, Fulin Deng, Tao Shi, Su Yi, Timon A. Hilker, Immanuel Bloch, and Xin-Yu Luo, ***Ultracold field-linked tetratomic molecules***. Accepted by Nature, arXiv:2306.00962 (2023).

- Fulin Deng, Xing-Yan Chen, Xin-Yu Luo, Wenxian Zhang, Su Yi, and Tao Shi, ***Formation and dissociation of field-linked tetramers***. in preparation.

* *Equal contributions*

Contents

Further discoveries in another field (liquefaction of helium) have made necessary, in an unexpected connection, the examination of many properties (of substances) in the neighborhood of absolute zero.[1]

Heike Kamerlingh Onnes

Chapter 1

Introduction

The field of ultracold molecules has recently experienced remarkable advancements. I am fortunate to have witnessed these exciting developments during my PhD, and to have had the opportunity to contribute to the frontier of this field. This introduction provides the necessary background for the work presented in this thesis, with a particular emphasis on recent breakthroughs in the creation of Fermi degenerate molecules, the characterization of sticky collisions, and the realization of collisional shielding.

1.1 Ultracold molecules

Matter exhibits fascinating behaviors at low temperatures. When prepared under ultracold conditions,[2] molecules display quantum properties [1–4], making them suitable for applications such as quantum simulation [5,6] and computation [7–9], ultracold chemistry [10,11], and precision measurements [12,13]. These applications stem from the intricate internal structure of molecules and the tunable long-range dipole-dipole interactions. However, the complexity of these molecules poses challenges for the implementation of cooling techniques [14–18].

[1] This excerpt from Onnes' Nobel lecture outlines his research into the properties of matter at low temperatures, facilitated by the production of liquid helium. In a parallel vein, the realization of ultracold atoms has spurred the assembly of ultracold molecules.

[2] The definition of the "ultracold regime" is context-dependent. Most molecules already exist in their rovibrational ground state at room temperature. Achieving the hyperfine ground state typically necessitates cooling to submillikelvin temperatures. Further cooling to the submicrokelvin range is requisite to control the orbital degree of freedom, ensuring that the lowest partial wave predominantly governs intermolecular collisions. In the scope of this thesis, we focus on the 100-nK regime, where dipole-dipole interactions become the dominant force governing molecular collisions. At even lower temperatures, the gas reaches quantum degeneracy, laying the groundwork for the preparation of many-body ground states. This is the regime requisite for quantum simulation and is the ultimate goal of our experimental endeavors.

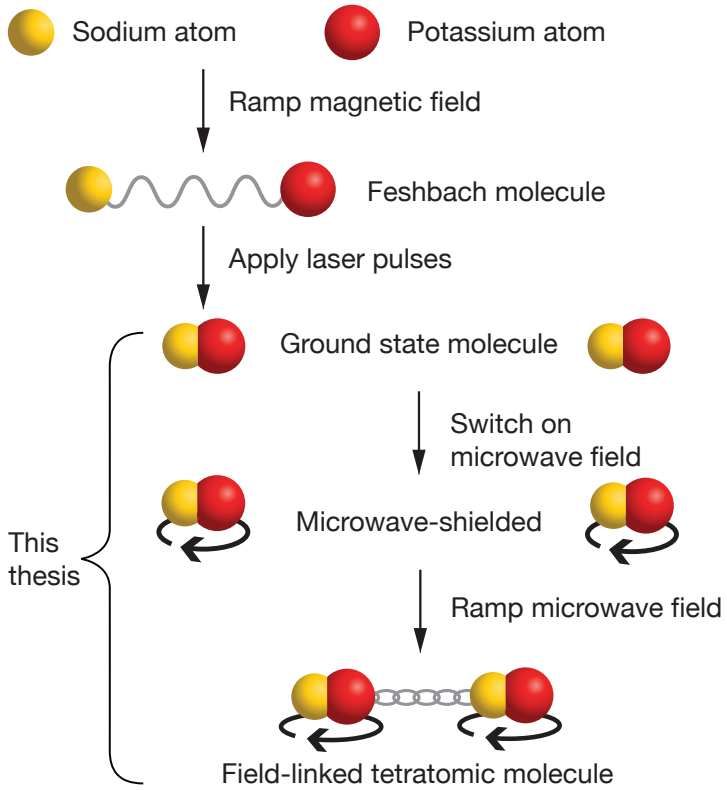

Figure 1.1: Assembly of ultracold tetratomic molecules. Starting from an ultracold mixture of sodium and potassium atoms, we first ramped the magnetic field through a Feshbach resonance to associate weakly bound Feshbach molecules. Next the diatomic molecules are transferred to their ground state via stimulated Raman adiabatic passage (STIRAP) by applying two coherent laser pulses. We subsequently switch on a microwave field, causing the molecules to rotate and interact via dipole-dipole interactions. By ramping the microwave field through a field-linked resonance, two sodium-potassium molecules come together to form a weakly bound tetratomic molecule. Figure inspired by Ref. [29].

The first molecules prepared under submicrokelvin temperatures were weakly bound homonuclear dimers, associated from degenerate atomic gases by photoassociation [19, 20] or magnetoassociation [21–23]. These assembled molecules inherit the ultracold temperatures of the degenerate atomic gases. The process of magnetoassociating a Bose-Einstein condensate (BEC) of Feshbach molecules [24–26] from a superfluid of two-component degenerate Fermi gases [27] represents the BCS–BEC crossover [28], a phenomenon with rich physics that has sparked a field of its own.

Following the success of homonuclear dimers, interest in heteronuclear dimers has grown. Heteronuclear dimers in the deeply bound state exhibit a large dipole moment, making them intriguing candidates for quantum simulation of many-body systems with long-range

interactions and the search for the electron electric dipole moment. The first ultracold ground-state polar molecules were realized at JILA, where ^{40}K^{87}Rb molecules were associated from an atomic mixture by magnetoassociation and transferred to the rovibrational ground state by stimulated Raman adiabatic passage (STIRAP) [30]. A similar technique was also demonstrated for homonuclear Cs_2 molecules [31]. Since then, several bialkali ground-state molecules, including ^{87}Rb^{133}Cs [32, 33], ^{23}Na^{40}K [34, 35], ^{23}Na^{87}Rb [36], ^{23}Na^{39}K [37], ^{23}Na^{7}Li [38], ^{23}Na^{133}Cs [39, 40], and ^{6}Li^{40}K [41, 42] have been created in this manner. NaCs [43], ^{85}Rb^{87}Rb [44], and RbCs [45] molecules have also been assembled from atoms trapped in optical tweezers.

Over the past decade, direct laser cooling [46–48] has made significant progress, catching up with the progress of molecular assembly. This has been achieved through breakthroughs in magneto-optical trapping (MOT) [49], sub-Doppler cooling [50–54], and subsequent loading of molecules into optical tweezer arrays [55–57] and sideband cooling [58,59]. These molecules can be directly imaged with high fidelity, offering an advantage for the detection and manipulation at the single molecule level. Moreover, theoretical calculations indicate that certain large polyatomic molecules can be laser cooled with a manageable number of lasers [60, 61]. While symmetric top molecules have been successfully laser-cooled in one dimension [62], the efficacy of laser cooling for larger molecules (tetratomic or beyond) in three dimensions — and down to the submicrokelvin regime — remains an open question.

The work presented in Chapter 7, together with Ref. [63], has allowed the molecule assembly method to enter the realm of ultracold polyatomic molecules. We formed ultracold tetratomic molecules from pairs of diatomic polar molecules, as shown in Fig. 1.1. The success of assembly relies on starting with a degenerate gas, ensuring that the wave functions of the dimers overlap sufficiently. The following sections present the challenges in achieving quantum degeneracy of these diatomic molecules.

1.2 Reaching quantum degeneracy

Homonuclear Feshbach molecules created from fermionic atoms were quickly brought to Bose-Einstein condensation shortly after their initial creation [24–26]. The key was to maintain the Feshbach molecules in a weakly bound state, allowing Pauli blocking to effectively suppress both atom-dimer and three-body losses. This suppression is absent in a heteronuclear mixture, and the collisional losses hinder efficient magnetoassociation. More than a decade after their first creation, heteronuclear molecules finally achieved quantum degeneracy. Here, Fermi degenerate Feshbach molecules were created from a BEC of Rb and a degenerate Fermi gas of K, where about 43% of Rb was converted into molecules [65]. This efficient conversion contradicted previous observations and simulations from the same group, which suggested that association efficiency decreases with the onset of the BEC due to the different quantum statistics of the mixed gases [66,67]. The puzzling high efficiency of KRb formation motivated us to investigate the mechanism behind the

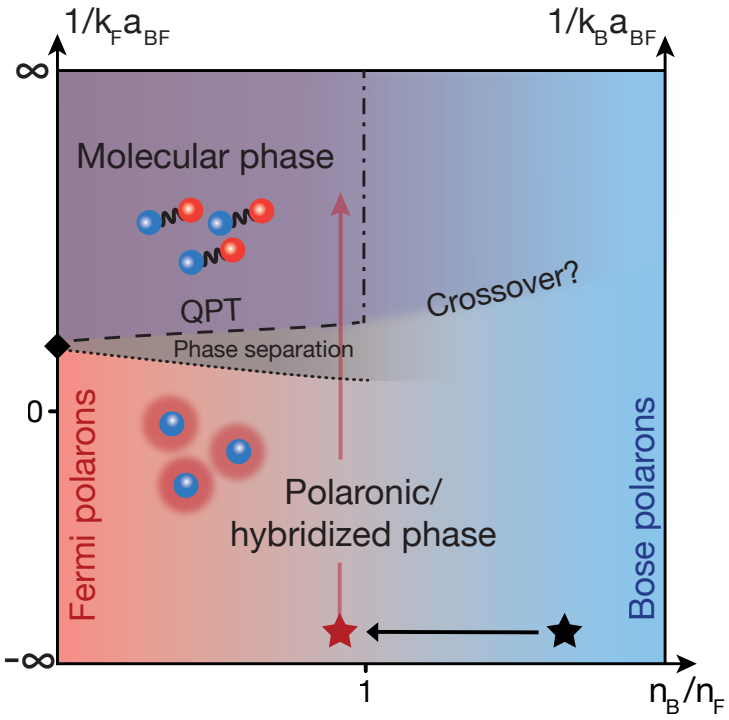

Figure 1.2: Quantum phase transition in a density-matched Bose–Fermi mixture. Phase diagram of degenerate Bose–Fermi mixtures, characterized by the density ratio n_B/n_F and the dimensionless interaction strength $(k_i a_{BF})^{-1}$. When $n_B < n_F$, a quantum phase transition between Polaronic and Molecular phases is expected. This transition may be of either first order, accompanied by phase separation, or second order. The long-dashed line in the diagram represents the critical point for the complete depletion of the condensate, given by $(k_F a_{BF})_c^{-1}$, while the dotted line marks the onset of phase separation at $(k_F a_{BF})_{\mathrm{ps}}^{-1}$ in cases where it occurs. Additionally, the dash-dotted line indicates a possible further quantum phase transition of unknown order. Experimental realization is achieved through a dual-color optical trap that allows for the density matching of the Bose–Fermi mixture (indicated by the red star). By ramping across a Feshbach resonance, Fermi degenerate Feshbach molecules are created (red arrow). Figure reproduced from Ref. [64].

magnetoassociation of a degenerate Bose–Fermi mixture.

Initially, magnetoassociation from a double-degenerate mixture did not yield successful results in our experiment due to the lighter mass of the Na and K atoms and the associated one-order-of-magnitude higher unitary losses near the Feshbach resonance [68, 69]. To overcome these losses, we matched the density between the mixed gases so that the BEC could be efficiently depleted and thus not simultaneously present with the dimers. With the suppressed losses, we investigated the process of magnetoassociation in the degenerate regime. As illustrated in Fig. 1.2 the high association efficiency should be understood as a result of an underlying quantum phase transition from Fermi polarons to molecules, whose order parameter can be directly probed by the condensate fraction [64]. Near the transition point, Bose and Fermi statistics are blended by the strong interspecies coupling, thus resolving the puzzle of phase space overlap.

The Fermi degenerate Feshbach molecules were subsequently transferred to the ground state by STIRAP. However, due to the limited STIRAP efficiency (80-90%), it randomly creates 10-20% holes in the Fermi sea, leading to heating. Moreover, the recoil energy and the sudden change of magnetic levitation after magnetoassociation further heat up the sample. Therefore, we still need a method to further cool down the molecules after their creation.

1.3 Sticky collisions

Historically, evaporative cooling has served as the final step in achieving quantum degeneracy in ultracold atoms. A prerequisite for evaporative cooling is collisional stability, i.e., a high ratio of elastic-to-inelastic collisions. Since the creation of the ground-state KRb molecules, the JILA group observed collisional loss in the optical trap [72]. They observed a *universal*[1] two-body loss [73], implying that every collision reaching short range results in a loss. This universal loss also occurs in the presence of a d.c. electric field [77], where the centrifugal barrier is reduced for collisions along the head-to-tail direction, leading to an increase in loss with the electric field strength. To suppress these reactions, they confined the molecules in a deep 3D optical lattice [78], and for the first time, observed dipolar spin-exchange interactions between molecules [79].

The realization of ultracold molecules has triggered extensive theoretical studies on their

[1] In this thesis, the term "universal" is employed in various contexts, and we summarize its use here. In every instance, "universal" refers to the broad applicability of the scattering calculation, which relies solely on the long-range potential and mass, regardless of the specifics of short-range interactions. First, "universal loss" assumes a unitary loss probability at short range, so the loss rate is entirely dictated by the long-range van der Waals and dipolar interaction, and the mass of the molecules [73, 74]. Second, the dipolar elastic collision between two polar molecules is governed exclusively by the dipole moment and the mass of the molecules [75]. Third, the field-linked resonance is universal because it stems from microwave-induced long-range interactions [76].

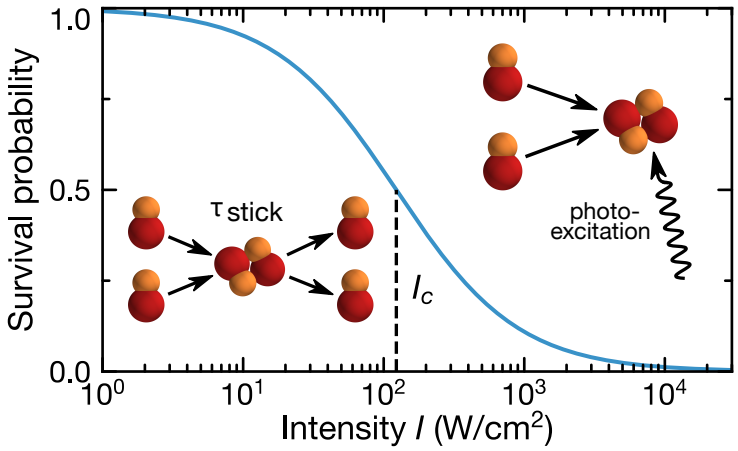

Figure 1.3: Sticky collisions of ultracold molecules. The survival probability of two molecules following a collision under the influence of 1064-nm light is calculated according Ref. [70]. In each collision, an intermediate sticky complex is formed. At high light intensities, these complexes are almost invariably lost through photoexcitation. Conversely, at low intensities, the complex is allowed to decay back into ground-state molecules, characterized by a mean sticking time of $\tau_{\text{stick}} = 18\,\mu$s [70]. The distinction between these two behaviors is characterized by a critical intensity I_c, marking the point at which the survival probability is 50%. Figure reproduced from Ref. [71].

collisional properties. However, the seemingly simple scattering problem of two diatomic molecules surprisingly remains poorly answered, due to the limited accuracy of the four-body potential energy surfaces [80] and a large number of intermediate states [81]. At that time, it was believed that the universal loss of KRb molecules was due to their chemical instability against the reaction to form K_2 and Rb_2, and that chemically stable molecules, including NaK, NaRb, NaCs, KCs, and RbCs, should be collisionally stable [82]. Encouraged by these perspectives, several experiments began to study these chemically stable molecules. However, nearly all the bialkali molecules studied so far [32,37,38,40,71,77,83–85], have exhibited nearly universal two-body losses, irrespective to their chemical stability. In 2022, a Feshbach resonance between NaLi in the spin-triplet state was reported [86]. For other bialkali molecules in the absolute ground state,[1] the occurrence of such resonances is less likely due to their greater mass and the absence of a magnetic moment.

To understand the mystery of universal loss, a series of papers proposed and refined the hypothesis of sticky collisions [70, 87–89]. This theory predicts that the intermediate product of the collision, i.e., the collisional complex, remains together long enough that the loss is due to photoexcitation or three-body collisions of these complexes before they are able to dissociate back. Two key parameters in this theory are the sticky time and the photoexcitation rate of the complex, as shown in Fig. 1.3. However, the sticky time is

[1] Here, the "absolute ground state" refers to the spin-singlet rovibrational ground state, which is of particular interest as it uniquely exhibits a large dipole moment in bialkali molecules.

challenging to calculate. Theory predictions from statistical models vary by several orders of magnitude, depending on whether or not the hyperfine state is preserved during the collision.

In a calculation by Christianen et al. [89], the sticky time was predicted to be much shorter than the inelastic collision rates of the molecules. Instead, they predicted that the complex lifetime would be limited by photoexcitation due to the trapping light [70]. If the theory is correct, the collisional loss can be suppressed by either trapping the molecules in the dark or chopping the trap to increase the dark time. Initially, experiments with KRb [90] and RbCs [91] agreed with the theory. The experiment in the Ni group was particularly convincing as they directly detected the intermediate complex by photoionization and mass spectroscopy [92]. However, subsequent experiments with fermionic NaK [71], bosonic NaK and NaRb [93], and NaCs [94] disagreed with the theory's prediction on either complex lifetime or photoexcitation rates by up to 5 orders of magnitude. To date, the sticky collision remains a mystery, but we have provided experimental bounds to the lifetime and photon scattering rates of the complexes for theory to work with [81], and new apparatuses to directly probe these complexes are under constructions.

Studies on atom–molecule collisions have also been conducted, with the perspective of sympathetically cooling molecules with atoms. In contrast to molecule–molecule collisions, many atom–molecule collisions show non-universal losses, and Feshbach resonances have been observed in NaK + K [95], NaLi + Na [96], NaRb + Rb [97]. Moreover, the Ketterle group has demonstrated sympathetic cooling, effectively cooling NaLi molecules using Na atoms, facilitated by a low collisional loss rate [98].

Ultimately, we need to overcome the universal loss of molecules to create a collisionally stable molecular sample, and collisional shielding appears to be the most promising approach.

1.4 Collisional shielding

Collisional stability of molecular gases has been achieved using shielding techniques with either d.c. or a.c. electric fields. The first instance of shielding was demonstrated by Jun Ye's group with KRb molecules confined in 2D pancake traps with a d.c. field perpendicular to the strong confinement [99]. In a 2D geometry, head-to-tail collisions are suppressed, leading to a predominance of repulsive side-by-side collisions [100, 101]. Later, the same group demonstrated Förster resonance[1] shielding in both 2D and 3D for molecules in the rotationally excited state [102–105]. This was accomplished by applying a targeted d.c. electric field to mix the rotational states and induce an avoided crossing, ensuring that the

[1]Typically, scattering resonances are associated with the emergence of a zero-energy bound state from the collisional threshold. In contrast, Förster resonances are not resonances mediated by specific tetramer bound states, as emphasized in Ref. [102]. In that context, resonance refers to the degeneracy of two threshold energies rather than the interaction with a particular bound state.

molecules remain on the repulsive branch of the potential energy surfaces.

However, d.c. field shielding requires a large electric field, which varies with the molecular species. For NaK, resonant shielding occurs at around 7 kV/cm [103]. Achieving this high electric field is challenging and requires careful design of the electrodes. Unfortunately, our in-vacuum electrodes are placed less than 1 cm from the glass cell. We observed stochastic charging of the glass cell for electric fields above 1 kV/cm. These charges shift the STIRAP transition and need to be removed by applying UV lights for approximately half an hour.

An alternative shielding method using a.c. electric fields was first demonstrated by the Doyle group with CaF in optical tweezer arrays [106]. This approach employs a high-power, circularly polarized microwave, that is blue-detuned to the first rotational transition of the molecules. Following this approach, we achieved a high ratio of elastic-to-inelastic collision rates with NaK molecules, enabling us to evaporatively cool them down to 21 nK and $0.36\,T_F$ [107]. Afterwards, microwave shielding was also realized in NaCs [108] and NaRb [109].

1.5 Manipulating interaction potentials: a route to field-linked tetramers

Microwave shielding is more than just a shielding technique. The versatile tuning capabilities of the microwave — power, frequency, and polarization — allow us to engineer the shape and depth of the interaction potential with a high degree of control. This is in stark contrast to collisions in the presence of static fields, where the potentials can only be relatively shifted by the Stark shift of the entrance channel.

With this unprecedented level of control over the interaction potential, we can induce scattering shape resonances,[1] known as field-linked (FL) resonances, between the microwave-shielded polar molecules [76,111,112]. This universal type of resonance provides a long-sought tool for ultracold molecules, enabling us to control the scattering length as is routinely done with ultracold atoms via Feshbach resonances.

Furthermore, we can gradually adjust the potential depth to adiabatically populate the long-range bound states associated with the FL resonances. In doing so, we create, for the first time, tetratomic molecules in the 100-nK regime with a phase space density (PSD) only two orders of magnitude below quantum degeneracy [113]. The FL tetramers represent an increase in PSD of eleven orders of magnitude compared to the coldest tetratomic molecules created prior to this work, see Table 1.1.

[1] A shape resonance in quantum mechanics is caused by a temporary trapping of a pair of particles within their interaction potential due to the shape of the potential energy curve, as depicted in Fig. 1.4. Unlike a Feshbach resonance, where the resonance occurs due to an interaction between two different channels, a shape resonance occurs within the same scattering channel.

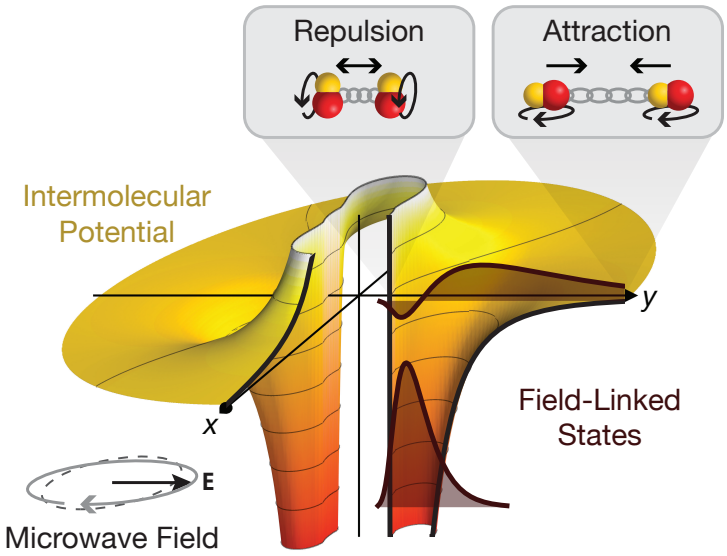

Figure 1.4: Field-linked resonances. Colliding dipolar molecules experience both attractive and repulsive interactions in a rotating microwave field. With a suitable elliptical deformation of the field, so-called field-linked states are created. Figure reproduced from Ref. [110].

Table 1.1: Polyatomic molecules that have achieved submillikelvin temperatures. The asterisk superscript denotes that the molecule is in a weakly bound state.

Molecule	Method	Temperature	PSD	Source
CaOH	direct laser cooling	57(8) μK (in trap)	$9(5) \times 10^{-8}$	[114]
NaK_2^*	magnetoassociation	$\sim$ 100 nK	$\sim$ 0.05	[63]
H_2CO	optoelectrical cooling	420(90) μK	5×10^{-13}	[115]
$(NaK)_2^*$	electroassociation	134(1) nK	0.040(3)	[113]

Looking back on the time when we realized evaporative cooling, we could have never predicted our progress with microwave shielding. Yet, this is merely the beginning. By optimizing initial conditions, it is possible to generate a BEC of tetratomic molecules and achieve a dipolar BCS–BEC crossover [116]. Furthermore, the FL tetramers provide an ideal starting point for optical transfer to deeply bound states. The physics of microwave-shielded molecules is a vast territory waiting to be further explored, promising many more developments in the near future.

1.6 This thesis

This thesis delves into the physics of microwave-shielded polar molecules. Chapter 2 provides an overview of the experimental setup, with a focus on the preparation of ultracold

^{23}Na^{40}K molecules and a 3D magic lattice for rotational qubits. Chapter 3 presents a microwave setup designed to realize microwave shielding. Chapter 4 covers the theory and experiment of microwave shielding and the process of evaporative cooling to achieve Fermi degeneracy. Chapter 5 presents the loading of microwave-shielded molecules into predominantly a single layer of a 3D optical lattice and the signature of spin-exchange interactions. Chapter 6 describes the realization of field-linked scattering resonances. Chapter 7 discusses the association of field-linked tetratomic molecules. Chapter 8 provides a comparative analysis between microwave shielding with other existing shielding techniques. Finally, Chapter 9 concludes the thesis and offers an outlook on potential future experiments.

Shall we do it NOW?[1]

Xin-Yu Luo (罗鑫宇)

Chapter 2

Experimental setup

This chapter covers the experimental setup. We discuss the preparation and detection of an ultracold gas of ^{23}Na^{40}K molecules, and a three-dimensional rotational-state independent magic optical lattice. The magic lattice plays a crucial role in enhancing the rotational coherence time of the molecules, a prerequisite for studying lattice spin models.

2.1 Making and probing ultracold ^{23}Na^{40}K molecules

The NaK apparatus was constructed by the first generation of students, Nikolaus Buchheim [117], Zhen-Kai Lu [118], and Frauke Seeßelberg [119]. Since then, our generation, including Roman Bause [120], Marcel Duda [121], and myself, have made several improvements, enabling us to routinely create $25,000$ ground state molecules at a temperature of $200\,\mathrm{nK}$ [121]. This ultracold molecular gas serves as the starting point for the work described in this thesis.

2.1.1 Double-degenerate atomic mixture

To create fermionic NaK molecules, we utilize the naturally occurring isotope of bosonic sodium, ^{23}Na, and the only stable fermionic potassium isotope, ^{40}K. The core of the setup is the ultra-high vacuum system (see Fig. 2.1). It comprises the main chamber, the science cell, and two oven regions for each of the two species. Sodium atoms from the oven travel through a Zeeman slower, while potassium atoms are transversely cooled by a 2D-MOT. We further increase the flux of potassium with a resonant pushing beam. Both sodium and potassium are then loaded into a MOT followed by a compressed MOT in the main chamber. We optionally perform gray molasses cooling for sodium at the end of the MOT, as described in my master's thesis [122]. After a typical MOT loading time of

[1] Thumbs up to Xin-Yu, who never allows technical challenges to deter him from pursuing new ideas.

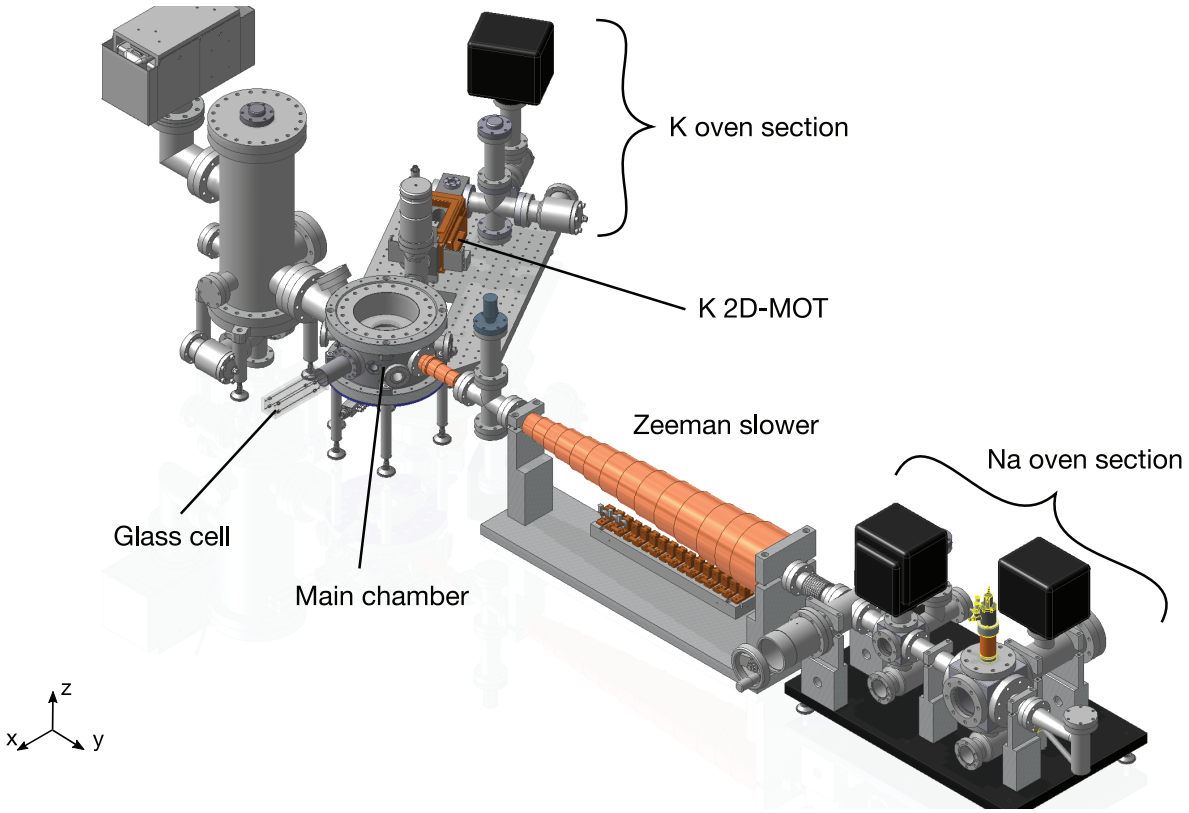

Figure 2.1: The vacuum system. The vacuum system of the NaK apparatus. The oven sections for sodium and potassium are connected to the central chamber via a Zeeman slower for sodium and a 2D-MOT chamber for potassium. Within the main chamber, both species are loaded into a 3D-MOT. Following evaporation within the magnetic trap, the atoms are transported to the glass cell where the experiments are conducted. Figure reproduced from Ref. [121]

2 s, both sodium and potassium are transferred to a plugged (532 nm) magnetic trap [123] and prepared in their stretched, low-field seeking hyperfine states, $|F, m_F\rangle = |2, 2\rangle$ and $|9/2, 9/2\rangle$. Sodium is then evaporated with a radio-frequency (RF) knife, while potassium is sympathetically cooled via elastic collisions. This process essentially conserves the number of potassium atoms, allowing us to start with small ^{40}K numbers, which is convenient because the fermionic isotope has a very low abundance — even in the enriched sample we use, only 3% are ^{40}K atoms. We then load the 6 μK cold mixture into an X-shaped transport trap generated by two 1064 nm laser beams at a 2.6° angle (power in each beam: 11 W, beam waist: $(w_x, w_z) = (100, 50)\,\mu$m), which we send in through the front facet of the glass cell. Right after loading the dipole trap, we transfer the sodium atoms into $|1, 1\rangle$ to minimize their collisional loss with potassium. We can move the atoms by 27 cm from the MOT chamber to the science cell, simply by shifting the focal point of the transport beam (13.5 cm in 1.1 s) using an air-bearing translation stage (Aerotech MTC150P). The X-shape design increases the transverse confinement to increase the speed of the transport.

To compress the mixture in the glass cell, we add a second far-detuned optical dipole beam horizontally, which forms a crossed dipole trap with the transport beam. Initially, we used a 1550 nm beam, but later replaced it with 1064 nm as we observed unexpected one-body loss which increases linearly with the power of the beam. We suspect that we hit some 1550 nm + 1064 nm transition of the molecules. In the crossed trap, the atoms are further evaporatively cooled to a mixture of 2.5×10^5 potassium atoms at $T/T_F = 0.2$, and 1.0×10^5 sodium atoms with a condensed fraction of more than 60%. Finally, we prepare the potassium in $|9/2, -9/2\rangle$ at a magnetic field of 80 G, right above the Feshbach resonance which we use to create molecules.

2.1.2 Molecular assembly

The sequence of molecule creation is shown in Fig. 2.2. First, a density-matched, double-degenerate mixture of ^{23}Na and ^{40}K atoms are associated into weakly bound Feshbach molecules via magnetoassociation, a process that involves ramping the magnetic field across a Feshbach resonance at 78.3 G. Detailed descriptions of the preparation process can be found in Refs. [121], and a reference of the relevant molecular states evolved is provided in Appendix A.

The key to creating a degenerate molecular gas lies in starting with a degenerate atomic mixture, and converting atoms to molecules as efficiently and adiabatically as possible. This is a challenging task due to the unitary collisional loss near the Feshbach resonance, which sets a lower limit for the ramp speed across the resonance. We have systematically characterized all loss processes involved [68, 69] and devised a density-matching technique to mitigate them [64]. By using a dual-color dipole trap, we differentially trap the potassium degenerate Fermi gas and the sodium BEC to match their 3D density distributions. This ensures that no global mass transport is needed for the gas to maintain thermal equilibrium during the association. More importantly, density matching efficiently converts the

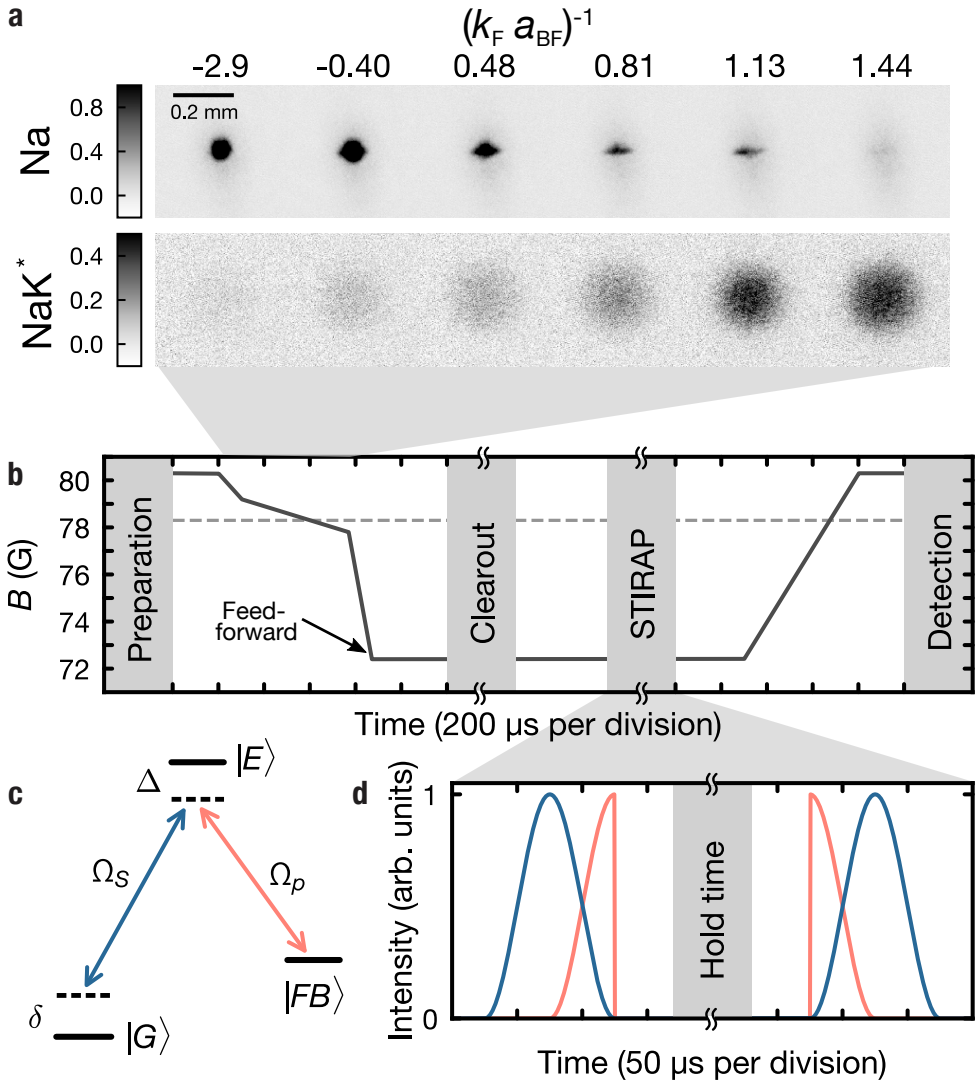

Figure 2.2: Magnetoassociation and STIRAP. a, Absorption images of the optical density (OD) of sodium (Na) atoms and Feshbach molecules (NaK*) following an 18-ms time of flight. These images capture the transition from the polaronic phase to the molecular phase. **b**, Magnetic field ramps utilized for the association and dissociation of Feshbach molecules. The term "Clearout" refers to a 20-ms magnetic field gradient pulse that serves to remove any unassociated atoms. The dashed gray line denotes the location of the Feshbach resonance. **c**, Schematic of the three-level system in STIRAP. The intermediate excited state $|E\rangle$ is linked to the Feshbach-molecule state $|FB\rangle$ by means of the pump beam (bright red), and to the ground state $|G\rangle$ via the Stokes beam (dark blue). **d**, Pulse shapes for the pump and Stokes beams in the STIRAP process. Figure reproduced from Ref. [64, 124].

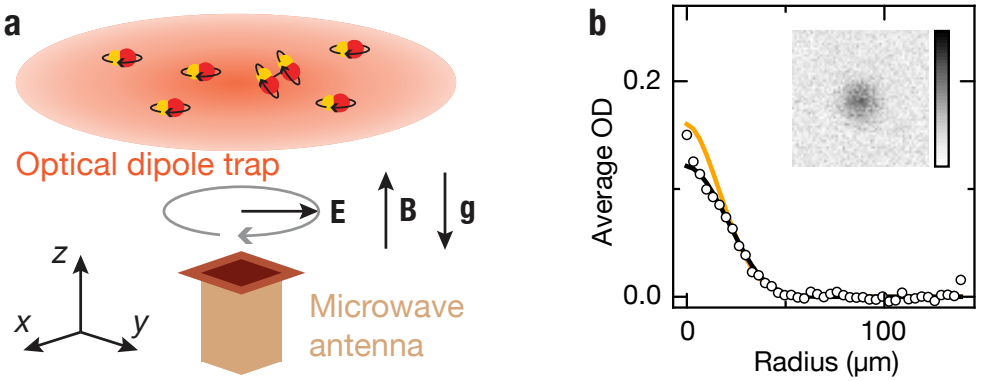

Figure 2.3: Trapped molecular gas. a, ground-state molecules driven by the microwave electric field emitted from a waveguide antenna. **b**, Time-of-flight image of molecules after evaporative cooling. Azimuthally integrated optical densities (OD) extracted from time-of-flight absorption images (inset). The black line is a fit to the Fermi–Dirac distribution Eq. (2.1), the orange line is a Gaussian fit to the thermal wing Eq. (2.4). The extracted temperature is 21(5) nK, corresponding to $T/T_F = 0.36(9)$.

BEC into molecules, thereby eliminating any remaining sodium atoms that could undergo inelastic collisions with the molecules. Using this technique, we can create up to 60,000 Feshbach molecules at a temperature of 120 nK, corresponding to $T/T_F \approx 0.3$, where T_F is the Fermi temperature. However, it should be noted that the Feshbach molecules are not in global thermal equilibrium as there are no elastic collisions to thermalize them.

Following magnetoassociation, the deeply bound Feshbach molecules can no longer be levitated by gravity due to their low magnetic moment, causing them to slosh in the trap. To compensate for this, we ramp up the magnetic field gradient to levitate the molecules while kicking out the atoms. Once the sloshing is mitigated, we are left with 70-80% of the molecules, which are heated up to 150 nK. Subsequently, the molecules are transferred to their rovibrational and hyperfine ground state via stimulated Raman adiabatic passage (STIRAP). The cloud is again heated by the two-photon recoil from the STIRAP beams, leaving us with typically 25,000 molecules at 200 nK, corresponding to $T/T_F \approx 1$. This provides the starting point for microwave shielding. Figure 2.3a illustrates the trapped molecules and the microwave antenna. Details about the microwave field generation is discussed in Chapter 3.

2.1.3 Imaging and thermometry

We use time-of-flight absorption imaging to obtain number and temperature of the molecules, as shown in Fig. 2.3b. If the microwave is applied to dress the molecules, we first need to ramp it off to transfer the molecules back to the non-dressed ground state. Subsequently, the dipole trap is turned off and return STIRAP pulses are applied to bring the molecules back into the weakly bound state. After time of flight, typically 10 ms, the

atoms are dissociated by ramping the magnetic field back over the Feshbach resonance. The magnetic field has to cross the Feshbach resonance slowly to minimize the release energy. In the end, the dissociated molecules are imaged via absorption imaging. We estimate that the derived temperature of the molecular sample could be overestimated by about 7(3) nK due to the residual release energy. This heating is confirmed by directly image the Feshbach molecules without dissociation. Nevertheless, we note that the values of T and T/T_F reported in this work do not account for the released energy [107].

To obtain the temperature of the molecular sample, we fit the absorption images with the Fermi–Dirac distribution

$$n_{\mathrm{FD}}(x,z) = n_{\mathrm{FD},0}\,\mathrm{Li}_2\left[-\zeta\exp(-\frac{x^2}{2\sigma_x^2}-\frac{z^2}{2\sigma_z^2})\right], \tag{2.1}$$

where $n_{\mathrm{FD},0}$ is the peak density, $\mathrm{Li}_2(x)$ is the dilogarithmic function, ζ is the fugacity and $\sigma_{i=x,z}$ are the cloud widths in the x- and z-direction. Given a cloud width σ_i, we can calculate the temperature T_i by

$$\sigma_i = \frac{\sqrt{1+\omega_i^2 t_{\mathrm{TOF}}^2}}{\omega_i}\sqrt{\frac{k_{\mathrm{B}}T_i}{M}}, \tag{2.2}$$

where ω_i is the trapping frequency in the i-th direction, t_{TOF} is the time of flight and M is the mass of the molecules. The fugacity can be associated to the ratio of the temperature T and the Fermi temperature T_F with the relation

$$\left(\frac{T}{T_F}\right)^3 = -\frac{1}{6\,\mathrm{Li}_3(-\zeta)}, \tag{2.3}$$

where $\mathrm{Li}_3(x)$ is the trilogarithmic function. $T_F = (6N)^{1/3}\hbar\bar{\omega}/k_{\mathrm{B}}$ is given by the molecule number N and the geometric mean trap frequency $\bar{\omega} = (\omega_x\omega_y\omega_z)^{1/3}$. By rewriting ζ and fixing T_F, we are only left with the fitting parameters $n_{\mathrm{FD},0}$, T_x, and T_z. We note that the temperature in the direction of the imaging beam T_y is assumed to be equal to T_x.

We can also independently fit the thermal wings of the cloud to a Gaussian distribution

$$n_{\mathrm{th}}(x,z) = n_{\mathrm{th},0}\exp\left(-\frac{x^2}{2\sigma_x^2}-\frac{z^2}{2\sigma_z^2}\right), \tag{2.4}$$

where $n_{\mathrm{th},0}$ is the peak density. Similar to Ref. [99], we first fit a Gaussian distribution to the whole cloud. We then constrain the Gaussian distribution to the thermal wings of the cloud by excluding a region of 1.5σ around the center of the image.

2.2 A magic 3D optical lattice

The molecules can be loaded into a three-dimensional (3D) magic lattice in the glass cell to establish the necessary conditions for realizing the desired Hamiltonian for quantum

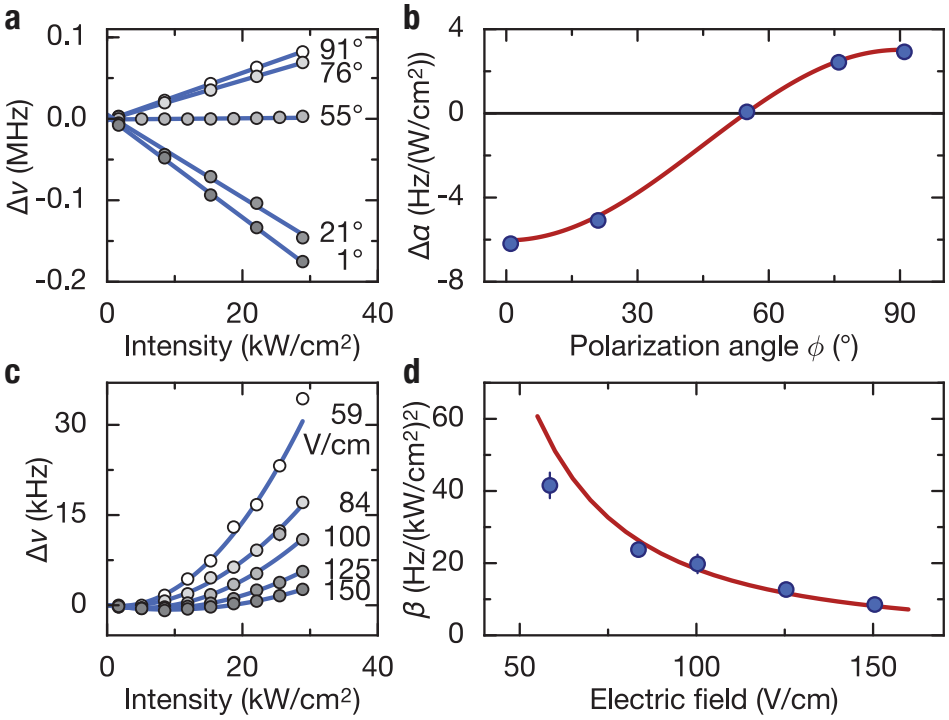

Figure 2.4: Polarizability and hyperpolarizability of a 1550 nm magic-angle trap. a, a.c. Stark data at $E = 144.3$ V/cm to extract the differential polarizability, $\Delta\alpha$. **b**, Differential polarizability $\Delta\alpha$ for various lattice polarization angles. At approximately 54° a magic trapping condition is fulfilled and the differential polarizability vanishes. **c**, a.c. Stark data to extract the hyperpolarizability β for five electric field values in units of V/cm. **d**, Hyperpolarizability β at the magic angle for various DC electric fields. The red lines in **b** and **c** show theory calculation. Figure reproduced from Ref. [119].

simulation. The lattice comprises a horizontal 2D lattice built by Scott Eustice [125] and a vertical shallow-angle lattice built by Quentin Redon [126] and Renhao Tao [127]. The lattice setup has previously been utilized to characterize photon scattering rates near a 866 nm narrow line transition [128], and to generate a double insulator for the creation of Feshbach molecules. Later, we adapted the setup to the magic conditions for the rotational molecular qubits and use it to study lattice spin models.

2.2.1 Magic trapping of diatomic molecules

Qubits encoded in rotational states of polar molecules, naturally interact via dipolar spin-exchange interactions. Given the long lifetime of ground state molecules, this platform is promising for studying spin dynamics and extended Hubbard models. To extend the coherence time of rotational qubits, it is crucial to eliminate the differential light shift between the rotational states, thereby achieving the so-called *magic* trapping.

Optical trapping, which utilizes the a.c. Stark shift from electric dipole transitions, is widely used for ultracold particles due to its flexibility in controlling the trap's shape and depth [129]. In a single-mode light field, the differential light shift between the states of interest, $|\downarrow\rangle = |J=0\rangle$ and $|\uparrow\rangle = |J=1, M_J\rangle$, can be expanded as a function of light intensity I

$$\delta\omega_{\downarrow\leftrightarrow\uparrow} = \frac{1}{\hbar}\left(\alpha I + \beta I^2 + \mathcal{O}\left(I^3\right)\right), \tag{2.5}$$

where α and β are the first- and second-order differential polarizability, which can be obtained from second-order and fourth-order perturbation theory. Magic trapping is achieved when the first-order differential light shift vanishes, with the leading order given by higher-order polarizabilities.

The a.c. Stark shift from second-order perturbation theory is described by the Hamiltonian [130, 131]

$$H_{\text{a.c.}} = -(\alpha^{(0)} + \alpha^{(2)} P_2(\cos\theta))I, \tag{2.6}$$

where θ is the angle between the laser polarization and the internuclear axis of the molecule. Translating to the lab frame, the Hamiltonian has the following matrix elements

$$\begin{aligned}\langle J', M_J'|I\alpha|J, M_J\rangle &= I\alpha^{(0)}\delta_{JJ'}\delta_{M_J M_J'} \\ &+ I\alpha^{(2)}\sum_M d^2_{0M}(\phi)(-1)^{M_N'}\sqrt{(2J+1)\,(2J'+1)} \\ &\times \begin{pmatrix} J' & 2 & N \\ 0 & 0 & 0 \end{pmatrix}\begin{pmatrix} J' & 2 & J \\ -M_J' & M & M_J \end{pmatrix},\end{aligned} \tag{2.7}$$

where $d^2(\phi)$ is the Wigner d-matrix, and ϕ is the angle between the polarization and the quantization axis. To avoid mixing by the off-diagonal coupling between rotational and hyperfine states, a large electric or magnetic bias field is applied so that the d.c. Stark

shift or the Zeeman splitting is larger than the off-diagonal coupling. In such cases, we can consider only the diagonal a.c. Stark shift, which yields

$$\alpha = \frac{2}{5}\alpha^{(2)} P_2(\cos\phi), \tag{2.8}$$

for $|\uparrow\rangle = |1,0\rangle$.

An approximation for β can be derived by considering the contribution from four-photon couplings to the excited states and back. It is related to the tensor polarizability $\alpha^{(2)}$ by [132]

$$\beta(E,\phi) = \frac{3B_{\mathrm{rot}}}{5d_0^2E^2}(\alpha^{(2)})^2 \sin^2(2\phi), \tag{2.9}$$

where B_{rot} is the rotational constant of the ground state manifold, d_0 is the dipole moment in the body-fixed frame of the molecule, and E is the amplitude of the d.c. electric field.

There are two general methods to realize magic trapping of polar molecules. The first method involves aligning the molecules to a "magic angle" of $\phi \approx 54°$ to the external field, where the tensor term $P_2(\cos\phi)$ vanishes. In this case, the hyperpolarizability is present but can be suppressed with a moderate electric field [132], see Fig. 2.4. This magic trapping scheme has been demonstrated in KRb [133], NaK [132], RbCs [134, 135], NaRb [136, 137], and CaF [138]. The magic-angle scheme works for linear polarization. An alternative off-resonant magic trapping scheme, which explores elliptical light polarization, was demonstrated with NaCs [139].

The off-resonant magic trapping scheme can be implemented with conveniently available trapping lasers, however, at the cost of high sensitivity to fluctuations of the polarization and the intensity of the laser. These problems are overcome in the second method, which does not require a specific alignment but requires trapping at a "magic wavelength" that is near-resonant to rotational or vibrational transitions between the ground state and a narrow-line excited electronic state. This adds additional terms to Eq. (2.6) which represent the near-resonant coupling. For state $|i\rangle = |\uparrow\rangle$ or $|\downarrow\rangle$, the near-resonant polarizability is given by

$$\alpha_i = -\sum_j \frac{z_{ji}^2}{2\hbar\epsilon_0 c}\frac{1}{\Delta_{ji}}. \tag{2.10}$$

Here $z_{ji} = |\langle j|\hat{\boldsymbol{d}}\cdot\boldsymbol{\epsilon}|i\rangle|$ denotes the coupling strength of a laser with polarization $\boldsymbol{\epsilon}$ on a dipole-allowed transition between states $|i\rangle$ and $|j\rangle$, and $\hat{\boldsymbol{d}}$ denotes the dipole-moment operator. Differential coupling can be achieved through the rotational selection rule. As illustrated in Fig. 2.5a, for $|\downarrow\rangle = |J=0\rangle$ the dominant contribution is the coupling to $|J'=1\rangle$ in the excited state, while for $|\uparrow\rangle = |J=1, m_J=0\rangle$ there is coupling to both $|j\rangle = |J'=0\rangle$ and $|J'=2\rangle$. By changing the detuning to these transitions, magic trapping can be achieved at various polarizations. Remarkably, for the magic wavelength at $\phi = 0$,

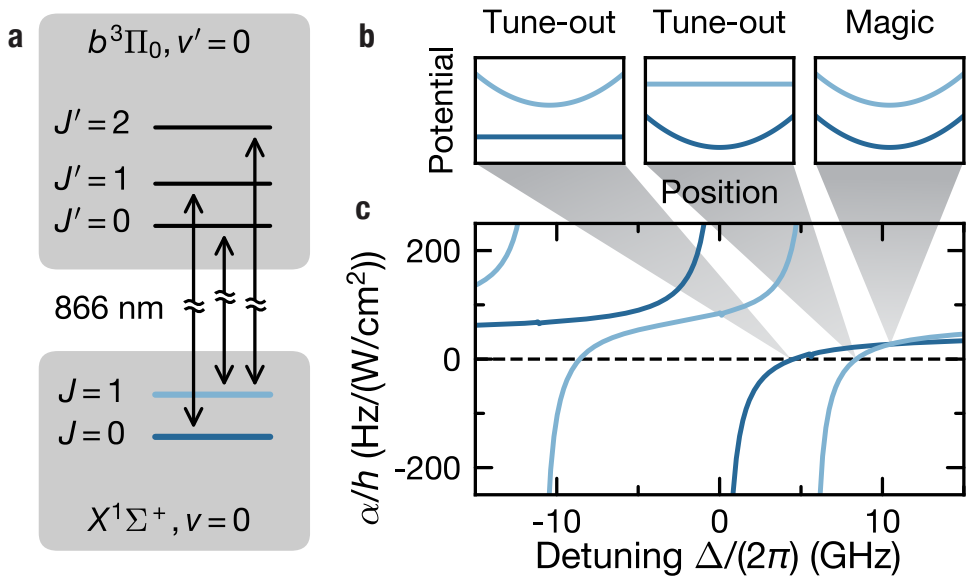

Figure 2.5: Magic-frequency trapping near the $X \leftrightarrow b$ transition. **a**, Level diagram of the NaK molecule, showcasing the $X \leftrightarrow b$ transition from $|\downarrow\rangle$ and the two nearest transitions from state $|\uparrow\rangle$. **b**, Schematic representation of the potential experienced by $|\downarrow\rangle$ (dark blue) and $|\uparrow\rangle$ (bright blue) molecules in a dipole trap. The left panel demonstrates the tune-out detuning for $|\downarrow\rangle$, the center panel shows the tune-out detuning for $|\uparrow\rangle$, and the right panel illustrates the magic detuning condition. **c**, Frequency-dependent polarizability for states $|\downarrow\rangle$ (dark blue) and $|\uparrow\rangle$ (bright blue), with the assumption of light polarization parallel to the quantization axis. Each pole in the graph corresponds to one of the transitions depicted in **a**. h denotes the Planck constant. Figure reproduced from Ref. [128].

the hyperpolarizability vanishes as well [124]. The same transition can also be used to realize tune-out and anti-magic trapping schemes.

We use the transition to the lowest electronic state manifold for the magic wavelength trapping of our molecules. This transition has a linewidth of 13.0(5) kHz, which is much narrower than the rotational constant, allowing for a large dynamic range of frequency tuning, and the photon scattering can be negligible at a detuning of a few GHz. The relevant constants of this transition can be found in Appendix A. Similar narrow-line transitions were explored in KRb [140], NaRb [141], and RbCs [142].

In the current experiment, we observe a maximum Ramsey coherence time of $T_2 \approx 1\,\mathrm{ms}$, which is limited by the d.c. electric field inhomogeneity of roughly 10 mV/cm [128]. With additional compensation electrodes, which are currently absent, we have achieved a Ramsey coherence time of 10 ms [132].

2.2.2 Basics of optical lattices

Two interfering laser beam generates a periodic lattice potential

$$V(x) = V_{\mathrm{lat}} \sin^2\left(\frac{\pi}{a}x\right), \tag{2.11}$$

with a lattice spacing $a = \lambda/2\sin(\theta/2)$ determined by the wavelength and the relative angle θ between the beams. The lattice depth V_{lat} depends on the intensity of the laser and the polarizability of the particles.

The lattice introduces a new energy scale, which is the recoil energy $E_{\mathrm{r}} = \hbar^2(\pi/a)^2/2m$. When the lattice is sufficiently deep $V_{\mathrm{lat}} \gtrsim 5E_{\mathrm{r}}$, the motion of a particle in the lattice is described by its quasimomentum q and the energy band $E(q)$. The dispersion relation of the ground band, which is of the most interest, can be approximated by [143]

$$E(q) = -2t\cos(qa) \tag{2.12}$$

$$t \approx \frac{4}{\sqrt{\pi}} s^{3/4} e^{-2\sqrt{s}} E_{\mathrm{r}}, \tag{2.13}$$

where t is the nearest-neighbor tunneling amplitude, $s = V_{\mathrm{lat}}/E_{\mathrm{r}}$ is the lattice depth normalized by E_{r}. In a deep lattice $s \gg 1$, each lattice site can be approximated by a harmonic trap with trapping frequency

$$\omega = 2\sqrt{s}E_{\mathrm{r}}/\hbar, \tag{2.14}$$

and the band gap can be approximated by $\hbar\omega$.

2.2.3 3D lattice and light sheet

The lattice beams are illustrated in Fig. 2.6. We employ two orthogonal, retroreflected 1064 nm beams to form a square lattice in the horizontal plane, with a lattice constant of

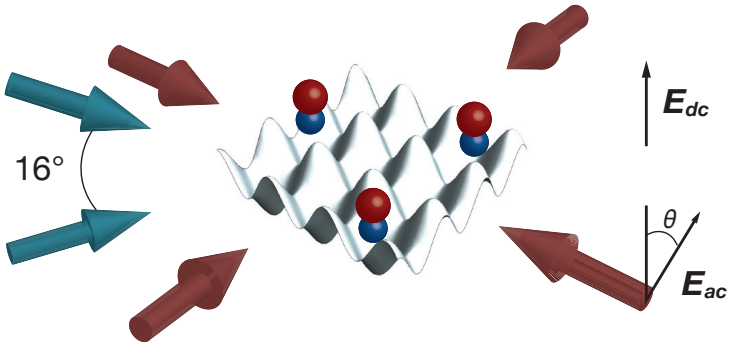

Figure 2.6: Schematics of the 3D lattice. Molecules loaded into a single plane formed by a 866 nm shallow-angle lattice (blue arrow). The horizontal lattice is formed by two pairs of retroreflected 1064 nm laser beams (red arrows). The polarization of the horizontal lattice is at the magic angle $\sim 54°$ to the vertical direction, which is also the quantization axis defined by the d.c. electric field.

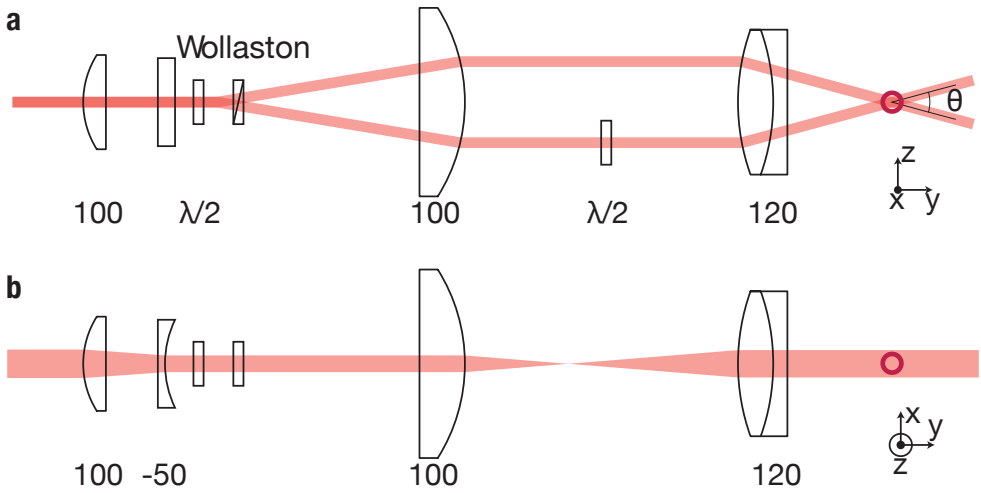

Figure 2.7: Shallow-angle lattice setup. Optics as projected on the plane along (**a**) or perpendicular (**b**) to the gravity axis. Non-labeled optics correspond to cylindrical lenses with a flat curvature in the projected plane. Lenses are labeled by their focal lengths in millimeters. The red circle marks the position of the molecules. Figure reproduced from Ref. [127].

532 nm, see Fig. 2.10. For the vertical lattice, we use two 866 nm beams propagating at an angle of 16°, forming a vertical lattice with a lattice constant of 3.1 μm. These two beams are derived from a Wollaston prism placed at the focus of a convex lens, see Fig. 2.9.

A light sheet at 785 nm, with a beam waist of 24 μm (the same beam used for density matching of the atomic mixture), is used to compress the molecules and enhance the loading efficiency into a single layer of the shallow-angle lattice. To maximize the contrast of the lattice, the polarization of the two beams should be aligned and linearly polarized in the lattice plane. This requirement leads us to use the magic wavelength method for the shallow-angle lattice. Using two pairs of half-wave plates, we align the polarization of the horizontal lattice beams to be at the magic angle with respect to the quantization axis defined by the electric field, which is in the vertical direction.

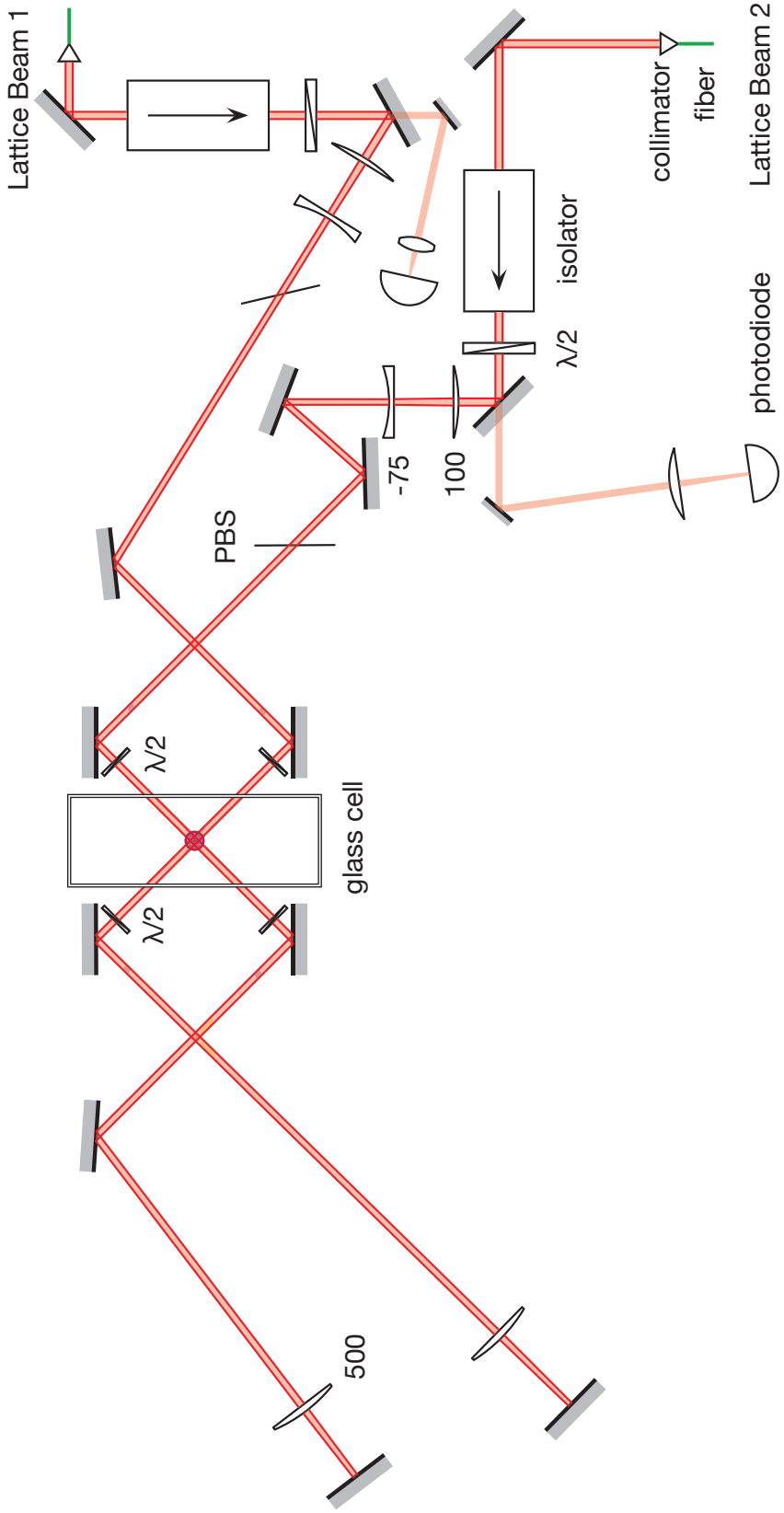

Figure 2.8: Horizontal lattice setup. Optics as projected in the horizontal plane. Lenses are labeled by their focal lengths in millimeters. Only the optics for the lattice beam 2 are labeled, as the same optics are duplicated for the other lattice beam. The red circle marks the position of the molecules. Figure reproduced from Ref. [125].

2.2.4 Calibration of the lattice depths

We calibrate the depth of the lattices using Kapitza–Dirac (KD) scattering of a BEC off the lattice potential. By pulsing the lattice, the BEC is diffracted into plane-wave components. The population dynamics of the diffraction pattern can be used to determine the lattice depth. For a strong pulse $s \gg 1$, the BEC will be significantly depleted and a number of diffraction peaks with momentum $\pm 2n\hbar k$ will be populated with a fraction proportional to [144]

$$P_n = J_n^2(sE_\mathrm{r}t/2\hbar), \tag{2.15}$$

where t is the pulse width and J_n is the ordinary Bessel function of order n. For the shallow-angle lattice, it is easy to enter the strong pulse regime, as the large lattice constant leads to a small E_r. The diffraction pattern and the extracted populations for the first 5 diffraction orders are shown in Fig. 2.9.

For a weak pulse $s \lesssim 4$, high-order diffraction is suppressed. We observe a coherent oscillation between $n = 0$ and 1, as shown in Fig. 2.10. The lattice depth can be obtained from the oscillation period T by [144]

$$s = \sqrt{2\left(\frac{h}{TE_\mathrm{r}}\right)^2 - 32}. \tag{2.16}$$

For the horizontal lattices, we can reach a maximum lattice depth of $180E_\mathrm{r,NaK}$ in each direction at a power of 10 W, corresponding to a band gap of 53 kHz. For the shallow-angle lattice, we can reach $440E_\mathrm{r,NaK}$ at a power of 150 mW in each beam, corresponding to a band gap of 3.4 kHz. For the shallow-angle lattice, we also double check the band gap with the parametric heating method. We modulate the lattice power to excite atoms from the ground band to the second excited band of the lattice, leading to heating and loss of atoms. The result is consistent with the KD scattering method.

With a BEC loaded into the 3D lattice we can also characterize the lattice depth by the superfluid to Mott insulator transition [145]. In addition, the lattice stability can be probed by measuring the lifetime of the superfluid. With an old vertical lattice setup we measured the lifetime of superfluid in the 3D lattice to be more than 9 s, indicating a heating rate less then 100 nK/s [125].

The 3D magic lattice provides the starting point for simulating dipolar lattice Hamiltonian, which will be the topic of Chapter 5. With the integration of a high NA objective [146] and Raman sideband cooling of ^{40}K atoms, we plan to realize a quantum gas microscope [147–149] for our molecules.

In the following chapter, we will introduce the microwave setup, a critical technique for microwave shielding that deserves its own dedicated chapter.

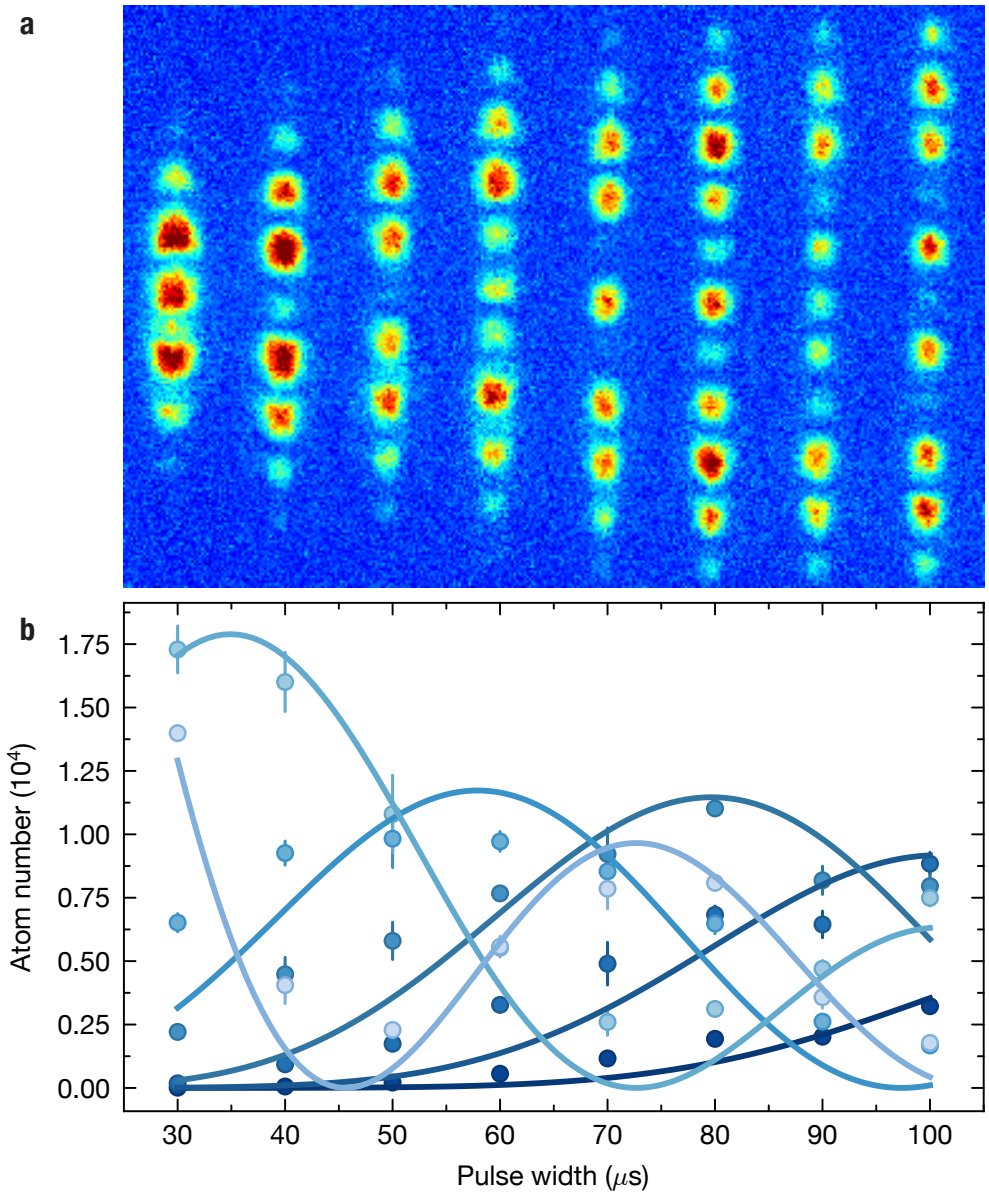

Figure 2.9: Kapitza–Dirac scattering of a Na BEC by the shallow-angle lattice. **a**, Time-of-flight images of a Na BEC after pulsing on the shallow-angle lattice beam at 180 mW power. **b**, Population oscillation extracted from **a**. The higher orders are represented by darker colors. The solid lines are obtained from a combined fit to Eq. (2.15).

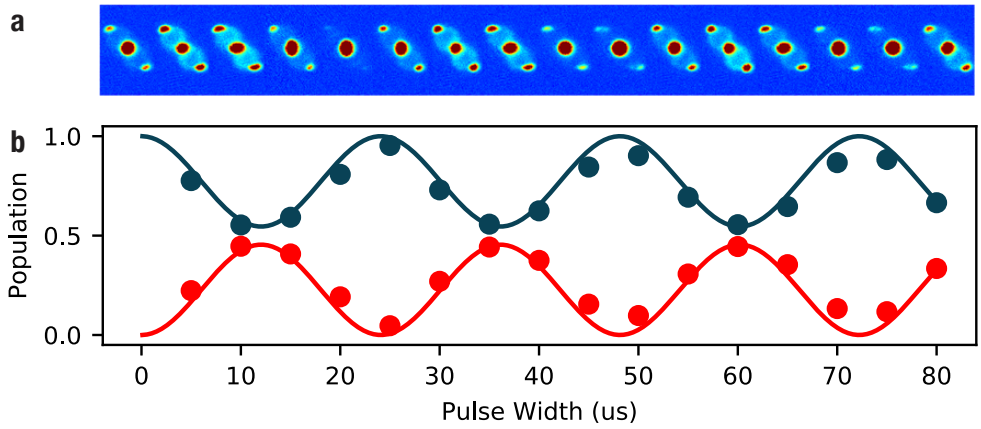

Figure 2.10: Kapitza–Dirac scattering of a Na BEC by the horizontal lattice. **a**, Time-of-flight images of a Na BEC after pulsing on one of the horizontal lattice beam at 2 W power. **b**, Population oscillation extracted from **a**. The main peak (dark blue) and the first diffraction peak (red) are fitted to a common oscillation period. Figure reproduced from Ref. [125].

You guys are really good with your hands![1]

PCB manufacturing company

Chapter 3

Microwave field generation

Microwave shielding serves as a versatile tool for stabilizing and manipulating intermolecular collisions. The primary challenge in realizing microwave shielding lies in generating a low-noise high-power microwave field with a clean circular polarization. Here, we present a setup designed to address this task. The microwave setup is capable of generating a high-power 5.6 GHz microwave field with tunable polarization and ultra-low phase noise, enabling us to explore microwave shielding and field-linked resonances. We have also implemented a monitoring setup to detect the actual output of the microwave field and actively stabilize the output power.

3.1 Microwave antennas

An antenna bridges the microwave circuits and free space, converting wave signals from a transmission line into electromagnetic waves that propagate through free space.

The antenna used for microwave shielding should fulfill two key requirements: it should produce a highly concentrated radiation field at the position of the molecules as well as offer tunable polarization. The ability to tune the polarization provides us with the flexibility to compensate for distortions caused by reflections from surrounding metal structures, including the steel vacuum chamber, magnetic field coils, and optics mounts.

3.1.1 Radiation fields

Given the geometric constraints of the glass cell, we need to operate the antenna (outside the vacuum) at a certain distance from the molecules. As a result there is an optimum gain/directivity which trades off the field concentration in the near-field and the divergence

[1] When the company's sales representatives inquired about the intended use of the ordered PCBs, we showcased our hand-soldered waveguide antenna (see Fig 3.3).

at the position of the molecules.[1] We can understand this optimization process with a Gaussian beam approximation to the radiation field.

Let us consider the radiation field of an antenna in free space. For a radiation power P, the maximum power density at distance r far away from the antenna is given by

$$p(r) = \frac{G_i P}{4\pi r^2} \quad (r \to \infty), \tag{3.1}$$

where G_i is the antenna directivity or gain. The corresponding field strength (amplitude) is given by

$$E_{\mathrm{mw}}(r) = \sqrt{\frac{G_i P Z_0}{2\pi r^2}}, \quad (r \to \infty), \tag{3.2}$$

where $Z_0 = \mu_0 c \approx 4\pi \times 30\,\mathrm{Ohm}$ is the vacuum impedance.

The radiation field in the near field can be approximated by a Gaussian beam

$$E_{\mathrm{mw}}(r) = \frac{E_0}{\sqrt{1 + (r/z_R)^2}}, \tag{3.3}$$

where the maximum field strength $E_0 = \sqrt{4PZ_0/(\pi w_0^2)}$ at an effective beam waist $w_0 = \sqrt{\frac{G_i}{2}}\frac{\lambda}{2\pi}$, with an effective Rayleigh range $z_{\mathrm{R}} = \frac{\pi w_0^2}{\lambda} = \frac{G_i}{8\pi}\lambda$. The formula approaches the simple $1/r$ equation when $r \gg z_R$. The Gaussian beam approximation works well when the effective beam waist w_0 is much larger than the wavelength λ, which is however not the case for our antenna. However, it provides a good starting point for more sophisticated numerical simulations.

From Eq. (3.3), the optimum gain to optimize the field strength at a given distance r is given by,

$$G_{i,\mathrm{opt}} = \frac{8\pi r}{\lambda}, \tag{3.4}$$

and the optimum field strength is

$$E_{\mathrm{opt}} = \sqrt{\frac{2PZ_0}{\lambda r}}. \tag{3.5}$$

For a frequency of 5.6 GHz and a distance $r = 22\,\mathrm{mm}$, the formula yields $G_{i,\mathrm{opt}} = 10\,\mathrm{dBi}$. With 10 W power, the optimum field strength is $E_{\mathrm{opt}} = 25\,\mathrm{V/cm}$.

The electric field corresponds to a Rabi frequency of

$$\Omega = \frac{dE_{\mathrm{mw}}(r)}{\hbar}, \tag{3.6}$$

[1] In the literature, it is common to encounter angular plots of antenna directivities, which characterize far-field radiation patterns. These plots may give readers the impression that higher directivity is always better. However, this notion can be misleading when it comes to near-field operations, as discussed in this text.

where $d = d_0/\sqrt{3}$ is the transition dipole moment between the ground and the first rotational excited state of the molecule. For NaK, the body-fixed dipole moment is $d_0 = 2.73(6)\,\mathrm{D}$ [150]. A field strength of $25\,\mathrm{V/cm}$ corresponds to a Rabi frequency of $\Omega = 2\pi \times 20\,\mathrm{MHz}$.

The a.c. electric field can be decomposed into σ^+ (σ^-) polarizations

$$\mathbf{E}_{\mathrm{mw}}(r) = \frac{E_{\mathrm{mw}}(r)}{2} e^{-i\omega t}(\hat{\mathbf{e}}_1 \cos\xi + \hat{\mathbf{e}}_{-1} \sin\xi) + \mathrm{c.c.} \tag{3.7}$$

where $\hat{\mathbf{e}}_{\pm 1} = \mp(\hat{\mathbf{e}}_x \pm i\hat{\mathbf{e}}_y)/\sqrt{2}$, and the angle ξ describes the ellipticity.

3.1.2 Different types of antennas

Various types of antennas have been employed in experiments involving ultracold molecules, including helical antennas [107], microwave horns [151], and phase arrays of loops [152] or helical [106] antennas. In this section, we will concentrate specifically on the antennas that have been utilized in our experimental setup, namely the helical antenna and the dual-feed waveguide antenna.

Dipole antenna

A dipole antenna comprises two opposing wires or one wire installed on a ground plane, with its mirror image serving as the counter feed. When the operation wavelength is a quarter of the wire's length, the antenna functions in the resonant mode, where the electromagnetic wave forms a standing wave within the wire. The radiation peaks in the wire's orthogonal plane, with a gain of $G_{i,\mathrm{dipole}} = 2.15\,\mathrm{dBi}$. Figure 3.1, shows a homemade dipole antenna with a large ground plane. We use it as a quick calibration tool for the microwave probe mentioned in the next section.

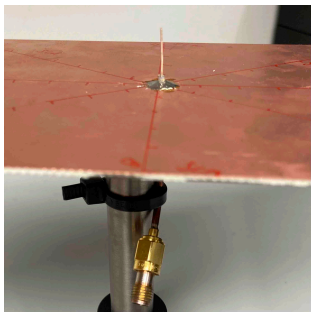

Figure 3.1: Dipole antenna.

Helical antenna

A straightforward method to generate a circularly polarized field is by employing a helical antenna, which consists of a helical wire mounted perpendicular to a ground plane. When the helix's circumference approximates the wavelength of operation, the antenna functions in the so-called axial mode, which directs the traveling wave away from the feedpoint. In this mode, the radiation is oriented along the helix axis, and the polarization is circular. The orientation of the radiation field aligns with the helix's winding, opposing the direction of radiation. Impedance matching is accomplished by adjusting the wire near the feedpoint, which serves as an impedance transformer between the helix and the ground plate. The gain of a helical antenna varies with its geometry and can be simulated numerically [153]. In general, the gain increases with the number of turns. For enhancing field strength, one

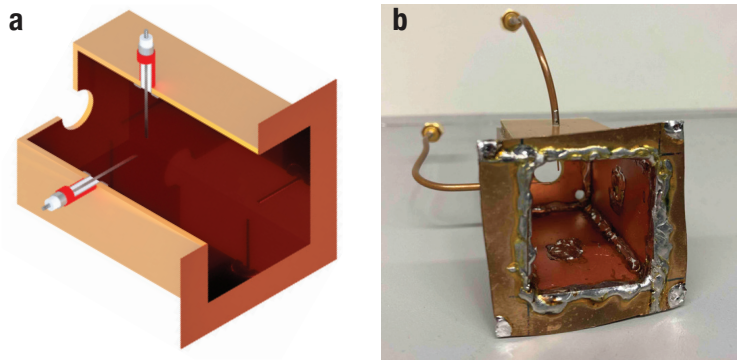

Figure 3.3: Dual-feed waveguide antenna. **a**, A cross-sectional view of the waveguide antenna, revealing the interior of the waveguide and illustrating the transition from the coaxial cable, distinguished by its red jacket, to the feed. **b**, Prototype of the waveguide antenna.

can combine four helical antennas to create a phase array [154] and connect each field to an amplifier. The amplified interference among the feeds can boost the field strength by a factor of four compared to a single helical antenna.

For the initial demonstration of microwave shielding and evaporative cooling, we utilize a single 5-turn helical antenna,[1] with a diameter of 18.8 mm and a vertical separation between turns of 12.4 mm, as shown in Fig. 3.2. Despite its high gain, it is incapable of compensating for the polarization distortion caused by the surrounding metals at the position of the molecules. Therefore, we have to adjust the polarization by wrapping a metal sheet around it. The sheet opening breaks its rotation symmetry, and can compensate for the imperfect polarization from the antenna [155].

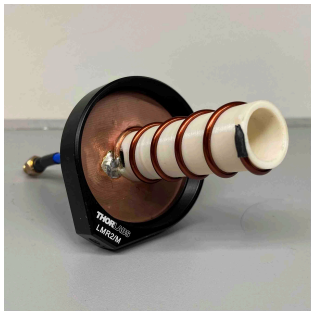

Figure 3.2: Helical antenna used in Ref. [107]

Waveguide antenna

Achieving tunable polarization requires additional degrees of freedom by incorporating more antennas. A simple method to synthesize tunable polarization involves summing two orthogonal linearly polarized fields with a controllable phase difference. Each linearly polarized field can be generated utilizing a dipole antenna.

To increase the gain of a dipole antenna, we can confine its radiation by mounting the antenna within a waveguide. In our experiment, the waveguide is manually soldered from copper-coated glass-fiber-reinforced epoxy laminates. The waveguide's inner dimensions are $w \times d \times h = 33 \times 33 \times 58$ mm. A flange of 10 mm broadens the effective opening of the

[1] The antenna is manufatured by Causemann Flugmodellbau. Similar antennas are widely used for controlling model aircraft, as circular polarization can maintain a more consistent signal than linear polarization when the orientation between the transmitter and the receiver are constantly changing.

waveguide and enhances the gain. The waveguide's width is selected such that the cut-off frequency $\omega_c = \pi c/w$ of the transverse electric (TE_{10}) mode is beneath the rotational transition frequency of the molecules at 5.6 GHz and that the microwave field strength at the position of the molecules is optimal. Impedance matching is achieved with two feeds, each 13 mm long, corresponding to a quarter wavelength in free space. In practice, the feed lengths are fine-tuned by minimizing the return loss using a network analyzer. To excite the base TE mode of the waveguide, the dipole feeds are placed 22 mm from the waveguide's backplate, roughly a quarter wavelength in the waveguide. The two feeds are orthogonal to each other, and each produces a nearly linearly polarized electric field at the position of the molecules, approximately 25 mm from the waveguide's top. Balancing the field strengths of these subfields and adjusting the relative phase of the feeds facilitates straightforward tuning of the field polarization. A relative phase of approximately 90° (−90°) results in a σ^+ (σ^-) polarized field, while approximately 0° (180°) produces a linearly polarized field along the y (x) direction.

The gain of an open-ended waveguide antenna is approximately given by [156]

$$\begin{aligned} G\ (\mathrm{dBi}) = -10.02819 + 41.30528 \left(\frac{\omega}{\omega_c}\right) - 51.80386 \left(\frac{\omega}{\omega_c}\right)^2 \\ + 36.23459 \left(\frac{\omega}{\omega_c}\right)^3 - 12.70621 \left(\frac{\omega}{\omega_c}\right)^4 + 1.751408 \left(\frac{\omega}{\omega_c}\right)^5, \end{aligned} \tag{3.8}$$

for $1.1 \leq \omega/\omega_c \leq 2$. The formula yields $G = 5.69$ dBi for the described geometry, which is less than numerical simulation with COMSOL, yielding $G = 6.47$ dBi. The discrepancy is partially attributed to the formula excluding the flange's enhancement.

Figure 3.4 shows the simulated radiation field by feeding a single feed with 10 dBm microwave power. Additionally, we include the glass cell and four electrodes in the simulation. The simulation matches the field strengths measured with a microwave probe (see Section 3.2).

There are several improvements to make for the current antenna setup. Firstly, the gain is lower than optimum gain estimated in Eq. (3.4). In a later version we increase the gain of the antenna by incorporating an additional horn, which realizes a higher field strength at the position of the molecules [151]. However, the horn's size is too large to accommodate our setup. Thus we fill the horn with Teflon to decrease the wavelength, thereby reducing the horn's size and also achieving a better impedance matching with the glass cell. Secondly, the cross talk between the two feeds can be reduced with a rectangular waveguide, which allows placing the two feeds at different heights [151].

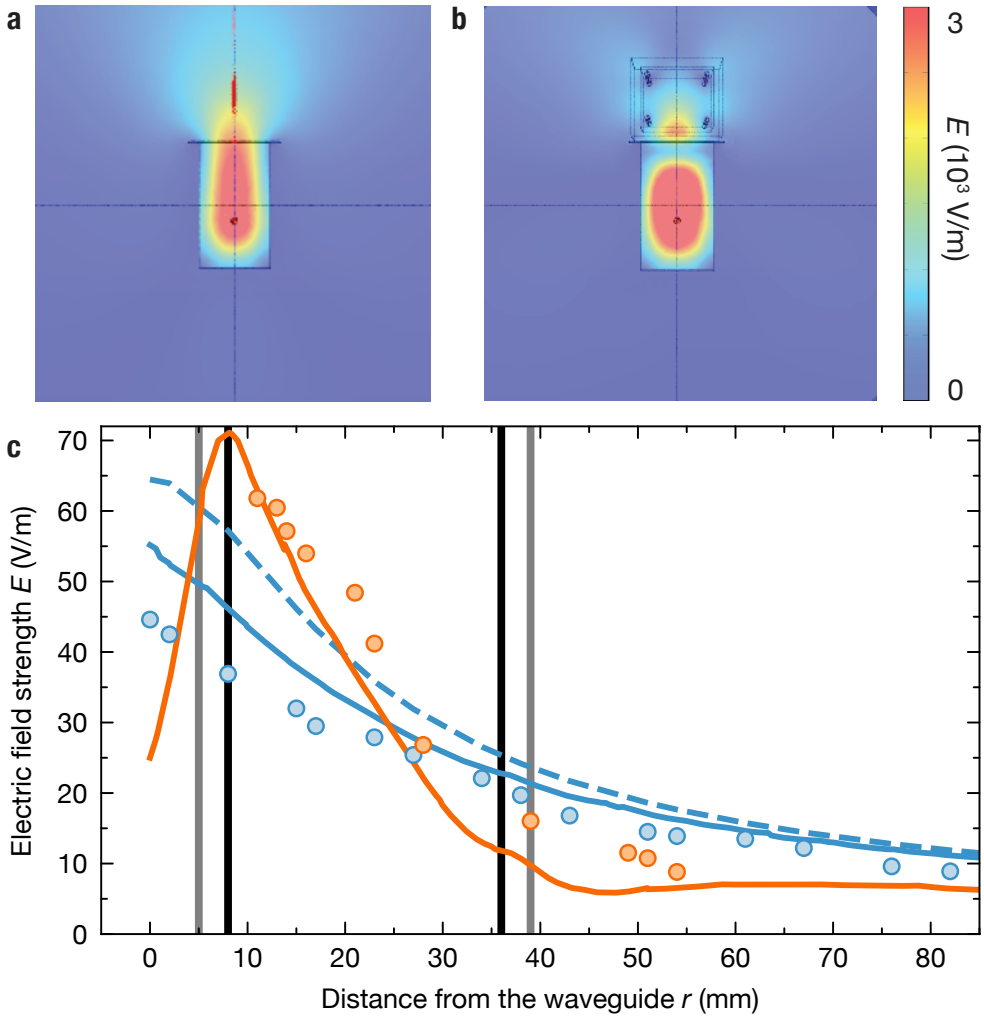

Figure 3.4: Radiation pattern of the waveguide antenna. COMSOL simulation of the radiation pattern with (**a**) and without (**b**) the glass cell and electrodes. The simulation is performed with 10 W in one feed, and the second feed being terminated. **c**, Electric field strength along the center of the waveguide. Blue and orange color represent with and without glass cell and electrodes, respectively. The vertical black lines represents the position of the electrodes and the vertical gray lines represents the glass cell. The solid data points are measurements with the microwave probe (see Section 3.2). The measurements are performed with 10 mW in one feed, and the second feed being terminated. The solid lines are the COMSOL simulation. The dashed line is the Gaussian beam approximation Eq. (3.3), which deviates from simulation in the near field.

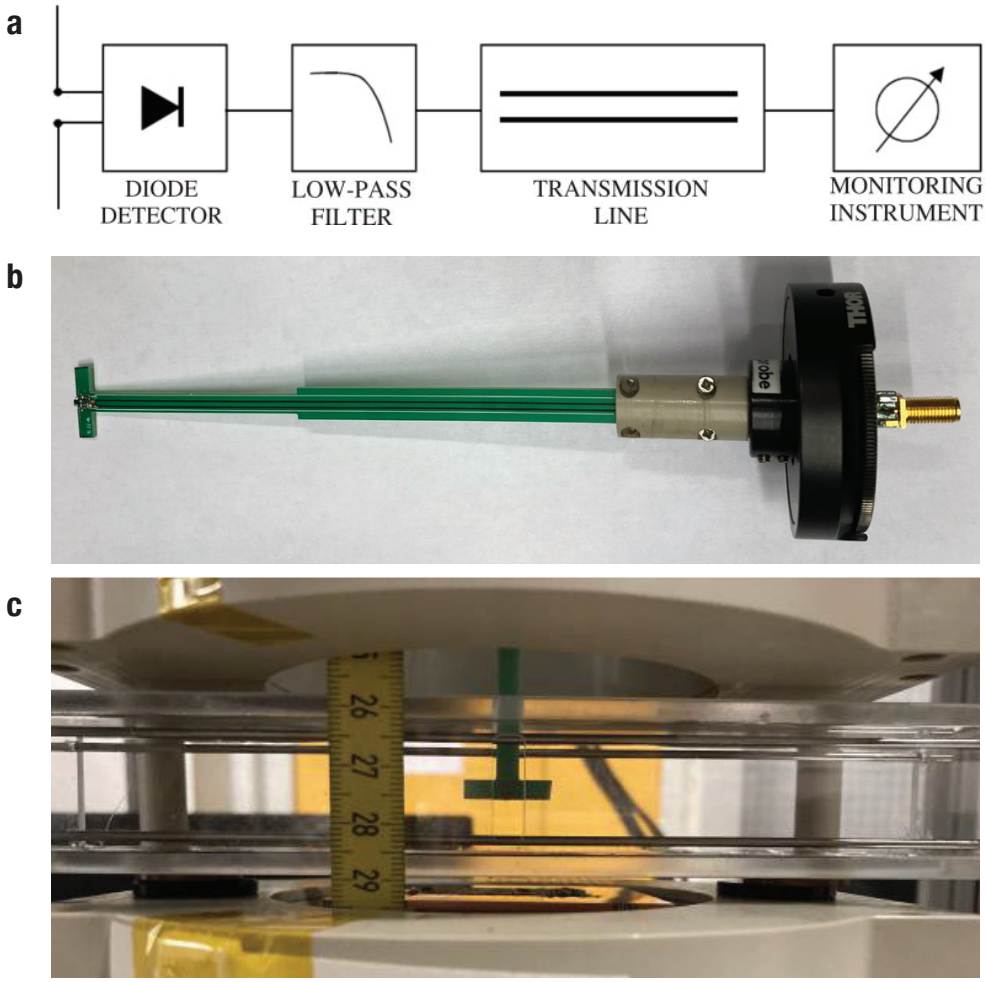

Figure 3.5: Dipole microwave probe. **a**, Schematics of the dipole probe. It consists of five main components: a short dipole printed on dielectric substrate, a nonlinear detector (zero-bias Schottky diode) connected between dipole arms, a low-pass filter, a resistive transmission line (printed carbon) and a monitoring instrument. Figure reproduced from Ref. [157]. **b**, Photo of the probe attached to a rotation mount. **c**, Test setup for simulating the electric field strength inside the glass cell, surrounded by four electrodes and the magnetic coils.

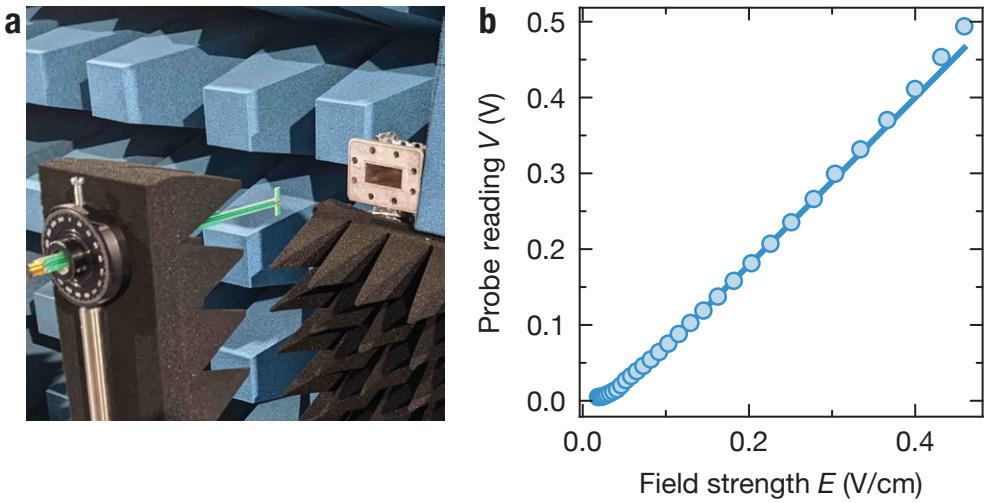

Figure 3.6: Calibration of the microwave probe. **a**, Calibration of the probe against a standard waveguide antenna. The measurements are conducted in an anechoic chamber and the setup is covered by microwave-absorptive materials. **b**, Probe reading vs. electric field strength. The solid line is a fit to Eq. (3.9). The measurement was conducted by Shrestha Biswas and Christian Buchberger.

3.2 A dipole microwave probe

3.2.1 Design

To swiftly iterate through various antenna designs, we have constructed a dipole probe based on the design in Ref. [157]. The dipole antenna samples the a.c. electric field, which is then followed by a rectifying diode and a low-pass filter that converts the signal into d.c. The rectifying diode is a BAT15-03W Schottky diode with a high speed and a small offset. We utilize a combination of 100 kΩ and 1 nF for the low-pass filter, corresponding to a cutoff frequency of 1.6 kHz.

The length of the dipole is approximately $\lambda/3 = 18$ mm for the operating frequency, representing a compromise between sensitivity and spatial resolution. To minimize disturbance to the microwave field by the probe, we connect the dipole probe to a high impedance (1 MΩ) voltage meter via 200 mm long carbon wires with a high resistance of 7.5 kΩ.

3.2.2 Calibration of the sensitivity

We calibrate the probe's response to electric field at our working frequency using a commercial waveguide antenna with a well-simulated gain. The measurements are conducted in an anechoic chamber, with all nearby metal surfaces covered in microwave-absorptive materials. These materials, structured like a series of cones, essentially eliminate normal reflections from the surface.

The relationship between the probe reading and the field strength is dictated by the response of the rectifier diode, which behaves quadratically in the small signal regime and linearly in the large signal regime. We have derived an empirical expression to fit the response curve,

$$\left(\frac{V - V_0}{a}\right)^2 - \left(\frac{E - E_0}{b}\right)^2 = 1, \tag{3.9}$$

which results in $E_0 = 4.04\,\mathrm{mV/cm}$, $V_0 = -43.7\,\mathrm{mV}$, $a = 44.4\,\mathrm{mV}$, $b = 39.8\,\mathrm{mV/cm}$.

3.2.3 Characterizing the waveguide antenna

Using the probe, we assess the field strength and ellipticity of the antenna. As shown in Fig. 3.5c, we devise a setup resembling the glass cell, electrodes, and magnetic field coils, and place the probe at the position of the molecules. The probe measures a field strength which aligns with the simulation. By individually feeding 2.5 dBm to each feed and measuring the field with the probe over a full 360° rotation, we found that each feed emits an almost linearly polarized field, with an axial ratio of about 4:1. The deviation from linearity is likely due to cross-talk between the two feeds. In subsequent designs, we experiment with rectangular waveguides, where the feeds can be placed at different heights, thereby reducing cross-talk and improving the axial ratio to 10:1 [151].

3.3 Characterizing the microwave field with molecules

3.3.1 Microwave transitions

We utilize the rotational transition between the $J = 0$ and $J = 1$ states for microwave shielding. The full hyperfine structure of the excited rotational state $J = 1$ is showcased in Fig. 3.7a. The molecular Hamiltonian and the relevant constants are provided in Appendix A. Unlike the situation in CaF [106], NaK, similar to all bialkali molecules, lacks fine structure in the electronic ground state. Therefore, the rotationally excited states, which can couple to the absolute ground state and possess $(m_{i,\mathrm{Na}}, m_{i,\mathrm{K}}) = (3/2, -4)$ character, are distributed over just a few hundred kilohertz, substantially less than the microwave detunings utilized for shielding. Here, $m_{i,\mathrm{Na}}$ and $m_{i,\mathrm{K}}$ represent the projections of the nuclear spins of Na and K onto the magnetic field axis, respectively. In a strong microwave field, the nuclear spin projections are purified, maximizing the transition dipole moment (TDM) to the value of $d_0/\sqrt{3}$.

3.3.2 Field strength

We measure the effective Rabi frequency $\Omega_{\mathrm{eff}} = \sqrt{\Omega^2 + \Delta^2}$ at detunings sufficiently large to inhibit coupling to undesired transitions. For these measurements, we temporarily deactivate the optical dipole traps to circumvent ac Stark shift from the trapping light. We then generate a rectangular microwave pulse using a fast microwave switch that controls the

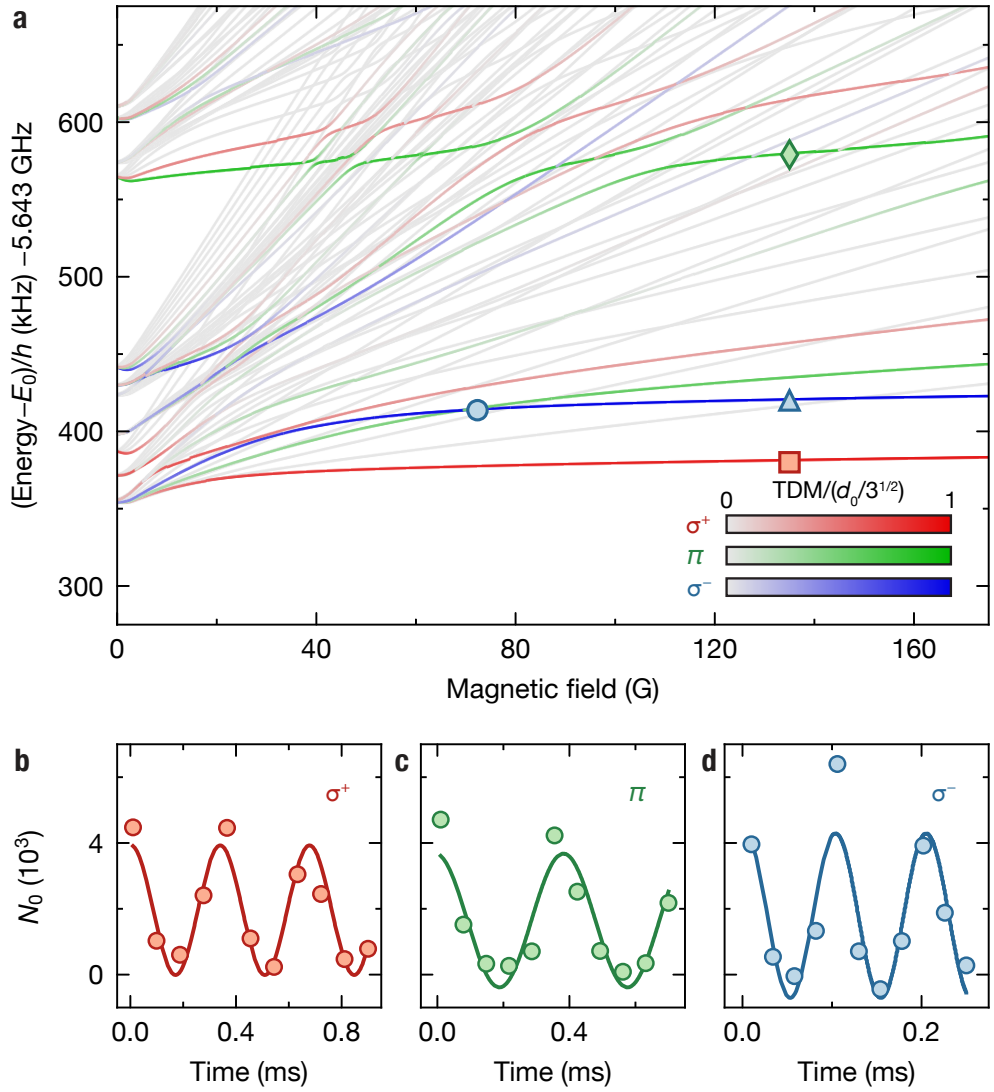

Figure 3.7: Microwave transitions of NaK molecules. **a**, Zeeman diagram illustrating the microwave transition frequencies from the absolute ground state (with energy E_0) to the hyperfine manifold of the excited rotational state ($J = 1$). The color scales represent the transition dipole moment (TDM) for different microwave polarizations. The assumption is that the ground state has the nuclear spin projections $(m_{i,\mathrm{Na}}, m_{i,\mathrm{K}}) = (3/2, -4)$, a good approximation for magnetic fields exceeding 3 G. The state energies and TDMs are computed using the code from Ref. [158] and the parameters detailed in Appendix A. Symbols indicate specific transitions: the circle marks the σ^- transition used for microwave shielding, while the diamond, triangle, and square highlight the microwave transitions employed to probe the polarization of the microwave field. **b**–**d**, Resonant Rabi oscillations at the σ^+ (**b**), π (**c**), and σ^- (**d**) transitions shown in **a**, taken at 135 G. The sinusoidal fits yield Rabi frequencies of $2\pi \times 2.96(8)$ kHz, $2\pi \times 2.58(13)$ kHz, and $2\pi \times 9.9(4)$ kHz, respectively. The microwave power is attenuated by 55 dB in **b** and 61 dB in **c** and **d**. Figure reproduced from Ref. [107].

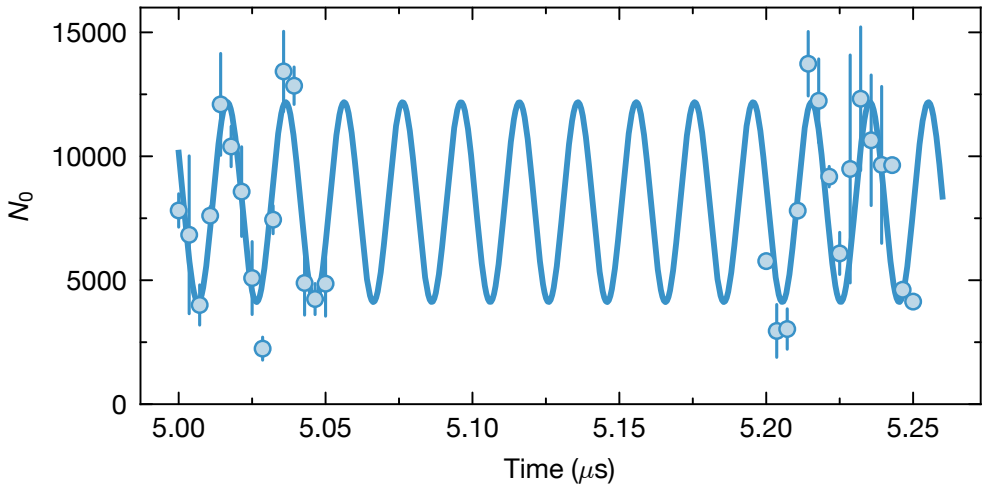

Figure 3.8: Fast Rabi oscillation. Off-resonant Rabi oscillations at full microwave power with a detuning of $\Delta = 2\pi \times 8\,\mathrm{MHz}$ from the σ^- transition at 72.35 G. The data show the number of molecules in the absolute ground state N_0 as a function of the pulse time. The error bars are the standard error of the mean of two repetitions. The line is a sinusoidal fit function that yields a Rabi frequency $\Omega = 2\pi \times 49.6(2)\,\mathrm{MHz}$.

input of our microwave amplifier. The microwave pulse induces Rabi oscillations between the rotational states, as depicted in Fig. 3.8. We exclude the oscillations during the initial $5\,\mu$s of the microwave pulse from the fit, as the amplifier requires some time to reach full output power. These measurements are conducted at low molecule density to prevent dephasing and inelastic collisions between the molecules. At the maximum achievable power, i.e. 100 W in each feed, we achieve $\Omega = 2\pi \times 49.6(2)\,\mathrm{MHz}$.

3.3.3 Polarization

We use different microwave transitions of the molecules to characterize the polarization of the microwave field in situ. In order to resolve the individual transitions, only weak microwave fields can be applied. As a result, the microwave polarization can only be characterized in the frame of the d.c. magnetic field which defines the quantization axis at such low microwave field strengths. We probe the polarization at 135 G, where we can still stabilize the magnetic field and where the used transitions, marked in Fig. 3.7a, are reasonably isolated. The TDMs of the selected σ^+, π, and σ^- transitions are $0.875\,d_0/\sqrt{3}$, $0.789\,d_0/\sqrt{3}$, and $0.989\,d_0/\sqrt{3}$, respectively. From the measured Rabi frequencies, the relative microwave power, and the TDMs, we can determine the ratio of the electric field amplitudes. The measurements, shown in Fig. 3.7(b–d), are performed similarly to the measurements of Ω_{eff} as described earlier. However, here we measure on resonance and the microwave power is attenuated by 55–61 dB. The microwave power has to be low enough to avoid off-resonant coupling to neighboring transitions but strong enough to realize Rabi oscillations of at least $2\pi \times 2\,\mathrm{kHz}$, because we can only turn off the dipole traps for about

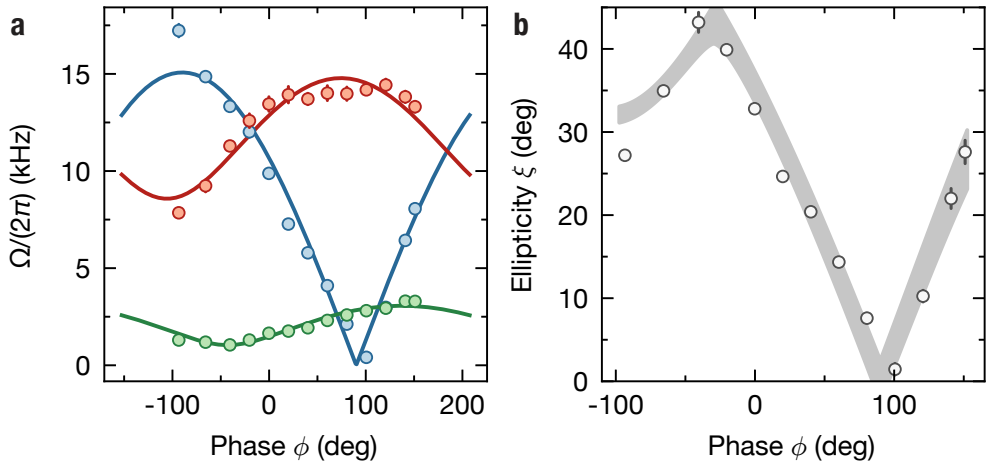

Figure 3.9: Calibration of the field polarization. **a**, Rabi frequencies of rotational σ^+ (red), π (green), and σ^- (blue) transitions at low microwave power as a function of the phase shift ϕ between the antenna feeds. The error bars show the fitting error of the Rabi oscillations. The solid lines are fits to Eq. (3.11). **b**, Ellipticity of the microwave field in the frame of the microwave. The data points show the ellipticity angle ξ calculated from the data in **a**. The error bars denote the uncertainty of ξ that originates from the projection from the frame of the magnetic offset field to the frame of the microwave field due to the unknown phase relation between the three field components (see Appendix C). The gray band, derived from Eq (3.10), accounts for the uncertainty of both the microwave orientation and the offset phases ϕ_0, with its width encapsulating these combined uncertainties. Figure reproduced from Ref. [112]

1 ms before we start losing molecules.[1]

The measured field components at low fields are relative to the quantization axis defined by the magnetic field, which is vertical in the lab frame. At high fields, however, the quantization axis is defined by the microwave, and due to environmental reflections, it is not necessarily vertical. We need to obtain the ellipticity relative to the microwave frame. If the orientation of the microwave is unknown, we can only provide a possible range of the ellipticity, leading to a systematic uncertainty of the ellipticity

$$\frac{1}{2}\arcsin\left(\frac{2E_+E_- - E_\pi^2}{E_+^2 + E_-^2 + E_\pi^2}\right) \leq \xi \leq \frac{1}{2}\arcsin\left(\frac{2E_+E_- + E_\pi^2}{E_+^2 + E_-^2 + E_\pi^2}\right). \tag{3.10}$$

Here $E_i = \hbar\Omega_i/d_i$ denotes the electric field strengths for the ith component, where $i = \sigma^\pm$ or π. With additional knowledge about the orientation angles, we can unambiguously determine the ellipticity (see Appendix C).

3.3.4 Polarization tuning

When we change the relative phase ϕ between the feeds, each field component, and thus each Rabi frequency, individually oscillates with a period of 360° due to the interference between the two subfields, as shown in Fig. 3.9a. We fit these oscillations with the function

$$\Omega(\phi) = \sqrt{\Omega_1^2 + \Omega_2^2 + 2\Omega_1\Omega_2\cos(\phi + \phi_0)}, \tag{3.11}$$

with the fit parameters Ω_1 and Ω_2, which define the contributions of the two individual feeds, as well as their relative phase ϕ_0. The offset phases ϕ_0 have an uncertainty of 2.9°, which we attribute to the hysteresis and imperfect tuning of the mechanical phase shifters. Note, for the calibration measurements presented in Fig. 3.9a, the power balance between the feeds was tuned to minimize the σ^- component around $\phi = 90°$. Fig. 3.9b shows the calculated the ellipticity ξ from the fitted Rabi frequencies for each individual relative phase using Eq. (3.10). The finite ellipticity of the subfields causes the field strengths at other angles of ϕ to be unbalanced, so that we do not get pure σ^+ polarization at $\phi = -90°$ and the phases values that provide linear polarization shift away from 0° and 180°.

3.4 Microwave circuits

3.4.1 Design principles of low-noise microwave circuits

Building a microwave setup that delivers high power while maintaining low phase noise is challenging, primarily due to the additional noise introduced by microwave amplifiers.

[1] This occurs because the molecules fall outside the coverage of the STIRAP beam and are consequently not converted back to atoms for imaging. In Chapter 7, we enlarge the STIRAP beam, enabling a time-of-flight duration of 5.5 ms of ground state molecules without sacrificing counts. We note that Feshbach molecules can be detected after a time-of-flight up to 20 ms, limited only by the size of the imaging beam.

This noise typically takes two forms: one contributes to the noise floor sufficiently away from the carrier, while the other contributes to the noise close to the carrier.

The increased noise floor introduced by an amplifier can be characterized by its noise factor F or noise figure $NF = 10\log_{10}(F)$. The noise factor is defined as the ratio between the signal-to-noise ratio (SNR) at the amplifier's output and input. When multiple devices are chained together, the total noise factor can be calculated using the Friis' formula

$$F = F_1 + \frac{F_2 - 1}{G_1} + \cdots + \frac{F_n - 1}{G_1 G_2 \cdots G_{n-1}}, \tag{3.12}$$

In this formula, F_n is the noise factor for the nth device, and G_n represents the power gain (linear, not in dB) of the nth device. The first amplifier in a chain generally has the most substantial effect on the total noise factor. This is because the noise factors of subsequent stages are reduced by the amplifier gains of the previous stages. Therefore, using a low-noise preamplifier with a high gain is beneficial for suppressing noise factor of the subsequent power amplifier. The noise floor $\mathcal{L}_0$ is given by

$$\mathcal{L}_0 = \frac{k_B T_0 F}{P_c}, \tag{3.13}$$

where $k_B T_0 = -174\,\mathrm{dBm/Hz}$ is the thermal noise[1] at $T_0 = 290\,\mathrm{K}$, and P_c is the carrier power. Given $F < 3\,\mathrm{dB}$ achieved in our setup, the noise floor is negligible for a carrier power exceeding 40 dBm.

In the vicinity of a carrier, the noise level no longer remains constant; instead, it often rises as the frequency gets closer to the carrier. This noise originates from the near-d.c. noise which is up-convereted by the amplifier. Since the near-d.c. noise is added independently to the carrier power, it is not suppressed by preamplification [160]. However, it can be efficiently suppressed using bandpass filters for narrowband applications.

3.4.2 The setup

The microwave setup is illustrated in Fig. 3.10. To achieve independent control over the two feeds of the antenna, the microwave signal from the source is split into two paths by a power splitter. Each path consists of a voltage-controlled attenuator (VCA), a phase shifter, a 3 W preamplifier, a cavity filter, and a 100 W power amplifier.

We use a mechanical phase shifter in one of the path and a voltage-controlled phase shifter in the other path. The VCPS facilitates dynamic phase control, which is useful for electroassociation (see Chapter 7) and for compensating phase shift at different microwave

[1] Also known as the Johnson-Nyquist noise. It arises from fluctuations in electron density in the resistors, which occur because the electrons are in thermal equilibrium with the surrounding environmental thermal radiation. According to the equipartition theorem, the noise power generated by a resistor within a bandwidth Δf is given by $P = k_B T \Delta f$ [159].

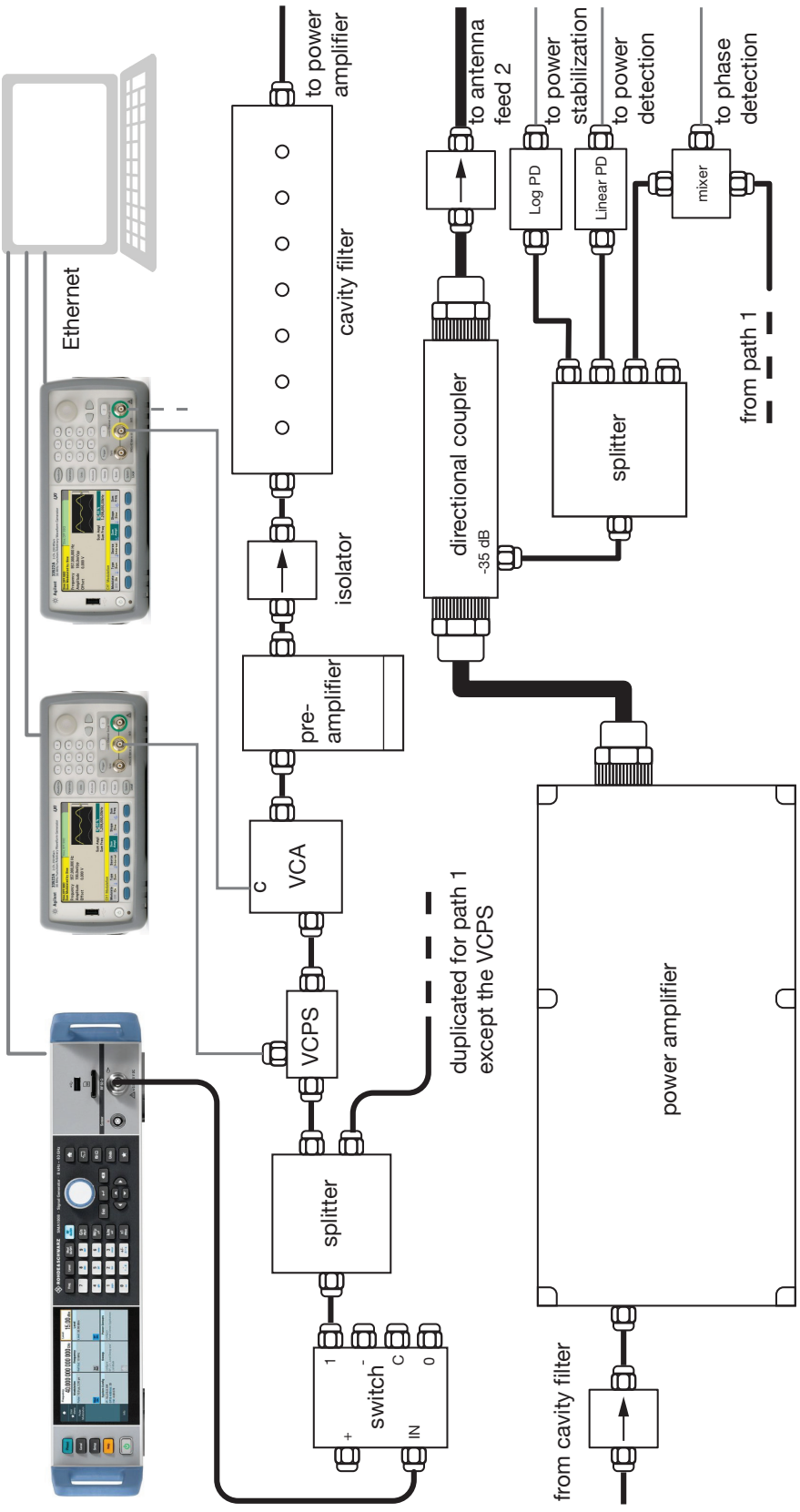

Figure 3.10: Microwave setup. The setup for micowave generation, amplification, and monitoring. Black lines represents microwave cables or connectors. Gray lines represents Ethernet or analog signals. Duplicated components for the other feed of the waveguide antenna are omitted for clarity.

frequencies due to the difference in the length of the two paths. We have inserted an additional cable of 15 cm to reduce for path difference introduced by the mechanical phase shifter, ensuring that the phase difference between the two paths does not exceed 2π.

As shown in Fig. 3.10, the output of the power amplifier is partially divided by a directional coupler and then further split into four paths. The first path connects to a linear power detector (PD) for power monitoring, the second leads to a logarithmic power detector for power stabilization, the third path is directed into a mixer for phase monitoring, and the fourth path left free for debugging.

Source

We utilize a Rohde & Schwarz SMA100B signal generator (which employs a yttrium-iron-garnet oscillator) equipped with the noise suppression option SMAB-B711 as our microwave source. With this configuration, the phase noise is $-160\,\mathrm{dBc/Hz}$ at a 10 MHz offset, and the output power ranges from $-120\,\mathrm{dBm}$ to $20\,\mathrm{dBm}$.

VCA

Each path incorporates a D1954 voltage-controlled attenuator (VCA) for power control. This VCA provides a nominal transfer function of 10 dB attenuation per volt and a maximum attenuation of 60 dB. The VCA exhibits a nonlinear phase shift versus attenuation. To minimize their phase shifts, we typically operate below 10 dB attenuation during microwave shielding.

Phase shifters

For path 1, we utilize a mechanical phase shifter QMPS60. For path 2, a voltage-controlled phase shifter (VCPS) PA0408 is employed, offering a 360° dynamic range for input voltages from 0 V to 9 V. Initially, we were concerned that the VCPS might introduce additional phase noise, but we did not observe a significant increase in phase noise when a d.c. voltage was applied. We only noted an increased phase noise of 10 dBm when a white noise of amplitude $5\,\mathrm{mV_{pp}}$ was applied. Applying a white noise also revealed that the bandwidth of the VCPS is around 30 MHz.

Preamplifier

Each path employs an ERZ-HPA-0200-1800-30 amplifier for preamplification. The small signal gain is 32 dB, the maximum power is 33 dBm, and $P_{1\,\mathrm{dB}} \approx 32\,\mathrm{dBm}$. The noise figure is measured to be less than 2 dB.

Cavity filter

We employ cavity filters (Qualwave QBF-passband-13) to filter out phase noise on the order of the Rabi frequency. The cavity permits transmission at the resonant frequency while

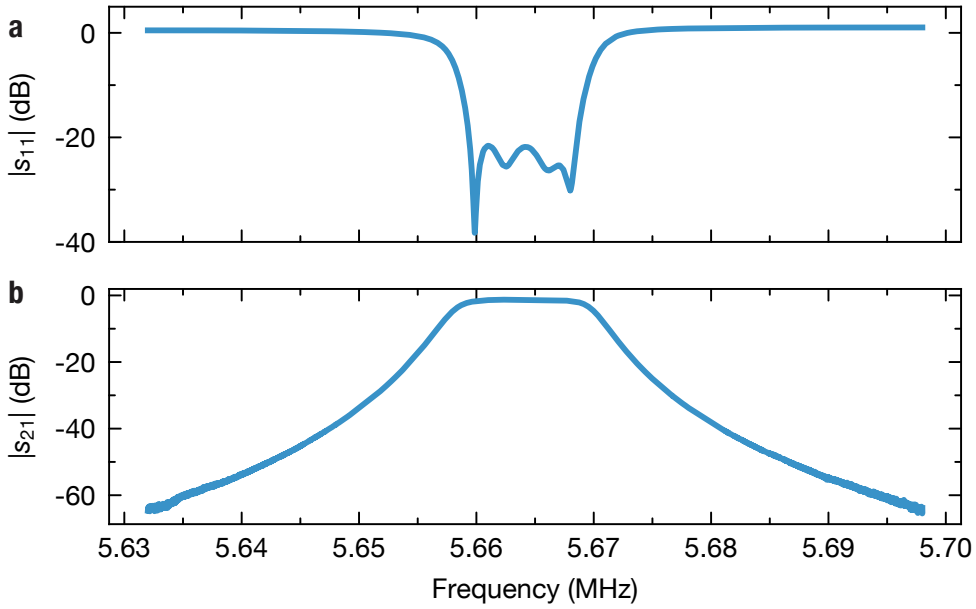

Figure 3.11: Scattering parameters of the cavity filter. Example $|s_{11}|$ (**a**) and $|s_{21}|$ (**b**) of a cavity filter. The measurement was performed with a Rohde-Schwarz ZNL14 vector network analyzer.

reflecting other nearby frequencies. The $-3\,\mathrm{dB}$ bandwidth is roughly 5 MHz, determined by the cavity's quality factor (around 100). The insertion loss at the operating frequency is $-2\,\mathrm{dB}$. At a 10 MHz detuning from the resonant frequency, the relative attenuation is about $-20\,\mathrm{dB}$. Therefore, we have to manually switch between different filters with different transmission frequencies to cover a large range of microwave detunings. Since these cavities cannot handle the full power of the power amplifiers, we position them between the preamplifier and the power amplifier.

Power amplifier

Each path utilizes a Qualwave QPA-5600-5800-18-47 amplifier with a maximum output power of 100 W. The noise figure is measured to be 17 dB. The two power amplifiers exhibit different gains and saturation powers due to manufacturing variations. For certain input powers, self-oscillation in the output power can lead to spectrum spikes with 1 MHz spacing and a power of $-140\,\mathrm{dBc}$. The frequencies of these spikes are unstable and average out in the displayed average spectrum. This self-oscillations are caused by the switching noise of the digital electronics at the gate of the amplifier chip. We bypass part of the digital circuits to get rid of this noise.

We also measure the phase shift versus input power using a network analyzer (R&S ZNL14) that can vary the output power. We observe a constant phase below $P_{1\,\mathrm{dB}}$ and a significant increase in phase in the saturation regime, see Fig 3.12. To maintain a stable

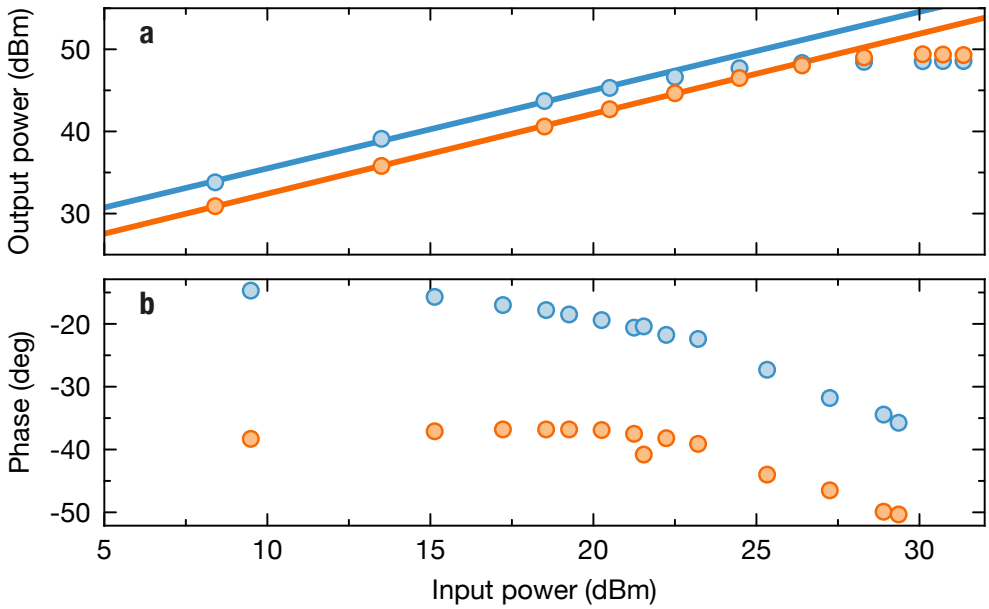

Figure 3.12: Power and phase of the microwave at the output of the power amplifiers. **a**, Power output as a function of the input power. This measurement is performed with an Agilent MXA N9020A spectrum analyzer. The input is provided by a preamplified signal source. **b**, Output phase as a function of the input power. This measurement is performed with a Rohde-Schwarz ZNL14 vector network analyzer, whose Port 1 is connected to the input of the preamplifier and Port 2 is connected to the output of the power amplifier after the directional coupler. The preamplifier works below the saturation regime so we ignore its phase shift.

relative phase between the two paths, we operate below the saturation regime.

Logarithmic power detector

To achieve a control voltage that scales linearly with the output power in dBm, we use a logarithmic power detector (Mini-Circuits ZX47-40+) for power feedback control in each path. This power detector is sensitive to environmental microwave fields and power input noise, so we shield the detector inside an aluminum box and apply a 1.9 MHz low-pass filter to its d.c. power input. The control electronics is presented in the next section.

Linear Power Detector

For power monitoring, we use a linear power detector (DZR124AA) in each path. This detector is passive, and offers greater sensitivity in the high power regime.

Mixer

We utilize a mini-circuits ZMX-8GLH mixer as a phase detector. To calibrate the output voltage versus the phase difference, we conduct a linear phase scan using the VCPS and record the mixer output. The response is a sinusoidal oscillation of period 2π. The amplitude of the response function depends on the power in the two paths and has to be calibrated for different combinations.

3.4.3 Phase noise

Measurement with a spectrum analyzer

A straightforward method for measuring the phase noise of a microwave signal is through a spectrum analyzer (Agilent MXA N9020A). This method assumes that the noise around the carrier is predominantly phase noise, which is a reasonable assumption for our setup.

The measurement procedure is as follows: firstly, we record the carrier power P_c. Then, we shift to a specified frequency offset f, which lies on one side of the sideband, and measure the noise power P_n over a bandwidth of B. The single-sideband noise can then be calculated using the following equation

$$\mathcal{L}(f) = P_n\,(\text{dBm}) - P_c\,(\text{dBm}) - 10\log_{10}(B\,(\text{Hz})),\ (\text{dBc/Hz}). \tag{3.14}$$

When measuring noise close to the spectrum analyzer's noise floor, we subtract the noise floor from the sideband noise P_n, as shown in Fig. 3.14b.

Measurement near the carrier can increase the noise floor and reduce the dynamic range of the phase noise measurement. This is caused by the spectral leakage from the carrier, which saturates the internal ADCs even when it lies outside the measurement region. Moreover, the signal-to-noise of the measurement will be limited by the phase noise of the

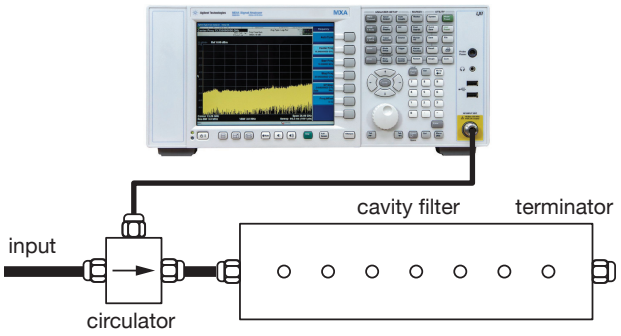

Figure 3.13: Using the cavity reflection as a notch filter to improve the dynamic range of phase noise measurements.

internal signal source of the spectrum analyzer used for heterodyne detection. The Agilent MXA N9020A spectrum analyzer has a nominal dynamic range of -148 dBc/Hz at 10 MHz offset frequency.[1]

Notch Filter

We observe that if the carrier power is excessively high, its spectral leakage occurs even for detunings greater than 1 MHz. To suppress the carrier and to further enhance the dynamic range of the phase noise measurement, we employ a notch filter to reduce the carrier power, as shown in Fig. 3.13. We use the reflection of the cavity filter as a notch filter, which suppresses the signal within its bandwidth. We achieve a 25 dB suppression for the carrier, which correspondingly increases the dynamic range of the phase noise measurement, yielding -173 dBc/Hz.

Phase noise performance

First, we measure noise of the signal source. For the test measurement here, we use R&S SMF100A which has a higher noise of about -150 dBc/Hz at 10 MHz. Next, we examine the output of the power amplifier. Within the filter bandwidth, there is a small increase of phase noise by the amplifier. Outside the filter bandwidth the noise is suppressed as the frequency offset increases. Beyond 30 MHz, the measured noise measurement is limited by the noise floor of the spectrum analyzer. We obtain a phase noise of $\lesssim -180$ dBc/Hz after subtracting the noise floor of the spectrum analyzer.

[1] We typically detuning our measurement regime more than 1 MHz from the carrier to reduce the effect of spectral leakage. This could slightly improve the dynamic range of the phase noise measurement.

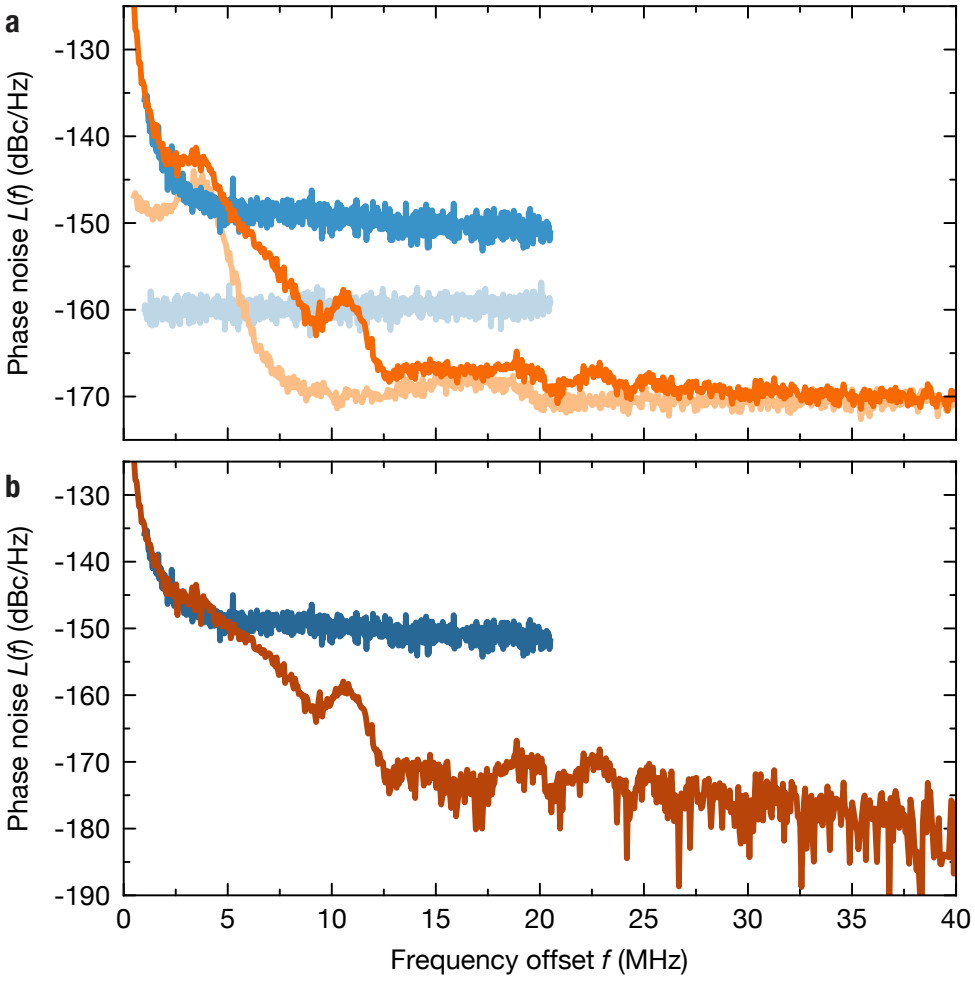

Figure 3.14: Phase noise. **a**, Phase noise at the output of the signal source (blue) and the power amplifier (orange), and their corresponding noise floor (light blue and orange). In this measurement the source is R&S SMF100A, which has a 10 dB higher noise floor compared to R&S SMA100B. The measured carrier of the signal source is 10 dBm, while for the power amplifier is only -9.2 dBm due to the notch filter. The noise floor with the notch filter (light orange) shows the enhanced dynamic range at offset frequencies exceeding the filter band width. **b**, Phase noises with the noise floor subtracted.

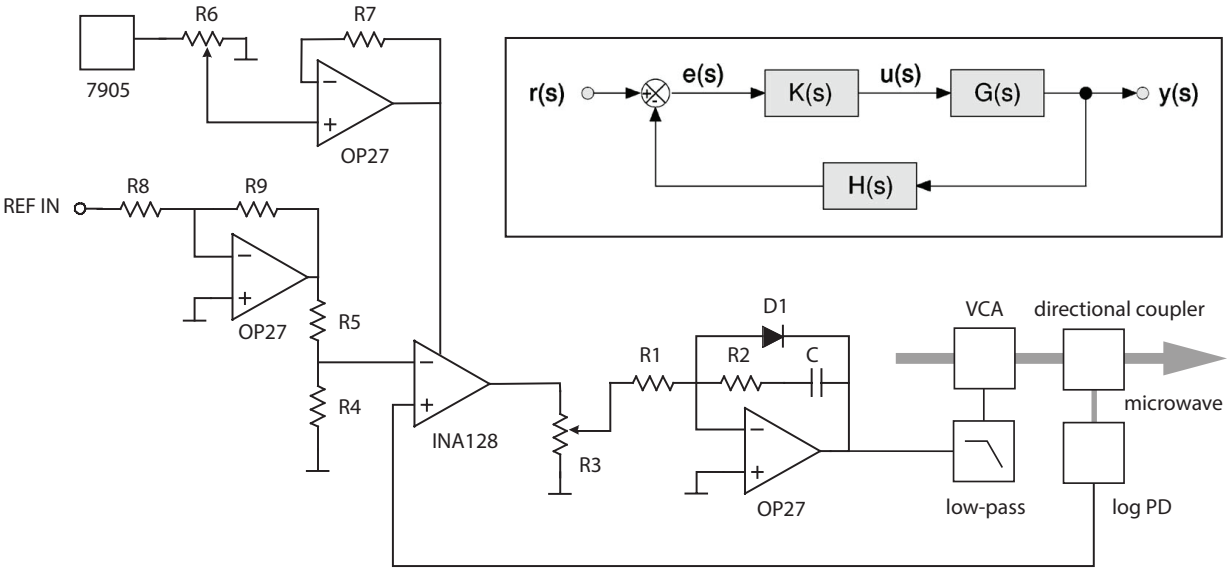

Figure 3.15: Schematics of the power control circuit. Power controller for one feed of the antenna. The circuit can be powered by a ±15 V linear power supply. The power supply and its decoupling low pass filters are omitted in the drawing for clarity. Inset shows the block diagram of an abstract feedback loop [161].

3.5 Control electronics

3.5.1 Power control

The output power of the power amplifier is controlled via a feedback circuit. Several benefits can be derived from employing this method. Firstly, a systematic change in microwave power versus detuning is observed, due to the nonlinear frequency response of the amplifiers. The power feedback, when paired with phase control, can compensate for this systematic deviation. Secondly, the feedback loop can mitigate unwanted amplitude modulation from the power amplifiers. Lastly, feedback control is more convenient to manage and more resilient to adjustments made to the setup.

Figure 3.15 displays the schematics of the power feedback loop, which comprises three main parts: the controller, the system being controlled, and the sensor circuits. The closed-loop transfer function is given by [161]

$$L = \frac{KG}{1 + KGH}, \tag{3.15}$$

where K, G, and H are the transfer functions of the controller, the system, and the sensor, respectively.

PI controller

The core of the control circuit is a single operational amplifier PI controller. The transfer function is given by

$$K(s) = K_t K_p (1 + \frac{1}{i\omega T_i}), \tag{3.16}$$

whose parameters are determined by the resistance values (R_1 and R_2) and capacitance (C). The P gain is defined as $K_p = R_2/R_1$, and the integration time is $T_i = R_2 C$. The total gain ($K_t = K_{R3} K_{\text{ref}}$) is adjustable by the potentiometer (R_3) and the voltage divider at the reference voltage, where $K_{\text{ref}} = R_4/(R_4 + R_5) \approx 0.25$. An IN4148 diode (D1) is utilized to keep the output voltage positive.

System response

Next we discuss the system response to the control signal. In the operation regime of the logarithmic PD, the output voltage is linearly dependent on the input power in dBm, i.e., $P \approx 80 - 40 V_{\text{PD}}\,(\text{dBm})$. With no microwave input, the PD outputs its offset voltage $V_{0,\text{PD}} \approx 2.1\,\text{V}$. The VCA also has a linear attenuation of power in dB versus voltage, such that $P \approx 50 - 10 V_{\text{VCA}}\,(\text{dBm})$. The output power is regulated by the VCA and the low-pass filter. In sum, the total transfer function of the system is given by

$$G(s) = G_{\text{low-pass}}(s) G_{\text{mw}}, \tag{3.17}$$

where G_{mw} is the gain of the rest of the system, whose delay is negligible compared to the low-pass filter. In the linear regime, G_{mw} is simply the attenuation factor of the VCA, which is $-10\,\text{dBm/V}$.

Sensing electronics

The output power is sensed by a directional coupler and converted to voltage by a logarithmic PD. The voltage signal is processed by the sensing circuit and compared with the reference voltage V_{ref} to produce the error signal. The transfer function of the sensing circuit is defined as:

$$H(s) = (-1) H_{\text{PD}}/K_{\text{ref}}, \tag{3.18}$$

where $H_{\text{PD}} = -0.25\,\text{V/dBm}$ in the linear regime. The additional minus sign results from the inverted polarity at the instrumentation amplifier (INA128).

Stationary operation

In addition, we examine the circuit's stationary operation. A reference voltage of 0 V sets the feedback to open loop, i.e., it outputs the maximum voltage to the input of the VCA. This translates into $V_{\text{PD}} = V_{0,\text{PD}}$ for $V_{\text{ref}} = 0\,\text{V}$. Thus, we apply an offset voltage $V_{0,\text{PD}}$ to the instrumentation amplifier. Under stationary operation, we get

$$P \approx 10 V_{\text{ref}}\,(\text{dBm}), \tag{3.19}$$

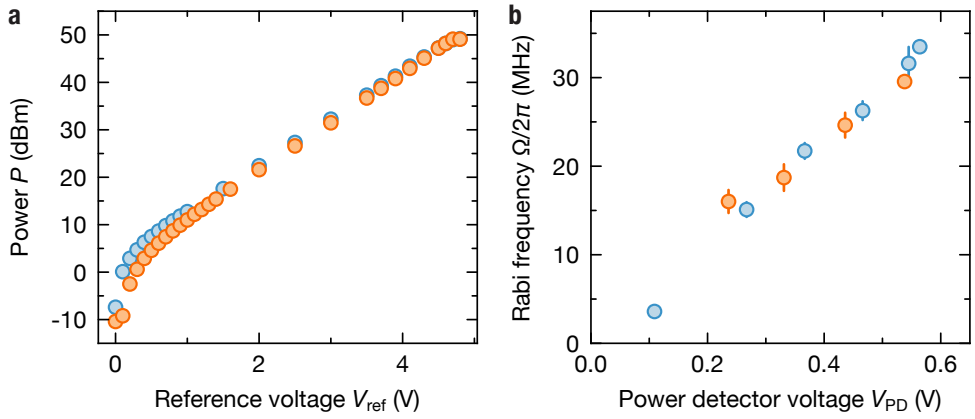

Figure 3.16: Calibration of the power control and monitoring. a, Power output as a function of control voltage. The powers are measured after the directional coupler at different control voltages for feed 1 (blue) and 2 (orange). **b**, Microwave Rabi frequency as a function of the voltage of the linear power detectors with only feed 1 (blue) or 2 (orange) activated.

in the linear regime, and the maximum attenuation at $V_{\text{ref}} = 0\,\text{V}$. Eq. (3.19) is confirmed in the measurement shown in Fig. 3.16a.

Feedback bandwidth

The response time of the VCA and the amplifiers are faster than $1\,\mu$s. Instead, the cut-off frequency of the low-pass filter constrains the bandwidth of the feedback loop. For each cut-off frequency, we optimize feedback by switching capacitors and adjusting the gain via the potentiometer. The capacitors, typically within the range of 10∼50 pF, are selected such that the integration time is roughly the inverse of the cut-off frequency. For the final setup, we use a combined 1.9 MHz and third-order 100 kHz filter to limit the d.c. noise from the control signal, thereby restricting the response time to $10\,\mu$s.

3.5.2 Phase control

We apply a time-dependent voltage to the VCPS to dynamically control the relative phase and thus the ellipticity of the microwave field. The VCPS has a bandwidth of 30 MHz. We implement a low-pass filter with a 1.9 MHz cut-off frequency to reduce d.c. noise from the control voltage, which limits the response time to $0.5\,\mu$s.

3.5.3 Arbitrary waveform generation

We utilize two dual-channel Agilent 33522 arbitrary waveform generators (AWG), with one controlling the power and the other controlling the phase. The AWG features a maximum sampling rate of 30 MSa/s, memory of 16 MSa, and can output ±10 V for 1 MOhm output

impedance. We employ the *waveform sequencing* option to generate the waveform for the experiment. A sequence comprises segments that are either played once or repeated a specified number of times. Only the segments are stored in the memory, so repeating a segment does not increase memory usage. However, the communication between our timing system and the AWG limits the available number of samples, likely due to inadequacies in the implemented driver. We typically use up to 50 kSa to avoid system crashes due to communication delays. To make efficient use of the samples, we adapt the sampling rates for different measurements.

3.6 Conclusion and outlook

Equipped with this microwave setup, we are well-positioned to delve into the study of microwave-shielded polar molecules. Potential future upgrades to the system could include increasing the field strength by incorporating additional amplifiers. Another valuable upgrade would be the integration of a third antenna emitting a microwave field with a polarization orthogonal to that generated by the waveguide antenna. This would enable the synthesis of arbitrary polarizations in any spatial orientation.

The configuration detailed in this chapter represents the latest generation of our microwave setup and was employed in Chapter 7. Earlier generations, discussed in Chapters 4, 5, and 6, each employed progressively more sophisticated setups than their predecessors.

Antishielding! It's something![1]

The first nonzero signal

Chapter 4

Microwave shielding and evaporative cooling

During Christmas 2020, we successfully created Fermi degenerate Feshbach molecules via magnetoassociation and subsequently transferred them into their ground state. Since then, our research has focused on identifying signatures of dipolar interactions and exploring methods of evaporative cooling, whether in bulk or within optical lattices. However, we encountered two challenges.

Firstly, it was necessary to apply a strong d.c. electric field to polarize the molecules to induce dipole-dipole interactions (see Fig. 4.1), and to carry out Förster resonance shielding [99, 104, 105]. For NaK, the required field strength for resonant shielding is around 7 kV/cm [103]. However, in our setup, when the field strength exceeded 1 kV/cm, we observed sporadic charging events in the glass cell due to the electrodes. It can take up to 30 minutes for these to fully discharge using UV LED illumination. Following this, the machine requires another warm-up period. We found this process to be quite time consuming.

We have also tried to work in a 3D lattice to pin down the molecules and avoid collisions. To achieve this, we loaded the Feshbach molecules into the optical lattice and subsequently performed STIRAP. However, the loading process is not adiabatic and the efficiency is low, due to the fact that the fermionic Feshbach molecules are non-interacting away from the atomic Feshbach resonance [69].

In February 2021, a paper that demonstrated microwave shielding with CaF in optical tweezer arrays drew our attention [106]. Previous experiments with NaK [162] and NaRb

[1] Excerpt from the lab book dated May 19, 2021: The very next day, we successfully achieved microwave shielding.

[163] had only observed microwave enhanced losses rather than suppression. We had been preparing the hardware for microwave shielding, including amplifiers and antennas, but had yet to conduct any experiments, given the perceived difficulty in generating a clean, circularly polarized microwave [76, 164, 165].

Inspired by the work with CaF, we proceeded to construct a microwave setup for shielding. The setup is straightforward, encompassing a signal source (Keysight E8267D), a VCA, a 10 W amplifier (Kuhne PA510590), and a custom-made helical antenna. No monitoring or active feedback was implemented. It is fortunate that the rotational transition frequency of NaK molecule (5.6 GHz) lies near the WiFi band, so that microwave components are readily available. To our delight, the simple helical antenna, combined with a metal sheet designed to protect the coil mount from UV LED lights, generated a fairly clean circular polarization. We fine tuned the polarization by adjusting the orientation of the metal sheet relative to the helical antenna, optimizing shielding in the process.

With the use of a bulk gas, comprising a few ten-thousand molecules, we are able to measure both elastic and inelastic collisions, achieving a high gamma ratio. Additionally, the bulk gas possesses a much higher phase space density compared to what was achieved in optical tweezers, providing a good initial condition for evaporation. Starting from a near-degenerate molecular sample, we evaporatively cool the samples down to a remarkable $0.36\,T_F$ and 21 nK. The collisionally stable Fermi degenerate polar molecules provides new opportunities for exploring dipolar many-body physics.

Results of publications [107, 116] are contained in this chapter.

4.1 Microwave dressing of the rotational states

4.1.1 Dressed states and their preparation

Before diving into the scattering problem between two molecules, we examine a single molecule in the presence of a strong microwave field. The microwave is near-resonant with the rotational transition between the ground and the $J = 1$ rotational excited state. When the microwave Rabi frequency greatly exceeds the hyperfine coupling, the hyperfine states are decoupled, thereby remaining preserved throughout the collisional process. Consequently, only the rotational degree of freedom is relevant, and we focus on the Hilbert space defined by the internal states of a molecule represented by four states: $|J, M_J\rangle = |0, 0\rangle$, $|1, 0\rangle$, $|1, -1\rangle$, and $|1, 1\rangle$.

Furthermore, a heteronuclear diatomic molecule's electric dipole moment is expressed as $d_0\hat{\mathbf{d}}$ with $\hat{\mathbf{d}}$ representing the unit vector along the internuclear axis of the molecule. The molecules are driven by an elliptically polarized microwave field represented as $\mathbf{E}_{\mathrm{mw}} = (E_{\mathrm{mw}}e^{-i\omega t}e^{ik_z z}(\hat{\mathbf{e}}_1\cos\xi + \hat{\mathbf{e}}_{-1}\sin\xi) + \mathrm{c.c.})/2$, propagating along the z axis. Here, E_{mw} is the microwave amplitude, ω_0 is the microwave frequency, $\hat{\mathbf{e}}_{\pm1} = \mp(\hat{\mathbf{e}}_x \pm i\hat{\mathbf{e}}_y)/\sqrt{2}$ denote the

basis vectors, and ξ is the ellipticity angle.

The coupling between the microwave and the molecular rotational states within the internal-state Hilbert space gives rise to the Hamiltonian as follows

$$\hat{h}_{\mathrm{mw}} = \frac{\hbar\Omega}{2} e^{-i\omega_0 t} |\xi_+\rangle\langle 0,0| + \mathrm{h.c.}, \tag{4.1}$$

where $\Omega = E_{\mathrm{mw}} d_0/(\sqrt{3}\hbar)$ denotes the Rabi frequency and $|\xi_+\rangle$ is defined as $\cos\xi\,|1,1\rangle + \sin\xi\,|1,-1\rangle$. Consequently, in the interaction picture, the eigenstates of the internal-state Hamiltonian — given by

$$\hat{h}_{\mathrm{in}} = \hat{h}_{\mathrm{rot}} + \hat{h}_{\mathrm{mw}}$$

— are spanned by $|0\rangle \equiv |1,0\rangle$, $|\xi_-\rangle \equiv \cos\xi\,|1,-1\rangle - \sin\xi\,|1,1\rangle$, $|+\rangle \equiv u|0,0\rangle + v|\xi_+\rangle$, and $|-\rangle \equiv u|\xi_+\rangle - v|0,0\rangle$. Here $u = \sqrt{(1+\Delta/\Omega_{\mathrm{eff}})/2}$ and $v = \sqrt{(1-\Delta/\Omega_{\mathrm{eff}})/2}$, where $\Omega_{\mathrm{eff}} = \sqrt{\Omega^2+\Delta^2}$. The corresponding eigenenergies are denoted as $E_0 = E_{\xi_-} = 0$ and $E_\pm = (\Delta \pm \Omega_{\mathrm{eff}})/2$. A schematic representation of the molecular level structure is provided in Fig. 4.1b.

In our experiment, the dressed states are generated by maintaining a fixed detuning Δ while gradually increasing the Rabi frequency Ω. In the rotating frame aligned with the microwave frequency, the Bloch vector of the dressed state adiabatically follows the orientation dictated by the driving field. Specifically, the vector's direction changes from pointing towards the pole to aligning towards the equator as the ratio Δ/Ω decreases. After the ramp, the microwave remains on to continuously to suppress dephasing. If the microwave is turned off after the ramp, the dressed state will quickly dephase due to trap inhomogeneity and dipolar interactions, which occurs on a faster time scale (~ 1 ms) than the collisional loss between the molecules.

To investigate the necessary timescale for the dressing to be adiabatic, we simulate this process by numerically solving the time-dependent Schrödinger equation with $\Omega = \Omega(t)$. Two types of ramps are utilized: a linear ramp of microwave power in dB and a linear ramp in Rabi frequency. The linear-dB ramp mirrors the actual experimental ramp by applying a linear voltage ramp on the VCA, which reduces the power attenuation from -60 dB to 0 dB. As shown in Fig. 4.2a, the timescale for adiabaticity in the dB ramp is 3 μs, whereas for the linear Rabi frequency ramp, it is more than 10 μs.

4.1.2 One-body lifetime

Another key practical aspect of microwave dressing involves the one-body lifetime of the dressed states in the presence of phase noise. Here I provide a simple derivation of the formula for the dressed state lifetime which generalizes to the case with detuning. The derived lifetime aligns with the derivation using the transition matrix provided in Ref. [166], and is a factor of two shorter than in Ref. [106, 167]. The discrepancy arises from the

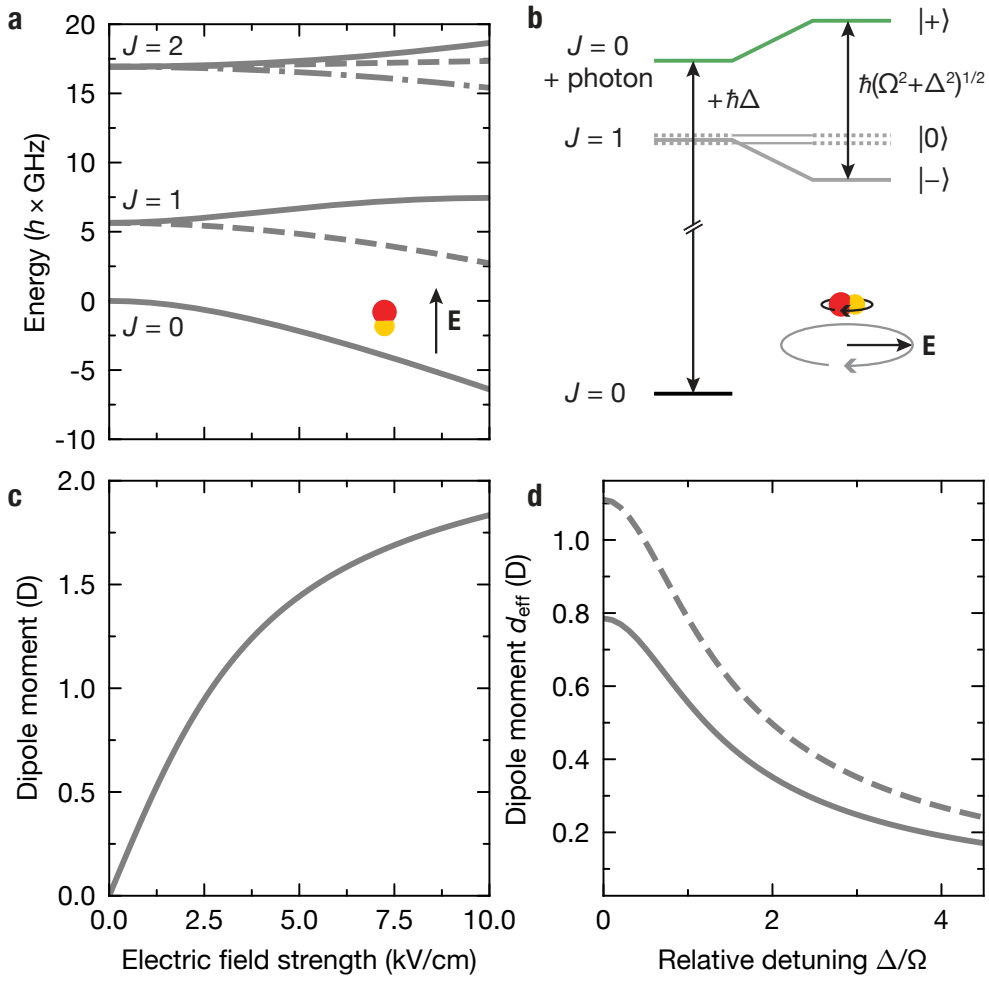

Figure 4.1: Energy shift and induced dipole moment of NaK. a, Energies of rotational states in a d.c. electric field. Different m_J states are decoupled. The solid, dashed, dashed-dotted lines correspond to $|m_J| = 0, 1, 2$, respectively. **b**, Energy levels of rotational states in an a.c. electric field. The inset illustrate the rotating dipole moment following the electric field. At large blue detuning, the rotation of the dipole is out of phase with the driving field. **c**, Induced dipole moment of the ground state as a function of the electric field strength. **d**, Induced rotating dipole moment as a function of the relative detuning Δ/Ω for circular (solid) and linear (dashed) polarizations.

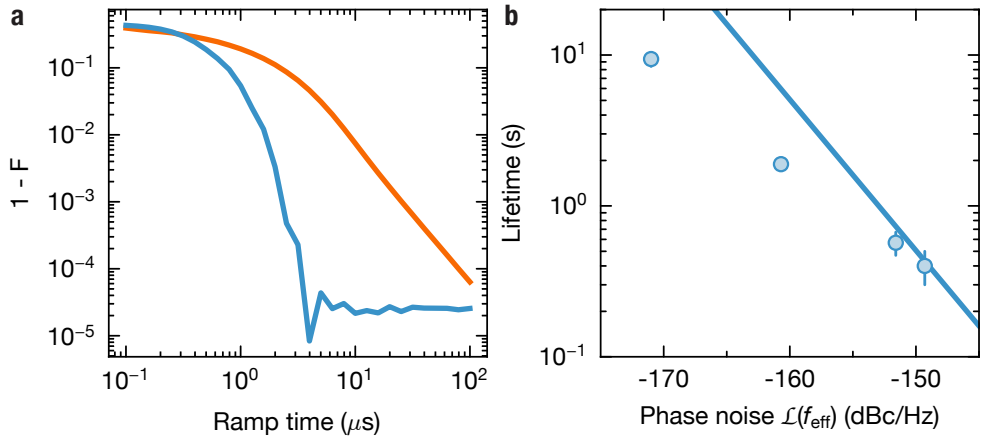

Figure 4.2: Dressed state preparation and decay. **a**, Infidelity of the dressed state preparation vs. ramp duration for exponential (blue) and linear (orange) ramps in Rabi frequency. **b**, One-body lifetime as a function of phase noise. Prediction from Eq. (4.6) (line) compared with experimental data (points). The error bar shows the fitting error of exponential fits to the measured decay curves.

omission of phase diffusion perpendicular to the equator of the Bloch sphere in Ref. [106, 167].

We add a phase fluctuation $\phi(t)$ to the microwave field defined in Eq. (3.7). The single-particle internal-state Hamiltonian in the rotating frame of the microwave can be expressed as

$$\hat{h}_{\text{in}} = \hbar\Delta|0,0\rangle\langle 0,0| + \left(\frac{\hbar\Omega}{2}e^{-i\phi(t)}|\xi_+\rangle\langle 0,0| + \text{h.c.}\right). \tag{4.2}$$

When dealing with a minor modulation amplitude, we retain the leading order of $\phi(t)$, transform the basis into $\{|+\rangle, |0\rangle, |\xi_-\rangle, |-\rangle\}$, and adopt a rotating wave approximation (RWA). This gives us

$$\hat{h}_{\text{in,RWA}} = \hbar\Omega_{\text{eff}}|+\rangle\langle +| + \phi(t)\frac{\hbar\Omega}{2}\left(|+\rangle\langle -| + \text{h.c.}\right). \tag{4.3}$$

To obtain the transition probability between $|+\rangle$ and $|-\rangle$, we use time-dependent per-

turbation theory [168], which yields

$$\begin{aligned} P_{+\leftrightarrow -} &= \lim_{T\to\infty} \frac{1}{T} \left| \frac{-i}{\hbar} \int_0^T \mathrm{d}t' \hat{h}_{mw}(t') e^{i\Omega_{\mathrm{eff}} t'} \right|^2 \\ &= \left(\frac{\Omega}{2}\right)^2 \lim_{T\to\infty} \frac{1}{T} \int_0^T \mathrm{d}t' \int_{-t'}^{T-t'} \mathrm{d}\tau e^{i\Omega_{\mathrm{eff}}\tau} \phi(t')\phi(t'+\tau) \\ &= \left(\frac{\Omega}{2}\right)^2 \int_{-\infty}^{\infty} \mathrm{d}\tau e^{i2\pi f_{\mathrm{eff}}\tau} \langle \phi(t)\phi(t+\tau)\rangle_t \\ &= \left(\frac{\Omega}{2}\right)^2 \mathcal{S}_\phi(f_{\mathrm{eff}}), \end{aligned} \tag{4.4}$$

where we introduce $\langle \phi(t)\phi(t+\tau)\rangle_t = \int_0^T \mathrm{d}t \phi(t)\phi(t+\tau)/T$ and $f_{\mathrm{eff}} = \Omega_{\mathrm{eff}}/2\pi$. Here, $\mathcal{S}_\phi$ represents the two-sided[1] power spectral density of the random phase, which is normalized by $\int_{-\infty}^{\infty} S_\phi(f)\mathrm{d}f = \phi^2_{\mathrm{RMS}}$. We have applied the Wiener–Khinchin theorem. The power spectral density in practice is measured as the single-sideband phase noise $\mathcal{L}(f) = \mathcal{S}_\phi(f)$. From the above derivation, we see that the population of in an isolated dressed state undergoes an exponential decay into a fully mixed state

$$P_+(t) = \frac{1}{2}\left[1 + \exp\left(-\frac{\Omega^2}{2}\mathcal{L}(f_{\mathrm{eff}})t\right)\right]. \tag{4.5}$$

When applying this formula, one needs to convert the phase noise given as $10\log_{10}(\mathcal{L}(f))$ which is in units of dBc/Hz, back to $\mathrm{rad}^2/\mathrm{Hz}$. For a trapped ensemble, molecules in the lower dressed state are anti-shielded and undergo drastic collisional loss with other molecules. Therefore, each transition leads to loss of two molecules and the number follows an exponential decay to zero

$$P_+(t) = \exp\left(-\frac{\Omega^2}{2}\mathcal{L}(f_{\mathrm{eff}})t\right). \tag{4.6}$$

Figure 4.2b compares the experimentally measured the one-body lifetime of different generation of the microwave setup. The number decay is measured with a shielded sample at low density to suppress collisional loss. All measurements are performed at $\Omega \approx 2\pi \times 10\,\mathrm{MHz}$ and $\Delta/\Omega \approx 0.5$ where two-body loss is suppressed. The phase noise of different microwave setups is summarized in Table 4.1. Their measurement are discussed in Section 3.4.3. The measured lifetime at low phase noises are limited by residual two-body collisions and photon scattering from the trap, and is shorter than the predicted one-body loss.

[1] Another common practice is to use the one-sided power spectral density $\mathcal{S}^I_\phi$, which aggregates noise at the positive and negative frequency offsets. Consequently, $\mathcal{S}^I_\phi(f) = 2\mathcal{S}_\phi(f)$ for $f > 0$ and undefined for $f < 0$.

Table 4.1: Microwave setup and phase noise at 10 MHz offset frequency from the carrier.

Source	Filter	Phase noise (dBc/Hz)
Rohde & Schwarz SMF100A	-	-149
Keysight E8267D	-	-152
Rohde & Schwarz SMA100B	-	-161
Rohde & Schwarz SMA100B	cavity filter	-171

4.1.3 Induced rotating dipole moment

The microwave field, which dresses the particles, induces a rotating dipole moment, as illustrated in Fig. 4.1b. This can be shown by evaluating the dipole moment operator in the rotating frame. The dipole moment in the laboratory frame can be expressed as

$$\mathbf{d}(t) = \sqrt{2} d_{\text{eff}} e^{-i\omega t}(\hat{\mathbf{e}}_1 \cos\xi + \hat{\mathbf{e}}_{-1} \sin\xi) + \text{c.c.}, \tag{4.7}$$

where $d_{\text{eff}} = d_0/\sqrt{12(1+(\Delta/\Omega)^2)}$. Eq. (4.7) implies that the time-averaged dipole moment is zero. However, all the molecules rotate in phase with the microwave, leading to a non-zero time-averaged interaction. The average interaction is given by

$$\begin{aligned} V_{\text{dd}}(\mathbf{r}) &= \frac{d_{\text{eff}}^2}{4\pi\epsilon_0 r^3}(3\cos^2\theta - 1 + 3\sin 2\xi \sin^2\theta \cos 2\phi) \\ &= \frac{d_{\text{eff}}^2}{4\pi\epsilon_0 r^3}\left[(1-\sin 2\xi)(3\cos^2\theta - 1) - 2\sin 2\xi(3\cos^2\theta' - 1)\right]. \end{aligned} \tag{4.8}$$

Written in this form, it becomes clear that at circular polarization $\xi = 0°$, the interaction $V_{\text{dd}}(\mathbf{r}) = \frac{d_{\text{eff}}^2}{4\pi\epsilon_0 r^3}(3\cos^2\theta - 1)$ represents a dipole-dipole interaction along the z-axis with an additional negative sign. While linearly oscillating dipoles $\xi = 45°$ interact via a normal dipole-dipole interaction $V_{\text{dd}}(\mathbf{r}) = \frac{2d_{\text{eff}}^2}{4\pi\epsilon_0 r^3}(1 - 3\cos^2\theta')$, with θ' representing the angle between $\mathbf{r}$ and the $y-$axis. Between linear and circular polarization, the interaction breaks rotational symmetry in all directions, but retains mirror symmetry along the x, y, and z axes.

The advantage of microwave dressing, compared to d.c. polarizing, is that microwave photons bridge the gap between rotational states and achieve strong rotational mixing even with a small electric field strength. In contrast, d.c. Stark shift is inhibited by the large rotational energies, as depicted in Fig. 4.1. However, microwave dressing has a drawback: the maximum dipole moment is constrained to $d_0/\sqrt{12}$ because only the $J = 1$ rotational state is involved. Meanwhile, a d.c. field off-resonantly couples all odd/even rotational states, allowing the molecule to be fully polarized at sufficiently high field strength. A more comprehensive comparison of various shielding schemes is provided in Chapter 8.

4.2 Microwave shielding

Having gained an understanding of a single microwave-dressed molecule, we now progress to discuss collisions between two such molecules. This section covers the theory and experiment of microwave shielding, which also lays a foundation for understanding field-linked resonances and tetramers in the subsequent chapters.

4.2.1 Theory of microwave shielding

The concept of suppressing inelastic collisions using a circularly polarized a.c. electric field has historical roots dating back to the 1990s. During that time, optical shielding of alkali atoms was observed in MOTs [169–171] and subsequently interpreted theoretically [172, 173]. In those collisions, a blue-detuned optical photon elevates the S state of the atom above the excited P state, creating an avoided crossing between the two states and yielding a repulsive potential. One limiting factor in this approach was the spontaneous emission from the excited state. A similar induced van-der-Waals interaction has been extensively studied in Rydberg dressing [174], in the regime of large detuning and strong dipole-dipole interaction.

In contrast to atoms, molecules exhibit rotational transitions that are free from spontaneous emission. These transitions occur within the microwave regime, leading to the terminology of "microwave shielding". Early proposals for microwave shielding advocated the use of large detuning and Rabi frequencies Ω similar to those in optical shielding [175–177]. However, microwave-dressed molecules typically exhibit weaker resonant dipole interactions than optically dressed atoms, necessitating larger values of Ω for optimal shielding [164]. A systematic investigation into this regime was conducted in Ref. [76, 164]. Subsequent calculations explored shielding with imperfect circular polarization [165, 178]. These theoretical studies eventually led to successful experimental realizations of microwave shielding [106–109].

More recently, optical shielding has been proposed for polar molecules [179, 180]. The feasibility of this approach remains an open question, particularly concerning the limited spontaneous emission rate of the electronic excited state, and the technical challenges associated with minimizing laser phase and intensity noise.

Physical picture

The goal of microwave shielding is to induce a repulsive interaction that effectively prevents molecules from experiencing short-range universal losses. This repulsive interaction can be sourced from the dipolar spin-exchange interaction between the ground and the $|J = 1\rangle$ states. To harness this, we excite the ground state with a microwave photon blue detuned to the rotational transition. This ensures the state $|J = 0, n_{\mathrm{mw}} = 1\rangle$ is positioned above the excited state in the interaction image, where n_{mw} denotes the number of microwave

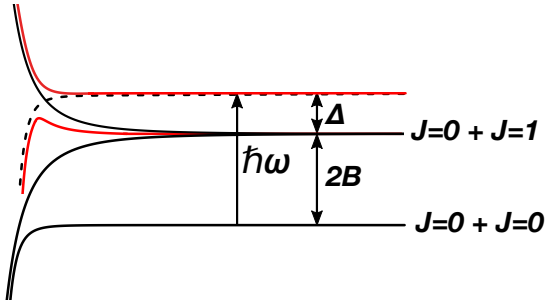

Figure 4.3: Principle of microwave shielding. Collisional shielding of ground state rotational molecules $J = 0$, using a blue-detuned $\Delta > 0$, circularly polarized microwave field. The dipole-dipole interaction creates an effective repulsive adiabatic curve (red), preventing the molecules to approach at short-range. Note that to keep things simple we consider here a small Rabi frequency, which is not the regime for efficient shielding. Figure adapted from Ref. [76].

photons, as depicted in Fig. 4.3. The resulting avoided crossing between the upper channel and the lower ones leads to a repulsive interaction for the dressed ground state molecules.

Alternatively, the shielding potential can be understood as a result of realignment of the colliding dipoles. This realignment originates from a competition between the dipole-dipole interaction and the Stark shift. Beyond a certain separation, the dipole-dipole interaction begins to dominate over the Stark shift. As shown in Fig. 4.4b and c, two compass needles realign themselves from side-by-side to head-to-tail as they approach each other to minimize the total energy. As a result, the dipolar force also flips sign from repulsive to attractive. In the quantum realm, the dipoles can realign to either minimize or maximize the total energy, depending on their internal states. In the maximum-energy branch, the dipoles reorient themselves into a repulsive arrangement, which is opposite to the classical analog. A similar flipping of the dipoles occurs between polar molecules in a d.c. electric field [104, 105], between Rydberg atoms [181], and between ions and Rydberg atoms [182].

A "classical simulation" is performed to demonstrate the realignment process, utilizing two floating compass needles.[1] Fig. 4.5 illustrates the progression during the collision process. Each compass needle was positioned atop a floating piece of paper on water, and the collision was initiated by pushing the left needle towards the right. Initially aligned parallel to the Earth's magnetic field, the needles encountered a repulsive dipole-dipole force as they approached each other perpendicularly to the magnetic field, deflecting their collision course. Concurrently, the dipoles began to realign into a head-to-tail attractive configuration. Following contact, the needles formed a collective dipole that eventually reoriented itself parallel to the magnetic field, completing the simulated process.

Multichannel scattering theory

Understanding microwave shielding quantitatively necessitates an examination of the multichannel scattering problem. Here we follow the formalism developed in Ref. [116]. The Schrödinger equations that govern the relative motion of two colliding molecules are pre-

[1] The needles are obtained from the compasses in Fig. 4.4b.

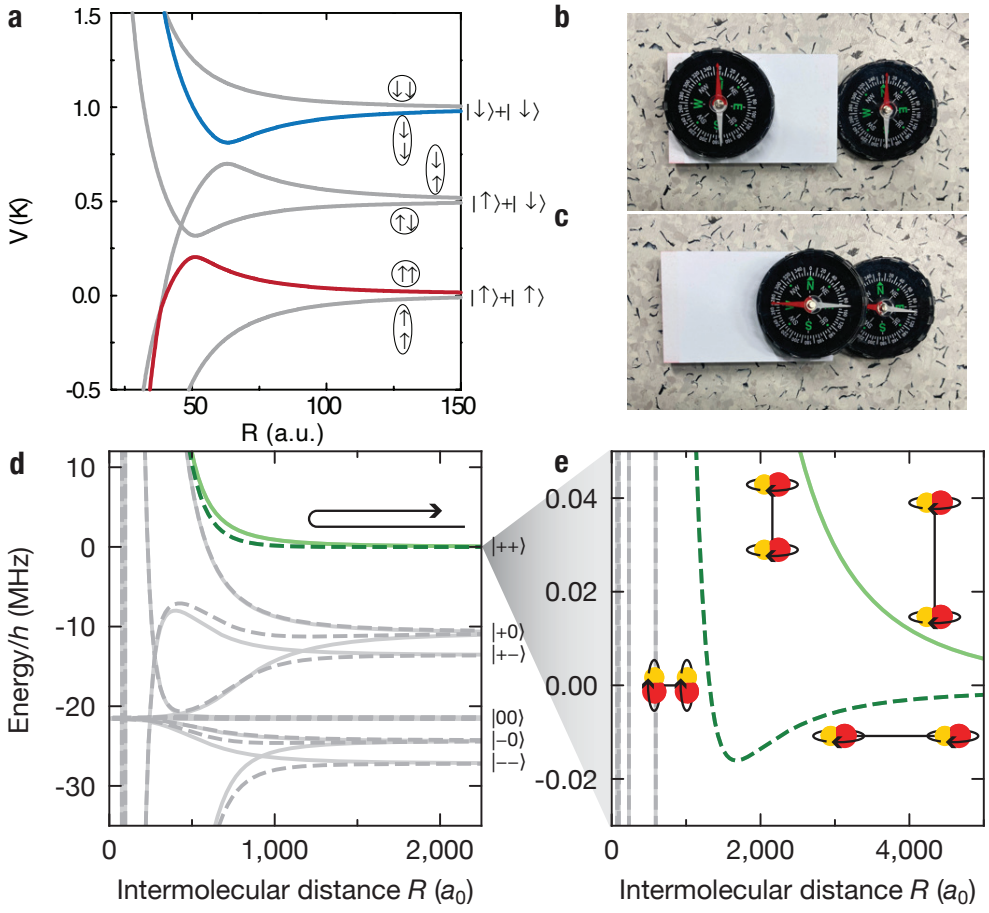

Figure 4.4: Interaction potentials and their classical analog. **a**, Adiabatic potential energy curves for $(OH)_2$. The flipping of dipoles occurs in both the highest (blue) and the lowest (red) channel. Figure reproduced from Ref. [111]. **b** and **c**, two compasses realign themselves at close distance, demonstrating the classical analog of the interaction (red) in (**a**). The compass on the left is elevated with paper, such that the two compasses can be placed closer. **d**, Potential curves for microwave-shielded NaK molecules, with circular polarization, $\Delta = 2\pi \times 8\,\mathrm{MHz}$ and $\Omega = 2\pi \times 11\,\mathrm{MHz}$. The solid and dashed lines show the potential energy of molecules colliding along ($\theta = 0°$) and orthogonal ($\theta = 90°$) to the microwave propagation direction, respectively. Here a_0 is the Bohr radius. **e**, Close-up of the shielded collisional channel $|++\rangle$. The inset shows the alignment of the rotating molecules with respect to each other. At intermediate range, the molecules align with respect to the intermolecular axis.

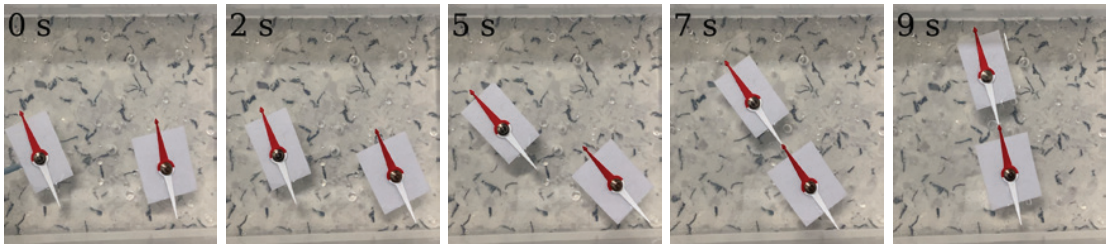

Figure 4.5: Classical simulation of dipolar collisions. A series of images during the collision between two floating compass needles. The top left legends show the time stamps in seconds.

sented below

$$\sum_{\nu'=1}^{7}\left(-\frac{\hbar^2\nabla^2}{M}\delta_{\nu\nu'}+V_{\nu\nu'}\right)\psi_{\nu'}(\mathbf{r})=\frac{\hbar^2k_\nu^2}{M}\psi_\nu(\mathbf{r}). \tag{4.9}$$

In this equation, $\psi_\nu(\mathbf{r})$ is the wave function of the νth scattering channel, $V_{\nu\nu'}=\langle\nu|V|\nu'\rangle$, and $k_\nu=\sqrt{k_1^2-M\mathcal{E}_\nu/\hbar^2}$ represents the incident momentum of the νth scattering channel. For two molecules with dipole moments $d_0\hat{\mathbf{d}}_1$ and $d_0\hat{\mathbf{d}}_2$, their dipole-dipole interaction is expressed as follows

$$V(\mathbf{r})=\frac{d_0^2}{4\pi\epsilon_0 r^3}\left[\hat{\mathbf{d}}_1\cdot\hat{\mathbf{d}}_2-3(\hat{\mathbf{d}}_1\cdot\hat{\mathbf{r}})(\hat{\mathbf{d}}_2\cdot\hat{\mathbf{r}})\right], \tag{4.10}$$

Here, ϵ_0 denotes the electric permittivity of the vacuum, $r=|\mathbf{r}|$, and $\hat{\mathbf{r}}=\mathbf{r}/r$. The two-particle Hamiltonian $\hat{H}_2=\sum_{j=1,2}\hat{h}_j+V(\mathbf{r}_1-\mathbf{r}_2)$ is noted to possess a parity symmetry, hinting at the decoupling of the symmetric and antisymmetric two-particle internal states in the Hamiltonian $\hat{H}_2$. This analysis focuses on the ten-dimensional symmetric subspace where the shielding states of the molecules lie. It turns out that, under the rotating-wave approximation, $V(\mathbf{r})$ in the seven-dimensional (7D) symmetric subspace, $\mathcal{S}_7\equiv\{|\nu\rangle\}_{\nu=1}^7$, is decoupled from the remaining three-dimensional symmetric subspace, where $|1\rangle=|+,+\rangle$, $|2\rangle=|+,0\rangle_s$, $|3\rangle=|+,\xi_-\rangle_s$, $|4\rangle=|+,-\rangle_s$, $|5\rangle=|-,0\rangle_s$, $|6\rangle=|-,\xi_-\rangle_s$, and $|7\rangle=|-,-\rangle$ with $|i,j\rangle_s=(|i,j\rangle+|j,i\rangle)/\sqrt{2}$. Correspondingly, with respect to the asymptotical state $|\nu=1\rangle$, the energies of these states are $\mathcal{E}_\nu=\{0,\frac{1}{2}(\delta-\Omega_{\text{eff}}),\frac{1}{2}(\delta-\Omega_{\text{eff}}),-\Omega_{\text{eff}},\frac{1}{2}(\delta-3\Omega_{\text{eff}}),\frac{1}{2}(\delta-3\Omega_{\text{eff}}),-2\Omega_{\text{eff}}\}$.

In order to solve the above equations, we first expand the wave functions $\psi_\nu(\mathbf{r})=\sum_{lm}Y_{lm}(\hat{\mathbf{r}})\phi_{\nu lm}(r)/r$ in the partial-wave basis, where l is odd for indistinguishable fermions. This expansion yields a set of equations for $\phi_{\nu lm}$ which can be numerically evolved using Johnson's log-derivative propagator method. By comparing the results with the asymptotical boundary condition, we can derive the scattering amplitude and cross section for the (νlm) to $(\nu' l' m')$ scattering.

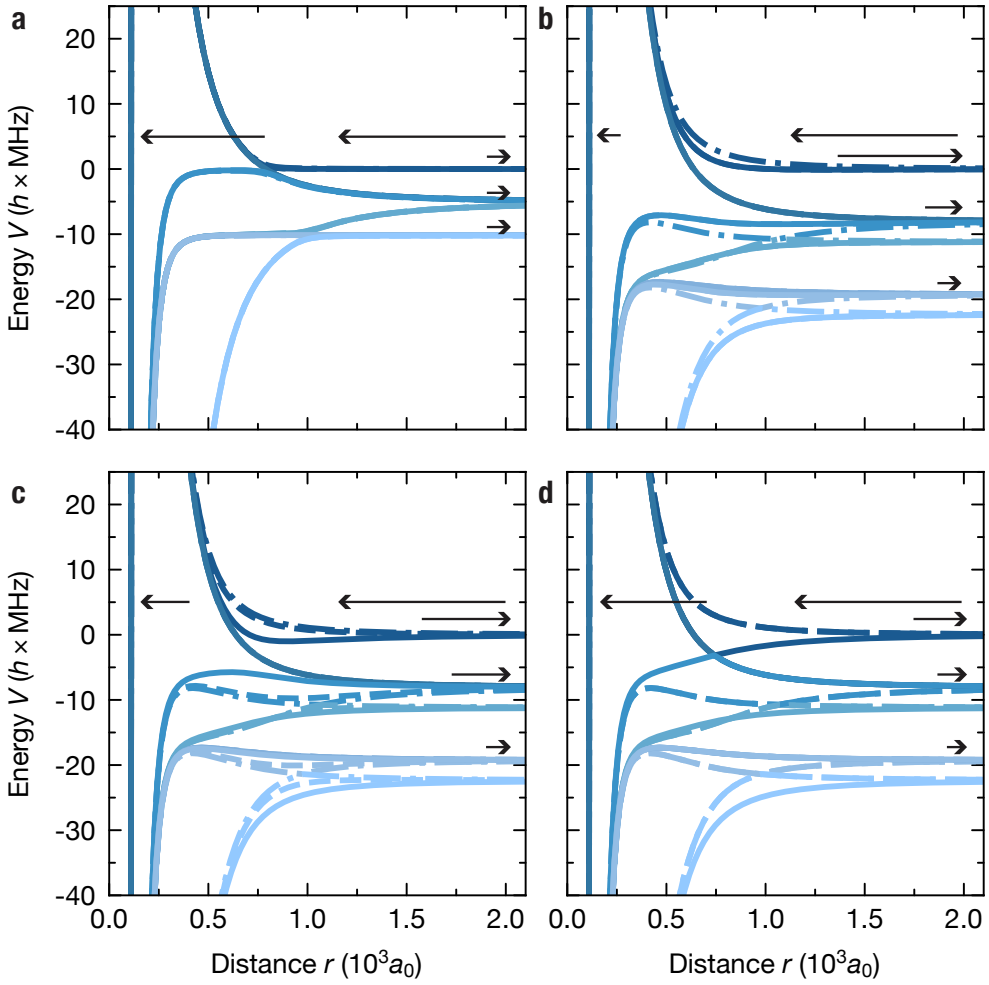

Figure 4.6: Interaction potentials and loss mechanisms. The arrows quantitatively shows the direction and relative strength of the scattering amplitude in different collisional channels. The detuning is fixed to $\Delta = 2\pi \times 5\,\mathrm{MHz}$, while Ω and ξ differs. **a**, $\Omega = 2\pi \times 1\,\mathrm{MHz}$ and $\xi = 0°$. **b**, $\Omega = 2\pi \times 10\,\mathrm{MHz}$ and $\xi = 0°$. **c**, $\Omega = 2\pi \times 10\,\mathrm{MHz}$ and $\xi = 20°$. **d**, $\Omega = 2\pi \times 10\,\mathrm{MHz}$ and $\xi = 45°$. The solid, dashed, and dash-dotted lines represents collision along z, x, and y axis, respectively. Calculated with the help of Fulin Deng.

Adiabatic potentials and loss mechanisms

To establish a link between the multichannel scattering problem and the simplified physical picture of microwave shielding, we consider the adiabatic potential curves under the Born-Oppenheimer approximation. This approximation holds true when the kinetic energy of the molecules is much less than the energy level spacing between internal states ($\sim \Omega_{\text{eff}}$). Upon diagonalizing $V(\mathbf{r})$ in $\mathcal{S}_7$, we identify seven adiabatic potentials that correspond to different dressed-state channels, as shown in Fig. 4.6. By inspecting these potential curves we can identify the parameter regime for efficient shielding.

There are two loss mechanisms between colliding microwave-shielded molecules: the first is entering short range and undergoing universal loss, and the second is tunneling to lower dressed states and release energy on the order of $\hbar\Omega$, sufficient to eject molecules from the optical dipole trap. The first loss process is suppressed by a large shielding core (see Fig. 4.7a), which reduces the wave function leakage to short range. The second loss process is suppressed by the energy gap between the upper and lower potentials. While the size of the shielding core increases with detuning Δ, the energy gap reduces. These two competing effect leads to an optimum detuning which minimizes loss rates. The optimum detuning Δ/Ω increases as the temperature reduces, as the two loss processes are energy dependent, as shown in Fig. 4.10a.

The angular distribution of the shielding core and the energy gap are crucial for the understanding of shielding at different microwave polarizations. Figure 4.6 shows the potential curves under the sudden approximation, which consider collisions along a fixed direction θ while neglecting nonadiabatic coupling involving $\mathrm{d}/\mathrm{d}\theta$ [165]. A closer look at the interaction potentials at various polarizations reveals that the interaction potential is most attractive along the direction of the microwave ellipse. This direction also experiences the largest collisional loss. Figure 4.7 shows the shielding core and the energy gap between the upper channel and the attractive channel calculated using the effective potential Eq. (6.3). As the ellipticity increases, both the shielding core and the energy gap diminish along the y-axis. The shielding core deforms from a "dumbbell" into a "bioconcave disc",[1] while the gap deforms from a sphere into an apple shape. As a result, increasing the tunneling rates to short range and the lower dressed states. The effect of polarization tuning and the resulting scattering field-linked resonances will be discussed in more detail in Chapter 6.

At low temperatures and near the optimum detuning for shielding, the inelastic collision rate follows the Wigner threshold law. For indistinguishable fermions, the loss rate coefficient scales linearly with the collisional energy, resulting from the scaling of the tunneling rate either through the rotational barrier into short range [73, 74] or to the lower dressed states.

The loss coefficient in presence of shielding is often compared with the universal loss rate

[1] The shape of a red blood cell.

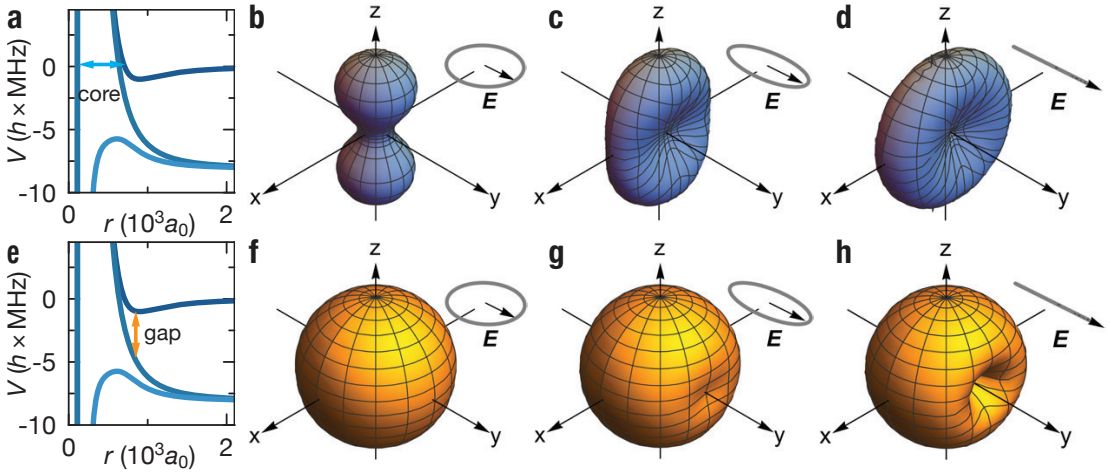

Figure 4.7: Angular distribution of the shielding core and the energy gap. **a** and **e**, Close-up of the potential curves in Fig. 4.6c for collisions along the y axis. The vertical arrow marks the gap between the two highest channels. The horizontal arrow marks the shielding core. The shielding core (**b-d**) and the energy gaps (**f-h**) are calculated with Rabi frequency of $\Omega = 2\pi \times 10\,\mathrm{MHz}$ and $\Delta = 2\pi \times 5\,\mathrm{MHz}$ for circular (**b** and f), $\xi = 20°$ (**b** and **g**) and, linear (**d** and **h**) polarizations. The size of the shielding core is calculated as the classical turning point for a given kinetic energy of 500 nK.

coefficient [73]

$$\beta_{\mathrm{universal}} = \frac{\Gamma(1/4)^6}{\Gamma(3/4)^2}\bar{a}^3\frac{k_B T}{h}, \tag{4.11}$$

where $\bar{a} = [2\pi/\Gamma(1/4)^2]\left(MC_{6d}/\hbar^2\right)^{1/4}$ is the characteristic length of the short-range potential [183]. For NaK, the direct van der Waals coefficient $C_{6\mathrm{d}} = 4.9 \times 10^{-74}\,\mathrm{kg\,m^8/s}$ [184], leading to a loss rate coefficient $\beta_{\mathrm{universal}} = 6.5 \times 10^{-12}\,\mathrm{cm^2/s}$ at 100 nK. In absence of the microwave, the measured loss coefficient agrees with the calculated universal loss.[1]

4.2.2 Inelastic collisions

We prepare samples at varying temperatures by adiabatically compressing the trap to different trapping frequencies following the magnetoassociation. After dressing the molecules, we hold them in trap for a variable amount of time before measuring the remaining number of molecules. The loss dynamics are fitted to a combination of one-body and two-body decay, accompanied by linear heating. The one-body lifetime is separately determined in an experiment conducted with a low number of molecules to minimize two-body loss.

One limitation of measurements at high Rabi frequencies is the impact of the microwave

[1]The measurements performed after we replaced the 1550 nm trapping laser with a 1064 nm one show a consistent result with the universal loss [112], while measurements prior to that are larger by a factor of 2 [71, 107]. The discrepancy could either be a systematic error in the density calibration, or some extra loss caused by the 1550 nm laser.

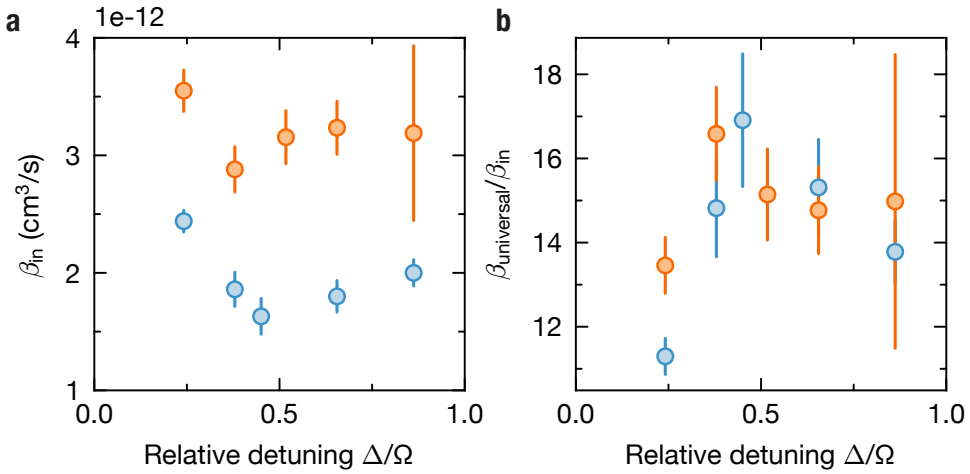

Figure 4.8: Suppression of inelastic collisions. Inelastic rate coefficient β_{in} (**a**) and shielding factor $\beta_{\text{universal}}/\beta_{\text{in}}$ (**b**) as a function of relative detuning Δ/Ω near circular polarization. The blue and orange points correspond to temperature around 460 nK and 780 nK. The Rabi frequency is $\Omega = 2\pi \times 14.5\,\text{MHz}$ and polarization tuned to circular by maximizing shielding for each detunings.

force. The inhomogeneity of the microwave field exerts a force on the molecules proportional to the a.c. Stark shift. This force reduces the trap depth, causing evaporation. Such evaporation leads to an effective two-body loss and cooling of the sample. To reduce evaporation during the loss measurements, we keep the truncation parameter $k_B T/U_{\text{trap}}$ above six, where U_{trap} is the trap depth. The results are shown in Fig. 4.8.

4.2.3 Elastic collisions

Universal dipolar scattering

When inelastic collisions are suppressed, scattering between polar molecules is dominated by the *universal* elastic dipolar scattering [75]. Unlike the case with atoms, where predicting the scattering lengths or volumes can be challenging, the low-energy collisions between polar molecules can be approximately determined given their mass and the induced dipole moment. This universal scattering occurs when the long-range dipole-dipole interaction dominates over the short-range potential. For indistinguishable bosons, the s-wave scattering length should be included in addition. For indistinguishable fermions, the short-range effect is suppressed by the rotational barrier, making detailed knowledge of the short-range scattering unnecessary. The dipolar scattering can also be influenced by scattering resonances, which we will discuss in the Chapter 6. Here, we focus on off-resonant scattering between indistinguishable fermions.

The nature of universal scattering is determined by the interplay between the de Broglie wavelength $\lambda = 1/k$ and the dipolar length $a_{\text{dd}} = M d_{\text{eff}}^2/8\pi\epsilon_0\hbar^2$. In the threshold regime

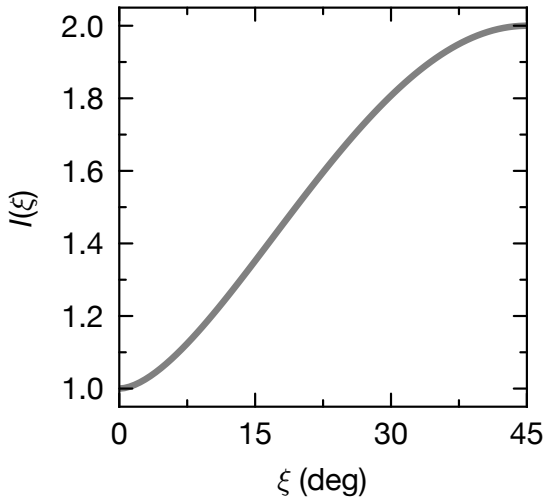

Figure 4.9: The function used in the Eikonal approximation (see Appendix B).

where $ka_{\mathrm{dd}} < 1$, we can employ the Born approximation, in which case the scattering cross section is expressed as

$$\sigma_{\mathrm{Born}} = \frac{32\pi}{15} a_{\mathrm{dd}}^2 (1 + 3\sin^2 2\xi). \tag{4.12}$$

When $ka_{\mathrm{dd}} > 1$, we transition to the semiclassical regime, where the Eikonal approximation can be applied

$$\sigma_{\mathrm{Ei}} = \frac{8\pi a_{\mathrm{dd}}}{3k} I(\xi), \tag{4.13}$$

where $I(\xi)$ is a monotonic function in the interval $0° \leq \xi \leq 45°$, with $I(\xi = 0°) = 1$ and $I(\xi = 45°) = 2$, as plotted in Fig. 4.9. A derivation for the scattering cross sections is provided in Appendix B. The Eikonal approximation fails at high energies when $\sqrt{a_{\mathrm{dd}}/k}$ becomes smaller than the length scale of the short-range interaction $\bar{a}$. However, this is typically not encountered in the ultracold regime.

Cross-dimensional thermalization

We measure the elastic collision rates from the rate of cross-dimensional thermalization, which is proportional to the collision rates and scaled by a geometric multiplication factor [105, 185]. For this purpose, we use parametric heating by modulating the intensity of the 1064-nm beam at twice the vertical trap frequency. The elastic and inelastic collision rate coefficients β_{el} and β_{in} are experimentally determined from the time evolution of the measured molecule number N, the average temperature $(2T_{\mathrm{h}} + T_{\mathrm{v}})/3$ and the differential temperature $T_{\mathrm{v}} - T_{\mathrm{h}}$ by numerically solving the differential equations [77, 105]

$$\frac{dN}{dt} = \left(-K \frac{2T_{\mathrm{h}} + T_{\mathrm{v}}}{3} n - \Gamma_1 \right) N, \tag{4.14}$$

$$\frac{dT_{\mathrm{h}}}{dt} = \frac{1}{12} K T_{\mathrm{v}} T_{\mathrm{h}} n + \frac{\Gamma_{\mathrm{th}}}{3} (T_{\mathrm{v}} - T_{\mathrm{h}}), \tag{4.15}$$

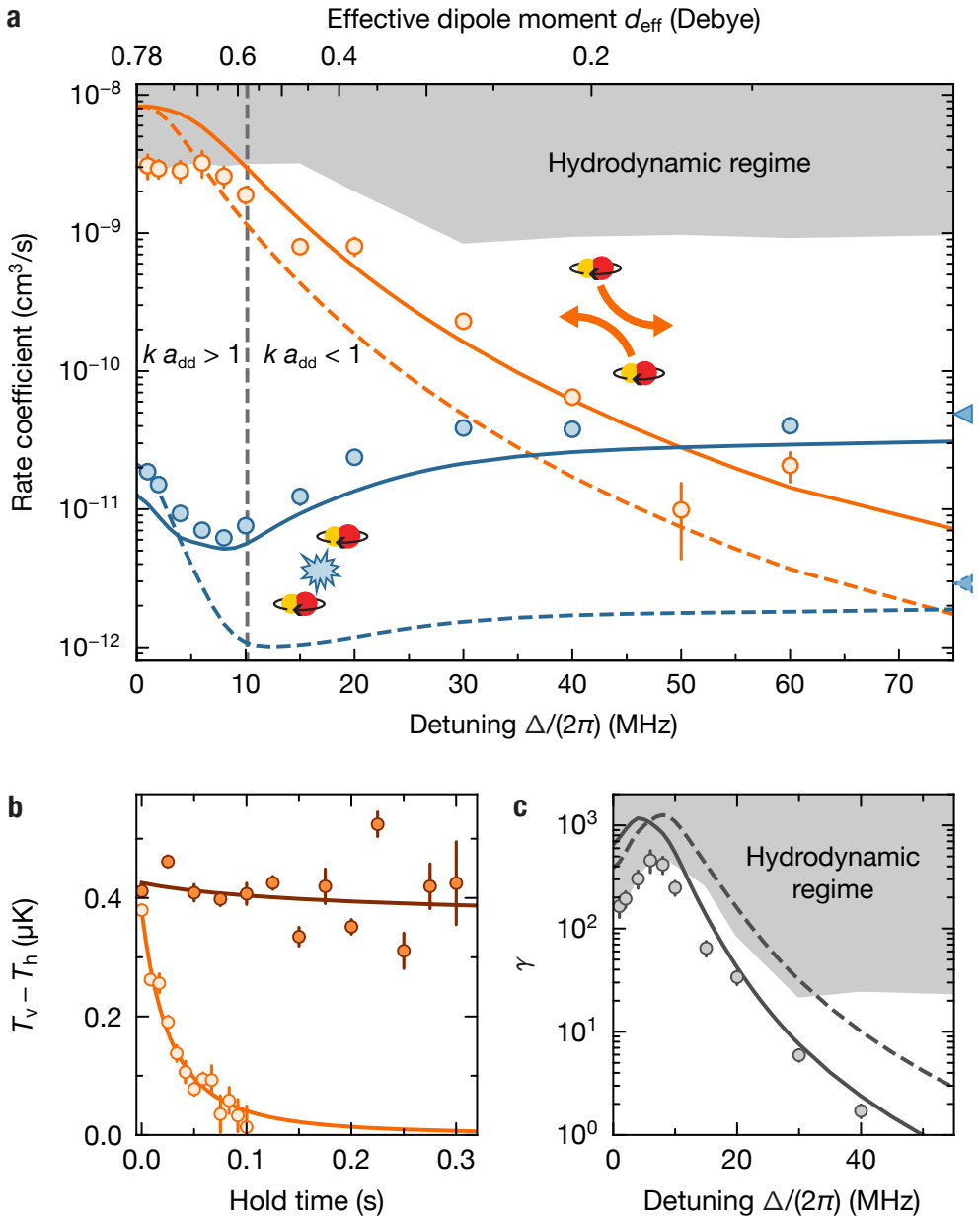

Figure 4.10: Elastic and inelastic collisions. **a**, Rate coefficients for elastic (orange) and inelastic (blue) scattering events. The colored solid and dashed lines show coupled channel calculations for a thermal sample with $T = 800\,\mathrm{nK}$ and a degenerate sample with $T = 30\,\mathrm{nK}$, respectively. The data points show the measurement results for $T = 800\,\mathrm{nK}$. The shaded area indicates the limit for measurements of the elastic collision rate imposed by the hydrodynamic regime. The vertical gray dashed line separates the semiclassical and threshold regime for 800 nK. The Rabi frequency is $\Omega \approx 2\pi \times 11\,\mathrm{MHz}$. The triangular markers on the side indicate the calculated inelastic rate coefficients in absence of a microwave field. **b**, Examples of cross-thermalization measurements at $\Delta = 2\pi \times 30\,\mathrm{MHz}$ (bright) and $\Delta = 2\pi \times 80\,\mathrm{MHz}$ (dark). The lines are fits of a coupled differential equation system modelling the collision rates. **c**, The ratio γ of elastic to inelastic collision rates based on the measurements presented in **a**. Figure reproduced from Ref. [107].

$$\frac{dT_\mathrm{v}}{dt} = \frac{1}{12}K(2T_\mathrm{h} - T_\mathrm{v})T_\mathrm{v}n - 2\frac{\Gamma_\mathrm{th}}{3}(T_\mathrm{v} - T_\mathrm{h}), \tag{4.16}$$

with the mean density

$$n = \frac{N}{8\sqrt{\pi^3 k_\mathrm{B}^3 T_\mathrm{h}^2 T_\mathrm{v}/M^3\bar{\omega}^6}}. \tag{4.17}$$

Here, K is the temperature-independent two-body loss coefficient, averaged for simplicity over all collision angles, and

$$\Gamma_\mathrm{th} = \frac{n\sigma_\mathrm{el}v}{N_\mathrm{col}} \tag{4.18}$$

is the rethermalization rate with the elastic scattering cross section σ_el and the thermally averaged collision velocity

$$v = \sqrt{16k_\mathrm{B}(2T_\mathrm{h} + T_\mathrm{v})/(3\pi M)}. \tag{4.19}$$

The average number of elastic collisions per rethermalization is taken from Ref. [185] as

$$N_\mathrm{col} = \bar{\mathcal{N}}_z(\phi) = \frac{112}{45 + 4\cos(2\phi) - 17\cos(4\phi)} \tag{4.20}$$

where ϕ is the tilt of the dipoles in the trap, which, in our case, corresponds to the tilt of the microwave wave vector with respect to the dc magnetic field. Following our characterization of the microwave polarization, we assume $\bar{\mathcal{N}}_z(29°) = 2.05$.

The anti-evaporation terms, i.e., the first terms in Eqs. (4.15) and (4.16), assume a linear scaling of the two-body loss rate with temperature. Our calculations predict that this assumption does not hold for small detunings ($\Delta < 2\pi \times 20\,\mathrm{MHz}$), as illustrated in Fig. 4.10. Our results, however, do not significantly change when we instead assume no temperature dependence in this regime.

Finally, after determining σ_el and K, the elastic and inelastic collision rate coefficients

$$\beta_\mathrm{el} = \sigma_\mathrm{el}v \tag{4.21}$$

and

$$\beta_\mathrm{in} = K(2T_\mathrm{h} + T_\mathrm{v})/3 \tag{4.22}$$

are plotted in Fig. 4.10a assuming a fixed temperature $T = T_\mathrm{h} = T_\mathrm{v}$.

Results

The results of the measurements are compared with coupled-channel calculations for a thermal sample at $T = 800\,\mathrm{nK}$ and 30 nK. The calculations account for a residual ellipticity of the microwave polarization. The inelastic cross section is also presented. The shielding is most efficient at $\Delta = 2\pi \times 8\,\mathrm{MHz}$, where β_in drops to $6.2(4) \times 10^{-12}\,\mathrm{cm}^3/\mathrm{s}$, corresponding to an order of magnitude suppression of the two-body losses, as illustrated in Fig. 4.10a. Note

that these measurements are performed with a single helical antenna where the ellipticity is limited to about $\xi \approx 6°$, thus not optimum for shielding.

For spin-polarized fermionic polar molecules, the elastic collision rate is dominated by dipolar scattering. For the temperature explored here, the scattering is in the threshold regime at large detunings, and enters the semiclassical regime for $\Delta/\Omega < 1$. The corresponding scattering cross section can therefore be tuned over multiple orders of magnitude with the detuning of the microwave. In the regime of weak interactions, i.e., at large detunings, the rethermalization rate is proportional to β_{el}. However, for $\Delta \leq 2\pi \times 10\,\mathrm{MHz}$ the elastic collisions become so frequent that the mean free path of the molecules is less than the size of the molecular cloud, even though here, we intentionally reduced the initial density to $n_0 = 0.7 \times 10^{11}\,\mathrm{cm}^{-3}$. In this hydrodynamic regime, the rethermalization rate is limited to about $\bar{\omega}/(2\pi) \approx 120\,\mathrm{Hz}$, where $\bar{\omega}$ is the geometric mean trap frequency [186]. Consequently, measured values of β_{el} saturate near the so-called hydrodynamic limit $N_{\mathrm{col}}\bar{\omega}/(2\pi n_0)$ where $N_{\mathrm{col}} \approx 2$ is the average number of collisions required for rethermalization in our system. This also limits the maximal measured value of γ to 460(110), as illustrated in Fig. 4.10c. Away from the hydrodynamic regime, we find excellent agreement between the experimentally determined and the calculated values of β_{el} and γ for $T = 800\,\mathrm{nK}$. Our calculations show that γ can exceed 1000 for ideal values of Δ. In the future, it should be possible to improve the shielding and achieve $\gamma \approx 5000$ by optimizing the purity of the microwave polarization.

4.3 Evaporation to Fermi degeneracy

With $\gamma \gtrsim 500$ at the optimum shielding detuning $\Delta = 2\pi \times 8\,\mathrm{MHz}$, evaporative cooling of our molecular sample proceeds straightforwardly. We begin with a low-entropy yet non-thermalized sample comprising roughly 2.5×10^4 molecules, produced from a density-matched degenerate atomic mixture [64]. The two horizontally propagating laser beams which hold the molecules against gravity and thus determine the effective trap depth U_{trap}. The trap depth is reduced exponentially over a span of 150 ms. This allows the most energetic molecules to escape the dipole trap in the direction of gravity. Subsequently, the remaining molecules rethermalize via elastic dipolar collisions, effectively lowering both T and T/T_{F}. The calculated elastic collision rate during evaporation is approximately 500 Hz, significantly surpassing the trap frequencies, leading to a saturation of the rethermalization rate at around $\bar{\omega}/(2\pi) \approx 60\,\mathrm{Hz}$.

To sustain a high rethermalization rate while reducing the trap depth, we enhance the horizontal confinement by exponentially increasing the power of an additional vertical beam, which is the same beam for density-matching the atomic mixture (see Chapter 2). Throughout the evaporation, we begin with near-degenerate molecules at frequencies of $2\pi \times (45, 67, 157)\,\mathrm{Hz}$ and stop at, for example, $2\pi \times (52, 72, 157)\,\mathrm{Hz}$ in case I, or $2\pi \times (42, 56, 99)\,\mathrm{Hz}$ in cases II and III (see Fig. 4.11).

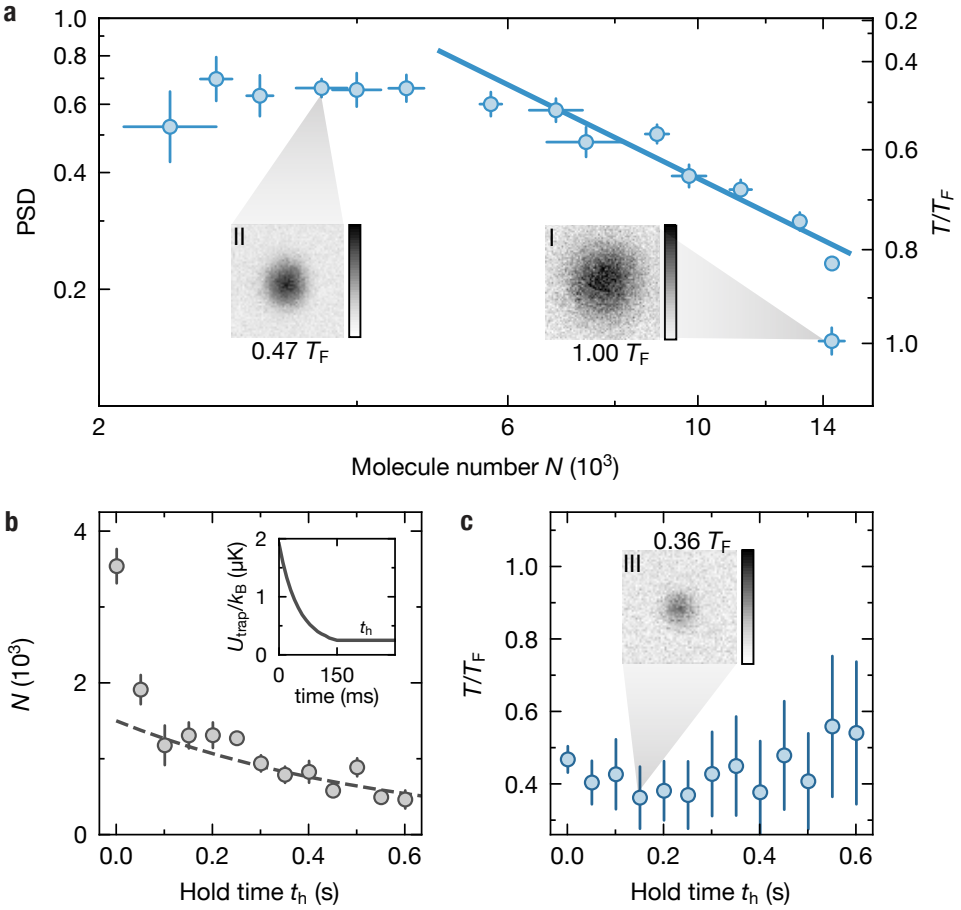

Figure 4.11: Evaporation. **a**, Phase space density (PSD) and T/T_F against the remaining number of molecules N following 150 ms of evaporative cooling, examined at various final trap depths. The line represents a linear fit in log scale to the data within the range $0.5 < T/T_F < 1$ and $N > 4000$, excluding consideration of the error bars. **b**, Number decay during the plain evaporation hold time t_h subsequent to 150 ms of forced evaporation. The dashed line is the fitted the one-body decay. Inset shows the trap depth during the evaporation sequence. **c**, Variation of T/T_F over the hold time t_h. The error bars for N in **a** and **b** are computed as the standard error of the mean across 5 to 20 repetitions. The error bars for T/T_F in **a** and **c** reflect the standard deviation derived from fitting the averaged images. Insets display the optical density of the samples after a 10 ms time-of-flight.

We characterize the evaporation when changing the final trap depth. Figure 4.11a illustrates T and T/T_F against the remaining number of molecules N after 150 ms of forced evaporation, with values derived from a polylogarithmic fit to the momentum distribution, imaged after a 10 ms time of flight (see Section 2.1.3). When the trap depth is maintained, the molecules will thermalize but not evaporate. Initially, the molecules display a sloshing motion in the trap due to photon-recoil transfer from the STIRAP pulses. Damping of such collective excitations and particle loss considerably diminish the phase space density of the sample. After 150 ms of holding at the initial trap depth, we obtain $1.43(5) \times 10^4$ molecules at a temperature of 176(5) nK with $T/T_\mathrm{F} = 1.00(3)$ (inset I). If we instead evaporate down to $3.6(3) \times 10^3$ molecules by reducing the final trap depth to about $k_\mathrm{B} \times 250\,\mathrm{nK}$, we reach 38(2) nK with $T/T_\mathrm{F} = 0.47(2)$ (inset II). However, the evaporation continues beyond this point. We can allow the molecular sample to remain for an additional hold time t_h in the trap to exploit plain evaporation, as depicted in Fig. 4.11b and 4.11c. This plain evaporation endures for about 100 ms, followed by an exponential decay in the molecule number with a $1/e$ lifetime of approximately 600 ms. At $t_\mathrm{h} = 150\,\mathrm{ms}$, we measure 21(5) nK with $T/T_\mathrm{F} = 0.36(9)$ (inset III).

We verified that the temperatures obtained from the Fermi–Dirac fit align with those deduced from a Gaussian fit to the thermal wing, where the potential influence of dipolar interactions is relatively minor. Intriguingly, the optical density in a small region of the cloud center exceeds the Fermi–Dirac fit in the coldest sample III (see also Fig. 2.3). However, the low signal-to-noise ratio precludes a conclusive determination of whether this discrepancy is due to imaging noise or potential dipolar interaction effects. Future investigations will likely shed light on the underlying mechanism.

4.4 Collective modes

As evidence of strong dipole-dipole coupling, we investigate the excitation spectrum of the confined dipolar gas through parametric heating. Following forced evaporation (case II), we ramp the microwave detuning in 50 ms to adjust the dipole-dipole interaction strength. We subsequently modulate the vertical beam for 50 ms to induce motional excitations of the gas. We image the molecules after an additional hold time of 20 ms and a time-of-flight of 8 ms. Since we start in a near-pancake trap with trapping frequency $\omega_x \approx \omega_y = \omega_\mathrm{r} < \omega_z$, modulation of ω_r predominantly excite the radial breathing mode of the trapped Fermi gas [187]. Nonetheless, given the trap's deviation from perfect cylindrical symmetry, other surface modes may also be excited. We selectively probe the modulation spectrum at frequencies below ω_z and above ω_r, which are not high enough to excite the axial mode, but suffice to probe the radial breathing or radial quadrupole modes. When the modulation frequency resonates with the frequency of the collective modes, it induces oscillations and heats up the sample along the horizontal direction.

Figure 4.12 shows the aspect ratio of the cloud after the expansion. At a 200 MHz detun-

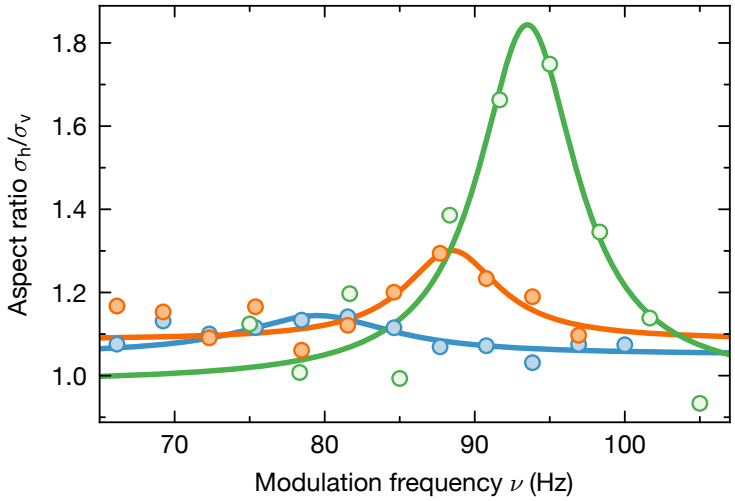

Figure 4.12: Parametric heating. Ratio of the cloud width along the horizontal σ_h and the vertical σ_v direction as a function of modulation frequency ν. The blue, orange, green colors correspond to microwave detuning $\Delta/2\pi$ of 8 MHz, 15 MHz, and 200 MHz respectively. The solid lines represent fits to a Lorentzian lineshape. The modulation amplitude of the vertical beam is 40% of its power.

ing, where the interaction strength is comparatively small, the modulation initiates parametric heating along the horizontal axis at a frequency approximately twice the trapping frequency, denoted as $2\omega_r$. For increased interaction strengths, the excitation peak broadens and shifts towards lower frequencies, signifying a transition from the non-interacting, collisionless regime to the hydrodynamic regime with collective mode frequencies $\sqrt{10/3}\omega_r$ (breathing mode) and $\sqrt{2}\omega_r$ (quadrupole mode) [188, 189].

Future experiments could be conducted in a single-beam, cigar-shaped trap with cylindrical symmetry, where axial and radial modes can be selectively excited and probed [190]. Time-domain measurements in such a setup would offer a more precise determination of the frequencies and damping rates of these collective modes. These elementary excitations provide crucial insights into the properties of the dipolar gas. They could serve as a precise test of the equation of state [191] under different interaction strengths and temperatures [192], reveal the anisotropy of dipole-dipole interactions [193], and detect the onset of superfluidity [194].

4.5 Prospects and challenges of reaching $0.1\,T_F$

Although the present achieved Fermi degeneracy is already sufficient to explore some many-body effects such as the deformation of Fermi surface [195] and the hydrodynamic modes [196], we want to further cool down the sample to below $0.1\,T_F$, which is required to explore p-wave superfluidity and achieve above 90% filling fraction after loading into optical lattices

(see Fig. 5.2). Here we discuss the challenges and their potential solutions.

First of all, it is always desirable to start with a better initial condition. In Ref. [64] we estimated based on particle loss the initial temperature of the non-thermalized ground-state molecules to be $0.52\,T_{\mathrm{F}}$. However, damping of collective excitations during the rethermalization in combination with particle loss leads to a sample temperature of about $1.0\,T_{\mathrm{F}}$ after 150 ms if we do not force evaporation. The initial phase space density can be increased by optimizing the magnetoassociation, the levitation of the Feshbach molecules, and the efficiency of STIRAP transfer.

Next, we need to enhance the efficiency of evaporation. The currently achieved efficiency, given by $-\mathrm{d}(\ln \mathrm{PSD})/\mathrm{d}(\ln N) = 1.1(1)$, is below what is typically realized with atoms [195,197,198]. To improve this efficiency, a longer evaporation time is required, thus necessitating a further reduction in collisional loss and various sources of heating. Firstly, we may operate at a larger Rabi frequency, while carefully avoiding the field-linked resonances near 90 MHz, as illustrated in Fig. 4.13. The sensitivity of the loss coefficient to ellipticity poses a challenge to the stability of the microwave polarization, which prompted us to develop the waveguide antenna and investigate the field-linked resonances in Chapter 6. Secondly, we can reduce the density of the cloud while avoiding the hydrodynamic regime, without sacrificing the thermalization rate. This approach is feasible due to the higher elastic scattering rate between microwave-shielded polar molecules compared to atoms. With these improvements, a two-body lifetime much longer than 10 s can be achieved, even for a hot sample as in our current initial condition. Thirdly, technical heating issues such as trap stability and intensity noise need to be minimized [199]. Ultimately, any cooling technique for fermions will be constrained by the escalating hole heating rate and Pauli blocking effect in the deep Fermi degenerate regime [200]. Therefore, a minimum number of molecules must be preserved to maintain the evaporative cooling rate against heating [201].

Once deep Fermi degeneracy is attained, it remains unanswered how to probe the temperatures in this regime. The time-of-flight images can no longer be fitted by the momentum distribution of a non-interacting gas. Fermi surface deformation, a phenomenon observed to affect only a few percent in magnetic atoms, will exceed 10% for our NaK molecules, consequently influencing the fitting to Eq. (2.1). Hence, a theoretical framework, such as Hartree–Fock–Bogoliubov theory [202], is needed to calculate the momentum distribution of a trapped dipolar Fermi gas within the Fermi degenerate regime at finite temperatures. Additionally, one could examine solely the momentum distribution of the thermal wing, which however, diminishes with Fermi degeneracy and thus requires an improvement to signal-to-noise ratio of the current imaging system. Damping and shifts of hydrodynamic modes [193], dispersion of sound waves [203] or RF ejection spectroscopy [204] might also serves as thermometry methods. If the temperature falls below the critical temperature for superfluidity, it may also be inferred from the associated tetramer fraction [25], a topic we will explore in Chapter 7.

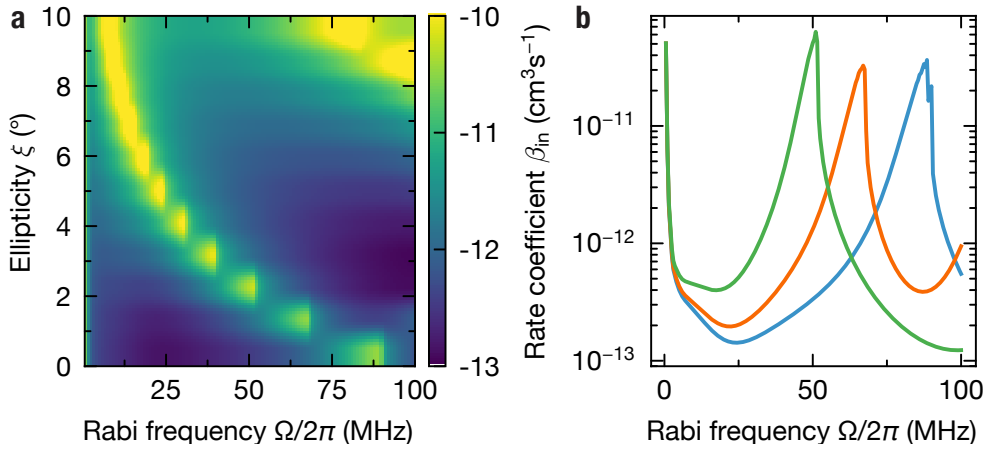

Figure 4.13: Inelastic rate coefficient at detuning $\Delta = 2\pi \times 1\,\mathrm{MHz}$ and temperature of 20 nK. **a**, 2D map of loss rate coefficient β_{in} as a function of Rabi frequency Ω and ellipticity ξ. **b**, Example loss rate coefficient for $\xi = 0°$ (blue), 1° (orange), and 2° (green). The discretization of the resonance feature at high Rabi frequencies is an artifact due to a finite step in ξ of 1°. Calculation performed by Tijs Karman.

4.6 Conclusion and outlook

In conclusion, we have demonstrated a general approach to evaporatively cool ultracold polar molecules to quantum degeneracy in 3D by dressing the molecules with a blue-detuned circularly polarized microwave, achieving very low temperatures together with strong tunable dipolar interactions. The simplicity of the technical setup makes our method directly applicable in a wide range of ultracold molecule experiments. Our results point to an exciting future of long-lived degenerate polar molecules for investigating novel quantum many-body phases with long-range anisotropic interactions and for other applications in quantum sciences.

With the coldest samples realized in our experiment, the dipolar interaction in the system corresponds to about 5% of the Fermi energy. This is three times higher than what was reached in degenerate Fermi gases of magnetic atoms [205]. In the near future, intriguing dipolar many-body phenomena such as modifications of collective excitation modes [193], hydrodynamic weltering motion [196], distortion [205] or the collapse [206] of the Fermi sea should be observable in suitable trap geometries and with improved detection of the cloud expansion. The collisionally stable sample also provides an ideal starting point for loading into optical lattices, as presented in Chapter 5.

Once we manage to reach temperatures below $0.1\,T_{\mathrm{F}}$, many intriguing quantum phases will be within reach [6,177,207–213]. Especially, fermionic polar molecules can pair up and form a superfluid with anisotropic order parameter and even a Bose–Einstein condensate of tetramers [207–209]. Up to now, such scenarios have rarely been theoretically investigated because it was believed that polar molecules could not be sufficiently stable under

conditions where both attractive and repulsive interactions play an important role. We will revisit this topic in Chapter 6 and 7. In the next chapter, we shift our focus from collisional studies to spin physics, where the dipole-dipole interactions continue to play the central role.

Let's measure something other than loss.

After two years' of loss measurements[1]

Chapter 5

Lattice loading and dipolar spin models

Quantum simulations using polar molecules in optical lattices has always been one of our scientific goals. In 2019, we managed to achieve only a filling fraction of a few percent, brought about by the Feshbach association from a Mott insulator of sodium atoms and a band insulator of potassium atoms in the 3D lattice. Back then the major limiting factor was the low quality of the vertical lattice potential, which was generated by sending a retroreflected laser beam through a high-NA objective [125]. Upon stabilizing the molecules via microwave shielding, we deemed it appropriate to return to the lattice. Half a year of subsequent efforts revealed that the performance of our microwave shielding still hindered us, which ultimately drove us to upgrade the system and delve deeper into collision studies, as presented in Chapter 6. Despite these challenges, our accomplishments thus far are promising. We have managed to prepare a molecular sample predominantly in a single layer of a vertical shallow-angle lattice, and in the ground band of the horizontal lattice, achieving around 24% filling fraction. These findings will be discussed in the following.

5.1 Ultracold polar molecules in optical lattices

In this section, we introduce the general Hamiltonian realized by polar molecules in optical lattices, and show how this Hamiltonian reduces to either the lattice spin model or the extended Hubbard model under specific conditions.

In the presence of a d.c. electric field, polar molecules in the ground band of an optical

[1] We often joke that we've done so many loss measurements, we might as well call it our version of "quantum simulation".

lattice yield the t-J-V-W model, represented by the following Hamiltonian [214–216]

$$H = -t \sum_{\langle i,j\rangle m} \left[c_{im}^{\dagger} c_{jm} + \text{ h.c. } \right] + \frac{1}{2} \sum_{i \neq j} \frac{1 - 3\cos^2\theta_{ij}}{r_{ij}^3} \times \left[\frac{J_\perp}{2} (S_i^+ S_j^- + \text{ h.c. }) + J_z S_i^z S_j^z + V n_i n_j + W (n_i S_j^z + n_j S_i^z) \right]. \tag{5.1}$$

Here, $c_{im}^{\dagger}$ (c_{im}) creates (annihilates) a molecule on site i in rotational state $m = 0$ or 1. The operator $n_i = \Sigma_m n_{im} = \Sigma_m c_{im}^{\dagger} c_{im}$ counts the number of molecules on site i. The operators $S_i^z = (n_{i1} - n_{i0})/2$, $S_i^+ = c_{i1}^{\dagger} c_{i0}$, and $S_i^- = (S_i^+)^{\dagger}$ are the usual spin-1/2 angular momentum operators on site i. The t-J-V-W Hamiltonian captures several key phenomena: the tunneling (t), the spin-1/2 exchange process ($J_\perp$), and the electric field-dependent processes (J_z, V, and W). The strength of the interactions depends on the choice of the excited rotational state. For $|\uparrow\rangle = |J = 1, M_J = 0\rangle$, the spin-exchange interaction is given by

$$J_\perp = 2 d_{\downarrow\uparrow}^2 / 4\pi\varepsilon_0 a^3, \tag{5.2}$$

where a is the lattice constant and $d_{\downarrow\uparrow} = d_{\uparrow\downarrow} = \langle\downarrow | \hat{d}_0 | \uparrow\rangle$ denotes the transition dipole moment between two spin states and $\hat{d}_q$ denotes the spherical components of the dipole operator. The other terms require a non-zero lab frame dipole moment and are therefore absent at zero electric field. They are related to the dipole matrix elements by $J_z = (d_\uparrow - d_\downarrow)^2$, $W = (d_\uparrow^2 - d_\downarrow^2)/2$, and $V = (d_\uparrow^2 + d_\downarrow^2)/4$, with $d_\uparrow = \langle\uparrow | \hat{d}_0 | \uparrow\rangle$, $d_\downarrow = \langle\downarrow | \hat{d}_0 | \downarrow\rangle$, and $1/4\pi\varepsilon_0 a^3$ omitted.

Figure 5.1a illustrates the example interactions of the t-J-V-W model. There, the couplings are evaluated in the spin decoupled basis and reduced to the single-particle dipole matrix elements

$$\langle\downarrow\downarrow | V_{\text{dd}} | \downarrow\downarrow\rangle = \frac{J_z}{4} + V - W = d_\downarrow^2, \tag{5.3}$$

$$\langle\uparrow\uparrow | V_{\text{dd}} | \uparrow\uparrow\rangle = \frac{J_z}{4} + V + W = d_\uparrow^2, \tag{5.4}$$

$$\langle\downarrow\uparrow | V_{\text{dd}} | \downarrow\uparrow\rangle = \langle\uparrow\downarrow | V_{\text{dd}} | \uparrow\downarrow\rangle = -\frac{J_z}{4} + V = d_\downarrow d_\uparrow, \tag{5.5}$$

$$\langle\downarrow\uparrow | V_{\text{dd}} | \uparrow\downarrow\rangle = \langle\uparrow\downarrow | V_{\text{dd}} | \downarrow\uparrow\rangle = \frac{J_\perp}{2} = d_{\downarrow\uparrow}^2. \tag{5.6}$$

Here again the prefactor $1/4\pi\varepsilon_0 r_{ij}^3$ is omitted. Note that the coupling extend beyond the nearest neighbor, and falls off with $1/r_{ij}^3$. The coupling strength are given in unit of d_0^2. Their dependence to electric field strength is shown in Fig. 5.1b. For NaK molecules with $d_0 = 2.72\,\text{D}$, we have $d_0^2/4\pi\varepsilon_0 a^3 = h \times 7.31\,\text{kHz}$ for a 532 nm spacing optical lattice. The electric field strength is in unit of $B/d_0 = 2.05\,\text{kV/cm}$.

In addition to the Hamiltonian described in Eq. (5.1), another key consideration is the substantial collisional loss between molecules. This losses suppress the occupancy of two

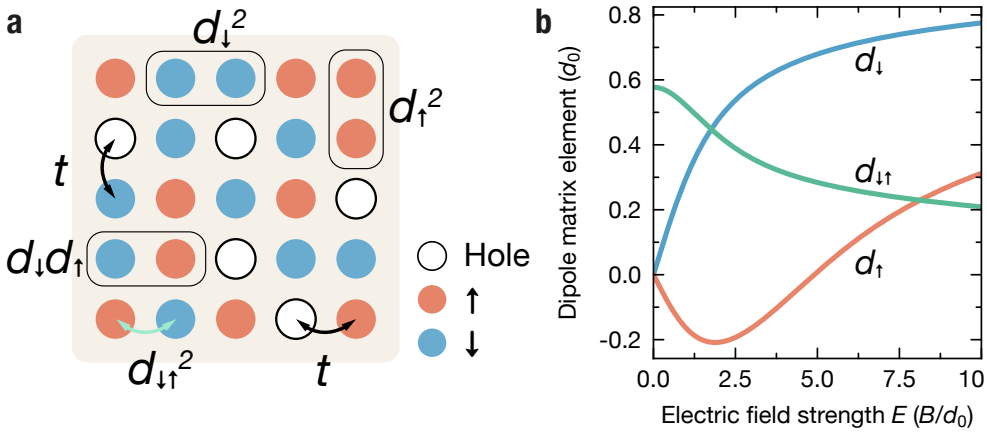

Figure 5.1: t-J-V-W **model.** **a**, Spin-1/2 dipolar fermions in a 2D optical lattice. Examples of direct spin-spin couplings are represented by rectangles, and spin-exchange interaction and tunneling are represented by two-headed arrows. **b**, Dipole coupling matrix elements as a function of d.c. electric field strength.

molecules on the same lattice site due to the Quantum Zeno effect [79, 217]. Typically, at the lattice depth when tunneling is relevant, the on-site interaction surpasses the band gap. This causes molecules to be excited to higher bands, leading to a loss rate that 5 times larger than what would be predicted by single-band calculations [217]. Therefore, it is desirable to reduce the collisional loss either by constraining the molecules within a deep lattice or by employing a shielding scheme to engineer a repulsive interaction.

In a deep lattice, the tunneling term becomes negligible, giving rise to the dipolar spin model. This model has gained recent attention across various platforms, particularly with trapped ions [218,219] and Rydberg atoms in optical tweezer arrays [220–224]. The field of Rydberg atoms has seen rapid progress, thanks in part to their fast cycling rates, adaptable atomic arrangements, and their scalability. However, the primary constraint with Rydberg atoms lies in their short lifetime, compounded by the fact that they are untrapped. Conversely, ground-state molecules typically exhibit a trapped lifetime on the scale of seconds, making them an attractive candidate for exploring long-term spin dynamics.

In terms of shielding, we are currently constrained to working with a single internal state. Consequently, we lose the spin degree of freedom and realize the extended Hubbard model

$$H = -t\sum_{\langle i,j\rangle}\left[c_i^\dagger c_j + \text{h.c.}\right] + \frac{1}{2}\sum_{i\neq j}\frac{1-3\cos^2\theta_{ij}}{r_{ij}^3}\left[V - W + \frac{J_z}{4}\right]n_i n_j \tag{5.7}$$

$$= -t\sum_{\langle i,j\rangle}\left[c_i^\dagger c_j + \text{h.c.}\right] + \frac{1}{2}\sum_{i\neq j}\frac{d_\downarrow^2(1-3\cos^2\theta_{ij})}{r_{ij}^3}n_i n_j \tag{5.8}$$

This Hamiltonian exhibits checkerboard and stripe phases, which have been previously

observed in dipolar excitons [225] and magnetic atoms [226]. Nevertheless, there is a wealth of physical phenomena still awaiting exploration at lower temperatures or with different lattice geometries [6]. Moreover, the shielding schemes of polar molecules are, in principle, insensitive to the hyperfine states of the molecules, allowing spin to be encoded in these hyperfine levels.

5.2 Lattice loading

One method to achieve a high filling fraction of molecules is to form them directly within the lattice. This process typically starts from a double insulator of the atomic mixture, where each site is occupied by one atom from each species, leading to a high conversion efficiency from atoms to molecules on sites. However, realizing a double insulator poses a significant challenge, especially when the tunneling and on-site interaction of the two atomic species differs considerably. So far, the highest filling fraction achieved using the double insulator method is approximately 30% [227–229]. This approach will ultimately be constrained by the efficiency of STIRAP, thus posing a challenge to attain unit filling.

Efficient shielding enables us to load molecules directly into the lattice. Here, the STIRAP only limits the detection efficiency instead of affecting the lattice filling fraction. As shown in Fig. 5.2, starting with a degenerate sample of $T/T_F = 0.36$ as obtained in our experiment, adiabatic loading would result in a filling fraction of 30%. With further cooling to $T/T_F < 0.1$, we expect a filling fraction above 96%.

The experiments in this chapter were conducted with the microwave setup of a single helical antenna, a signal source of $-149\,\mathrm{dBc/Hz}$ (Rohde&Schwarz SMF100A),[1] and a 10 W amplifier (Kuhne PA510590). The relatively high phase noise and imperfect polarization of the helical antenna limit the performance of microwave shielding, thus affecting the lattice loading efficiency. In the future, we plan to attempt lattice loading with the upgraded microwave setup.

5.2.1 Isentropic loading

We calculate the lattice filling fraction after loading from a 3D bulk gas. To estimate the maximum loading efficiency, we assume the the entropy is conserved and the gas is in thermal equilibrium. The final temperature and distribution can be obtained from entropy and molecule number conservation. The thermodynamic quantities of a Fermi gas is related to the density of states in the external potential.

$$N = \int_0^\infty \mathrm{d}\epsilon g(\epsilon) \frac{1}{e^{(\epsilon-\mu)/k_B T}+1}, \tag{5.9}$$

[1] This signal source, which we borrowed from the Rempe group, has greater phase noise in comparison to the one previously used in Chapter 4, which we borrowed from Walther Meißner Institute.

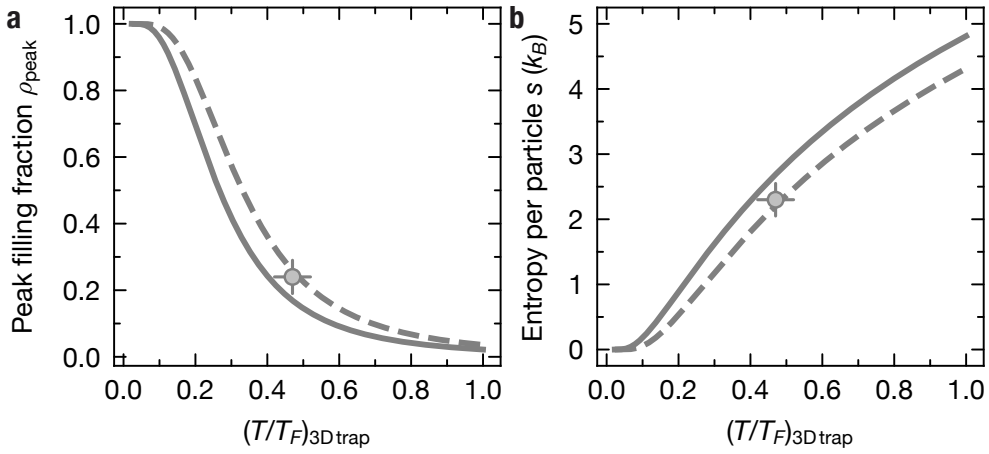

Figure 5.2: Isentropic loading from a 3D trapped gas into lattices. Filling fraction (**a**) and entropy per particle (**b**) as a function of the initial T/T_F in the trap. The solid and dashed lines show the case for 2D and 3D lattices, respectively. The circles mark the measured filling fraction and the calculated entropy per particle (Eq. (5.19)) starting from $(T/T_F)_{3\text{D trap}} = 0.46(5)$ after forced evaporation.

$$E = \int_0^\infty \mathrm{d}\epsilon g(\epsilon) \frac{\epsilon}{e^{(\epsilon-\mu)/k_BT}+1}, \tag{5.10}$$

$$\Omega = -k_BT \int_0^\infty \mathrm{d}\epsilon g(\epsilon) \ln(e^{(\mu-\epsilon)/k_BT}+1), \tag{5.11}$$

$$S = \frac{E-\mu N-\Omega}{T}, \tag{5.12}$$

where μ is the chemical potential, E is the energy, Ω is the grand potential, and S is the entropy. The density of states is related to the trapping frequency geometrically $\bar{\omega}$ averaged over all the confinement directions. For a trapped 3D gas, the density of states is

$$g_{3\text{D trap}}(\epsilon) = \frac{\epsilon^2}{2(\hbar\bar{\omega}_{3\text{D trap}})^3}. \tag{5.13}$$

While in a 2D/3D lattice in the tight binding limit, the density of states is given by [230]

$$g_{2\text{D lattice}}(\epsilon) = \frac{2\pi}{m\bar{\omega}^2_{2\text{D lattice}}a^2}, \tag{5.14}$$

$$g_{3\text{D lattice}}(\epsilon) = 2\pi\sqrt{\epsilon}\left(\frac{1}{2}ma^2\bar{\omega}^2_{3\text{D lattice}}\right)^{-3/2}. \tag{5.15}$$

These integrals can be evaluated analytically using the following result

$$\int_0^\infty \mathrm{d}\epsilon \epsilon^n F(\epsilon,\mu) = -(k_BT)^{n+1}\,\Gamma(n+1)\mathrm{Li}_{n+1}(-e^{\mu/k_BT}), \tag{5.16}$$

$$F(\epsilon,\mu) = (1+e^{(\epsilon-\mu)/k_BT})^{-1}. \tag{5.17}$$

where $\mathrm{Li}_n(x)$ is the polylogarithmic function of order n, $\Gamma(x)$ is the gamma function, and $F(\epsilon, \mu)$ is the Fermi–Dirac distribution function. We assume the the molecules remains in the ground band of the lattice. At zero temperature, the Fermi gas will form a band insulator in the center of the lattice, with unity filling fraction. At finite temperatures, the peak filling fraction can be calculated from the Fermi–Dirac distribution

$$\rho_{\mathrm{peak}} = F(0, \mu) = (1 + e^{-\mu/k_B T})^{-1}. \tag{5.18}$$

Figure 5.2 shows filling fraction loaded from a bulk gas into 2D/3D lattices. The entropy per particle is related to the filling fraction by

$$s(\rho) = -\frac{k_B}{\rho}(\rho \ln(\rho) - (1-\rho)\ln(1-\rho)). \tag{5.19}$$

5.2.2 Loading into the vertical lattice

Our aim is to load a degenerate gas of microwave-shielded molecules from the bulk into predominantly a single layer of the shallow-angle lattice, and then transfer them into the ground band of the horizontal lattice. As we are dealing with fermionic molecules, each layer has a maximum molecule number that can be populated, whereby the molecules form a band insulator. This is determined by the condition $E_F = \Delta E$, where $E_F = \hbar\bar{\omega}(6N)^{1/3}$ denotes the Fermi temperature, and $\Delta E \approx \hbar\omega_{\mathrm{s.a.lattice}}$ represents the band gap of the shallow-angle lattice. Given the on-site trapping frequencies of the shallow-angle lattice $2\pi \times (20, 20, 3.4 \times 10^3)$ Hz, this maximum number amounts to approximately 6000.

To achieve single-layer loading, we first transfer the molecular gas into a light sheet to decrease the vertical cloud radius before introducing the shallow-angle lattice. The light sheet compresses mainly vertically, with trapping frequencies $2\pi \times (20, 35, 520)$ Hz. Assuming adiabatic compression of a cloud of 3000 molecules at $T/T_F = 0.3$, we achieve a vertical cloud $1/e$ radius of $2\,\mu$m, which is smaller than the lattice constant. However, we observe substantial two-body loss and evaporation during the compression, due to the increased density after compression and the reduced trapping volume of the light sheet compared to the crossed dipole trap. The loss occurred during the single-layer loading has motivated us to upgrade the microwave setup to achieve higher power and tunable polarization.

We determine the molecule distribution using the matter-wave refocusing technique [231–233]. After loading, we switch off the lattice and switch on the light sheet, which provides a strong vertical confinement. The cloud oscillates in the light sheet for a quarter of its trapping period, mapping the vertical position r into the momentum $p = m\omega r$, where ω is the vertical trapping frequency. The cloud is then released from the trap and undergoes a time-of-flight of t_{tof}. The final real-space coordinate $r_{\mathrm{tof}} = (\omega t_{\mathrm{tof}})r$. With a large trapping frequency ω and a prolonged time-of-flight, the cloud is magnified by a factor of ωt_{tof}. For a finite time-of-flight, a pulse duration slightly less than a quarter period can eliminate the effect of the initial momentum spread and obtain a focused image.

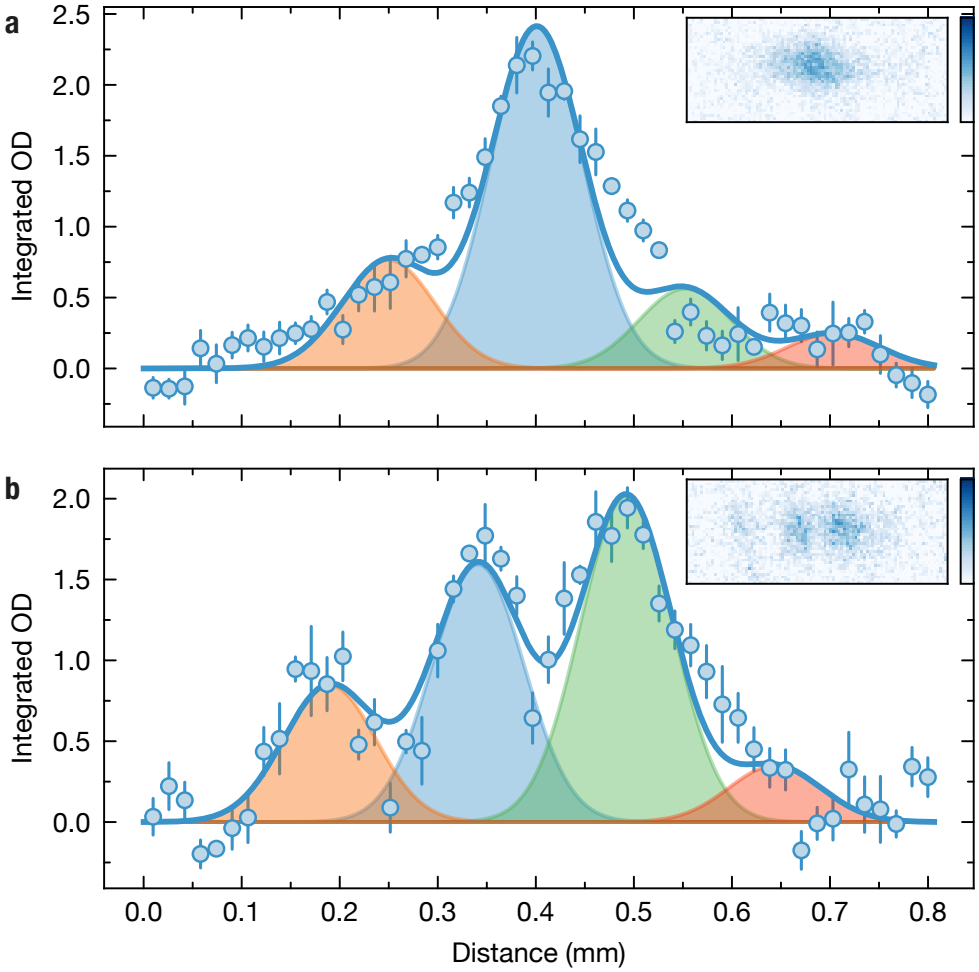

Figure 5.3: Matter wave refocusing of molecules in the vertical lattice. Molecules loaded after forced (**a**) and plain (**b**) evaporation. The data points show the distribution of the OD integrated along the horizontal direction. Each point representing an average over a 5-pixel range in the vertical direction. The solid line shows a combined Gaussian fit and the colored regions show contributions from the individual layers. The insets shows the absorption images, where the right and left correspond to up and down, respectively. Each image is averaged over 3 repetitions.

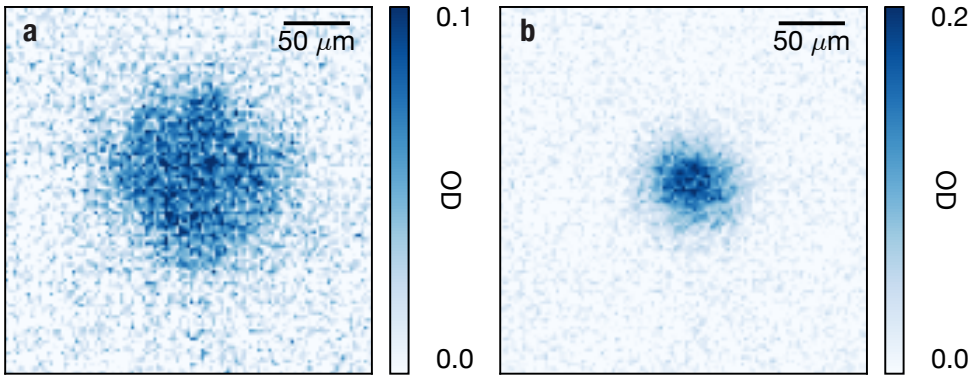

Figure 5.4: Quasimomentum and real space distributions of molecules in the lattice. Band-mapping (**a**) and in-situ images (**b**) in the 3D lattice. The imaging axis is vertical, perpendicular to the plane of the shallow-angle lattice. Each image is averaged over three repetitions.

Figure 5.3 shows the images after matter-wave refocusing, from which we infer the population distribution among the layers of the shallow-angle lattice. We use a time-of-flight of $t_{\mathrm{tof}} = 9\,\mathrm{ms}$ and a trapping frequency of $\omega = 2\pi \times 900\,\mathrm{Hz}$, leading to a magnification of 50. The fitted lattice spacing considering this magnification is 3.0 μm, consistent with the designed lattice spacing of the shallow-angle lattice. Starting from a molecular gas after forced evaporation, a majority of the population is loaded into the central layer. As a comparison, loading a thermal cloud at approximately 200 nK populated over three layers, with a lower peak OD in each layer. To quantitatively extract the population in each layer, we first extract the width of individual layers and their relative spacing by fitting to Fig. 5.3b. Next, we fix the extracted width and spacing, and fit only the relative populations in Fig. 5.3a. From the fit, we conclude that about 60% of the molecules are in the central layer.

5.2.3 Loading into the ground band of the horizontal lattice

Following the loading into the shallow-angle lattice, we ramp on the horizontal lattice in 50 ms. After loading, we use the band mapping technique to probe the band population [234, 235]. By slowly ramping down the lattice in 1 ms, a particle with a quasimomentum $\mathbf{q}$ in the extended Brillouin zone is adiabatically transferred to a momentum $\mathbf{p} = \mathbf{q}$ state in free space. Subsequently, a time-of-flight imaging directly probes the quasimomentum distribution, and thus the band occupation. Such a band mapping image is displayed in Fig. 5.4a. A distinct first Brillouin zone is visible, suggesting a high occupation of the ground band.

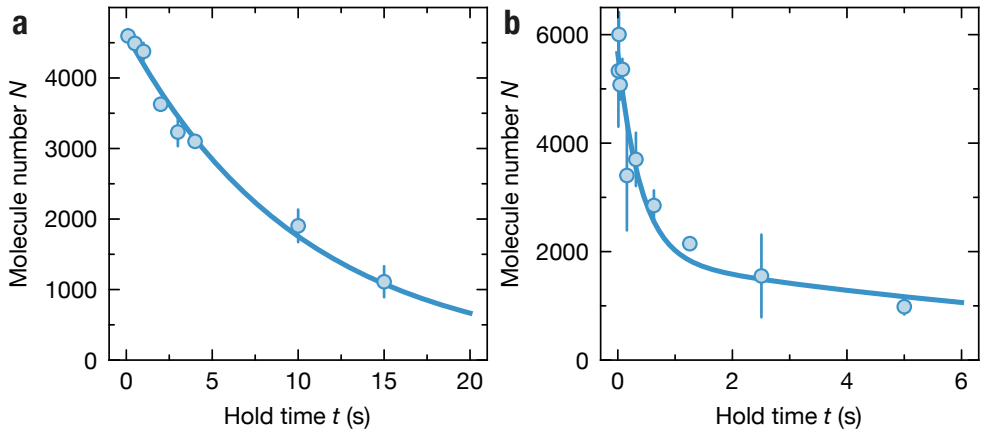

Figure 5.5: Lifetime of molecules in a deep lattice. **a**, Microwave is turned off after loading. A fit to exponential decay yields a lifetime of $\tau = 10.3(7)\,\mathrm{s}$. **b**, Microwave remains on after loading. A fit to yields a dressed-state lifetime of $\tau_1 = 0.4(1)\,\mathrm{s}$.

5.2.4 In-situ imaging

We use in-situ imaging to probe the density distribution and thereby estimate the filling fraction of the lattice, as shown in Fig. 5.4b. A Gaussian fit applied to the image gives a cloud radius of $R_x = 34\,\mu\mathrm{m}$ and $R_y = 30\,\mu\mathrm{m}$. From the matter-wave refocusing shown in Fig. 5.3, we deduce that $r_0 = 60\%$ of these molecules are loaded into a single layer. From the molecule number $N \approx 3900$, we obtain a peak filling fraction of $f_{\mathrm{peak}} = r_0 N a^2/\pi R_x R_y \approx 24\%$, which is consistent with the initial degeneracy of our molecules.

5.2.5 Lifetime of molecules in a deep lattice

Following the lattice loading, we measure the lifetime of the molecules in a deep horizontal lattice with a lattice depth of $V_{\mathrm{hor}} = 20\,E_{\mathrm{r}}$, see Fig. 5.5. If the microwave remains on, we observe an initial drop to half of the molecular count, succeeded by a slower decay. This initial decrease is attributed to the dephasing of the microwave-dressed states, as discussed in Section 4.1. After dephasing, the cloud becomes a 50/50 incoherent mixture of molecules in the ground and excited rotational states. Given that only the ground state can be transferred back by STIRAP, only half of the total count is detected. We thus fit the number decay to

$$N(t) = N_0 \left(e^{-t/\tau_1} + \frac{1}{2} \right) e^{-t/\tau}. \tag{5.20}$$

We obtain a one-body lifetime of $\tau_1 = 0.4(1)\,\mathrm{s}$, which is as expected due to the limited phase noise of $-149\,\mathrm{dBc/Hz}$. Alternatively, when the microwave is switched off after loading, the lifetime increases to 10 s, constrained primarily by the photon scattering of the lattice.

5.3 Spin dynamics

As an initial step towards quantum simulation with polar molecules in our setup, we explore the dipolar XY model, which is naturally realized in the presence of a moderate d.c. electric or magnetic field. We apply a d.c. field of 86 V/cm perpendicular to the lattice plane to decouple hyperfine spins, which suppresses hyperpolarizability as discussed in Section 2.2. The Hamiltonian can be expressed as

$$H = \sum_{i \neq j} \frac{J_\perp}{2r_{ij}^{-3}} (S_i^+ S_j^- + S_i^- S_j^+). \tag{5.21}$$

For $|\downarrow\rangle = |J = 0, m_J = 0\rangle$ and $|\uparrow\rangle = |J = 1, m_J = 0\rangle$, the interaction is antiferromagnetic with $J_\perp = d_0^2/6\pi\epsilon_0 a^3 > 0$, and for $|\uparrow\rangle = |J = 1, m_J = \pm 1\rangle$, the interaction is ferromagnetic with $J_\perp = -d_0^2/12\pi\epsilon_0 a^3$. The antiferromagnetic Hamiltonian is predicted to exhibit a rotational synchronization transition beyond a critical filling fraction of 15%, where a portion of the coherence is protected by the long-range dipole-dipole interaction [236]. At lower filling fractions, the spin dephasing time is inversely proportional to the mean-field dipolar interaction, offering an alternative method to calibrate the lattice filling fraction other than in-situ imaging.

5.3.1 Spin-echo Ramsey spectroscopy

We probe the spin dynamics using a spin-echo Ramsey spectroscopy sequence, as illustrated in Fig. 5.6. The spin-echo technique mitigates the residual single-particle dephasing arising from the inhomogeneous light shift across the molecular cloud, resulting in an extended coherence time. Starting from ground state $|\downarrow\rangle$, the initial $\pi/2$ pulse prepares the molecules in a superposition state $(|\downarrow\rangle + |\uparrow\rangle)/\sqrt{2}$. After an evolution time of $T/2$, an echo π-pulse is applied to reverse single-particle dephasing. After another evolution period of $T/2$, a second $\pi/2$ pulse is applied with a phase ϕ relative to the first pulse. By altering the phase ϕ and observing the number of molecules in the ground state, we can obtain a Ramsey fringe which follows $\frac{N_{\text{tot}}}{2}(1 + C\cos(\phi + \phi_0))$. The fringe contrast C represents the residual spin coherence. The phase offset ϕ_0 exhibits a linear increase with respect to the evolution time, scaling proportionally to $\chi_0 = J_z - J_\perp$ [237]. In experiments with KRb, the contrast follows an overall decay, and on top of that, an oscillation with a frequency of $J_\perp/2h$ due to the nearest-neighbor interaction [79]. For NaK, the oscillation is much faster and thus requires much finer sampling to resolve. Instead we focus on the overall decay. Figure. 5.6 displays the time evolution of the fringe contrast C and numerical simulation. The experimental fringe contrasts are systematically lower than the numerical simulation, suggesting additional decoherence mechanisms that are not cancelled by the spin-echo pulse.

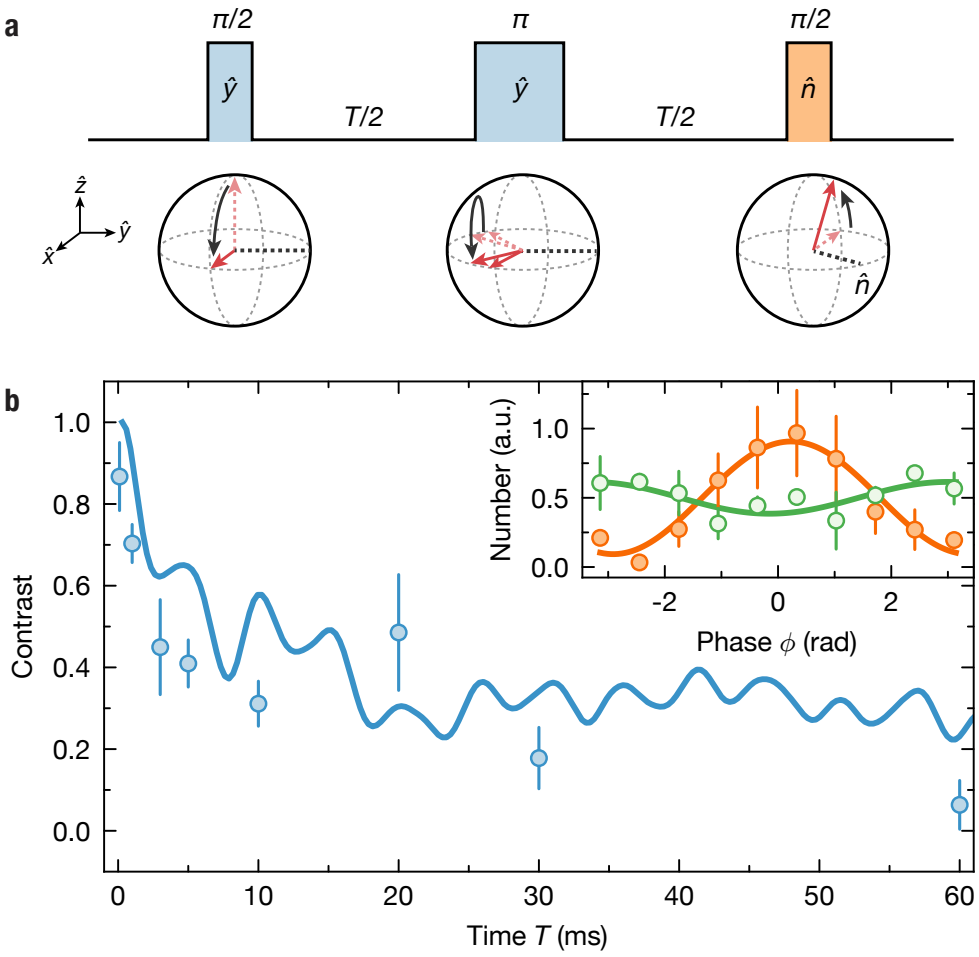

Figure 5.6: Spin dynamics of lattice dipolar XY model. a, sequence of spin-echo Ramsey spectroscopy. The phase of the second $\pi/2$ pulse is scanned to yield the fringes. **b**, measured (points) and simulated (line) contrast decay over the hold time T. Inset shows example Ramsey fringes for $T = 0.1\,\mathrm{ms}$ (orange) and $T = 30\,\mathrm{ms}$ (green).

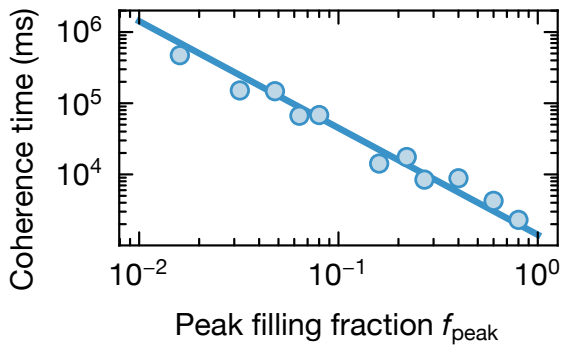

Figure 5.7: MACE simulation of dipolar decoherence rate as a function of filling fraction. Each point is extracted by an exponential fit to a MACE simulation. The solid line is a fit which yields Eq. 5.22.

5.3.2 Numerical simulation of the initial decoherence

At a low filling fraction $< 15\%$, comparing the spin dynamics with numerical simulations provides an alternative way to determine the filling fraction of the lattice. We anticipate the coherence time τ to scale with the molecule filling fraction ρ as $\tau \propto 1/\langle E_{\text{int}} \rangle \propto 1/J_\perp \rho^{3/2}$. We employ the Moving Average Cluster Expansion (MACE) method [216, 238] to calculate the spin dynamics at various filling fractions. In a MACE simulation, one generates a randomly distributed molecular sample, then divide the system into separate clusters. The dynamics of these clusters can be calculated precisely, and averaging over the clusters yields the global observable. For each molecule, we choose 8 nearest molecules to form a cluster, where the spin dynamics are calculated by exact diagonalization. As shown in Fig. 5.7, we extract the coherence time at different filling fraction ρ, then fit to the expected scaling, yielding

$$\tau \approx 1.44 \frac{h}{J_\perp \rho^{3/2}}. \tag{5.22}$$

We also plot the result of the MACE simulation at an expected 24% filling fraction, together with the data in Fig. 5.6.

5.3.3 Prospects of rotational synchronization and spin squeezing

The aforementioned MACE simulation does not consider coherence beyond the cluster size, which proves adequate at low filling fractions. However, as the filling fraction increases, dipolar interactions gradually overshadow the positional disorder due to random filling. In such cases, long-range coherence needs to be considered to accurately deduce the Ramsey spin dynamics. It has been predicted that beyond a critical filling fraction of $\rho_c \approx 15\%$, a fraction of coherence — which scales with $\sqrt{\rho - \rho_c}$ — will endure much longer than the initial fast dephasing [236]. This interaction-protected coherence is attributed to the long-range order of the dipolar XY model in the ferromagnetic regime at a negative spin temperature [239]. The emergence of long-range order at a finite temperature for a ground state with broken U(1) symmetry in 2D is a distinct feature of dipole-dipole interactions [240], which can be understood as a BEC of the spin waves [239]. To demonstrate that, a systematic measurement of spin dynamics at different filling fraction needs to be performed. Moreover, we can also probe the spin fluctuations, which is directly related to the condensate fraction of the spin wave and thus would provide a more direct evidence for such synchronization.

Rotational synchronization manifests following an extended evolution time[1] in excess of $10h/J_\perp$, during which spins either reach thermal equilibrium or enter a many-body localized state. Investigating this phenomenon necessitates the examination of spin dynamics over time intervals exceeding 100 ms. Currently, we are still constrained by technical decoherence, such as the instability of the electric field and noise in the microwave pulses.

[1] The required time scale for such evolution exceeds what is presently achievable on alternative platforms.

In the future, to extend the coherence time, we could employ more sophisticated dynamical decoupling schemes, such as the XY8 multi-pulse sequence [241], which are capable of enhancing the coherence time of polar molecules by more than one order of magnitude [56, 57, 237]. Alternatively, we can utilize the bootstrapping technique, which is also immune to the dephasing caused by shot-to-shot fluctuation of the d.c. electric field [242].

5.4 Conclusion and outlook

We have loaded a Fermi degenerate molecular sample from the bulk into predominantly a single layer of a 3D magic lattice, with the majority of the population in the ground band, and a 24% peak filling fraction. As a preliminary step towards quantum simulation, we have investigated the dipolar XY model by pinning down the molecules in a deep lattice. We have observed the decoherence due to dipolar spin-exchange interaction.

We are also constructing a bow-tie pinning lattice [243] and a setup for Raman sideband cooling of potassium atoms [147,148], with the goal of realizing a quantum gas microscope for NaK molecules [149]. Single-site imaging would give access to the correlation function of the many-body states, serving as a powerful probe of the system.

For bialkali molecules, the detection fidelity is inherently limited to 80-90% due to the STIRAP efficiency. This limitation arises from the natural linewidth of the intermediate state and laser phase noise [124, 244, 245]. However, employing active noise cancellation techniques, as demonstrated in Ref. [246], could potentially increase the STIRAP efficiency beyond 95%. Such an improvement would bring the imaging fidelity of bialkali molecules on par with that of directly laser cooled molecules [247, 248].

With the upgraded microwave setup presented in Chapter 3, and a better understanding of microwave shielding presented in Chapter 6 and 7, we plan to improve evaporation and revisit lattice loading, potentially achieving a lattice filling fraction close to unity.

Creating this "field-linked" state essentially means grabbing the molecules to stop them from slamming into each other.[1]

John Bohn

Chapter 6

Field-linked resonances

In the summer of 2021, while optimizing the shielding with the phase array antenna, we discovered unexpected resonance features in the molecule loss signal whenever the polarization deviated significantly from circular. These features were highly reproducible, leading us to believe there were new physics at play. However, we were unable to easily control the polarization with the phase array antenna. We tabled these observations temporarily to focus on lattice loading, but found ourselves again limited by inefficient shielding. Inspired by the need for better polarization control, we developed a dual-feed waveguide antenna (see Chapter 3), capable of conveniently tuning the polarization through a single parameter — the relative phase between the two feeds. After implementing this upgrade in early 2022, we systematically examined the resonances, which matched qualitatively with predictions from our theory collaborator, Tijs Karman. As we were drafting the paper, we began searching for a suitable term to describe these novel resonances. We came to realize that these so-called field-linked resonances had been predicted for molecules shielded by circularly polarized microwaves in 2018 [76], and in d.c. electric fields as far back as two decades ago [111].

Results of publications [112, 116] are contained in this chapter.

6.1 Field-linked bound states and scattering shape resonances

Scattering resonances, long-desired tools for ultracold polar molecules, have been instrumental in ultracold atom experiments for controlling contact interaction [250], creating strongly correlated quantum phases [251], and producing ultracold diatomic mole-

[1] Excerpt from a news article [249] published two decades ago, reporting the prediction of field-linked states.

cules [252]. Independent control over contact and long-range interactions using a scattering resonance in ultracold molecules could potentially allow the realization of novel quantum phenomena such as exotic self-bound droplets and supersolid quantum phases [210]. Furthermore, measurements of scattering resonances provide an accurate benchmark for calculations of the molecular potential energy surfaces (PESs) [11, 95] and pave the way for controlled quantum chemistry [96].

A scattering resonance occurs when the scattering state couples strongly to a quasibound state. Depending on whether the quasibound state is hosted by the same or a different channel than the scattering channel, the resonance is classified as either a shape resonance or a Feshbach resonance.

Shape and Feshbach resonances have been observed in atom-molecule and molecule-molecule collisions by adjusting the collision energy using molecular beams at kelvin and sub-kelvin temperatures [11, 253–256]. In the ultracold (sub-microkelvin) regime, scattering resonances are typically induced by an external electromagnetic field that shifts the relative energy between the quasibound state and the scattering state [257, 258]. Magnetically tunable Feshbach resonances have been observed in collisions between weakly bound Feshbach molecules and recently between NaLi molecules in the spin-triplet ground state [86].

However, the magnetic tuning scheme crucial to Feshbach resonances requires a nonzero electronic spin, making it unlikely to be applicable for bialkali molecules in the spin-singlet ground state. The spin-singlet absolute ground state of bialkali molecules is of particular interest because it is the only long-lived state where the molecules exhibit strong electric dipole-dipole interactions. Additionally, Feshbach resonances are not expected to occur between ground-state molecules due to nearly universal loss, resulting from the high density of tetramer states near the collisional threshold and the loss mechanisms associated with collisional complexes [87, 89, 259]. A general method to realize collisional resonances of ultracold dipolar molecules remains elusive.

Field-linked (FL) resonances offer a universal approach to creating such resonances in collisions between dipolar molecules by coupling them to the long-range FL states [111,260]. These weakly bound states are induced by the attractive long-range intermolecular potential via microwave dressing [76, 177]. Unlike conventional resonances, where an external field merely adjusts an existing short-range quasibound state into resonance, the long-range FL states exist solely in the presence of the microwave field. The sensitive dependence of the FL states on the microwave field offers an unprecedented level of control over intermolecular interactions. In this chapter, we showcase this tunability by observing two resonance branches in the inelastic scattering rate, whose peak positions shift continuously with the microwave frequency and polarization. We further characterize the change in the thermalization rate related to a diverging scattering length in a resonant collision channel.

6.1.1 Physical picture

Field-linked states are weakly bound states within the long-range interaction potential. They are held together by attractive dipole-dipole interactions, yet they remain distant from each other due to the presence of the shielding core. One can visualize field-linked states as two dipoles oscillating relative to each other while simultaneously flipping their orientation to balance attraction and repulsion, as illustrated in Fig. 4.4. When field-linked states emerge from the collisional threshold, they become energetically degenerate with the scattering waves, resulting in strong coupling. Consequently, a pair of scattering molecules can be temporarily trapped by their interaction potential and intensely interact with each other, leading to a scattering resonance.

6.1.2 Effective potential

In Chapter 4, we introduced the multichannel scattering problem of microwave-shielded polar molecules and their corresponding adiabatic potential curves. Although this multichannel scattering is crucial for the quantitative calculation of collisional cross sections, it can be cumbersome to handle. However, if our interest lies only in elastic collisions, we can approximate the process by considering solely the adiabatic potential of the upper channel. This allows us to construct an effective potential, capable of calculating the elastic cross section with high precision.

When expressing the two-body Hamiltonian $\hat{H}_2$ within the symmetric subspace $\mathcal{S}_7$ (defined in Section 4.2.1), it is clear that the upper channel $|1\rangle$ has direct coupling only with $|2\rangle$ and $|3\rangle$. By applying second-order perturbation theory to the upper channel, we derive [116]

$$E_1^{(2)}(\boldsymbol{r}) = [\hat{H}_2(\boldsymbol{r})]_{11} + \frac{[\hat{H}_2(\boldsymbol{r})]_{12}^2 + [\hat{H}_2(\boldsymbol{r})]_{13}^2}{\hbar(\Omega_{\text{eff}} - \Delta)/2} \tag{6.1}$$

with

$$\begin{aligned}
[\hat{H}_2'(\mathbf{r})]_{11} &= Du^2v^2(\cos^2\theta - \frac{1}{3} + \sin 2\xi \sin^2\theta \cos 2\varphi), \\
[\hat{H}_2'(\mathbf{r})]_{12} &= \frac{1}{2}Du^2v \sin 2\theta (e^{-i\varphi}\cos\xi - e^{i\varphi}\sin\xi), \\
[\hat{H}_2'(\mathbf{r})]_{13} &= \frac{1}{\sqrt{2}}Du^2v \sin^2\theta (e^{-2i\varphi}\cos^2\xi - e^{2i\varphi}\sin^2\xi),
\end{aligned} \tag{6.2}$$

where $D = d_0^2/(4\pi\epsilon_0 r^3)$. We observe that the first-order energy shift represents the induced dipole-dipole interaction V_{dd}, which is also obtained semiclassically in Section 4.1.3. The second-order energy shift illustrates the repulsive van der Waals interaction from the avoided crossing to the lower dressed state, thereby giving rise to the shielding potential.

Hence, we obtain the effective potential

$$V_{\text{eff}}(\mathbf{r}) \equiv E_1^{(2)}(\boldsymbol{r}) = \frac{C_3}{r^3}[3\cos^2\theta - 1 + 3\mathcal{F}_\xi(\varphi)\sin^2\theta] + \frac{C_6}{r^6}\sin^2\theta\{1 - \mathcal{F}_\xi^2(\varphi) + [1 - \mathcal{F}_\xi(\varphi)]^2\cos^2\theta\}, \tag{6.3}$$

where $\mathcal{F}_\xi(\varphi) = \sin 2\xi \cos 2\varphi$, $C_3 = d_0^2/\left[48\pi\epsilon_0(1+\delta_r^2)\right]$ and $C_6 = d_0^4/\left[128\pi^2\epsilon_0^2\hbar\Omega(1+\Delta_r^2)^{3/2}\right]$ with $\delta_r = \Delta/\Omega$. The effective potential provides a good approximation for the upper adiabatic potential for $\xi \lesssim 15°$ and $\Omega \lesssim 2\pi \times 20\,\text{MHz}$. Beyond this ellipticity, the higher-order coupling from the lower channels becomes non-negligible. Nevertheless, by extracting the C_6 coefficient from fitting the numerically calculated adiabatic potential, Eq. (6.3) can be applied to much larger Rabi frequencies.

A deviation from circular polarization breaks the azimuthal symmetry of the interaction and enhances the depth of the potential well along the y-axis, which deepens enough to support one or more bound states (see Fig. 6.1a–c). These bound states are the field-linked states, whose properties are strongly dependent on the external fields. By adjusting the binding energy of the FL state across the collisional threshold — for example, using microwave detuning (see Fig. 6.1d and e) — FL resonances occur, which drastically alter the scattering properties between the molecules.

6.1.3 Resonance condition

For a comprehensive understanding of the resonance, we deduce the elastic and inelastic scattering rate coefficients by employing the multichannel scattering theory detailed in Chapter 4. In Fig. 6.2b and c, we illustrate the elastic cross section $\sigma_{\nu lm}^{\nu' l' m'} = \sigma_{111}^{111}$ (in the multichannel context) and $\sigma_{lm}^{l'm'} = \sigma_{11}^{11}$ (using the effective potential) on the Ω–δ_r plane for $\xi = 0$ and $k_1 = 0.45k_F$. A prominent resonant peak emerges when the parameters satisfy $\delta_r \lesssim 0.3$ and $\Omega/(2\pi) \gtrsim 80\,\text{MHz}$.

Of particular interest is the observation that a minor ellipticity ξ can substantially reduce the Rabi frequency where the FL resonance occurs. The underlying explanation is as follows: with $\xi = 0$, the resonant bound states in channels $m = \pm 1$ remain degenerate. Introducing an elliptical polarization with $\xi > 0$ connects channels m and $m \pm 2$, removing the degeneracy and leading to a symmetric superposition of two bound states possessing reduced binding energy. As a result, resonances become more accessible with a reduced Ω. Since the bound state is predominantly of p-wave character, the angular part $Y_{11} + Y_{1-1} \sim \sin\theta \sin\varphi$ of its wave function indicates that the amplitude peaks along the y-axis, i.e., $\theta = \pi/2$ and $\varphi = \pm\pi/2$. This orientation aligns with the valley of the dipolar interaction within the effective potential in the xy plane.

Furthermore, the resonance condition can be interpreted through the WKB approximation. We also ignore the contribution from the centrifugal barrier, facilitating an analytical

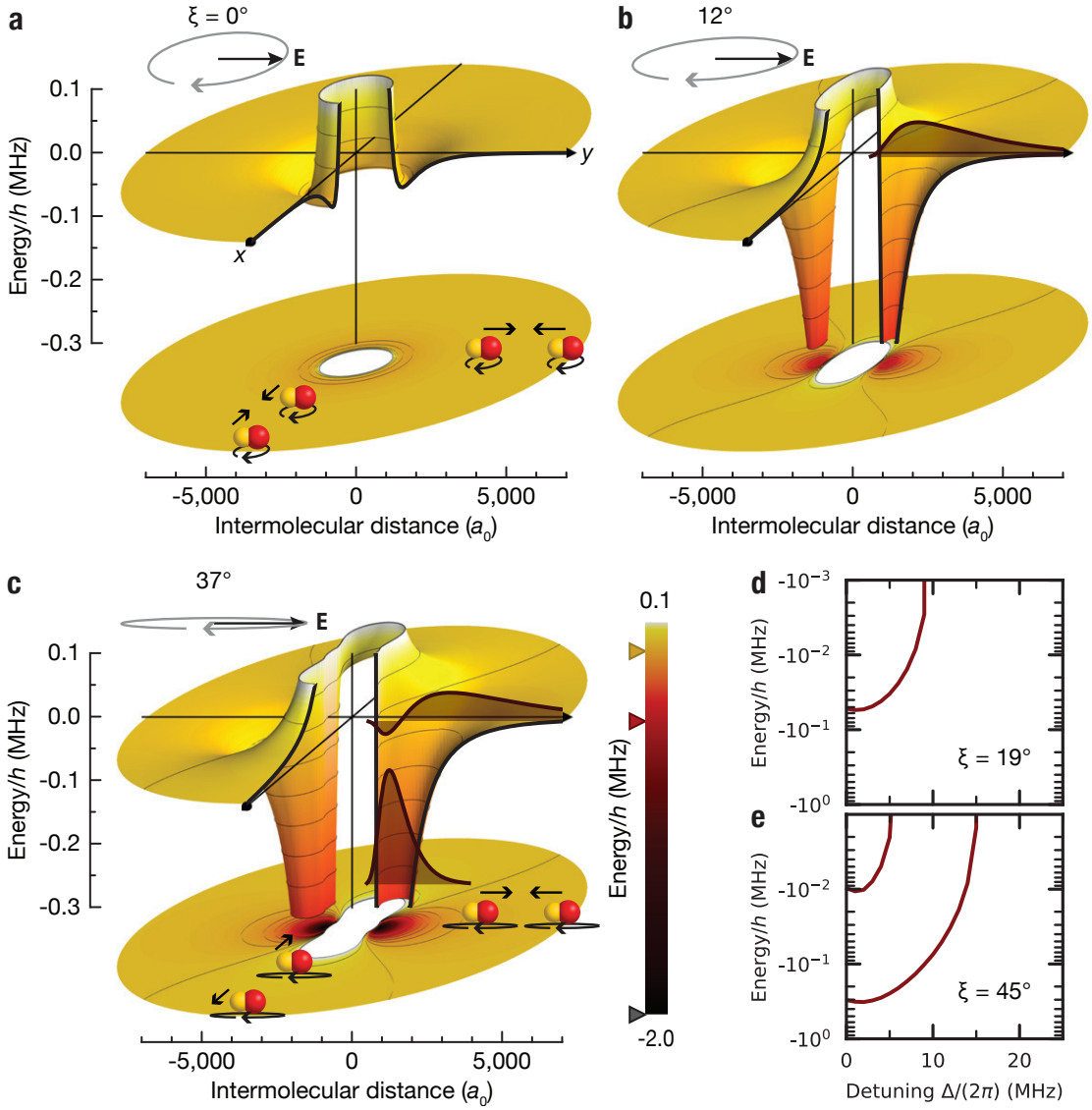

Figure 6.1: Interaction potentials and bound states of microwave-dressed ground-state molecules. a–c, The cut-open three-dimensional surfaces illustrate the interaction potentials $U(\mathbf{r})$ including the p-wave centrifugal potential between two molecules in the xy-plane for different ellipticity angles ξ. Below, a projection of the same potential is shown. The interaction potential along the z direction (not shown) is always repulsive. The microwave is on resonance ($\Delta = 0$). The shaded areas in **b** and **c** show the radial wave function of the bound states. The insets visualize the rotating electric field and sketch the interaction between the rotating dipoles colliding along the x or y direction. The markers on the color bar denote the potential depths for the three cases. **d** and **e**, Coupled-channel calculations of the energy of the tetramer bound states as a function of Δ for the indicated values of ξ. In all panels the Rabi frequency is set to $\Omega = 2\pi \times 10\,\mathrm{MHz}$. Figure reproduced from Ref. [112].

assessment of the integration. The WKB phase is expressed as [116]

$$\varphi_{\mathrm{WKB}} = \int_{v_1(r)\leq 0} \sqrt{-Mv_+(r)/\hbar^2}\mathrm{d}r \tag{6.4}$$

$$\propto \left[\frac{d_0^4\Omega}{(1+\delta_r^2)^{5/2}}\frac{(1+3\sin 2\xi)^4}{8+\sin 2\xi - 3\sin^2 2\xi}\right]^{1/6} \tag{6.5}$$

Here, $v_q(r) = \int \mathrm{d}\hat{r}|Y_{1q}(\hat{r})|^2 V_{\mathrm{eff}}(\boldsymbol{r})$ represents the projection of V_{eff} onto the partial waves Y_{1q}. Resonances occur when φ_{WKB} approximates $n\pi$, with n as a positive integer. We discern that the shape resonance manifests in the regime characterized by larger values of Ω or ξ, and smaller δ_r. Note that a precise prediction of the resonance position requires the diagonalization of the matrix corresponding to the effective potential in partial wave expansions. Subsequently, the lowest potential energy curve should be utilized for the calculation of the WKB phase. Further discussion of the WKB phase is presented in Chapter 8.

6.1.4 *p*-Wave scattering

In this section, we discuss the p-wave characteristics of the scattering cross section, as it dominates over all other partial waves for ultracold fermions. Figure 6.2a represent the Ω dependency of σ_{11}^{11} and σ_{111}^{111} for $\delta_r = 0.1$ and $k_1/k_F = 0.04$, 0.45, and 1. Here, k_1 is the wave number of the relative motion, $k_F = (6\pi^2 n_0)^{1/3}$ is the Fermi wave number, with $n_0 = 10^{12}\,\mathrm{cm}^{-3}$ denoting the peak density of the experimentally realized molecular gas.

We observe that for $k_1/k_F = 0.04$, σ_{111}^{111} exhibits minimal change as Ω varies over a broad range. A narrow scattering resonance then appears at $\Omega/(2\pi) \approx 87.7\,\mathrm{MHz}$, indicating the formation of a tetramer bound state. For $k_1/k_F = 1$, the resonant peak shifts to $\Omega/(2\pi) \approx 73.6\,\mathrm{MHz}$ with the width of the resonance significantly broadened.

To understand the effect of collisional momentum k_1, we note the existence of a centrifugal barrier for the p-wave potential. A scattering resonance at finite k_1 suggests that the incident particle is on resonance with a quasi-bound state localized inside the barrier. As k_1 increases, the energy of the quasi-bound state on resonance with the incident particle also rises, moving closer to the top of the barrier. As a result, the lifetime of the quasi-bound state is reduced due to a higher decay rate, leading to a broader resonance. Moreover, as k_1 increases, the quasi-bound state on resonance with the incident energy becomes more shallow, a condition achievable by increasing C_6. Hence, the resonant peak shifts towards the lower Ω direction as k_1 increases. Intriguingly, the observation that the p-wave scattering cross section can be efficiently tuned via Ω implies that the short-range potential (i.e., C_6) can have a substantial impact on the scattering properties due to the large shielding core.

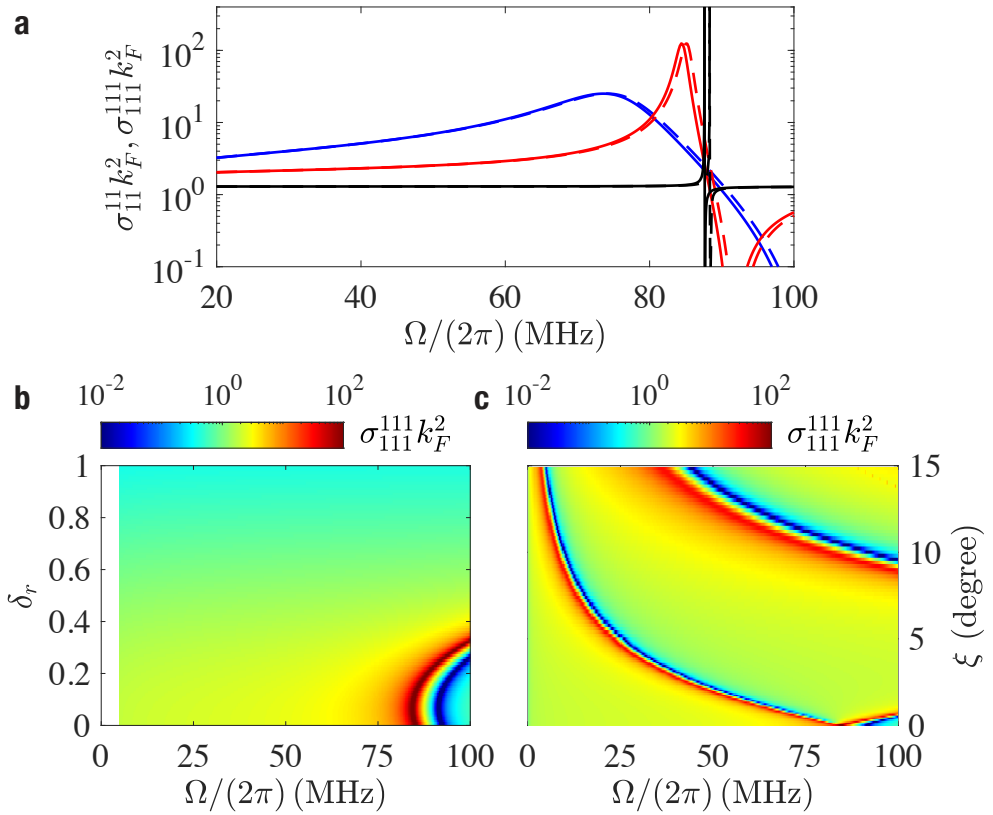

Figure 6.2: Elastic p-wave scattering. **a** p-wave scattering cross sections $\sigma_{11}^{11}k_F^2$ (solid lines) and $\sigma_{111}^{111}k_F^2$ (dashed lines) as functions of Ω for $\xi = 0$, $\delta_r = 0.1$ and $k_1/k_F = 0.04$ (black lines), 0.45 (red lines), and 1 (blue lines). **b** and **c** are the distributions of $\sigma_{111}^{111}k_F^2$ on the Ω-δ_r plane with $\xi = 0$ and Ω-ξ plane with $\delta_r = 0.1$, respectively, for $k_1/k_F = 0.45$. Figure reproduced from Ref. [116].

6.2 Experimental observations

In our experimental study, we observed the FL resonances by measuring the loss dynamics over a range of different detuning Δ and ellipticity ξ, at a static Rabi frequency at $\Omega \approx 2\pi \times 10\,\mathrm{MHz}$. The microwave was generated using a waveguide antenna powered by two 10-W amplifiers (Kuhne PA510590). The relative phase between the two feeds of the antenna was adjusted using two mechanical phase shifters. Neither monitoring nor feedback control were implemented. We noticed that variations in Ω is accompanied by a shift in the ellipticity ξ, originated from the differential phase shift between the two amplifiers for the two antenna feeds. Consequently, we decided to maintain Ω as a constant throughout the experiment. For the latest microwave setup presented in Chapter 3, this systematic phase shift is monitored and can be compensated with the VCPS.

6.2.1 Resonance map

We map out the resonances by measuring the inelastic rate coefficient β_{in} of collisions between the dressed molecules. For most measurements, the temperature T of the molecular ensemble is 230 nK and the initial average density n_0 is about $5 \times 10^{11}\,\mathrm{cm}^{-3}$. Next, the microwave is ramped on in 100 µs to dress the molecules. After a variable hold time the remaining molecules are released from the optical trap and we determine the number of molecules and the temperature from time-of-flight images (see Section 2.1.3).

As we tune the ellipticity of the microwave from circular to linear, up to two FL states emerge from the dressed potential. Figure 6.3a shows examplary loss rate coefficients for three different ellipticities. At $\xi = 6(2)^\circ$, the potential is too shallow to support a bound state thus no resonance is observed. In this regime, the inelastic collision is suppressed by the shielding potential at small detunings [107]. For $\xi = 19(2)^\circ$, the interaction potential supports a single bound state, leading to enhanced inelastic scattering at $\Delta \approx 2\pi \times 10\,\mathrm{MHz}$. For $\xi = 37(2)^\circ$, the potential becomes deep enough to support two bound states, leading to two resonance peaks.

A unique feature of the FL resonances is their sensitivity to external fields. We show that the resonance position continuously changes with the microwave parameters by mapping out the two resonance branches while varying the microwave detuning and polarization. Figure 6.3b shows two branches of FL resonances, starting at $\xi \approx 10^\circ$ and $\xi \approx 32^\circ$. As the polarization ellipticity ξ increases, less dipole-dipole interaction is needed to support bound states and the resonances therefore shift to larger detuning. However, the global inelastic rate coefficient increases as the polarization becomes more elliptical, due to the increased coupling to the other dressed states [261]. Overall our measurements show good agreement with our theory predictions (see Fig. 6.3c). We attribute the broadening and shift of the resonance peaks compared to theory to an increase of Rabi frequency as we scan the detuning. These systematic errors affect mostly the FL resonances near linear polarization, where the potential depth is more sensitive to the relative detuning.

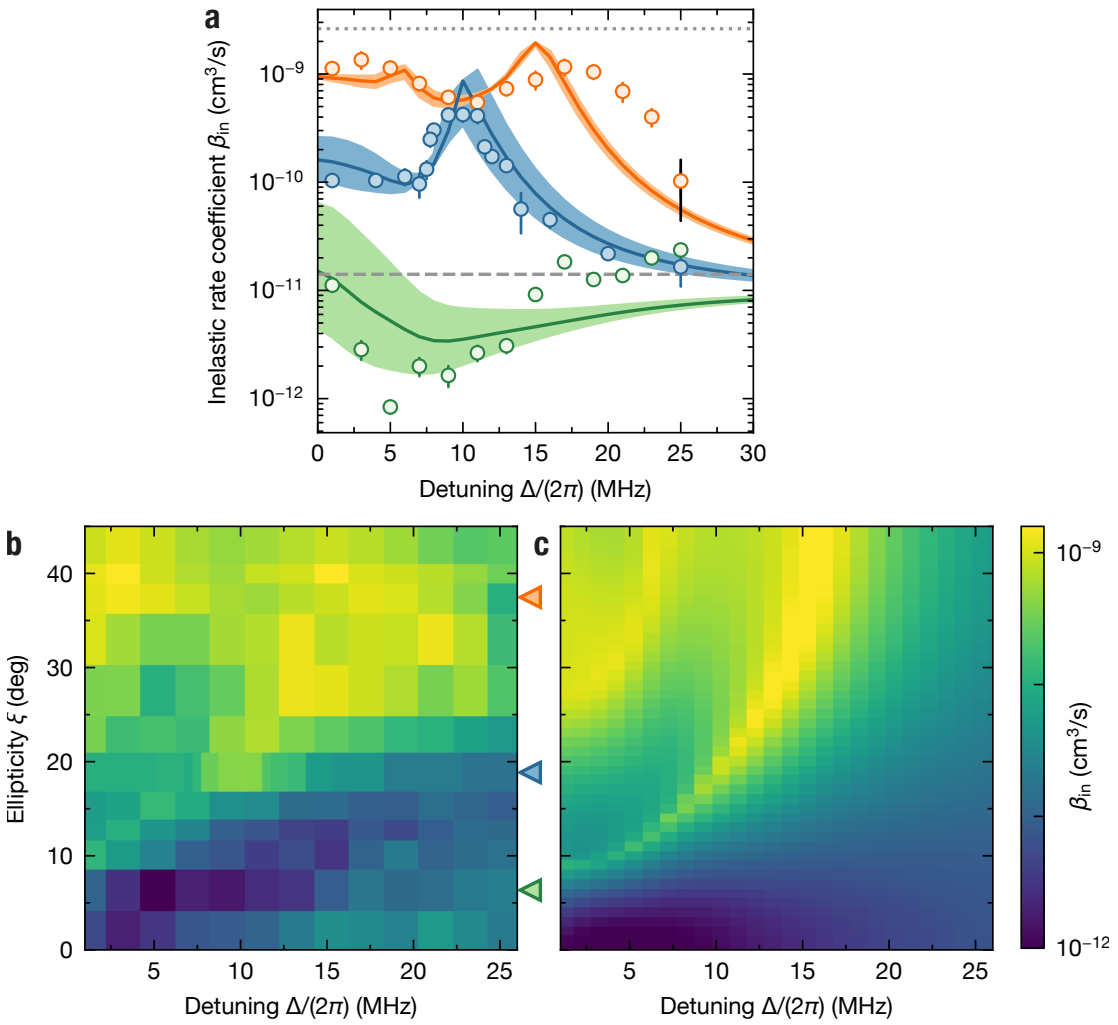

Figure 6.3: Field-linked resonances. **a**, Inelastic collision rate coefficient β_{in} between microwave dressed NaK molecules as a function of the microwave detuning Δ for various microwave polarizations with the ellipticity angle $\xi = 6(2)^\circ$ (green), $19(2)^\circ$ (blue), and $37(2)^\circ$ (orange) at the Rabi frequency $\Omega \approx 2\pi \times 10\,\text{MHz}$. The solid lines show the corresponding theory calculations. The shaded regions show the calculations within the uncertainty of ξ (see Section 3.2.2). The grey dashed line denotes the universal loss coefficient $\beta_{\text{universal}}$ and the grey dotted line denotes the single-channel unitarity limit. The colored error bars show the standard deviation of the fit results and the black error bar illustrates examplarily the systematic uncertainty. **b** and **c**, Color density maps of the experiment data **b** and the theory calculation **c** of the inelastic rate coefficient as a function of microwave detuning and ellipticity. The triangles on the right axis of **b** mark ellipticity for the data shown in **a**. Figure reproduced from Ref. [112].

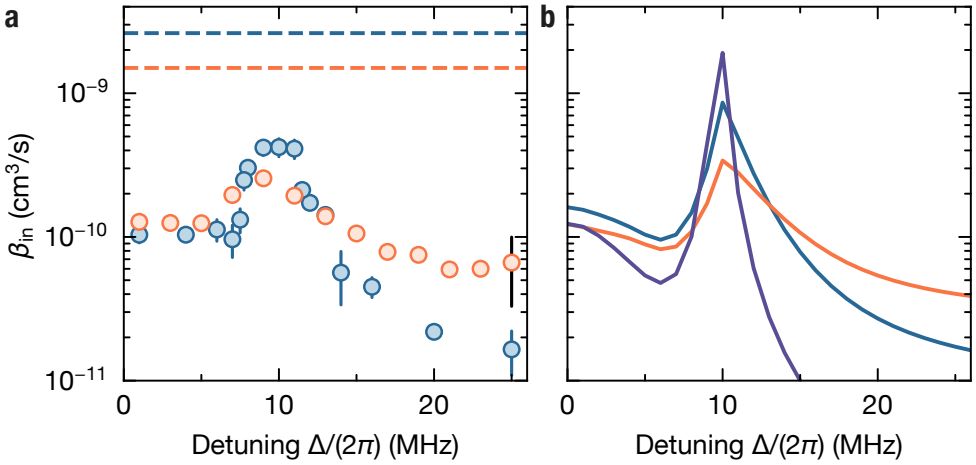

Figure 6.4: Temperature dependence of the inelastic scattering. Experimental results (**a**) and theoretical calculations (**b**) of the inelastic collision rate coefficient β_{in} are displayed as functions of the microwave detuning Δ at temperatures of 700 nK (orange), 230 nK (blue), and 20 nK (purple). The colored error bars represent fitting uncertainties, while the black error bar encompasses both fitting and systematic uncertainties. Solid lines correspond to coupled-channel calculations, and the dashed lines denote the unitarity limit for the respective temperatures. The measurements are performed with the molecules dressed by a microwave field characterized by an ellipticity of $\xi = 19(2)^\circ$ and a Rabi frequency of $\Omega \approx 2\pi \times 10$ MHz. Figure reproduced from Ref. [112].

6.2.2 Temperature dependence of the inelastic scattering

The temperature dependence of the inelastic scattering rate varies with the strength of the interaction. As discussed in Chapter 4, at a large detuning where the dipole-dipole interaction is reduced, the scattering is in the threshold regime. The inelastic scattering rate is universal [73] and scales linearly with temperature for indistinguishable fermions. At a small detuning, the scattering enters the semi-classical regime, where β_{in} is independent of the temperature [75]. On the scattering resonance, the collision rate has a temperature dependence that is reminiscent of the unitarity limit [96, 162], while the loss remains substantially smaller than this limit due to shielding. Meanwhile, the width of the resonance feature is broadened by thermal averaging. As a consequence, for temperatures as high as 700 nK, the resonance becomes less visible as shown in Fig. 6.4. When the collision energy becomes lower than the centrifugal barrier of the interaction potential, the resonance peak would be further narrowed due to the increased lifetime of the quasibound state. Therefore, reaching ultracold temperatures is crucial for the observation of FL resonances.

6.2.3 Elastic scattering

Scattering resonances are accompanied not only with enhanced losses of the molecules, but more importantly, the ability to control elastic scattering. With FL resonances, we can tune the elastic scattering rate while keeping the inelastic rate small.

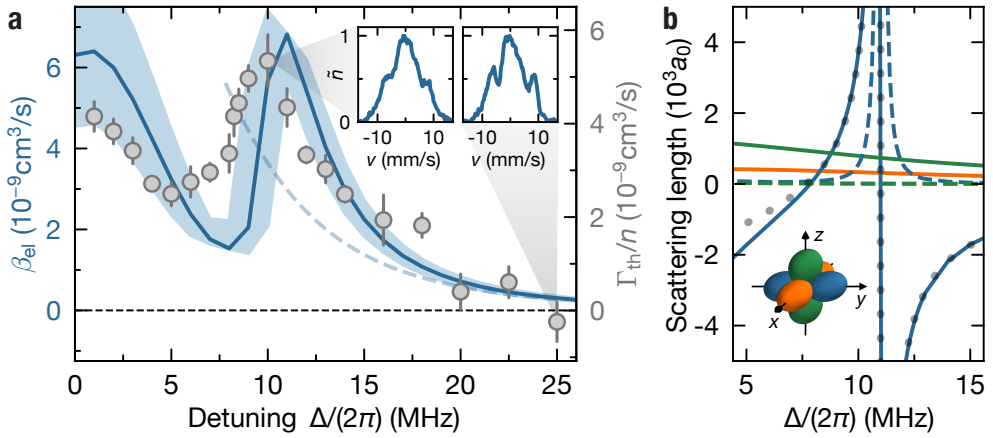

Figure 6.5: Elastic scattering. **a**, The data points display the thermalization rate Γ_{th} normalized by the mean in-situ density n as a function of the microwave detuning Δ at an ellipticity angle of $\xi = 19(2)^\circ$ and a Rabi frequency of $\Omega \approx 2\pi \times 10\,\text{MHz}$. The temperature is 230 nK. Error bars are the standard error of the mean of 7–16 repetitions. For comparison, the solid line shows the corresponding theory calculation of the elastic collision rate coefficient β_{el}. The uncertainty of ξ is taken into account by the shaded area. The dashed line is the Born approximation of the background collision rate coefficient, which holds in the threshold regime for detunings $\Delta \gtrsim 8\,\text{MHz}$. The insets show the normalized linear density $\tilde{n}$ along the lattice axis averaged over ten repetitions, as a function of the molecule velocity v in the lattice direction for $\Delta = 2\pi \times 10\,\text{MHz}$ and $2\pi \times 25\,\text{MHz}$. **b**, Coupled-channel calculations of the energy-dependent scattering length with the same microwave parameters and a fixed collision energy of $k_{\text{B}}T$, with $T = 230\,\text{nK}$. The solid (dashed) lines are the real (imaginary) part of the scattering lengths in the channel p_x (orange), p_y (blue), and p_z (green). The dotted line is a fit to Eq. (6.6). The inset illustrates the partial waves of the scattering channels. Figure reproduced from Ref. [112].

To characterize the effect of the FL resonances on the elastic collision rate, we measure the thermalization rate of the samples. Typically, this is accomplished by quenching the trapping confinement in one dimension and observing the global cross-dimensional thermalization [185]. However, for small Δ/Ω our samples are in the hydrodynamic regime, where the global thermalization rate is limited by the trapping frequencies [107]. Instead, we perturb the momentum distribution of the molecular cloud by pulsing on an optical-lattice beam for 300 µs. The lattice pulse diffracts some molecules and sends them to collide along the y-axis, defined as the long-axis of the microwave field (see Fig. 6.1), along which the dipole-dipole interaction is most attractive. Fast local thermalization smears out the diffraction pattern that is formed in momentum space during the lattice pulse (see insets in Fig. 6.5a). From the contrast of the diffraction pattern we can estimate the thermalization rate Γ_{th}.

We note that the measured thermalization rate follows a similar trend as the calculated

value of β_{el} (see Fig. 6.5a). Besides the contribution from the dipole-dipole interaction, which scales with d_{eff}^2 and decreases as Δ increases, a clear resonance feature is visible around the FL resonance. The shift of the resonance between the experiment data and theory is within the systematic uncertainty of the ellipticity. The average number of elastic collisions that is needed per particle to reach thermalization is so far unknown in the regime of elliptical microwave polarization. From the comparison between the measured Γ_{th}/n and β_{el} from our coupled-channel calculations, we find that this factor is close to 1 under the present experimental conditions.

The observed elastic scattering rate includes contributions from both contact interaction and long-range dipole-dipole interaction. The dipole-dipole interaction contributes in all partial wave channels, whereas the contact interaction only has significant contribution in the resonant channel, due to its unfavorable scaling with the wave vector. While such an interplay between contact interaction and dipole-dipole interaction limits the change in the total elastic scattering rate, the underlying scattering length, however, shows divergent behavior in the resonant channel. Figure 6.5b shows the energy-dependent scattering length $\tilde{a}_{lm}(k) = -\tan\delta_{lm}(k)/k$ [73, 262] for the three p-wave channels at the average collision energy. The real (imaginary) part of the scattering length corresponds to the elastic (inelastic) scattering. The FL resonance occurs in the p_y channel where the interaction is most attractive. The corresponding scattering length shows a resonance feature, where the real part can be tuned to large positive or negative values, while the imaginary part remains small. The ratio of elastic-to-inelastic collisions is about ten on the resonance, and can be further enhanced at smaller ellipticity, where the resonance shifts towards higher Rabi frequencies.

A simple analytic formula describing the resonant elastic scattering length is given by

$$\tilde{a}_{1y} = a_{\mathrm{dd}} \left(-\frac{1 + 3\sin 2\xi}{10} \right) \left(1 + \frac{\Delta^*(k)}{\Delta - \Delta_0(k)} \right), \tag{6.6}$$

where $\Delta_0(k)$ and $\Delta^*(k)$ denote the position and the width of the resonance. The width $\Delta^*(k) \propto k^2$ follows the scaling of the p-wave contact interaction. For the collision energy considered here, we extract $\Delta_0 \approx 2\pi \times 10.99$ MHz and $\Delta^* \approx 2\pi \times 3.29$ MHz from the fit to the coupled-channel calculations. The resonance position $\Delta_0(k)$ also has a weak energy dependence. As a consequence, the resonance position with thermal averaging is broadened and slightly shifted towards lower detuning. These thermal effects, however, will be greatly suppressed in a degenerate Fermi gas, where the scattering predominantly occurs near the sharp Fermi energy [116].

The elastic-to-inelastic collision ratio near the FL resonances can be improved with better shielding near circular microwave polarization and lower temperatures. Under these conditions, the FL resonance occurs at a much higher Rabi frequency compared to the observed resonances at more elliptical polarizations. However, this is still realistic to achieve by using an improved antenna design with increased microwave power. The ratio is then

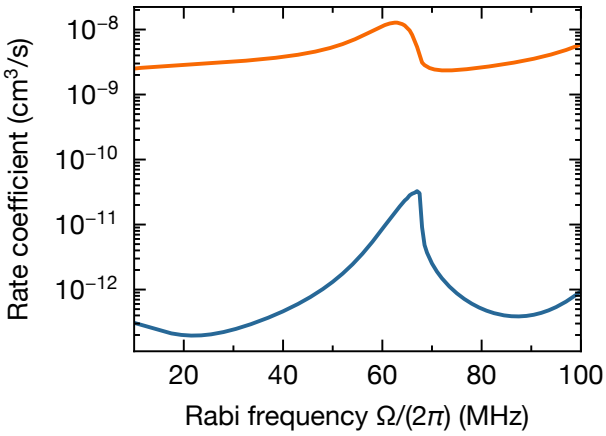

Figure 6.6: Field-linked resonance near circular microwave polarization. Coupled-channel calculations of the elastic (orange) and inelastic (blue) scattering rate coefficient at $T = 20\,\mathrm{nK}$, $\xi = 1°$, and $\Delta = 2\pi \times 1\,\mathrm{MHz}$. Figure reproduced from Ref. [112].

about 900 at the maximum elastic scattering rate and about 130 at the scattering resonance, as shown in Fig. 6.6.

6.3 Prospects of dipolar p-wave superfluid

Here we discuss an example application of FL resonance for studying many-body physics, namely the enhancement of the critical temperature for dipolar p-wave superfluidity. We have shown that a FL resonance can greatly enhance the p-wave scattering amplitude due to the tetramer bound state hosted in the long-range potential. The unitary scattering amplitude near the FL resonance increases the critical temperature of p-wave superfluidity to the critical temperature of BEC, i.e. $T_c \approx 0.137 T_F$. As shown in Fig. 6.7a, for lower Rabi frequencies away from the resonance, the critical temperature reduces. This enhanced interaction is due to the shrinking of the shielding core at higher Rabi frequency, and is present even for a fixed long-range dipole-dipole interaction. In fact, if we rely solely on the long-range interaction, the critical temperature for NaK at the same density would be less than $0.05 T_F$ [202, 208], which is not realistic to achieve given the present cooling technique.

The pairing wave function, as shown in Fig. 6.7b, displays a clear anisotropic distribution peaked at the Fermi momentum k_F, indicating the formation of Cooper pairs around the Fermi surface. In Fig. 6.7c for density $n_0 = 10^{12}\,\mathrm{cm}^{-3}$ and $\delta_r = 0.1$, $\psi_\Delta(\mathbf{k})$ along the k_x direction shows the broadening peak width with increasing Ω, which indicates the formation of Cooper pairs over a broader momentum range under a stronger attractive interaction.

6.4 Conclusion and outlook

Field-linked resonances provide a novel and universal tool to control the collisions between ultracold polar molecules. These resonances occur as long as the Rabi frequency is sufficiently large, such that the interaction potential is deep enough to support bound states.

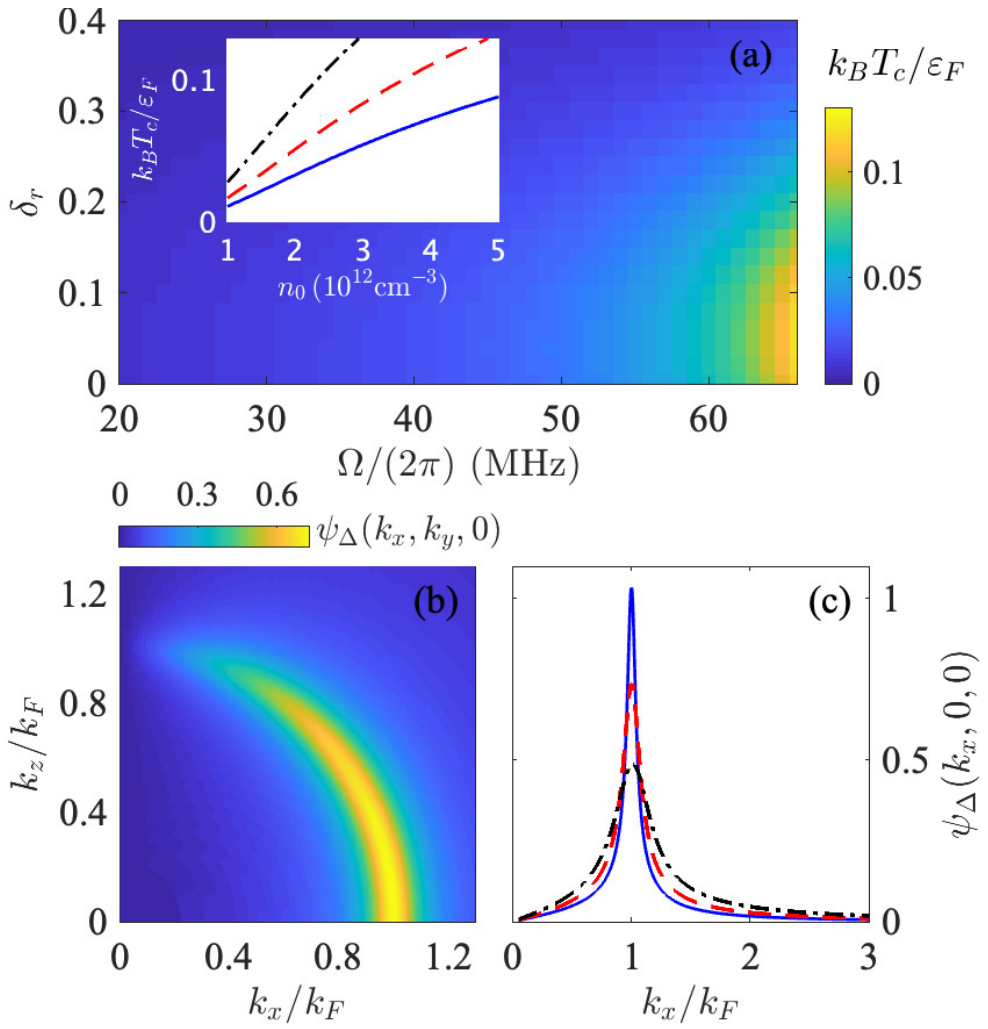

Figure 6.7: Dipolar p-wave superfluidity. **a**, Critical temperature T_c as a function of the Rabi frequency Ω and the relative detuning $\delta_r \equiv \Delta/\Omega$. The inset depicts the dependence of T_c on the peak density n_0 for $\delta_r = 0.1$ and $\Omega/2\pi = 28$ (solid line), 38 (dashed line), and 48 MHz (dash-dotted line). **b**, Momentum distribution of the normalized pairing function $\psi_\Delta(k_x, 0, k_z)$ for $\delta = 0.1$ and $\Omega/2\pi = 58$ MHz. **c**, Normalized pairing function $\psi_\Delta(k_x, 0, 0)$ along the k_x direction for $\delta_r = 0.1$ with $\Omega/2\pi$ values of 48 MHz (solid line), 58 MHz (dashed line), and 66 MHz (dash-dotted line). The density of the gas is maintained at $n_0 = 10^{12}$ cm^{-3}, unless otherwise stated. Figure reproduced from Ref. [116].

Quantitative predictions of FL resonances only require knowledge of the mass, the dipole moment, and the rotational structure of the individual molecules as well as their loss rate at short range. This is in stark contrast to molecular collisions involving close contact between the molecules, where a large number of collision channels are involved and the existing knowledge of the PES are too imprecise to predict the number of bound states, leave alone their position. Additionally, FL states can serve as an ideal starting point in photoassociation spectroscopy to probe short-range potentials [111].

The ability to control the scattering length through FL resonances paves the way for exploring many-body physics that incorporates both contact and dipole-dipole interactions. In a degenerate Fermi gas, the resonant interaction facilitates realization of dipolar superfluidity [177, 207, 208]. Specifically, pairing between molecules is enhanced due to the presence of the FL bound state. Therefore the critical temperature for Bardeen–Cooper–Schrieffer (BCS) superfluidity increases drastically near the FL resonance, i.e., to about 14% of the Fermi temperature for NaK molecules [116]. The anisotropic nature of such a dipolar superfluid gives rise to novel quantum phenomena such as gapless superfluidity [214] and topological $p_x + ip_y$ symmetry [263]. In a Bose–Einstein condensate (BEC), independent control over s-wave scattering length and dipolar length has led to the observation of self-bound droplets and the formation of supersolids in magnetic atoms [264]. Making use of FL resonance with bosonic polar molecules, whose dipolar lengths are orders of magnitude larger than magnetic atoms, would enable the study of such exotic phenomena in entirely unexplored regimes [265]. The superfluidity can be detected, for example, by stirring the cloud and measure heating, or by inducing vortices in a rotating trap or a rotating microwave field alignment [266].

FL resonances also confirm the existence of FL states, a novel class of long-range polyatomic molecular states. Tetramer molecules with approximately twice the dipole moment of the individual diatomic molecules could potentially be created by adiabatically ramping the microwave field across a FL resonance or by radio-frequency association. Those composite bosonic tetramers are expected to be long lived at small binding energies [260] and could be collisionally stable due to the shielding between the constituent molecules. Below the critical temperature, a tetramer gas could form a BEC [25] and may lead to a novel crossover from a dipolar BCS superfluid to a BEC of tetramers. The formation and dissociation of FL tetramers is presented in Chapter 7.

In summary, we have unveiled a novel type of universal scattering resonances among ultracold polar molecules that is associated with field-linked tetramer bound states in the long-range potential well. The resonances are highly tunable via microwave power, frequency, and polarization, which makes them a versatile tool for controlling molecular interactions. Since FL states are insensitive to species-dependent short-range interactions, the FL resonance is applicable to a wide range of polar molecules. These results provide a general route to strongly interacting molecular gases and open up new possibilities to investigate novel quantum many-body phenomena. Additionally, they facilitate the pro-

duction of long-lived dipolar tetramer molecules — a topic we will explore in the next chapter.

No problem, we can calculate it rigorously.[1]

Tao Shi (石弢)

Chapter 7

Field-linked tetratomic molecules

Our exploration of tetratomic molecules begins with a parallel between the atomic Feshbach resonances and the FL resonances. Feshbach resonances serve as an indispensable tool for controlling interactions in ultracold atoms, thereby making them as a promising platform for simulating many-body physics. Chapter 6 highlighted FL resonances as a universal tool to control the scattering lengths of polar molecules, which brings forth opportunities to investigate phenomena such as dipolar p-wave superfluidity and exotic dipolar supersolids. Beyond their role in interaction control, Feshbach resonances pave the way for the association of Feshbach molecules and the study of BCS–BEC crossover in degenerate Fermi gases.

Feshbach resonances, however, are challenging to observe in polar molecules. FL resonances, by contrast, are ubiquitous in polar molecules with a sufficiently large dipole moment, and the bound states associated with them are expected to be long-lived and collisionally stable (see Table 7.1). Given these properties, we foresee FL resonances possessing similar potential as atomic Feshbach resonances. In this study, we report the formation of tetratomic molecules, paving the way for realizing dipolar BCS–BEC crossover.

In October 2022, we consulted with theorists regarding the plausibility of associating tetramers. We were informed that, for fermionic molecules, threshold collisions are suppressed by the centrifugal barrier, making their association unlikely [267]. Despite this seemingly discouraging news, we were hopeful that in the degenerate regime, association efficiency can be enhanced by frequent collisions and other many-body effects. Although calculations in the degenerate regime surpass current theoretical capabilities, we decided to try it out experimentally. To our delight, electroassociation proved efficient in the deeply degenerate regime.

[1] Considering the complexity of molecular collisions, we are pleased to learn that our theorists can rigorously calculate many of our tetramer properties without resorting to free parameters.

Table 7.1: FL resonances vs. molecular Feshbach resonances.

	Field-linked	Feshbach
Number of channels	single	multiple
Tunability	electric	magnetic
Size of the bound state	$\sim 1000\,a_0$	$< 100\,a_0$
Lifetime of the bound state	up to 100 ms	$\sim 1\,\mu$s [86]
Induced dipole moment	nonzero	zero
Applicablity	universal to polar molecules	unique

Our experiment is conducted in close collaboration with Fulin Deng (邓富林), Tao Shi (石弢), and Su Yi (易俗), who have contributed extensively to the theory of FL tetramers. We concurrently carry out experiments and theoretical calculations, and subsequently compare the results. It appears that there is a remarkable agreement between the observed and expected binding energy and one-body lifetime of the tetramers, indicating a comprehensive understanding of these molecules. The theorists also assist us in comprehending the physics behind the modulation dissociation spectrum, the electroassociation process, and the dipole and quadrupole momenta of the tetramers.

Results of publications [113, 268] are contained in this chapter.

7.1 Introduction

The association of ultracold tetratomic molecules marks an important step in the context of ultracold polyatomic molecules. Ultracold polyatomic molecules have emerged as a powerful platform for various applications including tests of beyond-Standard-Model physics [269], non-equilibrium dynamics [92], and quantum information processing [270–272], thanks to their additional degrees of freedom compared to diatomic molecules. Significant progress has recently been made in the field of molecular cooling, enabling quantum degeneracy in ultracold gases of diatomic dipolar molecules [64, 65, 273]. However, for larger molecules, reaching the ultracold regime remains challenging due to their increased complexity and adverse collisional properties. Direct cooling techniques such as buffer gas cooling [15], supersonic expansion [17], beam deceleration [16], cryofuges [18], and optoelectrical Sisyphus cooling [274] have only marginally reached ultracold temperatures. Laser cooling of larger polyatomic molecules represents an active area of research [48, 54]. While symmetric top molecules have been laser-cooled in one dimension [62], the efficiency of laser cooling for large molecules (tetratomic or larger) in three dimensions remains unexplored. It is still an open question whether temperatures below the submicrokelvin regime can be achieved. Recently, magnetoassociation of ultracold molecules via Feshbach resonances has been extended to weakly bound triatomic NaK_2 molecules in the 100-nK regime [63],

where the molecules inherit the low temperature from the atom–diatomic molecule mixture. However, this technique requires resolvable Feshbach resonances between the collisional partners. For larger, polyatomic molecules, the high number of the intermediate collisional states and their fast loss mechanisms at short range results in a nearly universal collisional loss rate [81], preventing the occurrence of such Feshbach resonances.

Here with FL resonances, we demonstrate a novel and general approach to form weakly bound ultracold polyatomic molecules by electroassociation of smaller polar molecules [267, 268]. We create ultracold tetratomic $(NaK)_2$ molecules from pairs of microwave-dressed fermionic NaK molecules by ramping the microwave field across a field-linked (FL) scattering resonance [76, 111, 112, 275]. This approach benefits from the universality of FL resonances and can be applied to any molecule with a sufficiently large dipole moment. We measure a lifetime up to 8(2) ms of our FL tetramers near the dissociation threshold and achieve a phase space density of 0.040(3). With microwave-field modulation dissociation after time-of-flight, we directly image the tetramers and reveal the expected anisotropic angular distribution.

7.2 Electroassociation

By ramping the microwave field across a FL resonance, a pair of scattering NaK dimers can be adiabatically associated into a weakly bound $(NaK)_2$ tetramer, as depicted in Fig. 7.1a. We refer to this process as electroassociation [267], analogous to magnetoassociation using a magnetic Feshbach resonances [250].

The concept behind electroassociation involves a smooth transition from low-lying scattering states of a dimer pair to the bound tetramer state by gradually ramping the microwave field over time [267, 268]. The increase of the microwave field ellipticity, as depicted in Fig. 7.1b,c, enhances the depth of the interaction potential, leading to the emergence of the tetramer state from the collisional threshold and an increase in its binding energy (see Fig. 7.1d). Microwave shielding of the dimers leads to an enhanced collisional stability of the FL tetramers [106, 164, 268], which can therefore be efficiently associated from a low entropy gas of dimers.

7.3 Binding energy and lifetime

7.3.1 Theory

We utilize the same formalism as in Chapter 4 and 6 to compute the properties of tetramers. To obtain an approximated binding energy, we solve the eigenvalue problem of the effective potential. As we cross the scattering shape resonance, as indicated by the dashed line in Fig. 7.1c, a tetramer bound state, $|\psi_B\rangle = \int d\mathbf{r}\psi_B(\mathbf{r}) |\mathbf{r}\rangle |\alpha(\mathbf{r})\rangle$ emerges. By numerically solving the Schrödinger equation $H_{\text{eff}}\psi_B(\mathbf{r}) = \varepsilon_B\psi_B(\mathbf{r})$, we can acquire the wavefunction

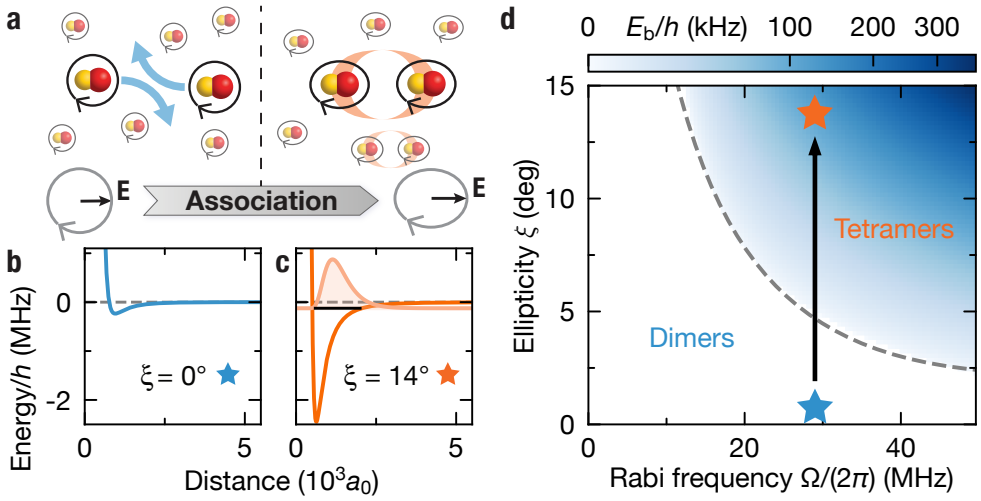

Figure 7.1: Electroassociation of field-linked (FL) tetramers. **a**, Microwave dressed NaK dimers are associated into $(NaK)_2$ tetramers as the microwave polarization is ramped from circular to elliptical. **b,c**, Interaction potentials between two dimers approaching along the long axis of the microwave field at $\xi = 0°$ (blue) and $\xi = 14°$ (orange). The potential depth increases and a tetramer bound state emerges from the collisional threshold. The light orange line shows the radial wave function of the tetramer, and the black solid line indicates its binding energy. **d**, Calculated binding energy of the tetramers. The FL resonance (dashed line) marks the onset of the tetramer state. The stars and the arrow mark the electroassociation trajectory in the experiment. Within the range of experimental parameters, there exists only a single FL tetramer state. Figure reproduced from Ref. [113].

$\psi_B(\mathbf{r})$ and the binding energy ε_B of the tetramer state. Here, the effective Hamiltonian is represented as $H_{\text{eff}} = -\hbar^2\nabla^2/M + V_{\text{eff}}(\mathbf{r})$.

Figure 7.1d shows the binding energy ε_B in the Ω–ξ plane. A positive $\xi > 0$ enhances the attractive DDI along the long axis of the microwave ellipse, and the overall depth of V_{eff} increases with Ω. As a result, the binding energy increases with either ξ or Ω. In the case of circularly polarized microwaves, i.e., $\xi = 0°$, the resulting rotational symmetry along the z-direction ensures the conservation of the projected angular momentum m, resulting in two nearly degenerate bound states for $m = \pm 1$. At $\xi > 0$, this degeneracy is lifted, and the new eigenstates are superpositions of $m = \pm 1$ (see Section 6.1.3).

To ensure a more precise calculation, we tackle the multichannel scattering problem, which includes lower dressed state channels and also accounts for the direct van der Waals interaction.[1] This allows us to extract both the binding energy and the one-body lifetime of the tetramers.

Without loss of generality, we concentrate on the cross section σ_{210}^{210} of the incident and out-going molecules in the channel (210). When the incident energy is resonant with the tetramer state, a peak appears in the cross section σ_{210}^{210}, where the width of the peak is the decay rate of the tetramer. The cross section σ_{210}^{210} quantitatively agrees with the lineshape

$$\sigma(E) = \frac{2\pi}{k_2^2}\left|ig^2G(E) + S_{\text{bg}} - 1\right|^2, \tag{7.1}$$

where $G(E) = 1/(E - E_b + i\Gamma/2)$ is the tetramer propagator, $k_2 = \sqrt{M(E - \mathcal{E}_2)}$ and S_{bg} are the incident momentum and the background scattering amplitude of molecules in the dressed state channel $|2\rangle$, respectively. By fitting σ_{210}^{210} and $\sigma(E)$, we obtain the binding energy E_b and the decay rate Γ of the tetramer. We remark that for the incident and out-going molecules in other channels $\alpha = 3 \sim 7$, the propagator $G(E)$ in Eq. (7.1) does not change. Therefore, fitting $\sigma_{\alpha lm}^{\alpha' l' m'}$ in a different scattering channel leads to the same binding energy E_b and decay rate Γ.

As was discussed in Chapter 4, near circular polarization, one of the primary loss mechanism is the tunneling from the upper channel to the lower channel, accompanied by a significant release of energy on the scale of MHz. This tunneling is suppressed by a high Rabi frequency and a low ellipticity. However, as the Rabi frequency continues to rise beyond the resonance, the binding energy increases and the tetramer becomes more confined, thus reducing the lifetime due to the increased wave function overlap between the tetramer state and the high momentum scattering state in the lower channel (see Fig 7.2).

[1] The same interaction determines the universal loss rate in absent of microwave, as discussed in Chapter 4.

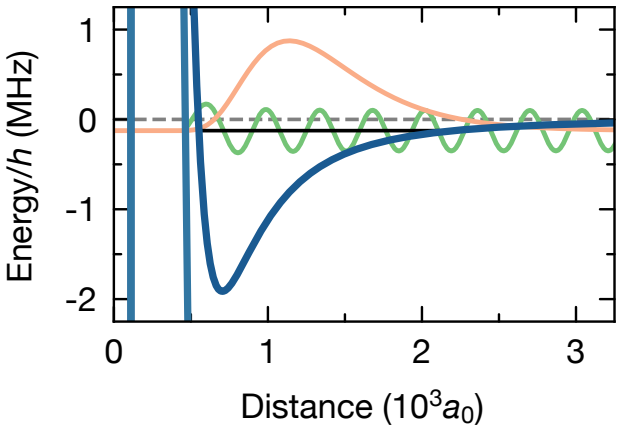

Figure 7.2: Potential curves and tetramer wave functions. The blue lines are the potential curves similar to Fig. 4.6. The orange line represents the tetramer wave function, and the black line marks the position of the binding energy. The green line represents the scattering wave function in the second channel. The microwave parameters are $\Omega = 2\pi \times 28.5\,\mathrm{MHz}$, $\Delta = 2\pi \times 9.5\,\mathrm{MHz}$, and $\xi = 14°$.

7.3.2 Experiment

Our experiments begin with trapped microwave-shielded molecules after evaporative cooling. Depending on the trap depth at the end of the evaporation, we prepare various initial conditions of the molecular gas. The minimum temperature is $T = 50(1)\,\mathrm{nK}$ at a dimer molecule number N_D of $5.7(3) \times 10^3$, corresponding to $T/T_\mathrm{F} = 0.44(1)$, where T_F is the Fermi temperature of the trapped gas. The trapping frequencies are $(\omega_{\tilde{x}}, \omega_{\tilde{y}}, \omega_z) = 2\pi \times (42, 61, 138)\,\mathrm{Hz}$, where z is the vertical direction.

We probe the binding energy of the tetramers via microwave-field modulation association spectroscopy. We start the experiment with a circularly polarized microwave field at a Rabi frequency $\Omega = 2\pi \times 29(1)\,\mathrm{MHz}$ and detuning $\Delta = 2\pi \times 9.5\,\mathrm{MHz}$ [107]. We then quickly ramp the microwave in 100 µs to a target ellipticity ξ above the FL resonance and modulate the ellipticity at various frequencies for up to 400 ms. The ellipticity ξ is defined such that $\tan\xi$ gives the ratio of the left- and right-handed circularly polarized field components. When the modulation frequency ν is slightly above the binding energy, tetramers are formed and subsequently decay into lower dressed states accompanied by a large release energy. This leads to a significant reduction of the remaining dimer number, which we detect in the experiment. As shown in Fig. 7.3a, we observe clear asymmetric lineshapes in the spectra, where the onset frequency of the tetramer association corresponds to the binding energy of the tetramer. We can thereby determine the binding energy of the tetramers at different target ellipticities (see Fig. 7.3b) and find excellent agreement between the experimental data and coupled channel calculations without free parameters.

We assume the dimer loss in the modulation spectra to be proportional to the number of formed tetramers. The lineshape can be modeled via Fermi's golden rule [276]

$$N_\mathrm{T}(\nu) \propto \int_0^\infty \mathrm{d}\epsilon_\mathrm{r} F(\epsilon_\mathrm{r}) g(\epsilon_\mathrm{r}) e^{-(h\nu - E_\mathrm{b} - \epsilon_\mathrm{r})^2/\sigma^2} \tag{7.2}$$

where ν is the modulation frequency and E_b is the binding energy of the tetramer. The function $g(\epsilon_\mathrm{r}) \propto e^{-\epsilon_\mathrm{r}/k_\mathrm{B}T}$ denotes the number of colliding pairs per relative kinetic energy

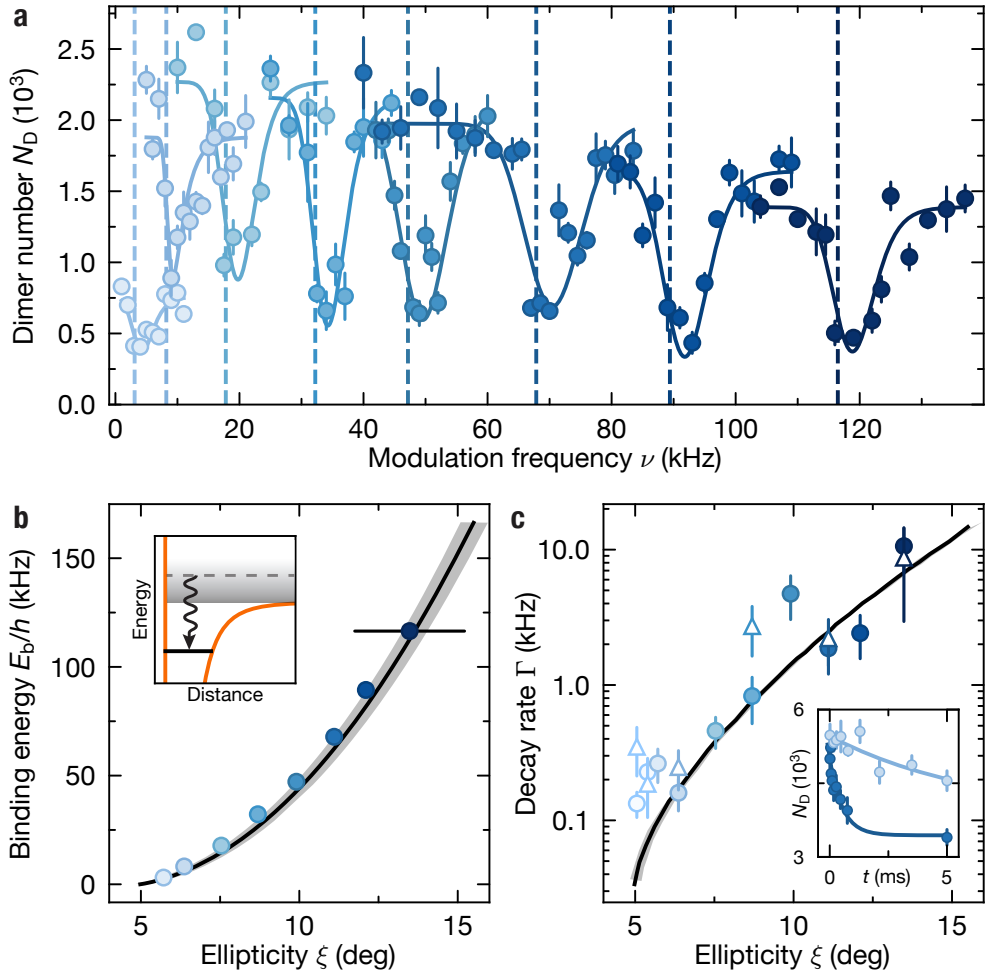

Figure 7.3: Tetramer binding energy and lifetime. a, Tetramer association spectra at various ellipticities are depicted, obtained by modulating the microwave ellipticity. The solid lines show the fitted lineshapes, and the dashed lines mark the binding energies. Line shapes are shifted and broadened by the linewidth of the tetramer states and other technical effects. The Rabi frequency is $\Omega = 2\pi \times 29(1)\,\mathrm{MHz}$ and the detuning is $\Delta = 2\pi \times 9.5\,\mathrm{MHz}$. We use a peak-to-peak modulation amplitude of 1°, and a modulation time of 100 ms, except for the lowest ellipticity where the amplitude is 0.5° and the duration is 400 ms. Error bars represent the standard error of the mean of four repetitions. **b**, Binding energy E_b, obtained from the spectra (circles), compared with theory (line). Statistical error bars are smaller than the symbol size. Black error bar marks the systematic uncertainty of ellipticity, and the shaded area shows theory calculations including the systematic uncertainty in Rabi frequency. The inset illustrates the association process. **c**, Decay rate Γ of tetramers in time-of-flight (circle) and in the trap (triangle), compared to theory (line). Error bars show fitting errors. The inset shows example decay curves at $\xi = 7(1)°$ and $\xi = 11(1)°$ in time-of-flight, with error bars representing the standard error of the mean of eight data sets. Figure reproduced from Ref. [113].

interval $\mathrm{d}\epsilon_\mathrm{r}$. Here, the temperatures T are obtained from the data located away from the association transitions. The function $F(\epsilon_\mathrm{r}) \propto \sqrt{\epsilon_\mathrm{r}}(1+\epsilon_\mathrm{r}/E_\mathrm{b})^{-2}$ denotes the Franck–Condon factor $F(\epsilon_\mathrm{r})$ between the unbound dimer state and the tetramer state, which we assume to take the same form as for Feshbach molecules [276]. The product $F(\epsilon_\mathrm{r})g(\epsilon_\mathrm{r})$ is convoluted with a Gaussian distribution with the width σ to account for the line width of the tetramer state and the finite energy resolution. The extracted line width shows a similar trend with ellipticity as the theoretical line width, but slightly larger.

Next, we probe the lifetime of the tetramers by measuring their loss dynamics. The dominant loss process for tetramers is spontaneous dissociation into lower microwave dressed states [164,268] accompanied by a large gain in kinetic energy, which, effectively, leads to a one-body decay of the tetramer number. In order to investigate this process, we first create tetramers by ramping the ellipticity to $\xi = 8(1)^\circ$ in 0.67 ms, and then quickly ramp to a target ellipticity in 20 µs. The quick ramp makes sure that the measurements at different ellipticities start with the same tetramer and dimer number. There we hold for a variable time, then reverse the ellipticity ramps to dissociate the tetramers back to dimer pairs to map the loss of tetramers during the hold time onto the total dimer number. We turn off the trap after the association to minimize collisional loss. We observe that when the binding energy is high, the observed dimer number quickly undergoes a fast initial decay and afterwards remains constant during the hold time. Near the collisional threshold, the decay is much slower (see inset of Fig. 7.3c). These initial decays are much faster than the expected dimer–dimer collisional loss rates, and are absent if we jump from $\xi = 0^\circ$ to the target ellipticity, so that no tetramers are expected to form. We therefore attribute this initial decay process to the one-body loss of the tetramers, in good agreement with theory predictions. The corresponding $1/e$ lifetime is longer than 6(1) ms when the binding energy is below 8.2(2) kHz, and a maximum of 8(2) ms lifetime is observed near the dissociation threshold. With higher Rabi frequencies and at circular polarization, theory predicts lifetimes in excess of 100 ms at $E_\mathrm{b} < h \times 4\,\mathrm{kHz}$, as shown in Fig. 7.4.

7.4 Estimation of collision rates of tetramers

7.4.1 Tetramer dipole moment

To estimate the dipolar scattering rates of dimer–tetramer and tetramer–tetramer collisions, we first determine the dipole moment $\mathbf{d}_\mathrm{tetra} = 2d \int d\mathbf{r}\, \langle\alpha(\mathbf{r})|\, \hat{\mathbf{d}}\, |\alpha(\mathbf{r})\rangle\, |\psi_B(\mathbf{r})|^2$ of the tetramer via $\psi_B(\mathbf{r})$. As shown in Fig. 7.5, the tetramer wavefunctions are localized around the minimum of the effective potential outside the shielding core, where $|\alpha(\mathbf{r})\rangle$ is predominantly described by $|+,+\rangle$. Thus, $\mathbf{d}_\mathrm{tetra} \sim 2d\, \langle+,+|\, \hat{\mathbf{d}}\, |+,+\rangle$ is approximately the dipole moment of two molecules. The difference in dipole moments between the two molecules and the tetramer is less than 10%.

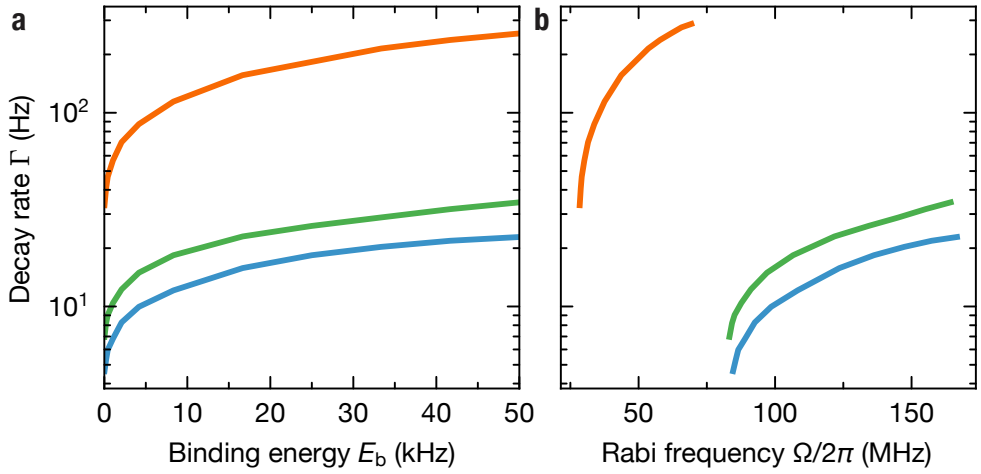

Figure 7.4: Theoretical tetramer decay rate. The decay rate Γ is depicted as a function of binding energy in **a** and the Rabi frequency in **b**. Each curve represents a calculation at a fixed ellipticity angle ξ, with varying Rabi frequencies, yielding a range of binding energies. Specifically, the orange curve corresponds to an ellipticity of $\xi = 5°$, while the blue and green curves are associated with circular polarization, representing angular momentum projections $m = 1$ and $m = -1$, respectively. The corresponding resonance positions are 83 MHz and 85 MHz for $m = 1$ and $m = -1$, respectively. Figure reproduced from Ref. [113].

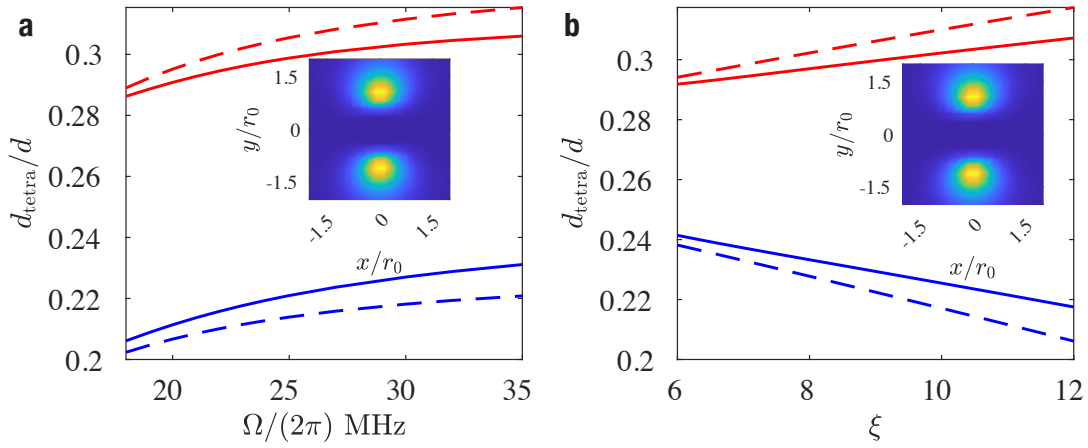

Figure 7.5: Dipole moment of a FL tetramer. The dipole moment of a FL tetramer along the x and y directions, represented by the solid blue and red curves, respectively. For comparison, the dashed blue and red curves depict the dipole moment of two individual molecules along the x and y directions. The parameters are set at an ellipticity of $\xi = 10°$ in **a** and a Rabi frequency of $\Omega = 2\pi \times 28.5\,\mathrm{MHz}$ in **b**. Insets shows the tetramer wave function distributions in coordinate space. Figure reproduced from Ref. [268].

7.4.2 Dipolar collision rate

The elastic scattering rate coefficient is given by $\beta = \sigma v$, where $v = \sqrt{8k_{\mathrm{B}}T/\pi\mu}$ denotes the average relative velocity and σ denotes the cross section. In the regime of large dipole moment $E > \hbar^6/\mu^3 d_1^2 d_2^2$ the cross section σ can be estimated using the semiclassical formula given by [75]

$$\sigma = \frac{2}{3}\frac{d_1 d_2}{\epsilon_0 \hbar}\sqrt{\frac{\mu}{2E}}. \tag{7.3}$$

Here d_1 and d_2 are the dipole moments of the two colliding particles, μ is the reduced mass, and E is the kinetic energy. We neglect the effect of a small ellipticity ξ, and estimate the effective dipole moment of the dimers to be $d_0/\sqrt{12(1+(\Delta/\Omega)^2)}$. The dipole moment of tetramers is roughly twice as large as dimers. With that, the above formula provides an estimation for the elastic scattering rates to be $9.7 \times 10^{-9}\,\mathrm{cm^3 s^{-1}}$ for dimer–tetramer and $1.9 \times 10^{-8}\,\mathrm{cm^3 s^{-1}}$ for tetramer–tetramer. This implies that tens of elastic collisions can occur within the lifetime of tetramers.

To investigate the collisional stability of tetramers, we measure their lifetimes while the dipole trap remains active. Our observations indicate a combined one-body and two-body loss of the detected dimer number, and we confirm that the two-body loss arises from dimer–dimer collisions. Apart from data near the collisional threshold $\xi = 5(1)^\circ$, where in-trap measurements are influenced by thermal dissociation, we do not detect notable additional loss of tetramers in in-trap measurements compared to those in time-of-flight experiments. The deduced inelastic collision rates are consistent with zero within error bar. We estimate that more than ten elastic collisions can occur throughout the lifetime of tetramers, which suggests that collisions with tetramers are predominantly elastic.

7.4.3 Upper bound for the inelastic collision rate

Figure 7.6b,c show the tetramer decay in trap and in free space are similar. The extracted decay rates differs by $9(9) \times 10^1\,\mathrm{Hz}$, which we use to obtain an upper bound for the inelastic scattering rate coefficients. By assuming that the additional loss is either purely dimer–tetramer or tetramer–tetramer, we estimate the upper bounds for their inelastic collision rate coefficients to be $2(2) \times 10^{-10}\,\mathrm{cm^3 s^{-1}}$ and $9(9) \times 10^{-10}\,\mathrm{cm^3 s^{-1}}$, respectively. Both values are consistent with zero within error bar. Even for the worst-case estimation, the inelastic collision rate coefficients remain orders of magnitude lower than the estimated elastic dipolar scattering rate coefficients.

7.5 Association and dissociation processes

We probe the association and dissociation process by ramping the ellipticity starting from $\xi = 0$ with a constant ramp speed of $14^\circ\,\mathrm{ms^{-1}}$ ($27^\circ\,\mathrm{ms^{-1}}$ for the dissociation) to a target ellipticity, as illustrated in Fig. 7.7b,c. To distinguish the tetramers from the unpaired

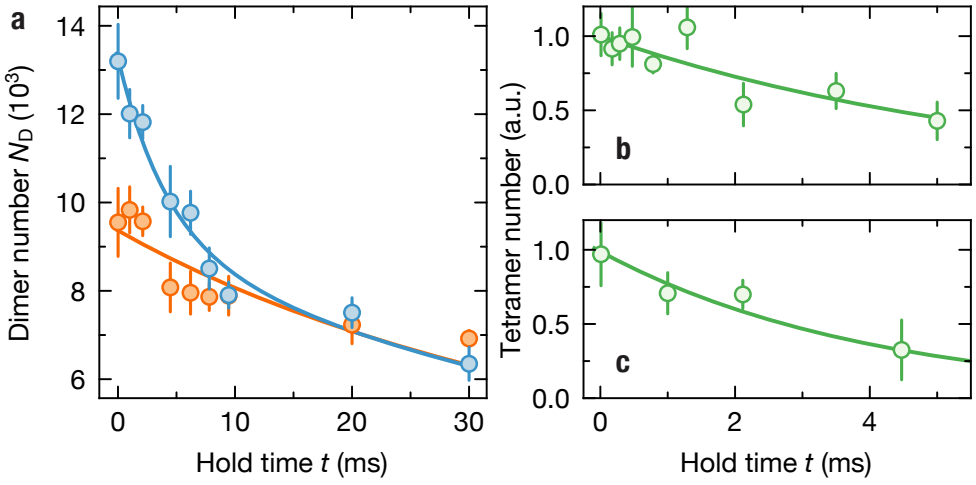

Figure 7.6: Tetramer lifetime in trap and in time-of-flight. **a**, Example loss of molecule number in the trap, illustrating the difference between the scenarios with (orange) and without (blue) removal of tetramers at an ellipticity of $\xi = 7(1)°$. **b**,Normalized tetramer decay measured during time-of-flight at the same ellipticity value ξ. **c**, Extracted tetramer number derived from the data in **a**, where no notable additional loss is evident when compared to **b**. The error bars included in the graphs represent the standard error of the mean, calculated from ten repetitions. Figure reproduced from Ref. [113].

dimers we selectively remove the tetramers from the dimer–tetramer mixture by quickly ramping the ellipticity to $\xi = 14(1)°$ in 20 µs and hold for 0.4 ms. At this point the tetramers are deeply bound and rapidly decay, which removes them from the sample.

Figure 7.7 shows the evolution of the detected dimer number during the association and the dissociation processes. The number of unpaired dimers (light blue in Fig. 7.7a) reduces as we ramp the ellipticity across the FL resonance, indicating tetramer formation. Remarkably, as shown in Fig. 7.7d, the number of detected dimers revives as we ramp back to circular polarization, indicating that the formed tetramers can be reversibly dissociated back into dimer pairs. In addition, we characterize the association process without removing the tetramers but followed by a dissociation ramp back to $\xi = 0°$. The detected dimer number (dark blue in Fig. 7.7a) partially revives until $\xi \gtrsim 12°$, where the tetramers decay during the ramps before they can be dissociated back into dimers.

7.6 Conditions for efficient electroassociation

We first investigate the tetramer formation in the dilute gas regime theoretically. We consider a slow ramp of either Ω or ξ across the shape resonance in a thermal molecular sample. As the parameters C_3, C_6, and $\mathcal{F}_\xi$ vary with time, the effective Hamiltonian $H_{\text{eff}}(t)$

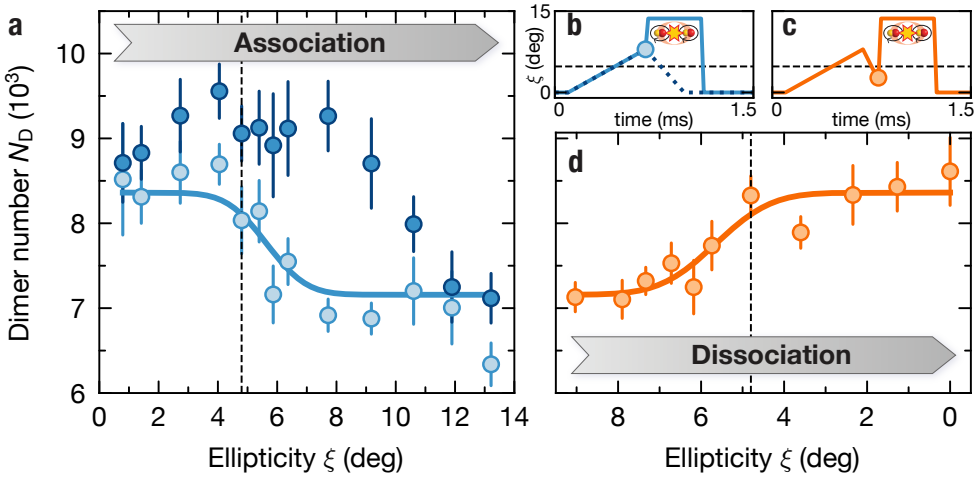

Figure 7.7: Association and dissociation processes. **a**, Remaining dimer number N_D after the association ramp. Dark blue circles represent the total number of dimers, including dissociated tetramers; light blue circles denote the dimer number after the tetramers' removal. Solid blue line corresponds to a fit using an error function; vertical dashed line indicates the theoretical resonance position. **b,c**, Waveforms of the association (**b**) and dissociation (**c**) ramps. In **b**, blue solid (dashed) line portrays the waveform with (without) removal of the tetramers; horizontal dashed lines mark the theoretically predicted resonance position. Circles in **b** and **c** represent the target ellipticity of the association or dissociation ramp, corresponding to the data plotted in **a** and **d**. **d**, Increase in detected dimer number during the dissociation ramp; solid orange line represents a fit to an error function; vertical dashed line denotes the predicted resonance position. Error bars stand for the standard error of the mean from ten experimental repetitions. Figure reproduced from Ref. [113].

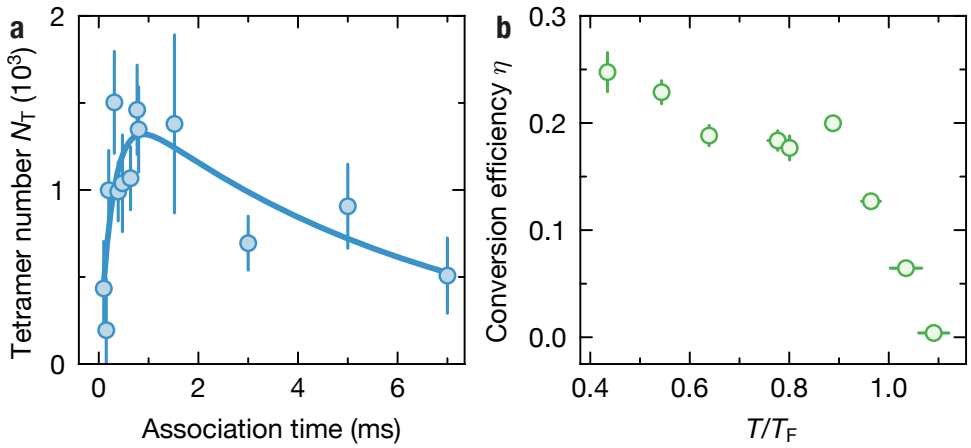

Figure 7.8: Conditions for efficient electroassociation. **a**, Tetramer number N_T plotted against the association time, with the solid blue line representing a fit to a double exponential function to capture both the formation and decay of the tetramers. Error bars denote the standard error of the mean, calculated from eight repetitions. **b**, Conversion efficiency η displayed as a function of the initial ratio T/T_F of the dimer gas temperature to the Fermi temperature. A ramp speed of $7°\,\mathrm{ms}^{-1}$ is used for the electroassociation, and the initial T/T_F values are extracted separately without performing electroassociation. Error bars indicate the standard error of the mean, based on four repetitions. Figure reproduced from Ref. [113].

is time dependent. The conversion efficiency [277]

$$c = 2n\lambda_T^3 \int d\mathbf{k} e^{-\beta\frac{k^2}{M}} p_{\mathbf{k}}^{\mathrm{a}} \tag{7.4}$$

to the tetramer can be evaluated using the density n of molecular gases, the thermal de Broglie wavelength $\lambda_T = (4\pi\beta/M)^{1/2}$ at the temperature $T = 1/k_B\beta$, and the transition probability $p_{\mathbf{k}}^{\mathrm{a}} = \left|\langle\psi_B|\,\mathcal{T}\exp[-i\int_0^{t_\mathrm{a}} dt H_{\mathrm{eff}}(t)]\,|\psi_{\mathbf{k}}\rangle\right|^2$ in the association time t_a. Here, the initial state $|\psi_{\mathbf{k}}\rangle$ is the scattering eigenstate of $H_{\mathrm{eff}}(0)$ in the molecule region, and the final state $|\psi_B\rangle$ is the bound state of $H_{\mathrm{eff}}(t_\mathrm{a})$ in the tetramer region. It should be noted that this result, obtained from two-body scattering calculations, is not valid in the saturation regime of c, where many-body effects must be considered using the non-Markovian Boltzmann equation [277].

We experimentally identify the optimum condition for electroassociation. We obtain the tetramer number from the difference between images with and without the tetramer removal process outlined previously. First, we probe the timescale of the tetramer formation. We ramp the ellipticity from $\xi = 0(1)°$ to $8(1)°$ and vary the ramp speed. As shown in Fig. 7.8a, we observe the formation of tetramers within 0.3(1) ms and subsequently decay due to the finite lifetime. We estimate that the tetramers scatter on average more than once during the association, bringing them close to thermal equilibrium with the remaining dimers.

We apply the following double exponential fit to the tetramer number as a function of ramp time t in Fig. 7.8a

$$N_{\mathrm{T}}(t) = N_0(1 - e^{-t/\tau})e^{-t_{\mathrm{T}}/\tau_{\mathrm{T}}}, \tag{7.5}$$

where τ gives the timescale for association and τ_{T} gives the timescale for tetramer decay. The time $t_{\mathrm{T}} \approx 0.4(t + t_{\mathrm{disso}})$ is the time where the ramp is above the FL resonance, which is about a factor of 0.4 of the association time t and the dissociation time $t_{\mathrm{disso}} = 0.5\,\mathrm{ms}$. We extract $\tau = 0.3(1)\,\mathrm{ms}$ and $\tau_{\mathrm{T}} = 2(1)\,\mathrm{ms}$.

Next, we investigate the role of quantum degeneracy for efficient electroassociation. For magnetoassociation of Feshbach molecules, it has been shown that a low entropy sample is crucial to achieve high conversion efficiency, due the improved phase-space overlap between the atoms [278]. Here we vary the degeneracy of our initial dimer samples by changing the final trap depth of the evaporation [107]. We observe an increase of the conversion efficiency η, that is the fraction of dimers converted into tetramers, with quantum degeneracy of the dimer gas. We achieve a maximum $\eta = 25(2)\%$ conversion efficiency at $T = 0.44(1)T_{\mathrm{F}}$. Similar as for magnetoassociation [278], a maximum unity conversion efficiency is expected at zero temperature.

7.7 Ramp dissociation and thermometry

To detect the tetramers, a dissociation process can be employed by converting it back into two molecules. Two dissociation protocols are proposed: a fast ramp by decreasing either Ω or ξ, and a modulation $\delta\xi(t) = \delta\xi_0 \sin\omega_{\mathrm{d}} t$ around the elliptic angle ξ, where $\delta\xi_0$ is the amplitude and ω_{d} is the modulation frequency.

For the dissociation time t_{d} in the first protocol, the probability to detect a pair of molecules with relative momentum $\mathbf{k}$ is $p_{\mathbf{k}}^{\mathrm{d}} = \left|\langle\mathbf{k}|\,\mathcal{T}\exp[-i\int_0^{t_{\mathrm{d}}} dt H_{\mathrm{eff}}(t)]\,|\psi_B\rangle\right|^2$, which is obtained via solving the time-dependent Schrödinger equation numerically. Figure 7.9 shows the energy distribution $p(E) = Mk\int d\Omega_k p_{\mathbf{k}}^{\mathrm{d}}/2$ in the final state for different ramp times of ξ and Ω, where $k = \sqrt{ME}$ and Ω_k is the solid angle in the momentum space. We also plot the thermal distribution $p_T(E) = Mk\int d\Omega_k e^{-\beta k^2/M}/2$ at $T = 100\,\mathrm{nK}$ as a reference. The insets in Fig. 7.9a,b depict the dissociation energy $E_{\mathrm{diss}} = \int d\mathbf{k} p_{\mathbf{k}}^{\mathrm{d}} k^2/M$ as a function of t_{d}^{-1}. As the ramp speed increases, the energy distribution $p(E)$ of the final state becomes broader, leading to a decrease in the peak value and a larger dissociation energy. The small overlap of $p(E)$ and $p_T(E)$ allows for the differentiation of molecules dissociated from tetramers and the thermal excitations.

In experiment however, we tried fast dissociation ramp but could not observe a clear increase in the dissociation energy. We instead focus on measuring the temperature with ramp dissociation, by doing a relatively long time-of-flight and only dissociate the tetramers (and subsequently dimers) at the end of the time-of-flight to reduce the effect of release energy in the time-of-flight. The images of the tetramer momentum distribution are obtained

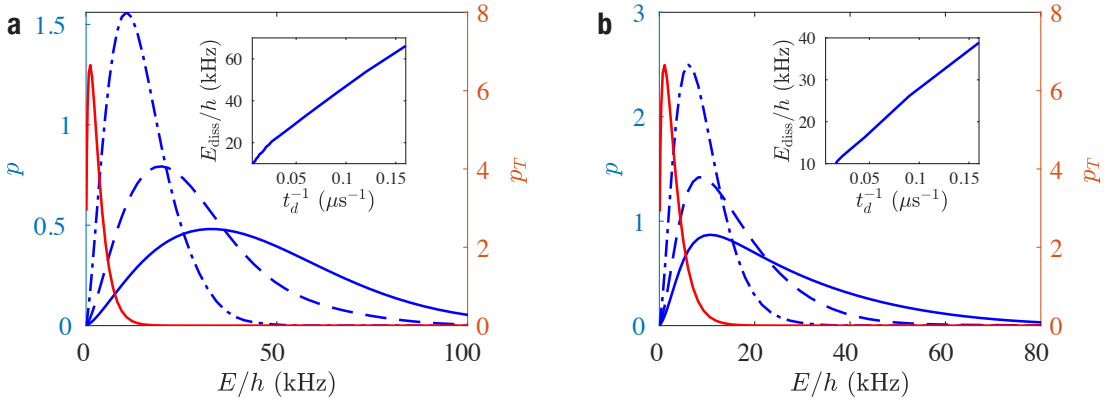

Figure 7.9: Dissociation via microwave ramp. a, Energy distributions of the final state in the dissociation for $\xi = 10°$, with a ramp of Ω from $2\pi \times 5\,\mathrm{MHz}$ to $2\pi \times 35\,\mathrm{MHz}$. The dissociation times are depicted as $t_\mathrm{d} = 11\,\mu$s (solid blue curves), $22\,\mu$s (dashed blue curves), and $67\,\mu$s (dash-dotted blue curves). The reference thermal distribution p_T is also plotted. Insets display the dissociation energy. The detuning is $\Delta = 2\pi \times 9.5\,\mathrm{MHz}$. **b**, Similar to **a**, but for $\Omega = 2\pi \times 28.5\,\mathrm{MHz}$ and a ramp of ξ from 1° to 12°. Figure reproduced from Ref. [268].

by subtracting images without from images with removal of tetramers at high ellipticity. Examples of such tetramer images are shown in Fig. 7.10. From a fit to such time-of-flight images and considering the mass of the particles, we determine the temperature of the tetramers to be 134(3) nK, which is slightly higher compared to the dimer temperature 97(6) nK. The fact that the tetramer cloud is smaller than the dimer background suggests partial thermalization and therefore elastic scattering during the electroassociation. Beyond that, heating might occur during the association and dissociation process. From the number and trapping frequencies, we obtain a peak density of $5.0(2) \times 10^{11}\,\mathrm{cm}^{-3}$ and a phase space density of 0.040(3) in the trap. We only consider the statistical error in this analysis.

7.8 Modulation dissociation and tetramer wave function

We image modulation-dissociated tetramers to probe the angular distribution of their single-particle wave function. A similar protocol has been demonstrated in the photodissociation of diatomic molecules [279]. Here we modulate the ellipticity at a modulation frequency $\nu > E_\mathrm{b}/h$, which couples the tetramer states to the scattering continuum. The coupled scattering state possesses a large wave function overlap with the tetramer state, and thus exhibits a similar momentum distribution, which is then probed by time-of-flight imaging. We note that the dissociation pattern is not a one-to-one mapping of the tetramer wave function, but only preserves its angular distribution.

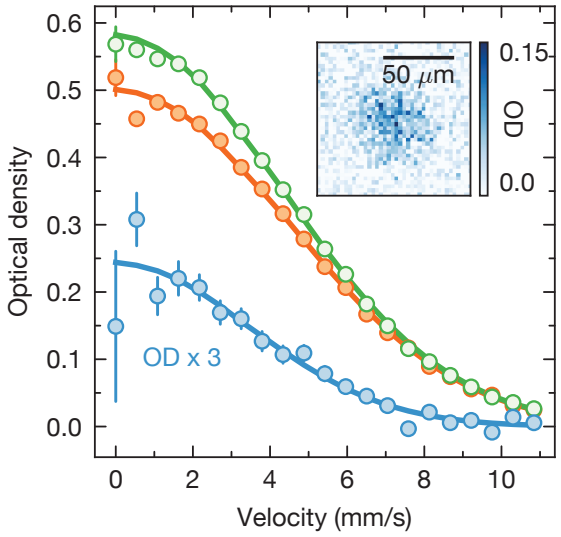

Figure 7.10: Momentum distributions of the ramped dissociated tetramers. Azimuthally averaged optical density (OD) of the samples is shown following ramp dissociation and a 4.5 ms time-of-flight. The difference (depicted in blue) between images with tetramer removal (orange) and without tetramer removal (green) reveals the momentum distribution of the tetramer cloud. The error bars represent the standard error of the mean, based on 60 repetitions. The inset displays the difference image. Figure reproduced from Ref. [113].

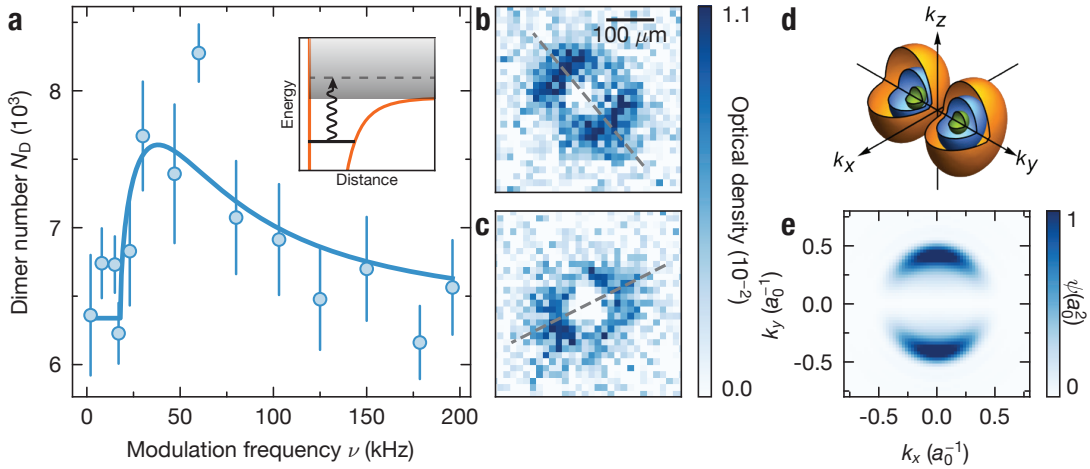

Figure 7.11: Momentum distributions of the modulation dissociated tetramers. **a**, Tetramer dissociation spectrum. Tetramers are created at $\xi = 8(1)°$ and the ellipticity is modulated with an amplitude of 1.4° for 2 ms. The solid line represents a fit to the dissociation lineshape, and the error bars denote the standard error of the mean based on ten repetitions. **b,c**, Time-of-flight images of modulation-dissociated tetramers, obtained using a modulation frequency of 30 kHz and an amplitude of 3.6° for 2 ms. Although the microwave ellipticity is approximately the same in **b** and **c**, the field orientation differs by about 90°. The dashed lines mark the extracted long axes of the patterns. The images are averaged over 84 and 40 measurements for **b** and **c**, respectively, with each pixel representing a binning of 5×5 pixels from the raw images. **d**, Theoretical tetramer wave function in momentum space, where the microwave field propagates along the z axis and its long axis is oriented along the y axis. The cut-open surfaces correspond to probability densities of $1.5 \times 10^8\,a_0^3$ (orange), $3.5 \times 10^8\,a_0^3$ (blue), and $6 \times 10^8\,a_0^3$ (green), respectively. **e**, The theoretical dissociation pattern integrated along the propagation axis of the microwave field, with the imaging plane (**b** and **c**) roughly perpendicular to the z axis. Figure reproduced from Ref. [113].

We begin by measuring the dissociation spectrum of the tetramers. We create tetramers at $\xi = 8(1)^\circ$ via electroassociation, then modulate the ellipticity for 2 ms to dissociate tetramers. Meanwhile, we turn off the trap to suppress further association of dimers. Afterwards we remove the remaining tetramers and let the dissociated dimers expand for another 6 ms before absorption imaging. The dissociation spectrum, depicted in Figure 7.11, demonstrates an increase in the observed dimer number N_D caused by the presence of dissociated tetramers when the modulation frequency ν exceeds the frequency associated with the binding energy of the tetramer $E_\mathrm{b}/h = 17.8(3)$ kHz. However, at higher frequencies, N_D declines due to a decrease in dissociation efficiency resulting from the diminished Franck–Condon factor. We fit the dissociation spectrum with a dissociation lineshape that is similar to the one used to describe dissociation of Feshbach molecules [250]

$$N_\mathrm{T}(\nu) \propto \Theta(\nu - E_\mathrm{b}/h)\frac{\sqrt{\nu - E_\mathrm{b}/h}}{\nu^2 + \gamma^2/4}, \tag{7.6}$$

where $\Theta(\nu - E_\mathrm{b}/h)$ is the step function, and $\gamma = 20(7)$ kHz accounts for the broadening of the signal.

We take the difference between images with and without modulation to obtain images of the dissociated tetramers. We verify that modulation at a higher frequency results in a larger pattern due to the higher dissociation energy. We choose a modulation frequency of $\nu = 30$ kHz to optimize the contrast of the images. As shown in Fig. 7.11, the dissociation pattern has two lobes, which are oriented along the long axis y of the microwave polarization[1] and match qualitatively with the theoretical wave function in Fig. 7.11d and e. Radial integration of the image reveals the angular distribution of the wave function, which follows p-wave symmetry [280] in the p_y channel $\cos^2\phi$, where ϕ is the angle from the y axis. The broken rotational symmetry along the quantization axis is a result of the elliptical microwave polarization. When we rotate the microwave field by roughly 90°, by flipping the sign of the relative phase between the two feeds of the antenna, the dissociation pattern is similar but rotated by about 90°, which demonstrates the tunable control of the tetramer wave function through the microwave field.

7.9 Prospects of electroassociation of complex polyatomic molecules

Field-linked resonances can be used to associate polyatomic polar molecules into even larger molecules. For molecules whose dipole moment is orthogonal to one of the axes of inertia, the same calculation can be performed within the corresponding rotational subspace, as shown in Ref. [76] for CaOH and SrOH. For more complex molecules where the body-frame

[1] Here we set the y axis along the long axis of the microwave, in order to be consistent with the convention of the effective potential Eq. (6.3). In Ref. [113], the x axis is defined to align with the long axis of the microwave.

dipole moment is not orthogonal to any of the three the axes of inertia, the microwave can induce the π transition between the ground state and the $m_J = 0$ rotational excited state. However, this detrimental π coupling can be suppressed by applying a d.c. electric field to shift the $m_J = 0$ state away from the $m_J = \pm 1$ states, so that the microwave can be off-resonant to the π transition, as shown in Ref. [178]. With that, a similar analysis of FL resonances can be applied.

7.10 Conclusion and outlook

By efficient electroassociation in a degenerate Fermi gas of diatomic molecules, we have created a gas of field-linked tetramers at unprecedentedly cold temperature. The associated weakly bound $(NaK)_2$ molecules are more than 3,000 times colder than any other tetratomic molecules produced so far [274]. The created tetramers possess a phase space density 11 orders of magnitude higher the previous record, and is only two orders of magnitude below quantum degeneracy. Remarkably, the lifetime of the long-range FL tetramers is much longer than those observed in polyatomic Feshbach molecules, which are either short lived ($< 1\,\mu s$) [86] or unstable in the presence of an optical trap [63]. These features make them a promising candidate for realizing a BEC of polyatomic molecules.

There are two possible ways to create a BEC of FL tetramers. Firstly, we can make use of the increasing conversion efficiency with lower temperatures. Starting below the critical temperature of $0.14T_F$, we expect a tetramer BEC to emerge from a degenerate Fermi gas of dimers [25], realizing a BCS–BEC crossover [28] which features anisotropic pairing due to the dipolar interactions [116], as illustrated in Fig. 7.12a. The other possibility is to extend the tetramer lifetime using the resonance at circular polarization, where the improved shielding increases tetramer lifetime to hundreds of milliseconds. As our experiments suggest that they are collisionally stable against dimer–tetramer collisions, it is promising to evaporatively cool tetramers to lower temperatures [24].

Another interesting direction is to study the excited states of the FL tetramers. At higher ellipticities and Rabi frequencies, the potential is deep enough to hold more than one bound state, which corresponds to rovibrational excitation of the tetramers. For vibrational (rotational) excitations, the radial (axial) wave function of the constituent dimers has one or more nodes [260]. Such excited FL states have more complex structures, which can be probed similarly with microwave-field modulation.

The creation of FL tetramers opens up a pathway to explore the rich landscape of the four-body potential energy surfaces. Similar to diatomic molecules, the long-lived weakly bound FL state provides an ideal starting point for deterministic optical transfer to deeply bound states within the PES [281–283]. For the PES of $(NaK)_2$ molecules, there are three energy minima which feature distinct geometries including D_{2h}, C_s, and C_{2v} symmetries [80], as illustrated in Fig. 7.12b. These states possess electric dipole and/or quadruple moments, and together with their rich rovibrational structures, opening up new

possibilities for studying eight-body collisions and quantum many-body phenomena with both strong dipolar and quadrupolar interactions.

The demonstrated electroassociation via FL resonances is applicable to any polar molecules with a sufficiently large dipole moment [76, 106, 108, 109, 267, 268]. For example, it can be applied to laser cooled polyatomic molecules, such as CaOH and SrOH [76], to form hexatomic molecules and beyond. It can also facilitate association of few-body bound states consisting of more than two polar molecules [275]. Electroassociation can be generalized to d.c. electric fields, where interspecies FL resonances could allow association of two molecules from distinct molecular species. One can even imagine a scalable assembling process, where we sequentially associate pairs of deeply bound molecules into weakly bound FL molecules, convert them into deeply bound states via optical transfer [281, 282], then associate these molecules into even larger FL molecules, as depicted in Fig. 7.12c.

In conclusion, we have created and characterized field-linked tetratomic $(NaK)_2$ molecules, which is so far the first tetratomic molecules attained in the 100 nK regime. The properties of these tetramers are highly tunable with the microwave field, and can be sufficiently long-lived and collisional stable. Thanks to the universality of field-linked resonance, our approach can be generalized to a wide range of polar molecules, including more complex polyatomic molecules. Our results provide a general approach to assemble weakly bound ultracold polyatomic molecules and open up possibilities to investigate new quantum many-body phenomena.

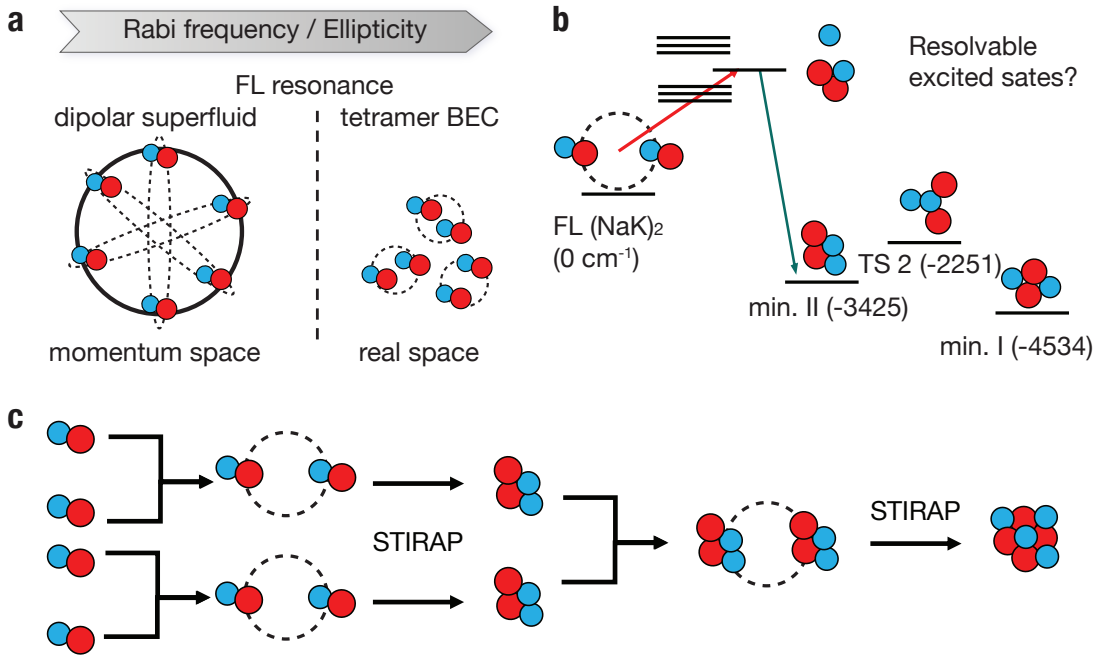

Figure 7.12: Future directions of FL tetramers. a, Dipolar BCS–BEC crossover. **b**, Optical transfer/STIRAP to deeply bound states via intermediate excited states. The energies of the bound states are calculated in Ref. [80]. The energies are in unit of cm^{-1}. **c**, Scalable assembly of large polyatomic molecules by alternating electroassociation and STIRAP.

What's your favorite molecule?[1]

The author

Chapter 8

Holistic view of shielding

With a comprehensive understanding of microwave shielding in hand, we are ready to compare it with other shielding schemes. In this chapter, I will discuss microwave shielding and Förster resonance shielding, comparing their respective advantages and disadvantages. The treatment is inspired by Ref. [116, 284], and for completeness, I will also mention shielding in confined geometries.

8.1 A simple model for resonant shielding

Both Förster resonance shielding and microwave shielding exploit an avoided crossing that couples the upper branch of the potential energy curve to a repulsive lower branch. The term "resonant" refers to the situation when the upper and lower branches become energetically degenerate. In the case of Förster resonance shielding, this degeneracy occurs between the states $|J = 1, M_J = 0\rangle|10\rangle$ and $|20\rangle|00\rangle$, while for microwave shielding, it occurs when dressing on resonance to the rotational transition $\Delta = 0$. Hereafter, we refer to Förster resonance shielding as d.c. shielding. Near this degeneracy, a two-level problem involving a 2×2 matrix can be considered [116, 284]

$$\begin{pmatrix} E_a(r,\theta) & W(r,\theta) \\ W(r,\theta) & E_b(r,\theta) \end{pmatrix}. \tag{8.1}$$

[1] A dimensionless analysis for shielding and FL resonance is presented in Table 8.1. The reader is welcome to look up their favorite molecule.

For d.c. shielding, the terms are defined as [284]

$$E_a(r,\theta) = \frac{d_{11}^2}{r^3}(1-3\cos^2\theta) + E_1, \tag{8.2}$$

$$E_b(r,\theta) = \frac{d_{00}d_{22}+d_{02}d_{20}}{r^3}(1-3\cos^2\theta) + E_2, \tag{8.3}$$

$$W(r,\theta) = \sqrt{2}\frac{d_{10}d_{12}}{r^3}(1-3\cos^2\theta). \tag{8.4}$$

Here, d_{ij} are the dipole matrix elements introduced in Chapter 4, and E_1 and E_2 represent the threshold energies of the two collisional channels. We adopt natural units with $4\pi\epsilon_0 = \hbar = 1$. For microwave shielding with circular polarization, the terms are [116]

$$E_a(r,\theta) = -\frac{d_0^2}{3r^3}u^2v^2(1-3\cos^2\theta), \tag{8.5}$$

$$E_b(r,\theta) = -\frac{d_0^2}{r^3}u^2(1+3\cos^2\theta) - \frac{1}{2}(\Omega_{\text{eff}}-\Delta), \tag{8.6}$$

$$W(r,\theta) = \frac{d_0^2}{\sqrt{2}r^3}u^2v\sin\theta\sqrt{1+\cos^2\theta}. \tag{8.7}$$

The coefficients are as defined in Chapter 6. The potential energy surfaces are given by the eigenvalues of the matrix

$$E_\pm(r,\theta) = \frac{1}{2}(E_a+E_b) \pm \frac{1}{2}\sqrt{(E_a-E_b)^2+4W^2}. \tag{8.8}$$

D.C. shielding is most effective at around $dE/B = 3.4$ [103], where $E_1 > E_2$. Thus, we can expand Eq. (8.8) for $W \ll E_1 - E_2$ and obtain an effective potential similar to Eq. (6.3) for microwave shielding

$$E_+ \approx E_a + \frac{W^2}{E_1-E_2}. \tag{8.9}$$

Ignoring the energy offset, we obtain a form analogous to Eq. (6.3)

$$V_{\text{eff,d.c.}} = \frac{C_3}{r^3}(1-3\cos^2\theta) + \frac{C_6}{r^6}(1-3\cos^2\theta)^2. \tag{8.10}$$

Here $C_3 = d_{11}^2$ and $C_6 = 2(d_{10}d_{12})^2/(E_1-E_2)$. The choice of C_6 ensures its s-wave contribution is the same as for microwave shielding. For comparison, Eq. (6.3) for the circularly polarized case is copied here

$$V_{\text{eff,mw}} = \frac{C_3}{r^3}(3\cos^2\theta-1) + \frac{C_6}{r^6}\sin\theta^2(1+\cos^2\theta). \tag{8.11}$$

Besides the difference in coefficients, the angular dependence of C_6 and the sign of the dipole-dipole interaction differ between the two shielding schemes. This is attributed to

the different symmetry of a d.c. field and a circularly polarized microwave. As we will discuss later, for a d.c. field, the first FL resonance occurs along the z-direction, in contrast to the xy-plane for microwave shielding.

As a further simplification, we can consider the projection of the effective potentials in the corresponding partial waves. For indistinguishable bosons, the dominant partial wave is s-wave, and the interaction averages as

$$\langle V_{\text{eff}}(r)\rangle = \int_0^\pi \frac{1}{2} V_{\text{eff}}(r,\theta)\sin\theta \mathrm{d}\theta = \frac{4}{5}\frac{C_6}{r^6}. \tag{8.12}$$

Interestingly, the C_3 contribution vanishes due to the scattering being isotropic. As a result, its leading-order contribution arises from coupling to d-wave, resulting in a $1/r^4$ potential, given by [75]

$$\langle V_{\text{eff}}^{(2)}(r)\rangle = -\frac{V_{\text{eff},0020}^2}{l(l+1)/Mr^2} = -\frac{2}{15}\frac{MC_3^2}{r^4}. \tag{8.13}$$

Here, I utilize the partial wave expansion provided in Appendix D.

For indistinguishable fermions, where the dominant partial wave is p-wave, the expressions for $m = 0$ and $m = \pm 1$ are as follows

$$\begin{aligned}\langle V_{\text{eff}}(r)\rangle &= \int_0^\pi \frac{3}{2} V_{\text{eff}}(r,\theta)\sin\theta\cos^2\theta \mathrm{d}\theta, \\ &= \begin{cases} -\dfrac{4}{5}\dfrac{C_3}{r^3} + \dfrac{44}{35}\dfrac{C_6}{r^6}, & \text{d.c.} \\ \dfrac{4}{5}\dfrac{C_3}{r^3} + \dfrac{4}{7}\dfrac{C_6}{r^6}, & \text{mw} \end{cases}\end{aligned} \tag{8.14}$$

and for $m = \pm 1$

$$\begin{aligned}\langle V_{\text{eff}}(r)\rangle &= \int_0^\pi \frac{3}{4} V_{\text{eff}}(r,\theta)\sin\theta\sin^2\theta \mathrm{d}\theta, \\ &= \begin{cases} \dfrac{2}{5}\dfrac{C_3}{r^3} + \dfrac{4}{7}\dfrac{C_6}{r^6}, & \text{d.c.} \\ -\dfrac{2}{5}\dfrac{C_3}{r^3} + \dfrac{32}{35}\dfrac{C_6}{r^6}, & \text{mw.} \end{cases}\end{aligned} \tag{8.15}$$

To evaluate C_3 and C_6 for d.c. shielding, we obtain the dipole matrix elements by diagonalizing the rotational Hamiltonian under the d.c. electric field. A similar calculation has been performed for the t-J-V-W model in Chapter 5, and the results are partially depicted in Fig. 5.1. The relative d.c. Stark shift is shown in Fig. 8.1a, and the avoided crossing between $|10\rangle|10\rangle$ and $|20\rangle|00\rangle$ occurs at $F = 3.25$.

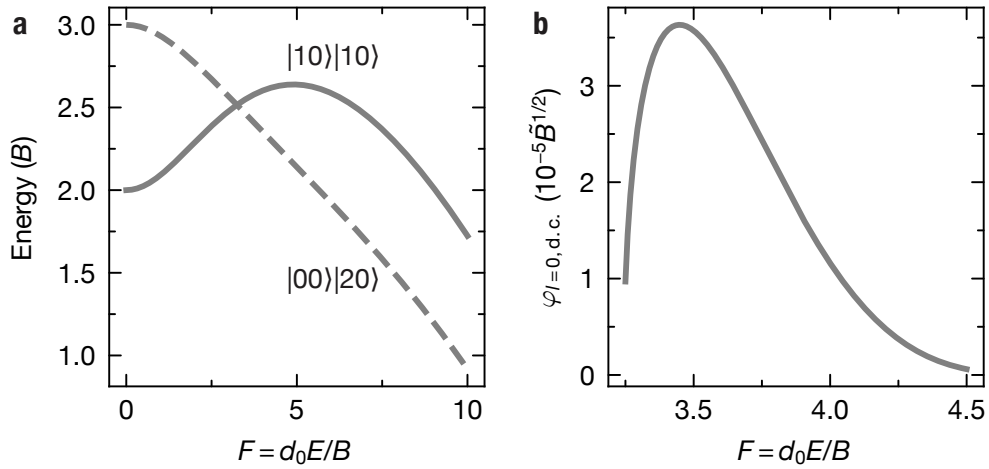

Figure 8.1: Dimensionless Analysis of d.c. Shielding. (a) Energies for the two pertinent channels in d.c. shielding, plotted as a function of the rescaled field $F = d_0 E/B$. **(b)** WKB phase of d.c. shielding versus F, as computed from Eq. (8.19).

Ref. [76, 103] performed a dimensionless analysis for both d.c. and microwave shielding. In both cases, the shielding performance is characterized by the rescaled rotational constant

$$\tilde{B} = \frac{BM^3}{\hbar^6}\left(\frac{d_0^2}{4\pi\epsilon_0}\right)^2. \tag{8.16}$$

For $\tilde{B} > 10^8$, corresponding to all bialkali except KRb and NaLi, both d.c. and microwave shielding operate efficiently, achieving a gamma ratio above 1000. Even for a less favorable species, KRb, a gamma ratio of 10 has been observed in 3D [105].

8.2 D.C. and microwave FL resonances

In this section, I examine the condition for FL resonances using the WKB approximation, as previously described in Chapter 6. The WKB phase is given by

$$\varphi_{\mathrm{WKB}} = \int_{V(r)\leq 0} \sqrt{-MV(r)}\mathrm{d}r. \tag{8.17}$$

For a potential expressed as $V(r) = C_{2m}/r^{2m} - C_n/r^n$ with $n < m$, the integral can be analytically evaluated

$$\varphi_{\mathrm{WKB}} = \sqrt{M} C_{2m}^{\frac{2-n}{2(2m-n)}} C_n^{\frac{m-1}{2m-n}} \frac{\sqrt{\pi}\Gamma\left(\frac{n-2}{4m-2n}\right)}{2(m-1)\Gamma\left(\frac{m-1}{2m-n}\right)}. \tag{8.18}$$

The WKB phase can be calculated using the effective potentials. For bosons, we have

$$\varphi_{l=0} \approx 0.117 \frac{M^{3/2} C_3^2}{C_6^{1/2}} = \begin{cases} 0.117 \dfrac{\tilde{C}_3^2}{\tilde{C}_6^{1/2}} \tilde{B}^{1/2}, & \text{d.c.} \\ 0.0650 \dfrac{a_\mathrm{d}}{a_\Omega (1+\delta_r^2)^{5/4}}, & \text{mw.} \end{cases} \tag{8.19}$$

Here, $\tilde{C}_3$ and $\tilde{C}_6$ are numerical coefficients dependent on the field strength F, a_d is the dipolar length for $d = d_0$, and $a_\Omega = \sqrt{2\hbar/M\Omega}$. For fermions, we ignore the centrifugal potential to derive analytic expressions. For d.c. shielding, where only $m = 0$ is attractive, we find

$$\varphi_{l=1,\mathrm{d.c.}} \approx 1.51 \frac{M^{1/2} C_3^{2/3}}{C_6^{1/6}} = 1.51 \frac{\tilde{C}_3^{2/3}}{\tilde{C}_6^{1/6}} \tilde{B}^{1/6}. \tag{8.20}$$

For microwave shielding, where both $m = \pm 1$ are attractive, we obtain

$$\varphi_{l=1,\mathrm{mw}} \approx 1.00 \frac{M^{1/2} C_3^{2/3}}{C_6^{1/6}} = 0.52 \left(\frac{a_\mathrm{d}}{a_\Omega (1+\delta_r^2)^{5/4}} \right)^{1/3}. \tag{8.21}$$

The distinction between different molecular species ultimately lies in the rescaled rotational constant $\tilde{B}$ and a coefficient related to F. For microwave shielding, the rotational constant B in the WKB phase cancels out, thus only a_d, a_Ω and δ_r are relevant.It should be noted that the formulas derived here serve as leading-order approximations. When additional partial waves are incorporated into the calculations, higher-order terms related to the dimensionless parameter $M^{1/2} C_3^{2/3} C_6^{-1/6}$ will be included.

Resonance occurs when the WKB phase is sufficiently large. We can determine this phase by employing exemplary coupled-channel calculations. The first FL resonance of fermionic NaK occurs at 83 MHz ($\delta_r = 0$), leading to $\varphi_{l=1,\mathrm{mw}}/\pi \approx 1.6$. The first resonance of bosonic NaRb [285] occurs at 3 MHz, corresponding to $\varphi_{l=0,\mathrm{mw}}/\pi \approx 2.8$. For d.c. shielding, we refer to Ref. [103] and extract the phases for the first four resonances as $\varphi_{l=0,\mathrm{d.c.}}/\pi \approx 1.0$, 4.0, 10, and 17. As depicted in Fig. 8.1b, the dependence of $\varphi_{\mathrm{WKB,d.c.}}$ on F is not monotonic and reaches a maximum at $F = 3.44$. Consequently, FL resonances may either not occur, if the maximum WKB phase is too small, or may appear in pairs. The analytical results of d.c. and microwave FL resonances for different molecular species are summarized in Table 8.1.

8.3 Shielding in confined geometries

Shielding within confined geometries functions by constraining the direction of collisions through external confinement. By confining the molecules within one or two dimensions and polarizing them along the confinement direction, the collisions are dominated by the

Table 8.1: Shielding of polar molecules. For each molecule, the table lists the dipole moment d_0, dimensionless rotational constant $\tilde{B}$, electric field for shielding $E_{\text{d.c.}}^{\text{shield}}$, the number of FL resonances for d.c. shielding $N_{\text{d.c.}}^{\text{res}}$, and the Rabi frequency of the first microwave FL resonance $\Omega_{\text{a.c.}}^{\text{res}}$. The parameters used in the calculations are taken from Ref. [76, 120, 286]. The asterisks in the Rabi frequency represent the value for fermionic molecules. Given the simplified model and the approximations made, the results in the last column should be considered as qualitative estimations.

	d_0 (D)	$\tilde{B}$	$E_{\text{d.c.}}^{\text{shield}}$(kV/cm) $F = 3.25$ - 3.8	$N_{\text{d.c.}}^{\text{res}}$	$\Omega_{\text{a.c.}}^{\text{res}}/2\pi$(MHz) (approximated)
$^1\Sigma$					
NaLi	0.463	3.12×10^5	159 - 186	-	3.1×10^5
KRb	0.574	5.47×10^6	12.5 - 14.6	-	1.7×10^3, $5.1 \times 10^{3*}$
RbCs	1.17	1.62×10^8	2.70 - 3.16	-	26
NaK	2.72	8.51×10^8	6.70 - 7.83	-	28, 83*
KCs	1.906	1.40×10^9	3.15 - 3.68	-	5.6, 17*
LiK	3.45	2.37×10^9	14.6 - 17.1	-	28, 82*
NaRb	3.1	5.67×10^9	4.35 - 5.09	2	3.1
LiRb	4.0	3.00×10^{10}	10.7 - 12.4	2	1.8, 5.5*
NaCs	4.75	7.59×10^{10}	2.42 - 2.83	2	0.20
LiCs	5.52	3.26×10^{11}	6.78 - 7.93	4	0.15, 0.44*
FrAg	9.20	3.66×10^{12}	0.452 - 0.528	8	1.5×10^{-3}
$^2\Sigma$					
CaOH	1.465	1.88×10^8	44.2 - 51.7	-	4.5×10^2
RbYb	1.218	3.11×10^8	1.96 - 2.29	-	10
RbSr	1.54	3.34×10^8	2.26 - 2.64	-	14
CsYb	1.478	7.45×10^8	1.09 - 1.28	-	2.8
SrOH	1.9	2.21×10^9	25.4 - 29.7	-	29
CaF	3.07	4.12×10^9	21.6 - 25.2	-	21
CaH	2.53	7.88×10^9	323 - 378	2	1.4×10^2
SrF	3.47	2.94×10^{10}	14.0 - 16.4	2	2.2
BaF	3.17	5.57×10^{10}	13.2 - 15.4	2	1.0
YO	4.524	1.24×10^{11}	16.6 - 19.4	4	0.79

repulsive side-by-side collisions, while attractive head-to-tail collisions are suppressed [99–101]. If we assume the confinement and the induced dipole moment d are both aligned along the z-axis, the intermolecular interaction is given by [100]

$$V = \frac{\mu\omega_z^2 z^2}{2} + \frac{\hbar^2\left(m^2 - 1/4\right)}{M\rho^2} - \frac{C_{6\mathrm{d}}}{r^6} + \frac{d^2}{r^3}\left(1 - \frac{3z^2}{r^2}\right), \tag{8.22}$$

where $\mathbf{r} = (\rho, \phi, z)$ denotes the relative position between two molecules in cylindrical coordinates, and $r \equiv |\mathbf{r}|$. The harmonic trap of frequency is represented by ω_z, leading to a characteristic length $a_h = \sqrt{2\hbar/M\omega_z}$. The projection m of the relative angular momentum is conserved, and the term related to $C_{6\mathrm{d}}$ describes the short-range van der Waals interaction with a characteristic length as defined in Chapter 4.

Efficient shielding occurs in the dipolar-dominated regime, characterized by the separation of energy scales $a_{\mathrm{dd}} > a_h \gg \bar{a}$, where a_{dd} is the dipolar length as defined in Chapter 4. This is similar to the case for microwave shielding, whereas here the trapping frequency plays the role of the microwave Rabi frequency. As predicted in Ref. [100], a gamma ratio of 100 is attainable for $d > 0.3\,\mathrm{D}$ and $\omega_z/2\pi > 25\,\mathrm{kHz}$ for bosonic molecules. For fermions, a gamma ratio exceeding 100 can occur either near $d = 0.2\,\mathrm{D}$ (as demonstrated with KRb [99]) or for $d > 0.5\,\mathrm{D}$.

The confinement shielding scheme depends solely on the mass and the induced dipole moment of the molecules, which is similar to microwave shielding. However, the maximum dipole moment can reach d_0, which is a factor of $\sqrt{12}$ higher than microwave shielding, making it applicable to a broader range of molecular species. The drawback of confinement shielding lies in the limited tunability of the short-range potential. Since the potential is repulsive in 2D, it cannot host tetramer bound states and, consequently, cannot utilize FL resonances to control the scattering length. Additionally, in a confined geometry, the interaction is isotropic and thus is not suitable for probing the anisotropic effects of dipole-dipole interaction.

8.4 Comparison of shielding schemes

Table 8.2 offers a comparison of the three shielding schemes, each with its distinct benefits and limitations. For setups lacking in-vacuum electrodes, or where electrodes are situated too close to the glass cell, generating the requisite electric field for d.c. shielding becomes problematic. In such scenarios, microwave shielding serves as a valuable alternative, as the microwave setup can be placed outside vacuum and be easily maintained. Conversely, d.c. shielding is not constrained by one-body loss, as the electrodes inherently act as a low-pass filter for high-frequency noise corresponding to the energy splitting of the collisional channels, which is on the order of the rotational constant. However, this filtering advantage comes at the cost of slower dynamic responsiveness, unlike microwaves, which can be adjusted on a submicrosecond timescale. When the body-fixed dipole moment is a limiting

factor, d.c. shielding in a confined geometry is preferred due to its capability of fully polarizing the molecules.

Broadening the scope to consider molecules with large dipole moments, such as CsAg and FrAg [286], alleviates the difficulties in generating the necessary electric fields. Consequently, the choice between shielding schemes becomes less influenced by technical limitations. Microwave shielding then emerges as the more attractive option due to its flexibility in manipulating the interaction potential and its rapid dynamic response, which are particularly advantageous for both the preparation and probing of many-body quantum phases.

Table 8.2: Comparison of existing shielding schemes for polar molecules. The columns specify the technical requirements, applicability to various molecular species, existence of FL resonances, and the maximum effective dipole moment $d_{\max}$. The defined scope of applicability is such that a gamma ratio higher than 1000 can be achieved.

	Requirements	Applicability	FL resonance	$d_{\max}$
Microwave shielding	Low-noise, high power, circularly polarized microwave.	$\tilde{B} \gtrsim 10^8$ [76]	Universal. Tunable anisotropy with ellipticity.	$d_0/\sqrt{12}$
Förster resonance shielding	Stable high d.c. electric field.	$\tilde{B} \gtrsim 10^8$ [103]	$\tilde{B} \gtrsim 10^9$ [103]	$0.145 d_0$
D.C. shielding in 2D	Intermediate d.c. electric field, strong confinement.	$d_0 \gtrsim 0.4\,\mathrm{D}$ [100]	Not applicable	d_0

What are your one thousand and one plans?

To Xin-Yu

Chapter 9

Conclusion and outlook

In this thesis, we establish microwave shielding as a powerful tool for stabilizing molecular collisions for evaporative cooling, inducing scattering resonances to tune their interaction, and associating weakly bound tetratomic molecules. The application of this robust tool within our Fermi degenerate molecular gas offers ample opportunities for quantum simulations, particularly those involving long-range dipole-dipole interaction, as discussed in corresponding chapters. As a near term goal in our setup, we are striving to enhance the evaporation efficiency to reach below the critical temperature for dipolar p-wave superfluidity, and to create a BEC of FL tetramers.

Microwave shielding exhibits its utmost potential in molecules possessing a larger dipole moment, such as NaRb, NaCs, LiRb and LiCs, which are either predicted or observed to have a larger shielding factor than NaK [76,108,109]. Their large dipole moment allows for easier polarization and the attainment of a high Rabi frequency. Furthermore, the Rabi frequencies required for FL resonance in these molecules are considerably lower than in NaK, e.g. the first FL resonance for LiRb occurs at $2\pi \times 4\,\mathrm{MHz}$ which is 20 times smaller than for NaK [285]. With the same microwave power one can explore the regime of high order FL resonances and the excited states of tetratomic molecules.

From a theoretical perspective, the sizable shielding core of microwave-shielded molecules sets them fundamentally apart from atoms. Ultracold atomic scattering can be regarded as a contact interaction due to the phase shift rendering the details of the short-range potential at $\lesssim 10\,a_0$. However, with the shielding core of microwave-shielded molecules reaching up to $1000\,a_0$, comprising over 10% of the intermolecular distance, their interactions can no longer be approximated as zero-range. Consequently, conventional notions of scattering length/volume become insufficient, necessitating higher order momentum dependent terms [285]. In fact, this large-core interaction is a critical component of interactions in condensed-matter systems. For instance, it underlies the anti-bunching phenomenon in liquid helium superfluids, restricting the condensate fraction to 10%, which is in stark

contrast to a pure condensate of bosonic atoms. The tunable shielding potential thereby offers a platform to study such phenomena. Moreover, the shielding core challenges the mean-field treatment for dipolar gases, indicating the potential for a stable sample to exist even in the regime of mean-field collapse.

Microwave-shielded ultracold polar molecules have emerged as a novel platform for quantum simulation, teeming with unexplored quantum many-body phenomena. As various research groups strive to expand the boundaries of this platform, we anticipate that through combined theoretical and experimental efforts, we will enhance our control over ultracold polar molecules and deepen our understanding of their many-body physics in the near future.

Appendix A

^{23}Na^{40}K properties and constants

This appendix contains constants for the relevant molecular states presented in this thesis. The most relevant electronic states are $X^1\Sigma^+$(the ground state), $a^3\Sigma^+$(the Feshbach state), $b^3\Pi$ (the excited state for near-resonant trapping), $B^1\Pi \sim c^3\Sigma^+$(the STIRAP intermediate state). Here, the Σ states are close to Hund's case (b), while the Π states are close to Hund's case (a) [287].

A.1 Rotation and hyperfine structures

In Chapter 4, we present the rotational and hyperfine energy levels and coupling strengths of ^{23}Na^{40}K in the electronic and vibrational ground state by diagonalizing the Hamiltonian [289]

$$H = H_{\mathrm{r}} + H_{\mathrm{hf}} + H_{\mathrm{S}} + H_{\mathrm{Z}}, \tag{A.1}$$

where

$$H_{\mathrm{r}} = B_v \vec{J}^2 - D_v \vec{J}^2 \vec{J}^2, \tag{A.2}$$

$$H_{\mathrm{hf}} = \sum_{i=\mathrm{Na,K}} \vec{V}_i \cdot \vec{Q}_i + \sum_{i=\mathrm{Na,K}} c_i \vec{J} \cdot \vec{I}_i \tag{A.3}$$

$$+ c_3 \vec{I}_{\mathrm{Na}} \cdot \vec{T} \cdot \vec{I}_{\mathrm{K}} + c_4 \vec{I}_{\mathrm{Na}} \cdot \vec{I}_{\mathrm{K}}, \tag{A.4}$$

$$H_{\mathrm{S}} = - \vec{d} \cdot \vec{E}, \tag{A.5}$$

$$H_{\mathrm{Z}} = - g_r \mu_{\mathrm{J}} \vec{J} \cdot \vec{B} - \sum_{i=\mathrm{Na,K}} g_i \left(1 - \sigma_i\right) \mu_{\mathrm{J}} \vec{I}_i \cdot \vec{B}. \tag{A.6}$$

The Hamiltonian consists of four parts. Firstly, the rotational Hamiltonian H_{r} is related to the angular momentum $\vec{J}$ for rotation of the molecule about its center of mass. The rotational constants and centrifugal distortion are denoted as B_v and D_v, respectively.

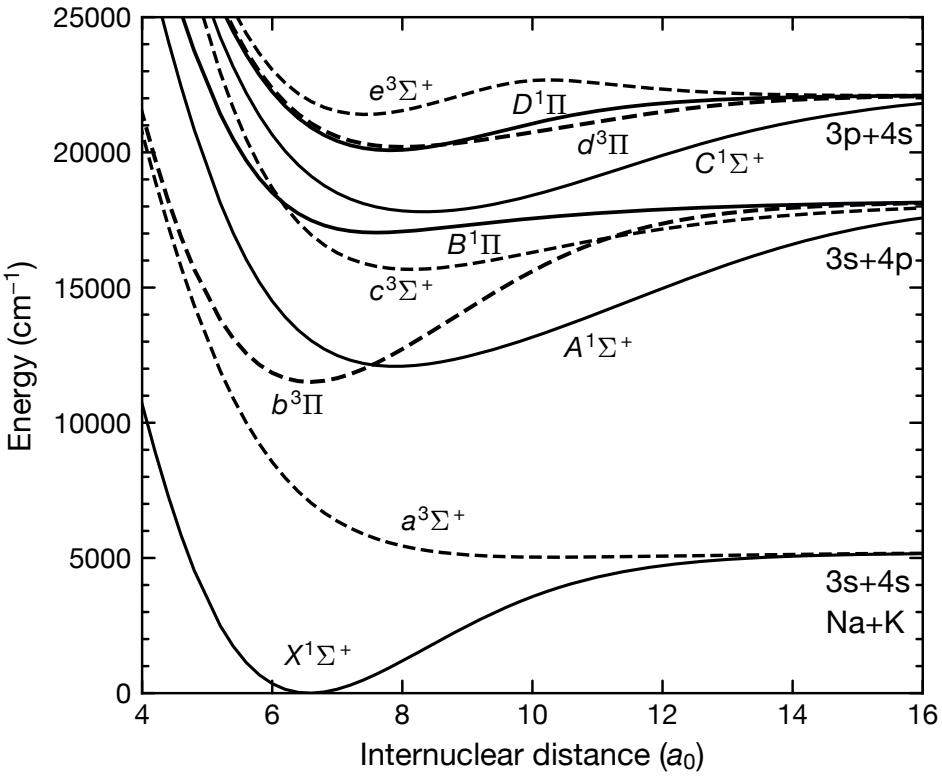

Figure A.1: Molecular potential curves for NaK. The potentials are calculated based on Ref. [288]. Internuclear distances are given in units of the Bohr radius a_0. Solid lines correspond to singlet states, dashed lines to triplets.

The second contribution is the hyperfine Hamiltonian H_{hf}, which is related to the nuclear spins I_i. It is comprised of four parts. The first term represents the electric quadrupole interaction, given by the coupling constants $(eqQ)_{\mathrm{Na}}$ and $(eqQ)_{\mathrm{K}}$. Following that, the second component describes the interaction between the nuclear magnetic moments and the magnetic field, which is generated by the molecule's rotation. The coupling constants c_{Na} and c_{K} are linked with this spin-rotation interaction. The third and fourth terms describe the tensor and scalar interactions between the nuclear magnetic moments, characterized by the tensor and scalar spin-spin coupling constants c_3 and c_4 respectively.

The next term H_{S} describes the Stark shift in a d.c. electric field, where $\vec{d} = d_0\hat{d}$ is the body-fixed dipole moment pointing along the internuclear axis $\hat{d}$. The electric field couples different rotational states with the same m_J, and induces a dipole moment in the lab frame, as shown in Fig. 4.1a and c.

The last term is the Zeeman Hamiltonian H_Z, which is related to the projection of the angular momentums along the magnetic field. This contribution includes two terms representing the interaction of rotational and nuclear components with an externally imposed magnetic field. The molecular rotation induces a magnetic moment proportional to the molecule's rotational g-factor (g_r). In a similar manner, the nuclear interaction is proportional to the nuclear g-factors ($g_{\mathrm{Na}}, g_{\mathrm{K}}$) and the nuclear shielding constants ($\sigma_{\mathrm{Na}}, \sigma_{\mathrm{K}}$) for each species.

We adapt the python script maintained by the Durham group [158] for diagonalizing this Hamiltonian.

A.2 The STIRAP scheme

To accurately model the STIRAP process, it is required to obtain the wave functions corresponding to the relevant molecular states, as well as their coupling matrix elements. Additionally, the natural linewidth of the excited state needs to be considered.

A.2.1 Feshbach state

We use a Feshbach resonance at 78.3 G between Na $|F = 1, m_F = 1\rangle$ and K $|9/2, -9/2\rangle$ for creating Feshbach molecules. The coupling from the Feshbach state $|FB\rangle$ to the excited state $|E\rangle$ is mostly contributed by the close channel component of the Feshbach state, whose fraction Z increased with the binding energy of the Feshbach molecule E_{b}. The closed-channel fraction is approximately given by the ratio of magnetic moment between the Feshbach state and the bare molecular state

$$Z \approx \frac{1}{\mu_{\mathrm{c}}} \frac{\partial E_{\mathrm{b}}}{\partial B},$$

Table A.1: Values of the coupling constants relevant to the NaK hyperfine Hamiltonian.

Constant	Value	Source
i_{Na}	3/2	
i_{K}	4	
d_0	2.72(6) D	[150]
$B_{v=0}$	$h \times 2.8217297(10)$ GHz	[290]
$D_{v=0}$	ignored	
$(eQq)_{\mathrm{Na}}$	$-h \times 0.187(35)$ MHz	[290]
$(eQq)_{\mathrm{K}}$	$h \times 0.899(20)$ MHz	[290]
c_{Na}	$h \times 117.4$ Hz	[289]
c_{K}	$-h \times 97.0$ Hz	[289]
c_3	$-h \times 48.4$ Hz	[289]
c_4	$-h \times 409(10)$ Hz	[290]
g_r	0.0253	[289]
$g_{\mathrm{Na}}(1-\sigma_{\mathrm{Na}})$	1.477	[289]
$g_{\mathrm{K}}(1-\sigma_{\mathrm{K}})$	−0.3236	[289]

where μ_{c} is the magnetic moment of the bare molecular state. We typically perform STIRAP at a magnetic field of 72.4 G, where the absolute magnetic moment of the Feshbach state vanishes $\mu_{\mathrm{o}} - \frac{\partial E_{\mathrm{b}}}{\partial B} = 0$, thus $|FB\rangle$ is insensitive to the magnetic field fluctuations, which is beneficial for the STIRAP stability. At that field, the close channel fraction is more than 80%.

The closed-channel wave function is dominated by the highest bound state in the triplet potential $a^3\Sigma$, with good quantum numbers $N = 0$, $S = 1$, and $J = 1$, where N is the total angular momentum excluding the electron spin. Its wave function can be written in the spin decoupled basis

$$|FB\rangle \propto \sum_{M_J m_{i_{\mathrm{Na}}} m_{i_{\mathrm{K}}}} c^f_{NSJM_J m_{i_{\mathrm{Na}}} m_{i_{\mathrm{K}}}} |NSJ, M_J m_{i_{\mathrm{Na}}} m_{i_{\mathrm{K}}}\rangle. \tag{S7}$$

The coefficients in the uncoupled basis are given by Table A.2, obtained from coupled-channel calculations provided by Eberhard Tiemann.

A.2.2 Intermediate excited state

The intermediate excited state $|E\rangle$ used for the new STIRAP scheme contains strong components of $|c^3\Sigma^+, v = 35, J = 1\rangle$ and $|B^1\Pi, v = 12, J = 1\rangle$, with 64% triplet and 36%

Table A.2: The closed-channel wave function of the Feshbach state.

M_J	$m_{i_{\mathrm{Na}}}$	$m_{i_{\mathrm{K}}}$	$c^f_{NSJ,M_J,m_{i_{\mathrm{Na}}},m_{i_{\mathrm{K}}}}$
-1	-3/2	-1	0.0614
-1	-1/2	-2	-0.236
-1	1/2	-3	0.365
-1	3/2	-4	-0.132
0	-3/2	-2	0.0663
0	-1/2	-3	0.160
0	1/2	-4	-0.585
1	-3/2	-3	-0.362
1	-1/2	-4	0.534

singlet fraction. The contribution of different hyperfine states is given in Table A.3. This state was characterized in Ref. [291].

A.2.3 Coupling strength

The total coupling strengths and the excited state line width are obtained experimentally from two-photon spectroscopy [124]. At 72.4 G, corresponding to a closed-channel fraction of 0.84, we found $\bar{\Omega}_{\mathrm{p}} = 2\pi\times 6.3(4)\,\mathrm{kHz}/\sqrt{\mathrm{mW/cm^2}}$ and $\bar{\Omega}_{\mathrm{S}} = 2\pi\times 142(8)\,\mathrm{kHz}/\sqrt{\mathrm{mW/cm^2}}$. The measured excited-state line width is $\gamma = 2\pi\times 11(1)\,\mathrm{MHz}$.

The relative contribution from each hyperfine states can be calculated from [292]

$$\begin{aligned}\Omega_{\mathrm{S}} &\propto \langle\psi_{B^1\Pi}|d_0|G\rangle \\ &\propto c^e_{J'\Omega' M_J m_{i_{\mathrm{Na}}} m_{i_{\mathrm{K}}}}(-1)^{J'-M_J}\begin{pmatrix} J' & 1 & J \\ M_J & q_{\mathrm{S}} & -M_J\end{pmatrix},\end{aligned} \tag{A.8}$$

and

$$\begin{aligned}\Omega_{\mathrm{p}} &\propto \langle\psi_{c^3\Sigma}|d_0|FB\rangle \\ &\propto \sum_{M_J m_{i_{\mathrm{Na}}} m_{i_{\mathrm{K}}}} c^e_{N'S'J'M_J m_{i_{\mathrm{Na}}} m_{i_{\mathrm{K}}}} c^f_{NSJM_J m_{i_{\mathrm{Na}}} m_{i_{\mathrm{K}}}}(-1)^{J'-M_J}\begin{pmatrix} J' & 1 & J \\ M_J & q_{\mathrm{p}} & -M_J\end{pmatrix},\end{aligned} \tag{A.9}$$

where q denotes the polarization, with $q_{\mathrm{p}} = 1$ denotes σ^+ for the pump beam, and $q_{\mathrm{S}} = -1$ denotes the σ^- for the Stokes beam.

Table A.3: Quantum numbers of the STIRAP intermediate state, $|E\rangle$. Only the eight strongest contributions, which together make up 99.2% of the weight, are shown [124].

Manifold	m_J	$m_{i_{\mathrm{Na}}}$	$m_{i_{\mathrm{K}}}$	amplitude
$B^1\Pi$	0	1/2	−3	0.120
	0	3/2	−4	−0.275
	1	−1/2	−3	0.0988
	1	1/2	−4	−0.508
$c^3\Sigma^+$	0	1/2	−3	−0.160
	0	3/2	−4	0.365
	1	−1/2	−3	−0.132
	1	1/2	−4	0.677

A.3 Polarizabilities

A.3.1 Off-resonant transitions

The background polarizabilities (as defined in Eq. (2.6)) at the experiment relavent wavelengths are given in Table A.4.

Table A.4: Background polarizabilities at different wavelengths.

Wave length (nm)	$\alpha_\parallel$ (Hz/(W/cm^2))	$\alpha_\perp$ (Hz/(W/cm^2))	Source
1550	34	12	[132]
1064	47.5	16.9	[293]
866	105(3)	20(1)	[128]

A.3.2 866 nm near-resonant transitions

The polarizability contributed from the $|X^1\Sigma^+, v=0, J\rangle \leftrightarrow |b^3\Pi_0, v'=0, J'\rangle$ transition is given by [128]

$$\alpha_{J=0} = -\frac{3\pi c^2}{2\omega_0^3}\frac{\Gamma}{\Delta}, \tag{A.10}$$

$$\alpha_{J=1,M_J=0} = -\frac{3\pi c^2}{2\omega_0^3}\left(\frac{\Gamma\cos^2\theta}{\Delta+2(B+B')/\hbar}+\frac{1}{5}\frac{\Gamma(\cos^2\theta+3)}{\Delta-2(2B'-B)/\hbar}\right), \tag{A.11}$$

for linearly polarized light, in the case where $\Delta=\omega-\omega_0$ is much larger than the hyperfine structure of the resonance. Here, θ is the angle between the light polarization and the quantization axis. The relevant constants are given in Table A.5.

The photon scattering rate of molecules in $|0\rangle$ near the $X \leftrightarrow b$ transition is given by

$$\gamma_{\mathrm{sc}} = \frac{3\pi c^2}{2\hbar\omega_0^3}\frac{\Gamma\Gamma_e}{\Delta^2} I, \tag{A.12}$$

where I is the light intensity and Γ_e is the natural linewidth of the excited state.

Table A.5: Summary of the molecular response at the $X \leftrightarrow b$ transition [128].

Quantity	Value
ω_0	$2\pi \times 346.123\,58(7)$ THz
Γ	$2\pi \times 301(10)$ Hz
Γ_e	$2\pi \times 13.0(5)$ kHz
B'	$h \times 2.79(2)$ GHz

A.3.3 785 nm near-resonant transitions

We characterize the 785 nm transition which we use for density matching the Na BEC and the K Fermi gas, and to compress molecules during evaporation and shallow-angle lattice loading.

$$\alpha = -\frac{3\pi_1 c^2}{2\omega_1^3}\frac{\Gamma_1}{\omega-\omega_1} - \frac{3\pi_2 c^2}{2\omega_2^3}\frac{\Gamma_2}{\omega-\omega_2} + \alpha_{0,785}, \tag{A.13}$$

$$\gamma_{\mathrm{sc}}/I = \frac{3\pi c^2}{2\hbar\omega_1^3}\frac{\Gamma_1\Gamma_{e1}}{(\omega-\omega_1)^2} + \frac{3\pi c^2}{2\hbar\omega_1^3}\frac{\Gamma_2\Gamma_{e2}}{(\omega-\omega_2)^2} + \beta_{0,785}, \tag{A.14}$$

Table A.6: Summary of the molecular response near 785 nm.

Quantity	Value
ω_1	$2\pi \times 379.785\,72(8)$ THz
ω_2	$2\pi \times 382.111\,59(8)$ THz
Γ_1	$2\pi \times 109(17)$ kHz
Γ_{e1}	$2\pi \times 34(5)$ MHz
Γ_2	$2\pi \times 123(18)$ kHz
Γ_{e2}	$2\pi \times 20(3)$ MHz
$\alpha_{0,785}$	$2\pi \times 255(21)$ kHz
$\beta_{0,785}$	$2\pi \times\ 5(1)\,\mathrm{mHz}/(\mathrm{W/cm^2})$

Appendix B

Elastic scattering between two rotating dipoles

Here I generalize the derivation in Ref. [75, 294] to polar molecules dressed with microwave with ellipticity ξ. The scattering amplitude under the Born approximation is the sum of the contribution form each term of the interaction potential, which reads

$$f_{\mathrm{Born}}(\boldsymbol{k}', \boldsymbol{k}) = \frac{2}{3}\left[(1-\sin 2\xi)(3\cos^2\theta_q - 1) - 2\sin 2\xi(3\cos^2\theta_q' - 1)\right], \tag{B.1}$$

where $\theta_q(\theta_q')$ is the angle between the momentum transfer $\boldsymbol{q} = \boldsymbol{k} - \boldsymbol{k}'$ and the $z(y)$-axis. Following that, the averaged total cross section for indistinguishable fermions is given by

$$\sigma_{\mathrm{Born}} = \frac{16\pi}{15}(1 + 3\sin^2 2\xi)a_{\mathrm{dd}}^2. \tag{B.2}$$

The eikonal cross section is generalized by noting that the interaction potential is no longer cylindrical symmetric, thus its orientation has to be parametrized by the three Euler angle (α, β, γ) instead of only (α, β). The angle (α, β) describes the propagation direction of the microwave $\hat{\epsilon}_\parallel$, and the angle γ described the orientation of the polarization ellipse $\hat{\epsilon}_\perp$. The eikonal phase is then given by

$$\begin{aligned}\chi &= -\frac{2}{kb^2}\left(-(1-\sin 2\xi)[1 - (\hat{k}_{\mathrm{avg}}\cdot\hat{\epsilon}_\parallel)^2 - 2(\hat{b}\cdot\hat{\epsilon}_\parallel)^2] + 2\sin 2\xi[1 - (\hat{k}_{\mathrm{avg}}\cdot\hat{\epsilon}_\perp)^2 - 2(\hat{b}\cdot\hat{\epsilon}_\perp)^2]\right) \\ &= \frac{2}{kb^2}(A(\alpha,\gamma)\cos(2\phi - 2\beta) + B(\alpha,\gamma)\sin(2\phi - 2\beta)),\end{aligned} \tag{B.3}$$

where b is the impact parameter, $\hat{k}_{\mathrm{avg}}$ is the unit vector along the average collision momentum between incident and scattered wave. Following that, the total cross section for incident wavevector $\hat{k}_i$ is given by

$$\sigma_{\mathrm{Ei}}(\hat{k}_i) = \frac{4\pi a_{\mathrm{dd}}}{k}\sqrt{A_\xi(\alpha,\gamma)^2 + B_\xi(\alpha,\gamma)^2}, \tag{B.4}$$

with

$$A_\xi(\alpha,\gamma) = \frac{1}{2}\left((\cos 2\alpha + 3)\cos 2\gamma \sin 2\xi - 2\sin^2\alpha\right), \tag{B.5}$$

$$B_\xi(\alpha,\gamma) = 2\cos\alpha \sin 2\gamma \sin 2\xi. \tag{B.6}$$

Averaging over the Euler angles we obtain the averaged total cross section

$$\sigma_{\mathrm{Ei}} = \frac{1}{2\pi}\int_0^{2\pi} \mathrm{d}\gamma \int \mathrm{d}\hat{k}_i \sigma_{\mathrm{Ei}}(\hat{k}_i) \tag{B.7}$$

$$= \frac{8\pi a_{\mathrm{dd}}}{3k}\frac{3}{(4\pi)^2}\int_0^{\pi}\sin\alpha \mathrm{d}\alpha \int_0^{2\pi}\mathrm{d}\beta \int_0^{2\pi}\mathrm{d}\gamma \sqrt{A_\xi(\alpha,\gamma)^2 + B_\xi(\alpha,\gamma)^2}$$

$$\equiv \frac{8\pi a_{\mathrm{dd}}}{3k} I(\xi). \tag{B.8}$$

Appendix C

Determination of the microwave ellipticity

In this Appendix, I will show that the ellipticity ξ can be uniquely determined from the electric field components, given the tilting angle of the microwave ellipse. This is experimentally relevant as the tilt angle of the projected microwave ellipse can be obtained from the dissociation pattern of the tetramers as shown in Fig. 7.11.

We define the xyz coordinates in the lab frame, where z is the vertical direction, and y is direction of the horizontal imaging. After a rotation along the z axis for an angle β we define $x'y'z'$ coordinates, where x' orients along the long axis of the microwave ellipse in the $x'y'$ plane. In this frame, we parametrize the microwave ellipse by

$$x'(t) = a' \cos t, \tag{C.1}$$
$$y'(t) = b' \sin t, \tag{C.2}$$
$$z'(t) = c' \cos(t + t_0), \tag{C.3}$$

where a', b', and c' are the field strengths, which related to the field strength in the $\sigma^{\pm}$ and π basis by a coordinate transform

$$a' = (E_+ + E_-)/\sqrt{2}, \tag{C.4}$$
$$b' = (E_+ - E_-)/\sqrt{2}, \tag{C.5}$$
$$c' = E_\pi. \tag{C.6}$$

The projection of the microwave ellipse in the xz plane is given by

$$x(t) = x' \cos\beta - y' \sin\beta = a' \cos\beta \cos t - b' \sin\beta \sin t, \tag{C.7}$$
$$z(t) = z' = c' \cos(t + t_0). \tag{C.8}$$

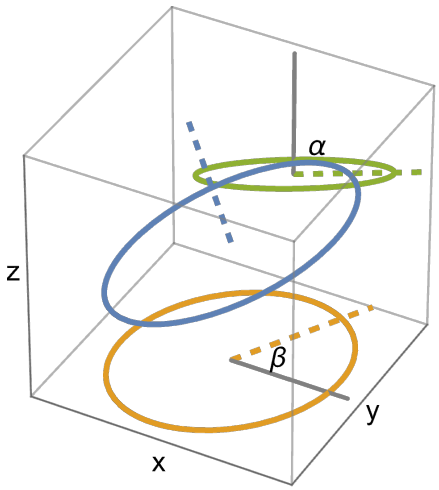

Figure C.1: Microwave ellipse. The ellipse of the a.c. electric field (blue) and its projection to the xy (orange) and yz (green) planes. The blue dashed line marks the direction of propagation. The orange and green dashed lines mark the direction of the long axis of the projected ellipse.

Now we make use of the angle α, which is the tilt of the projection of the ellipse in the xz plane, for an alternative parametrization

$$x(t) = a\sin\alpha\cos(t+t_1) - c\cos\alpha\sin(t+t_1), \tag{C.9}$$
$$z(t) = a\cos\alpha\cos(t+t_1) + c\sin\alpha\sin(t+t_1). \tag{C.10}$$

Comparing the two parametrization we obtain the following relation

$$a'\cos\beta = a\cos t_1\sin\alpha - c\sin t_1\cos\alpha, \tag{C.11}$$
$$b'\sin\beta = a\sin t_1\sin\alpha + c\cos t_1\cos\alpha, \tag{C.12}$$
$$c'\cos t_0 = a\cos t_1\cos\alpha + c\sin t_1\sin\alpha, \tag{C.13}$$
$$c'\sin t_0 = a\sin t_1\cos\alpha - c\cos t_1\sin\alpha. \tag{C.14}$$

Eq. (C.11)-(C.14) determine the offset phase t_0, thus determines the polarization.

To obtain the ellipticity we first calculate the long and short axis of the ellipse

$$a = \max(r(t)), \tag{C.15}$$
$$b = \min(r(t)), \tag{C.16}$$
$$r(t) = \sqrt{x^2+y^2+z^2}. \tag{C.17}$$

The ellipticity can then be calculated as

$$\tan\xi = \frac{a-b}{a+b}. \tag{C.18}$$

After simplification we obtain

$$\xi = \frac{1}{2}\arcsin\left(\frac{\sqrt{(a^2-b^2+c^2\cos(2t_0))^2+(c^2\sin(2t_0))^2}}{a^2+b^2+c^2}\right). \tag{C.19}$$

Without the angular information α and β, the unknown phase t_0 leads to a systematic uncertainty of the ellipticity between

$$\xi|_{t_0=0} = \frac{1}{2}\arcsin\left(\frac{2E_+E_- + E_\pi^2}{E_+^2 + E_-^2 + E_\pi^2}\right), \tag{C.20}$$

and

$$\xi|_{t_0=\pi} = \frac{1}{2}\arcsin\left(\frac{2E_+E_- - E_\pi^2}{E_+^2 + E_-^2 + E_\pi^2}\right). \tag{C.21}$$

Appendix D

Partial wave expansion of the effective potential

In the derivation of the WKB phase Eq. (6.4) and the effective potentials in Chapter 8, we use the following partial wave expansion of the effective potential [116]

$$
\begin{aligned}
V_{\mathrm{eff},lml'm'}(\mathbf{r}) = & \frac{2C_3}{r^3}\sqrt{\frac{2l'+1}{2l+1}}C^{l0}_{l'020}[C^{lm}_{l'm'20} + \sqrt{\frac{3}{2}}\sin 2\xi(C^{lm}_{l'm'22} + C^{lm}_{l'm'2-2})] \\
& + \frac{2C_6}{r^6}\sqrt{\frac{2l'+1}{2l+1}}\{[\frac{2}{5}(1-\frac{1}{3}\sin^2 2\xi)\delta_{ll'}\delta_{mm'} \\
& - \frac{1}{7}C^{l0}_{l'020}[2(1-\frac{2}{3}\sin^2 2\xi)C^{lm}_{l'm'20} + \sqrt{\frac{2}{3}}\sin 2\xi(C^{lm}_{l'm'22} + C^{lm}_{l'm'2-2})] \\
& - \sqrt{\frac{2}{35}}C^{l0}_{l'040}[\sqrt{\frac{2}{35}}(2+\sin^2 2\xi)C^{lm}_{l'm'40} \\
& + \frac{2}{\sqrt{7}}\sin 2\xi(C^{lm}_{l'm'42} + C^{lm}_{l'm'4-2}) + \sin^2 2\xi(C^{lm}_{l'm'44} + C^{lm}_{l'm'4-4})]\}. \qquad \text{(D.1)}
\end{aligned}
$$

For $l = 1$, $m_l = \pm 1$, we have

$$
v_{1111} = -\frac{2}{5}\frac{C_3}{r^3} + \frac{4}{35}\frac{C_6}{r^6}(8 - 3\sin^2 2\xi), \qquad \text{(D.2)}
$$

$$
v_{111-1} = -\frac{6}{5}\frac{C_3}{r^3}\sin 2\xi + \frac{4}{35}\frac{C_6}{r^6}\sin 2\xi. \qquad \text{(D.3)}
$$

For the Y_+ channel, we have

$$
\begin{aligned}
v_{1+} &= v_{1111} + v_{111-1}, \qquad \text{(D.4)} \\
&= -\frac{2}{5}\frac{C_3}{r^3}(1 + 3\sin 2\xi) + \frac{4}{35}\frac{C_6}{r^6}(8 + \sin 2\xi - 3\sin^2 2\xi). \qquad \text{(D.5)}
\end{aligned}
$$

Appendix E

Quantum gas gallery

A unique opportunity of working with ultracold bialkali fermionic molecules is the simultaneous access to thermal gases, BEC, and degenerate Fermi gases. These quantum gases are subjected to external electromagnetic fields, and various optical potentials including dipole traps, optical lattices, and patterns generated by a digital-micromirror-device (DMD) [295]. The interplay of the quantum gases and external forces give rise to complex dynamics, which we probed by absorption imaging. During the course of this thesis, we are constantly amazed by the fascinating images of our atoms and molecules, many of them are created by accident. We have already seen images such as the growth of the KD scattering pattern (Fig. 2.9) and the moon-shape dissociation pattern of tetramers (cover). Here I collect more of those images and briefly explain how they were created, without going into details about the underlying physics.

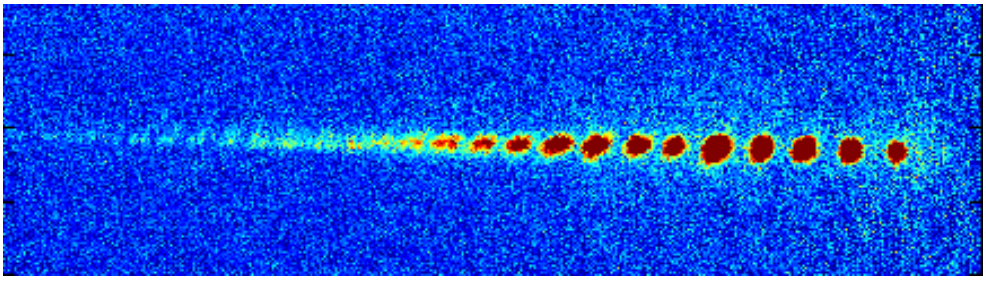

Figure E.1: "Atom laser".[1]This image shows a sodium BEC (unintentionally) leaking out of the shallow-angle lattice due to gravity (from left to right). The periodic patterns arise from matter wave interference between different layers [296]. Created on 2021.02.01.

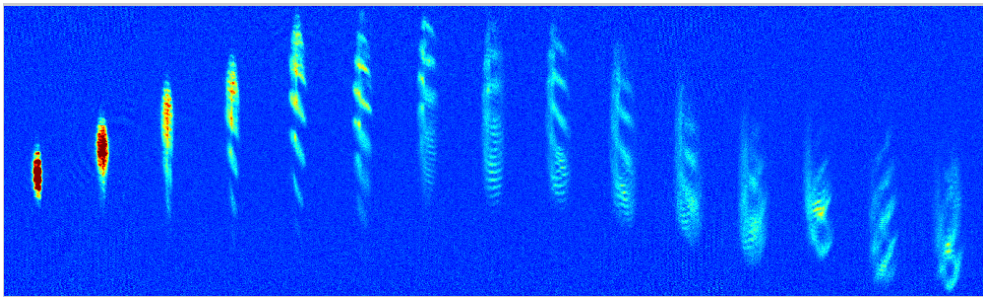

Figure E.2: "Double-helix". This series of images show the imperfect matter-wave refocusing of a BEC in the shallow-angle lattice. Different images correspond to different width of the refocusing pulse, which increases from left to right. The pattern arises due to the motion of the BEC during the refocusing. Created on 2021.11.17.

[1]For an atom laser, the gain medium is a thermal atomic ensemble, while the coherent wave is derived from a BEC. Atoms can be out-coupled from the confining trap through quantum tunneling of the potential barrier [297]. An optical lattice serves as one such out-coupling potential [296]. Alternative out-coupling schemes include radio-frequency [298–300] and two-photon transfers [301]. Interestingly, my supervisor, Immanuel, was among the pioneering researchers of atom lasers. Following our discussion, he remarked, "Yes, my PhD work!" in our laboratory chat room.

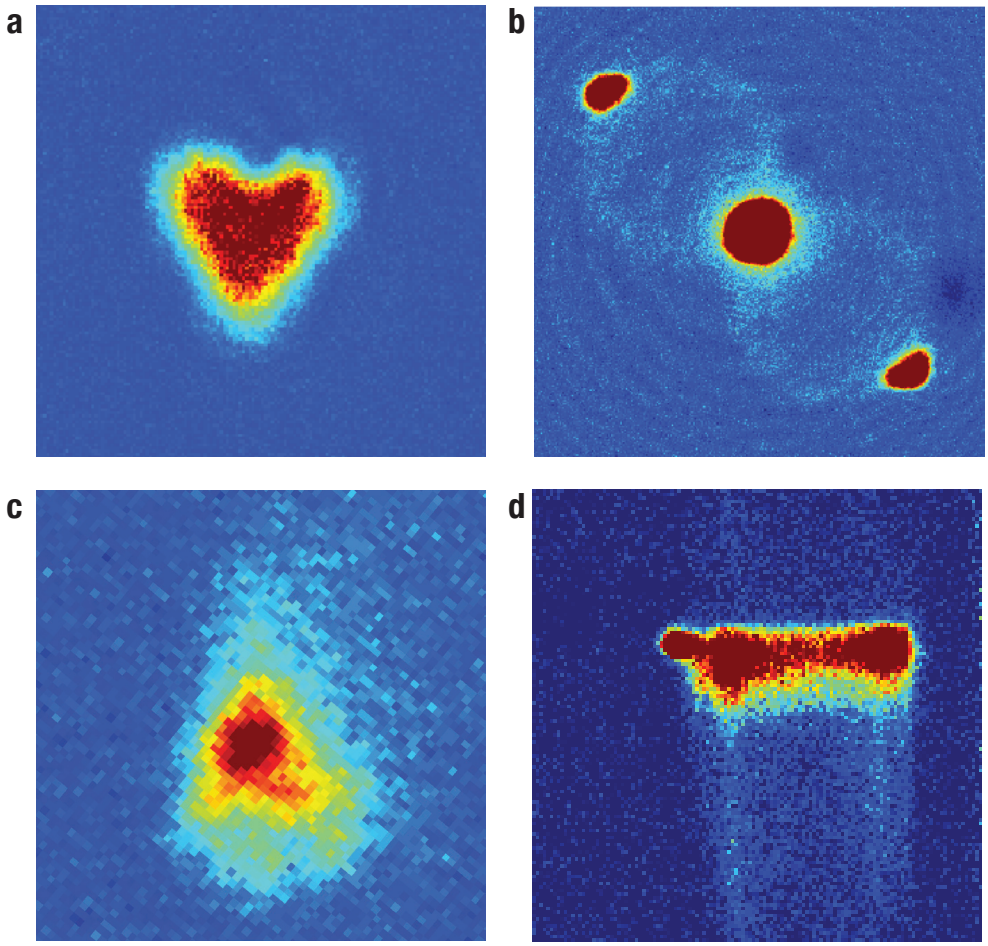

Figure E.3: a, **"Beating heart"**. Potassium atoms situated in a crossed dipole trap were subjected to a potent magnetic field gradient pulse. Although the aim was to initiate an oscillation and quantify the trapping frequency, the force applied was excessively strong, causing the atomic cloud to be overly perturbed. As a result, the "heart" of the cloud bet up and down with the oscillation in the trap. Created on 2019.03.02. **b**, **"Hourglass nebula"**. Kapitza–Dirac scattering of a BEC by a 1D horizontal lattice. The scattering pattern resembles the differential cross section of the atom–atom collisions. Created on 2021.10.19. **c**, **"Christmas tree"**. After implementing the DMD, we imprinted a isosceles triangle, onto a sodium BEC. The pattern is supposed to represent a Christmas tree, as a present for the group. Created on 2021.12.21. **d**, **"Parachute"**. Loading from crossed-dipole trap into a light sheet. The light sheet was misaligned, causing the atoms to spread into its flat potential. Created on 2023.04.22.

Bibliography

[1] Krems, R., Friedrich, B. & Stwalley, W. C. *Cold molecules: theory, experiment, applications* (CRC press, 2009).

[2] Carr, L. D., DeMille, D., Krems, R. V. & Ye, J. Cold and ultracold molecules: science, technology and. *New J. Phys.* **11**, 055049 (2009).

[3] Bohn, J. L., Rey, A. M. & Ye, J. Cold molecules: Progress in quantum engineering of chemistry and quantum matter. *Science* **357**, 1002–1010 (2017).

[4] Langen, T., Valtolina, G., Wang, D. & Ye, J. Quantum state manipulation and science of ultracold molecules (2023).

[5] Micheli, A., Brennen, G. K. & Zoller, P. A toolbox for lattice-spin models with polar molecules. *Nat. Phys.* **2**, 341–347 (2006).

[6] Baranov, M. A., Dalmonte, M., Pupillo, G. & Zoller, P. Condensed matter theory of dipolar quantum gases. *Chem. Rev.* **112**, 5012–5061 (2012).

[7] DeMille, D. Quantum Computation with Trapped Polar Molecules. *Phys. Rev. Lett.* **88**, 067901 (2002).

[8] Ni, K.-K., Rosenband, T. & Grimes, D. D. Dipolar exchange quantum logic gate with polar molecules. *Chem. Sci.* **9**, 6830–6838 (2018).

[9] Blackmore, J. A. *et al.* Ultracold molecules for quantum simulation: rotational coherences in CaF and RbCs. *Quantum Sci. Technol.* **4**, 014010 (2018).

[10] Krems, R. V. Cold controlled chemistry. *Phys. Chem. Chem. Phys.* **10**, 4079–4092 (2008).

[11] Balakrishnan, N. Perspective: Ultracold molecules and the dawn of cold controlled chemistry. *J. Chem. Phys.* **145**, 150901 (2016).

[12] The ACME Collaboration *et al.* Order of Magnitude Smaller Limit on the Electric Dipole Moment of the Electron. *Science* **343**, 269–272 (2014).

[13] Doyle, J. M., Augenbraun, B. L. & Lasner, Z. D. Ultracold Polyatomic Molecules for Quantum Science and Precision Measurements. *JPS Conf. Proc.* **37**, 011004 (2022).

[14] Friedrich, B. & Doyle, J. M. Why are Cold Molecules so Hot? *ChemPhysChem* **10**, 604–623 (2009).

[15] Hutzler, N. R., Lu, H.-I. & Doyle, J. M. The Buffer Gas Beam: An Intense, Cold, and Slow Source for Atoms and Molecules. *Chem. Rev.* **112**, 4803–4827 (2012).

[16] van de Meerakker, S. Y. T., Bethlem, H. L., Vanhaecke, N. & Meijer, G. Manipulation and Control of Molecular Beams. *Chem. Rev.* **112**, 4828–4878 (2012).

[17] Segev, Y. *et al.* Molecular beam brightening by shock-wave suppression. *Sci. Adv.* **3**, e1602258 (2017).

[18] Wu, X. *et al.* A cryofuge for cold-collision experiments with slow polar molecules. *Science* **358**, 645–648 (2017).

[19] Wynar, R., Freeland, R. S., Han, D. J., Ryu, C. & Heinzen, D. J. Molecules in a Bose-Einstein Condensate. *Science* **287**, 1016–1019 (2000).

[20] McKenzie, C. *et al.* Photoassociation of sodium in a bose-einstein condensate. *Phys. Rev. Lett.* **88**, 120403 (2002).

[21] Donley, E. A., Claussen, N. R., Thompson, S. T. & Wieman, C. E. Atom–molecule coherence in a Bose–Einstein condensate. *Nature* **417**, 529–533 (2002).

[22] Chin, C., Kerman, A. J., Vuletić, V. & Chu, S. Sensitive detection of cold cesium molecules formed on feshbach resonances. *Phys. Rev. Lett.* **90**, 033201 (2003).

[23] Regal, C. A., Ticknor, C., Bohn, J. L. & Jin, D. S. Creation of ultracold molecules from a fermi gas of atoms. *Nature* **424**, 47–50 (2003).

[24] Jochim, S. *et al.* Bose-Einstein Condensation of Molecules. *Science* **302**, 2101–2103 (2003).

[25] Greiner, M., Regal, C. A. & Jin, D. S. Emergence of a molecular Bose–Einstein condensate from a fermi gas. *Nature* **426**, 537–540 (2003).

[26] Zwierlein, M. W. *et al.* Observation of bose-einstein condensation of molecules. *Phys. Rev. Lett.* **91**, 250401 (2003).

[27] Zwierlein, M. W. *et al.* Condensation of pairs of fermionic atoms near a feshbach resonance. *Phys. Rev. Lett.* **92**, 120403 (2004).

[28] Zwerger, W. *The BCS-BEC Crossover and the Unitary Fermi Gas*. Springer (2012).

[29] Will, S. & Zelevinsky, T. Ultracold molecules find the sweet spot for collisions. *Nature* **614**, 35–36 (2023).

[30] Ni, K.-K. *et al.* A high phase-space-density gas of polar molecules. *Science* **322**, 231–235 (2008).

[31] Winkler, K. *et al.* Coherent optical transfer of feshbach molecules to a lower vibrational state. *Phys. Rev. Lett.* **98**, 043201 (2007).

[32] Takekoshi, T. *et al.* Ultracold Dense Samples of Dipolar RbCs Molecules in the Rovibrational and Hyperfine Ground State. *Phys. Rev. Lett.* **113**, 205301 (2014).

[33] Molony, P. K. *et al.* Creation of Ultracold ^{87}Rb^{133}Cs Molecules in the Rovibrational Ground State. *Phys. Rev. Lett.* **113**, 255301 (2014).

[34] Park, J. W., Will, S. A. & Zwierlein, M. W. Ultracold Dipolar Gas of Fermionic ^{23}Na^{40}K Molecules in Their Absolute Ground State. *Phys. Rev. Lett.* **114**, 205302 (2015).

[35] Seeßelberg, F. *et al.* Modeling the adiabatic creation of ultracold polar ^{23}Na^{40}K molecules. *Phys. Rev. A* **97**, 013405 (2018).

[36] Guo, M. *et al.* Creation of an Ultracold Gas of Ground-State Dipolar ^{23}Na^{87}Rb Molecules. *Phys. Rev. Lett.* **116**, 205303 (2016).

[37] Voges, K. K. *et al.* Ultracold Gas of Bosonic ^{23}Na^{39}K Ground-State Molecules. *Phys. Rev. Lett.* **125**, 083401 (2020).

[38] Rvachov, T. M. *et al.* Long-Lived Ultracold Molecules with Electric and Magnetic Dipole Moments. *Phys. Rev. Lett.* **119**, 143001 (2017).

[39] Cairncross, W. B. *et al.* Assembly of a Rovibrational Ground State Molecule in an Optical Tweezer. *Phys. Rev. Lett.* **126**, 123402 (2021).

[40] Stevenson, I. *et al.* Ultracold Gas of Dipolar NaCs Ground State Molecules. *Phys. Rev. Lett.* **130**, 113002 (2023).

[41] Yang, A. *et al.* Singlet Pathway to the Ground State of Ultracold Polar Molecules. *Phys. Rev. Lett.* **124**, 133203 (2020).

[42] He, C. *et al.* Efficient Creation of Ultracold Ground State ^{6}Li^{40}K Polar Molecules. *Preprint at https://arxiv.org/abs/2310.03300* (2023).

[43] Zhang, J. T. *et al.* An optical tweezer array of ground-state polar molecules. *Quantum Sci. Technol.* **7**, 035006 (2022).

[44] He, X. *et al.* Coherently forming a single molecule in an optical trap. *Science* **370**, 331–335 (2020).

[45] Ruttley, D. K. *et al.* Formation of Ultracold Molecules by Merging Optical Tweezers. *Phys. Rev. Lett.* **130**, 223401 (2023).

[46] Shuman, E. S., Barry, J. F. & DeMille, D. Laser cooling of a diatomic molecule. *Nature* **467**, 820–823 (2010).

[47] Tarbutt, M. R. Laser cooling of molecules. *Contemp. Phys.* **59**, 356–376 (2018).

[48] Augenbraun, B. L. *et al.* Direct Laser Cooling of Polyatomic Molecules. *Preprint at https://arxiv.org/abs/2302.10161* (2023).

[49] Barry, J. F., McCarron, D. J., Norrgard, E. B., Steinecker, M. H. & DeMille, D. Magneto-optical trapping of a diatomic molecule. *Nature* **512**, 286–289 (2014).

[50] Truppe, S. *et al.* Molecules cooled below the Doppler limit. *Nat. Phys.* **13**, 1173–1176 (2017).

[51] Anderegg, L. *et al.* Radio Frequency Magneto-Optical Trapping of CaF with High Density. *Phys. Rev. Lett.* **119**, 103201 (2017).

[52] Collopy, A. L. *et al.* 3D Magneto-Optical Trap of Yttrium Monoxide. *Phys. Rev. Lett.* **121**, 213201 (2018).

[53] Ding, S., Wu, Y., Finneran, I. A., Burau, J. J. & Ye, J. Sub-Doppler Cooling and Compressed Trapping of YO Molecules at μK Temperatures. *Phys. Rev. X* **10**, 021049 (2020).

[54] Vilas, N. B. *et al.* Magneto-optical trapping and sub-doppler cooling of a polyatomic molecule. *Nature* **606**, 70–74 (2022).

[55] Anderegg, L. *et al.* An optical tweezer array of ultracold molecules. *Science* **365**, 1156–1158 (2019).

[56] Holland, C. M., Lu, Y. & Cheuk, L. W. On-Demand Entanglement of Molecules in a Reconfigurable Optical Tweezer Array. *Preprint at https://arxiv.org/abs/2210.06309* (2022).

[57] Bao, Y. *et al.* Dipolar spin-exchange and entanglement between molecules in an optical tweezer array. *Preprint at https://arxiv.org/abs/2211.09780* (2022).

[58] Lu, Y., Li, S. J., Holland, C. M. & Cheuk, L. W. Raman Sideband Cooling of Molecules in an Optical Tweezer Array. *Preprint at https://arxiv.org/abs/2306.02455* (2023).

[59] Bao, Y. *et al.* Raman sideband cooling of molecules in an optical tweezer array to the 3-D motional ground state. *Preprint at https://arxiv.org/abs/2309.08706* (2023).

[60] Kozyryev, I., Baum, L., Matsuda, K. & Doyle, J. M. Proposal for Laser Cooling of Complex Polyatomic Molecules. *ChemPhysChem* **17**, 3641–3648 (2016).

[61] Zhu, G.-Z. *et al.* Functionalizing aromatic compounds with optical cycling centres. *Nat. Chem.* **14**, 995–999 (2022).

[62] Mitra, D. *et al.* Direct laser cooling of a symmetric top molecule. *Science* **369**, 1366–1369 (2020).

[63] Yang, H. *et al.* Creation of an ultracold gas of triatomic molecules from an atom–diatomic molecule mixture. *Science* **378**, 1009–1013 (2022).

[64] Duda, M. *et al.* Transition from a polaronic condensate to a degenerate Fermi gas of heteronuclear molecules. *Nat. Phys.* **19**, 720–725 (2023).

[65] De Marco, L. *et al.* A degenerate Fermi gas of polar molecules. *Science* **363**, 853–856 (2019).

[66] Zirbel, J. J. *et al.* Heteronuclear molecules in an optical dipole trap. *Phys. Rev. A* **78**, 013416 (2008).

[67] Cumby, T. D., Shewmon, R. A., Hu, M.-G., Perreault, J. D. & Jin, D. S. Feshbach-molecule formation in a Bose-Fermi mixture. *Phys. Rev. A* **87**, 012703 (2013).

[68] Chen, X.-Y. *et al.* Suppression of Unitary Three-Body Loss in a Degenerate Bose-Fermi Mixture. *Phys. Rev. Lett.* **128**, 153401 (2022).

[69] Duda, M. *et al.* Long-lived fermionic Feshbach molecules with tunable p-wave interactions. *Phys. Rev. A* **107**, 053322 (2023).

[70] Christianen, A., Zwierlein, M. W., Groenenboom, G. C. & Karman, T. Photoinduced Two-Body Loss of Ultracold Molecules. *Phys. Rev. Lett.* **123**, 123402 (2019).

[71] Bause, R. *et al.* Collisions of ultracold molecules in bright and dark optical dipole traps. *Phys. Rev. Res.* **3**, 033013 (2021).

[72] Ospelkaus, S. *et al.* Quantum-State Controlled Chemical Reactions of Ultracold Potassium-Rubidium Molecules. *Science* **327**, 853–857 (2010).

[73] Idziaszek, Z. & Julienne, P. S. Universal rate constants for reactive collisions of ultracold molecules. *Phys. Rev. Lett.* **104**, 113202 (2010).

[74] Quéméner, G. & Bohn, J. L. Strong dependence of ultracold chemical rates on electric dipole moments. *Phys. Rev. A* **81**, 022702 (2010).

[75] Bohn, J. L., Cavagnero, M. & Ticknor, C. Quasi-universal dipolar scattering in cold and ultracold gases. *New J. Phys.* **11**, 055039 (2009).

[76] Lassablière, L. & Quéméner, G. Controlling the Scattering Length of Ultracold Dipolar Molecules. *Phys. Rev. Lett.* **121**, 163402 (2018).

[77] Ni, K.-K. *et al.* Dipolar collisions of polar molecules in the quantum regime. *Nature* **464**, 1324–1328 (2010).

[78] Chotia, A. *et al.* Long-Lived Dipolar Molecules and Feshbach Molecules in a 3D Optical Lattice. *Phys. Rev. Lett.* **108**, 080405 (2012).

[79] Yan, B. *et al.* Observation of dipolar spin-exchange interactions with lattice-confined polar molecules. *Nature* **501**, 521–525 (2013).

[80] Christianen, A., Karman, T., Vargas-Hernández, R. A., Groenenboom, G. C. & Krems, R. V. Six-dimensional potential energy surface for NaK–NaK collisions: Gaussian process representation with correct asymptotic form. *J. Chem. Phys.* **150**, 064106 (2019).

[81] Bause, R., Christianen, A., Schindewolf, A., Bloch, I. & Luo, X.-Y. Ultracold Sticky Collisions: Theoretical and Experimental Status. *J. Phys. Chem. A* **127**, 729–741 (2023).

[82] Żuchowski, P. S. & Hutson, J. M. Reactions of ultracold alkali-metal dimers. *Phys. Rev. A* **81**, 060703 (2010).

[83] Ye, X., Guo, M., González-Martínez, M. L., Quéméner, G. & Wang, D. Collisions of ultracold ^{23}Na^{87}Rb molecules with controlled chemical reactivities. *Sci. Adv.* **4** (2018).

[84] Guo, M. *et al.* Dipolar Collisions of Ultracold Ground-State Bosonic Molecules. *Phys. Rev. X* **8**, 041044 (2018).

[85] Gregory, P. D. *et al.* Sticky collisions of ultracold RbCs molecules. *Nat. Commun.* **10**, 1–7 (2019).

[86] Park, J. J., Lu, Y.-K., Jamison, A. O., Tscherbul, T. V. & Ketterle, W. A Feshbach resonance in collisions between triplet ground-state molecules. *Nature* **614**, 54–58 (2023).

[87] Mayle, M., Ruzic, B. P. & Bohn, J. L. Statistical aspects of ultracold resonant scattering. *Phys. Rev. A* **85**, 062712 (2012).

[88] Mayle, M., Quéméner, G., Ruzic, B. P. & Bohn, J. L. Scattering of ultracold molecules in the highly resonant regime. *Phys. Rev. A* **87**, 012709 (2013).

[89] Christianen, A., Karman, T. & Groenenboom, G. C. Quasiclassical method for calculating the density of states of ultracold collision complexes. *Phys. Rev. A* **100**, 032708 (2019).

[90] Liu, Y. *et al.* Photo-excitation of long-lived transient intermediates in ultracold reactions. *Nat. Phys.* **16**, 1132–1136 (2020).

[91] Gregory, P. D., Blackmore, J. A., Bromley, S. L. & Cornish, S. L. Loss of Ultracold $^{87}Rb^{133}Cs$ Molecules via Optical Excitation of Long-Lived Two-Body Collision Complexes. *Phys. Rev. Lett.* **124**, 163402 (2020).

[92] Liu, L. R. *et al.* Ergodicity breaking in rapidly rotating C60 fullerenes. *Preprint at https://arxiv.org/abs/2305.05324* (2023).

[93] Gersema, P. *et al.* Probing Photoinduced Two-Body Loss of Ultracold Nonreactive Bosonic $^{23}Na^{87}Rb$ and $^{23}Na^{39}K$ Molecules. *Phys. Rev. Lett.* **127**, 163401 (2021).

[94] Stevenson, I. *et al.* Collisional Studies of Ultracold Ground-State NaCs Molecules. *Bulletin of the American Physical Society* (2023).

[95] Yang, H. *et al.* Observation of magnetically tunable Feshbach resonances in ultracold $^{23}Na^{40}K + {}^{40}K$ collisions. *Science* **363**, 261–264 (2019).

[96] Son, H. *et al.* Control of reactive collisions by quantum interference. *Science* **375**, 1006–1010 (2022).

[97] Shi, Z. *et al.* Chaotic scattering and microwave loss suppression in the narb system. *Bulletin of the American Physical Society* (2023).

[98] Son, H., Park, J. J., Ketterle, W. & Jamison, A. O. Collisional cooling of ultracold molecules. *Nature* **580**, 197–200 (2020).

[99] Valtolina, G. *et al.* Dipolar evaporation of reactive molecules to below the Fermi temperature. *Nature* **588**, 239–243 (2020).

[100] Micheli, A. *et al.* Universal Rates for Reactive Ultracold Polar Molecules in Reduced Dimensions. *Phys. Rev. Lett.* **105**, 073202 (2010).

[101] Quéméner, G. & Bohn, J. L. Dynamics of ultracold molecules in confined geometry and electric field. *Phys. Rev. A* **83**, 012705 (2011).

[102] Wang, G. & Quéméner, G. Tuning ultracold collisions of excited rotational dipolar molecules. *New J. Phys.* **17**, 035015 (2015).

[103] González-Martínez, M. L., Bohn, J. L. & Quéméner, G. Adimensional theory of shielding in ultracold collisions of dipolar rotors. *Phys. Rev. A* **96**, 032718 (2017).

[104] Matsuda, K. *et al.* Resonant collisional shielding of reactive molecules using electric fields. *Science* **370**, 1324–1327 (2020).

[105] Li, J.-R. *et al.* Tuning of dipolar interactions and evaporative cooling in a three-dimensional molecular quantum gas. *Nat. Phys.* **17**, 1144–1148 (2021).

[106] Anderegg, L. *et al.* Observation of microwave shielding of ultracold molecules. *Science* **373**, 779–782 (2021).

[107] Schindewolf, A. *et al.* Evaporation of microwave-shielded polar molecules to quantum degeneracy. *Nature* **607**, 677–681 (2022).

[108] Bigagli, N. *et al.* Collisionally Stable Gas of Bosonic Dipolar Ground State Molecules. *Preprint at https://arxiv.org/abs/2303.16845* (2023).

[109] Lin, J. *et al.* Microwave shielding of bosonic NaRb molecules. *Preprint at https://arxiv.org/abs/2304.08312* (2023).

[110] Microwaves direct the interplay of waltzing molecules. https://www.mpq.mpg.de/6809486/02-microwaves-direct-the-interplay-of-waltzing-molecules (2023).

[111] Avdeenkov, A. V. & Bohn, J. L. Linking ultracold polar molecules. *Phys. Rev. Lett.* **90**, 043006 (2003).

[112] Chen, X.-Y. *et al.* Field-linked resonances of polar molecules. *Nature* **614**, 59–63 (2023).

[113] Chen, X.-Y. *et al.* Ultracold field-linked tetratomic molecules. *Preprint at https://arxiv.org/abs/2306.00962* (2023).

[114] Hallas, C. *et al.* Optical trapping of a polyatomic molecule in an ℓ-type parity doublet state. *Phys. Rev. Lett.* **130**, 153202 (2023).

[115] Prehn, A. V. *An Ultracold Gas of Electrically Trapped Formaldehyde*. Ph.D. thesis, Technische Universität München (2018).

[116] Deng, F. *et al.* Effective potential and superfluidity of microwave-shielded polar molecules. *Phys. Rev. Lett.* **130**, 183001 (2023).

[117] Buchheim, N. *Dual-species apparatus for creating a dipolar quantum gas of $^{23}Na^{40}K$ molecules*. Ph.D. thesis, Ludwig-Maximilians-Universität München (2015).

[118] Lu, Z. *Towards many body physics with ultracold NaK molecules*. Ph.D. thesis, Ludwig-Maximilians-Universität München (2016).

[119] Seeßelberg, F. *Interacting gases of ultracold polar molecules*. Ph.D. thesis, Ludwig-Maximilians-Universität München (2019).

[120] Bause, R. *Understanding and controlling the collisions of ultracold polar molecules*. Ph.D. thesis, Ludwig-Maximilians-Universität München (2022).

[121] Duda, M. *Production of ground-state $^{23}Na^{40}K$ molecules in the quantum-degenerate regime*. Ph.D. thesis, Ludwig-Maximilians-Universität München (2022).

[122] Chen, X.-Y. *Gray molasses cooling of sodium atoms*. Master's thesis, Ludwig-Maximilians-Universität München (2019).

[123] Ketterle, W., Durfee, D. S. & Stamper-Kurn, D. Making, probing and understanding bose-einstein condensates. *Preprint at https://arxiv.org/abs/cond-mat/9904034* (1999).

[124] Bause, R. *et al.* Efficient conversion of closed-channel-dominated feshbach molecules of $^{23}Na^{40}K$ to their absolute ground state. *Phys. Rev. A* **104**, 043321 (2021).

[125] Eustice, S. *Ultracold NaK Molecules in a 3D Optical Lattice*. Master's thesis, Ludwig-Maximilians-Universität München (2018).

[126] Redon, Q. Building a filter cavity and a shallow angle lattice (2019).

[127] Tao, R. *Near-resonant Dipole Traps and Lattices for Ultracold Molecules*. Master's thesis, Ludwig-Maximilians-Universität München (2020).

[128] Bause, R. *et al.* Tune-out and magic wavelengths for ground-state $^{23}Na^{40}K$ molecules. *Phys. Rev. Lett.* **125**, 023201 (2020).

[129] Grimm, R., Weidemüller, M. & Ovchinnikov, Y. B. Optical dipole traps for neutral atoms. *Preprint at https://doi.org/10.48550/arXiv.physics/9902072.* (1999).

[130] Bonin, K. D. & Kresin, V. V. *Electric-dipole polarizabilities of atoms, molecules, and clusters* (World Scientific, 1997).

[131] Krems, R. V. *Molecules in Electromagnetic Fields* (2018).

[132] Seeßelberg, F. *et al.* Extending Rotational Coherence of Interacting Polar Molecules in a Spin-Decoupled Magic Trap. *Phys. Rev. Lett.* **121**, 253401 (2018).

[133] Neyenhuis, B. *et al.* Anisotropic Polarizability of Ultracold Polar $^{40}K^{87}Rb$ Molecules. *Phys. Rev. Lett.* **109**, 230403 (2012).

[134] Blackmore, J. A. *et al.* Controlling the ac Stark effect of RbCs with dc electric and magnetic fields. *Phys. Rev. A* **102**, 053316 (2020).

[135] Gregory, P. D., Blackmore, J. A., Bromley, S. L., Hutson, J. M. & Cornish, S. L. Robust storage qubits in ultracold polar molecules. *Nat. Phys.* **17**, 1149–1153 (2021).

[136] Lin, J., He, J., Ye, X. & Wang, D. Anisotropic polarizability of ultracold ground-state $^{23}Na^{87}Rb$ molecules. *Phys. Rev. A* **103**, 023332 (2021).

[137] Lin, J., He, J., Jin, M., Chen, G. & Wang, D. Seconds-Scale Coherence on Nuclear Spin Transitions of Ultracold Polar Molecules in 3D Optical Lattices. *Phys. Rev. Lett.* **128**, 223201 (2022).

[138] Burchesky, S. *et al.* Rotational Coherence Times of Polar Molecules in Optical Tweezers. *Phys. Rev. Lett.* **127**, 123202 (2021).

[139] Park, A. J. *et al.* Extended rotational coherence of polar molecules in an elliptically polarized trap. *Preprint at https://arxiv.org/abs/2306.07264* (2023).

[140] Kobayashi, J., Aikawa, K., Oasa, K. & Inouye, S. Prospects for narrow-line cooling of KRb molecules in the rovibrational ground state. *Phys. Rev. A* **89**, 021401 (2014).

[141] He, J. *et al.* Characterization of the lowest electronically excited-state ro-vibrational level of $^{23}Na^{87}Rb$. *New J. Phys.* **23**, 115003 (2021).

[142] Gregory, P. D. *et al.* Second-scale rotational coherence and dipolar interactions in a gas of ultracold polar molecules. *Preprint at https://arxiv.org/abs/2306.02991* (2023).

[143] Duchon, E., Loh, Y. L. & Trivedi, N. Optical Lattice Emulators: Bose and Fermi Hubbard Models. In *Noval Superfluids*, vol. 2 (Oxford University Press, 2013).

[144] Gadway, B., Pertot, D., Reimann, R., Cohen, M. G. & Schneble, D. Analysis of Kapitza-Dirac diffraction patterns beyond the Raman-Nath regime. *Opt. Express*

17, 19173–19180 (2009).

[145] Greiner, M., Mandel, O., Esslinger, T., Hänsch, T. W. & Bloch, I. Quantum phase transition from a superfluid to a Mott insulator in a gas of ultracold atoms. *Nature* **415**, 39–44 (2002).

[146] Bause, R. *A High-Resolution Absorption Imaging Setup for Ultracold Dipolar Molecules*. Master's thesis, Ludwig-Maximilians-Universität München (2016).

[147] Haller, E. *et al.* Single-atom imaging of fermions in a quantum-gas microscope. *Nat. Phys.* **11**, 738–742 (2015).

[148] Cheuk, L. W. *et al.* Quantum-Gas Microscope for Fermionic Atoms. *Phys. Rev. Lett.* **114**, 193001 (2015).

[149] Rosenberg, J. S., Christakis, L., Guardado-Sanchez, E., Yan, Z. Z. & Bakr, W. S. Observation of the Hanbury Brown–Twiss effect with ultracold molecules. *Nat. Phys.* **18**, 1062–1066 (2022).

[150] Gerdes, A., Dulieu, O., Knöckel, H. & Tiemann, E. Stark effect measurements on the NaK molecule. *Eur. Phys. J. D* **65**, 105–111 (2011).

[151] Gregorian, G.-O. *Dual-Feed Antenna for Microwave Dressing of Ultracold Polar Molecules*. Bachelor's thesis, Ludwig-Maximilians-Universität München (2023).

[152] Yuan, W. *et al.* A planar cloverleaf antenna for the creation of circularly polarized microwave fields. *arXiv* (2023).

[153] Braumandl, B. *Phased Array Microwave Antenna for Controlling Collisions of Molecules*. Bachelor's thesis, Ludwig-Maximilians-Universität München (2021).

[154] Djordfevic, A. R., Zajic, A. G., Ilic, M. M. & Stuber, G. L. Optimization of Helical antennas [Antenna Designer's Notebook]. *IEEE Antennas Propag. Mag.* **48**, 107–115 (2006).

[155] Molecules cooled in a microwave freezer. *Nature* https://doi.org/10.1038/d41586-022-01752-6 (2022).

[156] Enkhbayar, B., Bang, J., Cha, E. & Ahn, B. Formula for gain of open-ended rectangular waveguide. *Electronics letters* **45**, 1 (2009).

[157] Živković, Z., Senić, D., Šarolić, A. & Vučić, A. Design and testing of a diode-based electric field probe prototype. In *SoftCOM 2011, 19th International Conference on Software, Telecommunications and Computer Networks*, 1–5 (2011).

[158] Blackmore, J. A., Gregory, P. D., Hutson, J. M. & Cornish, S. L. Diatomic-py: A Python module for calculating the rotational and hyperfine structure of 1Σ molecules. *Comput. Phys. Commun.* **282**, 108512 (2023).

[159] Leighton, R. B., Sands, M. *et al. The Feynman lectures on physics* (Addison-Wesley Boston, MA, USA, 1965).

[160] Rubiola, E. *Phase noise and frequency stability in oscillators* (Cambridge University Press, 2008).

[161] Bechhoefer, J. Feedback for physicists: A tutorial essay on control. *Rev. Mod. Phys.* **77**, 783–836 (2005).

[162] Yan, Z. Z. *et al.* Resonant dipolar collisions of ultracold molecules induced by microwave dressing. *Phys. Rev. Lett.* **125**, 063401 (2020).

[163] He, J. *et al.* Observation of resonant dipolar collisions in ultracold $^{23}Na^{87}Rb$ rotational mixtures. *Phys. Rev. Res.* **3**, 013016 (2021).

[164] Karman, T. & Hutson, J. M. Microwave shielding of ultracold polar molecules. *Phys. Rev. Lett.* **121**, 163401 (2018).

[165] Karman, T. & Hutson, J. M. Microwave shielding of ultracold polar molecules with imperfectly circular polarization. *Phys. Rev. A* **100**, 052704 (2019).

[166] Chen, Z., Bohnet, J. G., Weiner, J. M. & Thompson, J. K. General formalism for evaluating the impact of phase noise on bloch vector rotations. *Phys. Rev. A* **86**, 032313 (2012).

[167] Burchesky, S. *Engineered Collisions, Molecular Qubits, and Laser Cooling of Asymmetric Top Molecules*. Ph.D. thesis, Harvard University (2023).

[168] Gehm, M. E., O'Hara, K. M., Savard, T. A. & Thomas, J. E. Dynamics of noise-induced heating in atom traps. *Phys. Rev. A* **58**, 3914–3921 (1998).

[169] Marcassa, L. *et al.* Optical Suppression of Photoassociative Ionization in a Magneto-Optical Trap. *Phys. Rev. Lett.* **73**, 1911–1914 (1994).

[170] Zilio, S. C. *et al.* Polarization Dependence of Optical Suppression in Photoassociative Ionization Collisions in a Sodium Magneto-optic Trap. *Phys. Rev. Lett.* **76**, 2033–2036 (1996).

[171] Muniz, S. R. *et al.* Optical suppression of hyperfine-changing collisions in a sample of ultracold sodium atoms. *Phys. Rev. A* **55**, 4407–4411 (1997).

[172] Suominen, K.-A., Holland, M. J., Burnett, K. & Julienne, P. Optical shielding of cold collisions. *Phys. Rev. A* **51**, 1446–1457 (1995).

[173] Weiner, J., Bagnato, V. S., Zilio, S. & Julienne, P. S. Experiments and theory in cold and ultracold collisions. *Rev. Mod. Phys.* **71**, 1–85 (1999).

[174] Balewski, J. B. *et al.* Rydberg dressing: understanding of collective many-body effects and implications for experiments. *New J. Phys.* **16**, 063012 (2014).

[175] Micheli, A., Pupillo, G., Büchler, H. P. & Zoller, P. Cold polar molecules in two-dimensional traps: Tailoring interactions with external fields for novel quantum phases. *Phys. Rev. A* **76**, 043604 (2007).

[176] Gorshkov, A. V. *et al.* Suppression of Inelastic Collisions Between Polar Molecules With a Repulsive Shield. *Phys. Rev. Lett.* **101**, 073201 (2008).

[177] Cooper, N. R. & Shlyapnikov, G. V. Stable topological superfluid phase of ultracold polar fermionic molecules. *Phys. Rev. Lett.* **103**, 155302 (2009).

[178] Karman, T. Microwave shielding with far-from-circular polarization. *Phys. Rev. A* **101**, 042702 (2020).

[179] Xie, T. *et al.* Optical Shielding of Destructive Chemical Reactions between Ultracold Ground-State NaRb Molecules. *Phys. Rev. Lett.* **125**, 153202 (2020).

[180] Karam, C. *et al.* Two-photon optical shielding of collisions between ultracold polar molecules. *Phys. Rev. Res.* **5**, 033074 (2023).

[181] Hollerith, S. *et al.* Quantum gas microscopy of Rydberg macrodimers. *Science* **364**, 664–667 (2019).

[182] Zuber, N. *et al.* Observation of a molecular bond between ions and Rydberg atoms. *Nature* **605**, 453–456 (2022).

[183] Julienne, P. S. Ultracold molecules from ultracold atoms: a case study with the KRb molecule. *Faraday Discuss.* **142**, 361–388 (2009).

[184] Żuchowski, P. S., Kosicki, M., Kodrycka, M. & Soldán, P. van der Waals coefficients for systems with ultracold polar alkali-metal molecules. *Phys. Rev. A* **87**, 022706 (2013).

[185] Wang, R. R. W. & Bohn, J. L. Anisotropic thermalization of dilute dipolar gases. *Phys. Rev. A* **103**, 063320 (2021).

[186] Ma, Z.-Y., Thomas, A. M., Foot, C. J. & Cornish, S. L. The evaporative cooling of a

gas of caesium atoms in the hydrodynamic regime. *J. Phys. B: At. Mol. Opt. Phys.* **36**, 3533–3540 (2003).

[187] Grimm, R. Ultracold fermi gases in the bec-bcs crossover: a review from the innsbruck perspective. *Preprint at https://arxiv.org/abs/cond-mat/0703091* (2007).

[188] Altmeyer, A. *et al.* Dynamics of a strongly interacting Fermi gas: The radial quadrupole mode. *Phys. Rev. A* **76**, 033610 (2007).

[189] Abad, M., Recati, A. & Stringari, S. Quadrupole oscillation in a dipolar Fermi gas: Hydrodynamic versus collisionless regime. *Phys. Rev. A* **85**, 033639 (2012).

[190] Vogt, E. *et al.* Scale Invariance and Viscosity of a Two-Dimensional Fermi Gas. *Phys. Rev. Lett.* **108**, 070404 (2012).

[191] Altmeyer, A. *et al.* Precision Measurements of Collective Oscillations in the BEC-BCS Crossover. *Phys. Rev. Lett.* **98**, 040401 (2007).

[192] Tey, M. K. *et al.* Collective Modes in a Unitary Fermi Gas across the Superfluid Phase Transition. *Phys. Rev. Lett.* **110**, 055303 (2013).

[193] Wächtler, F., Lima, A. R. P. & Pelster, A. Low-lying excitation modes of trapped dipolar Fermi gases: From the collisionless to the hydrodynamic regime. *Phys. Rev. A* **96**, 043608 (2017).

[194] Kinast, J., Hemmer, S. L., Gehm, M. E., Turlapov, A. & Thomas, J. E. Evidence for Superfluidity in a Resonantly Interacting Fermi Gas. *Phys. Rev. Lett.* **92**, 150402 (2004).

[195] Aikawa, K. *et al.* Reaching Fermi Degeneracy via Universal Dipolar Scattering. *Phys. Rev. Lett.* **112**, 010404 (2014).

[196] Wang, R. R. W. & Bohn, J. L. Viscous damping in weltering motion of trapped hydrodynamic dipolar Fermi gases. *Preprint at https://arxiv.org/abs/2306.00250* (2023).

[197] Lu, M., Burdick, N. Q. & Lev, B. L. Quantum Degenerate Dipolar Fermi Gas. *Phys. Rev. Lett.* **108**, 215301 (2012).

[198] Ravensbergen, C. *et al.* Production of a degenerate Fermi-Fermi mixture of dysprosium and potassium atoms. *Phys. Rev. A* **98**, 063624 (2018).

[199] Regal, C. *Experimental realization of BCS-BEC crossover physics with a Fermi gas of atoms*. Ph.D. thesis, University of Colorado (2006).

[200] Timmermans, E. Degenerate Fermion Gas Heating by Hole Creation. *Phys. Rev. Lett.* **87**, 240403 (2001).

[201] McKay, D. C. & DeMarco, B. Cooling in strongly correlated optical lattices: prospects and challenges. *Rep. Prog. Phys.* **74**, 054401 (2011).

[202] Zhao, C. *et al.* Hartree-Fock-Bogoliubov theory of dipolar Fermi gases. *Phys. Rev. A* **81**, 063642 (2010).

[203] Patel, P. B. *et al.* Universal sound diffusion in a strongly interacting Fermi gas. *Science* **370**, 1222–1226 (2020).

[204] Yan, Z. Z., Ni, Y., Robens, C. & Zwierlein, M. W. Bose polarons near quantum criticality. *Science* **368**, 190–194 (2020).

[205] Aikawa, K. *et al.* Observation of Fermi surface deformation in a dipolar quantum gas. *Science* **345**, 1484–1487 (2014).

[206] Veljić, V., Pelster, A. & Balaž, A. Stability of quantum degenerate Fermi gases of tilted polar molecules. *Phys. Rev. Research* **1**, 012009 (2019).

[207] You, L. & Marinescu, M. Prospects for p-wave paired Bardeen-Cooper-Schrieffer states of fermionic atoms. *Phys. Rev. A* **60**, 2324–2329 (1999).

[208] Baranov, M. A., Mar'enko, M. S., Rychkov, V. S. & Shlyapnikov, G. V. Superfluid pairing in a polarized dipolar fermi gas. *Phys. Rev. A* **66**, 013606 (2002).

[209] Shi, T., Zhang, J.-N., Sun, C.-P. & Yi, S. Singlet and triplet Bardeen-Cooper-Schrieffer pairs in a gas of two-species fermionic polar molecules. *Phys. Rev. A* **82**, 033623 (2010).

[210] Schmidt, M., Lassablière, L., Quéméner, G. & Langen, T. Self-bound dipolar droplets and supersolids in molecular bose-einstein condensates. *Phys. Rev. Research* **4**, 013235 (2022).

[211] Wu, Z., Block, J. K. & Bruun, G. M. Liquid crystal phases of two-dimensional dipolar gases and Berezinskii-Kosterlitz-Thouless melting. *Sci. Rep.* **6**, 19038 (2016).

[212] Bruun, G. M. & Taylor, E. Quantum phases of a two-dimensional dipolar fermi gas. *Phys. Rev. Lett.* **101**, 245301 (2008).

[213] Matveeva, N. & Giorgini, S. Liquid and crystal phases of dipolar fermions in two dimensions. *Phys. Rev. Lett.* **109**, 200401 (2012).

[214] Gorshkov, A. V. *et al.* Tunable superfluidity and quantum magnetism with ultracold

polar molecules. *Phys. Rev. Lett.* **107**, 115301 (2011).

[215] Gorshkov, A. V. *et al.* Quantum magnetism with polar alkali-metal dimers. *Phys. Rev. A* **84**, 033619 (2011).

[216] Wall, M. L., Hazzard, K. R. A. & Rey, A. M. Quantum Magnetism with Ultracold Molecules. 3–37 (Singapore, 2015).

[217] Zhu, B. *et al.* Suppressing the Loss of Ultracold Molecules Via the Continuous Quantum Zeno Effect. *Phys. Rev. Lett.* **112**, 070404 (2014).

[218] Britton, J. W. *et al.* Engineered two-dimensional Ising interactions in a trapped-ion quantum simulator with hundreds of spins. *Nature* **484**, 489–492 (2012).

[219] Franke, J. *et al.* Quantum-enhanced sensing on an optical transition via emergent collective quantum correlations. *Preprint at https://arxiv.org/abs/2303.10688* (2023).

[220] Scholl, P. *et al.* Quantum simulation of 2D antiferromagnets with hundreds of Rydberg atoms. *Nature* **595**, 233–238 (2021).

[221] Scholl, P. *et al.* Microwave Engineering of Programmable XXZ Hamiltonians in Arrays of Rydberg Atoms. *PRX Quantum* **3**, 020303 (2022).

[222] Chen, C. *et al.* Continuous symmetry breaking in a two-dimensional Rydberg array. *Nature* **616**, 691–695 (2023).

[223] Bornet, G. *et al.* Scalable spin squeezing in a dipolar Rydberg atom array. *Preprint at https://arxiv.org/abs/2303.08053* (2023).

[224] Eckner, W. J. *et al.* Realizing spin squeezing with Rydberg interactions in a programmable optical clock. *Preprint at https://arxiv.org/abs/2303.08078* (2023).

[225] Lagoin, C. *et al.* Extended Bose–Hubbard model with dipolar excitons. *Nature* **609**, 485–489 (2022).

[226] Su, L. *et al.* Dipolar quantum solids emerging in a Hubbard quantum simulator. *Preprint at https://arxiv.org/abs/2306.00888* (2023).

[227] Moses, S. A. *et al.* Creation of a low-entropy quantum gas of polar molecules in an optical lattice. *Science* **350**, 659–662 (2015).

[228] Covey, J. P. *et al.* Doublon dynamics and polar molecule production in an optical lattice. *Nat. Commun.* **7**, 1–8 (2016).

[229] Reichsöllner, L., Schindewolf, A., Takekoshi, T., Grimm, R. & Nägerl, H.-C. Quan-

tum Engineering of a Low-Entropy Gas of Heteronuclear Bosonic Molecules in an Optical Lattice. *Phys. Rev. Lett.* **118**, 073201 (2017).

[230] Köhl, M. Thermometry of fermionic atoms in an optical lattice. *Phys. Rev. A* **73**, 031601 (2006).

[231] Murthy, P. A. *et al.* Matter-wave Fourier optics with a strongly interacting two-dimensional Fermi gas. *Phys. Rev. A* **90**, 043611 (2014).

[232] Mukherjee, B. *et al.* Homogeneous Atomic Fermi Gases. *Phys. Rev. Lett.* **118**, 123401 (2017).

[233] Hueck, K. *et al.* Two-Dimensional Homogeneous Fermi Gases. *Phys. Rev. Lett.* **120**, 060402 (2018).

[234] Greiner, M., Bloch, I., Mandel, O., Hänsch, T. W. & Esslinger, T. Bose–einstein condensates in 1d-and 2d optical lattices. *Applied Physics B* **73**, 769–772 (2001).

[235] Bloch, I. Ultracold quantum gases in optical lattices. *Nat. Phys.* **1**, 23–30 (2005).

[236] Kwasigroch, M. P. & Cooper, N. R. Synchronization transition in dipole-coupled two-level systems with positional disorder. *Phys. Rev. A* **96**, 053610 (2017).

[237] Li, J.-R. *et al.* Tunable itinerant spin dynamics with polar molecules. *Nature* **614**, 70–74 (2023).

[238] Hazzard, K. R. A. *et al.* Many-Body Dynamics of Dipolar Molecules in an Optical Lattice. *Phys. Rev. Lett.* **113**, 195302 (2014).

[239] Kwasigroch, M. P. & Cooper, N. R. Bose-Einstein condensation and many-body localization of rotational excitations of polar molecules following a microwave pulse. *Phys. Rev. A* **90**, 021605 (2014).

[240] Peter, D., Müller, S., Wessel, S. & Büchler, H. P. Anomalous Behavior of Spin Systems with Dipolar Interactions. *Phys. Rev. Lett.* **109**, 025303 (2012).

[241] Gullion, T., Baker, D. B. & Conradi, M. S. New, compensated Carr-Purcell sequences. *Journal of Magnetic Resonance (1969)* **89**, 479–484 (1990).

[242] Tobias, W. G. *et al.* Reactions between layer-resolved molecules mediated by dipolar spin exchange. *Science* **375**, 1299–1303 (2022).

[243] Wei, D. *et al.* Observation of Brane Parity Order in Programmable Optical Lattices. *Phys. Rev. X* **13**, 021042 (2023).

[244] Yatsenko, L. P., Romanenko, V. I., Shore, B. W. & Bergmann, K. Stimulated Raman adiabatic passage with partially coherent laser fields. *Phys. Rev. A* **65**, 043409 (2002).

[245] Yatsenko, L. P., Shore, B. W. & Bergmann, K. Detrimental consequences of small rapid laser fluctuations on stimulated Raman adiabatic passage. *Phys. Rev. A* **89**, 013831 (2014).

[246] Li, L., Huie, W., Chen, N., DeMarco, B. & Covey, J. P. Active Cancellation of Servo-Induced Noise on Stabilized Lasers via Feedforward. *Phys. Rev. Appl.* **18**, 064005 (2022).

[247] Cheuk, L. W. *et al.* -Enhanced Imaging of Molecules in an Optical Trap. *Phys. Rev. Lett.* **121**, 083201 (2018).

[248] Holland, C. M., Lu, Y. & Cheuk, L. W. Bichromatic Imaging of Single Molecules in an Optical Tweezer Array. *Phys. Rev. Lett.* **131**, 053202 (2023).

[249] Winerman, L. Linked Molecules. *Physics* https://physics.aps.org/story/v11/st5 (2003).

[250] Chin, C., Grimm, R., Julienne, P. & Tiesinga, E. Feshbach resonances in ultracold gases. *Rev. Mod. Phys.* **82**, 1225–1286 (2010).

[251] Bloch, I., Dalibard, J. & Zwerger, W. Many-body physics with ultracold gases. *Rev. Mod. Phys.* **80**, 885–964 (2008).

[252] Köhler, T., Góral, K. & Julienne, P. S. Production of cold molecules via magnetically tunable Feshbach resonances. *Rev. Mod. Phys.* **78**, 1311–1361 (2006).

[253] Skodje, R. T. *et al.* Resonance-mediated chemical reaction: F + HD $\rightarrow$ HF + D. *Phys. Rev. Lett.* **85**, 1206–1209 (2000).

[254] Henson, A. B., Gersten, S., Shagam, Y., Narevicius, J. & Narevicius, E. Observation of resonances in Penning ionization reactions at sub-kelvin temperatures in merged beams. *Science* **338**, 234–238 (2012).

[255] Chefdeville, S. *et al.* Observation of partial wave resonances in low-energy O_2–H_2 inelastic collisions. *Science* **341**, 1094–1096 (2013).

[256] de Jongh, T. *et al.* Imaging the onset of the resonance regime in low-energy NO–He collisions. *Science* **368**, 626–630 (2020).

[257] Chin, C. *et al.* Observation of Feshbach-like resonances in collisions between ultracold molecules. *Phys. Rev. Lett.* **94**, 123201 (2005).

[258] Wang, F., Ye, X., Guo, M., Blume, D. & Wang, D. Observation of resonant scattering between ultracold heteronuclear Feshbach molecules. *Phys. Rev. A* **100**, 042706 (2019).

[259] Liu, Y. & Ni, K.-K. Bimolecular Chemistry in the Ultracold Regime. *Annu. Rev. Phys. Chem.* **73**, 73–96 (2022).

[260] Avdeenkov, A. V., Bortolotti, D. C. E. & Bohn, J. L. Field-linked states of ultracold polar molecules. *Phys. Rev. A* **69**, 012710 (2004).

[261] Karman, T., Yan, Z. Z. & Zwierlein, M. Resonant and first-order dipolar interactions between ultracold $^1\Sigma$ molecules in static and microwave electric fields. *Phys. Rev. A* **105**, 013321 (2022).

[262] Hutson, J. M. Feshbach resonances in ultracold atomic and molecular collisions: threshold behaviour and suppression of poles in scattering lengths. *New J. Phys.* **9**, 152 (2007).

[263] Levinsen, J., Cooper, N. R. & Shlyapnikov, G. V. Topological $p_x + ip_y$ superfluid phase of fermionic polar molecules. *Phys. Rev. A* **84**, 013603 (2011).

[264] Chomaz, L. *et al.* Dipolar physics: a review of experiments with magnetic quantum gases. *Rep. Prog. Phys.* **86**, 026401 (2022).

[265] Schmidt, M., Lassablière, L., Quéméner, G. & Langen, T. Self-bound dipolar droplets and supersolids in molecular Bose-Einstein condensates. *Phys. Rev. Research* **4**, 013235 (2022).

[266] Klaus, L. *et al.* Observation of vortices and vortex stripes in a dipolar condensate. *Nat. Phys.* **18**, 1453–1458 (2022).

[267] Quéméner, G., Bohn, J. L. & Croft, J. F. E. Electroassociation of ultracold dipolar molecules into tetramer field-linked states. *Phys. Rev. Lett.* **131**, 043402 (2023).

[268] Deng, F. *et al.* Formation and Dissociation of Field-Linked tetramers. *In preparation* .

[269] Hutzler, N. R. Polyatomic molecules as quantum sensors for fundamental physics. *Quantum Sci. Technol.* **5**, 044011 (2020).

[270] Tesch, C. M. & de Vivie-Riedle, R. Quantum computation with vibrationally excited molecules. *Phys. Rev. Lett.* **89**, 157901 (2002).

[271] Wall, M. L., Maeda, K. & Carr, L. D. Realizing unconventional quantum magnetism with symmetric top molecules. *New J. Phys.* **17**, 025001 (2015).

[272] Albert, V. V., Covey, J. P. & Preskill, J. Robust encoding of a qubit in a molecule. *Phys. Rev. X* **10**, 031050 (2020).

[273] Cao, J. *et al.* Preparation of a quantum degenerate mixture of ^{23}Na^{40}K molecules and ^{40}K atoms. *Phys. Rev. A* **107**, 013307 (2023).

[274] Prehn, A., Ibrügger, M., Glöckner, R., Rempe, G. & Zeppenfeld, M. Optoelectrical cooling of polar molecules to submillikelvin temperatures. *Phys. Rev. Lett.* **116**, 063005 (2016).

[275] Huang, S.-J. *et al.* Field-induced long-lived supermolecules. *Phys. Rev. A* **85**, 055601 (2012).

[276] Klempt, C. *et al.* Radio-frequency association of heteronuclear Feshbach molecules. *Phys. Rev. A* **78**, 061602 (2008).

[277] Hanna, T. M., Köhler, T. & Burnett, K. Association of molecules using a resonantly modulated magnetic field. *Phys. Rev. A* **75**, 013606 (2007).

[278] Hodby, E. *et al.* Production efficiency of ultracold feshbach molecules in bosonic and fermionic systems. *Phys. Rev. Lett.* **94**, 120402 (2005).

[279] McDonald, M. *et al.* Photodissociation of ultracold diatomic strontium molecules with quantum state control. *Nature* **535**, 122–126 (2016).

[280] Gaebler, J. P., Stewart, J. T., Bohn, J. L. & Jin, D. S. p-Wave Feshbach Molecules. *Phys. Rev. Lett.* **98**, 200403 (2007).

[281] Lepers, M., Vexiau, R., Aymar, M., Bouloufa-Maafa, N. & Dulieu, O. Long-range interactions between polar alkali-metal diatoms in external electric fields. *Phys. Rev. A* **88**, 032709 (2013).

[282] Gacesa, M., Byrd, J. N., Smucker, J., Montgomery, J. A. & Côté, R. Photoassociation of ultracold long-range polyatomic molecules. *Phys. Rev. Res.* **3**, 023163 (2021).

[283] Cao, J. *et al.* Observation of photoassociation resonances in ultracold atom-molecule collisions. *Preprint at https://arxiv.org/abs/2307.15917* (2023).

[284] Lassablière, L. & Quéméner, G. Model for two-body collisions between ultracold dipolar molecules around a F\"orster resonance in an electric field. *Phys. Rev. A* **106**, 033311 (2022).

[285] Shi, T. & Deng, F. Private communications.

[286] Śmiałkowski, M. & Tomza, M. Highly polar molecules consisting of a copper or silver

atom interacting with an alkali-metal or alkaline-earth-metal atom. *Phys. Rev. A* **103**, 022802 (2021).

[287] Nikitin, E. E. & Zare, R. N. Correlation diagrams for Hund's coupling cases in diatomic molecules with high rotational angular momentum. *Mol. Phys.* **82**, 85–100 (1994).

[288] Aymar, M. & Dulieu, O. Calculations of transition and permanent dipole moments of heteronuclear alkali dimers NaK, NaRb and NaCs. *Mol. Phys.* **105**, 1733–1742 (2007).

[289] Aldegunde, J. & Hutson, J. M. Hyperfine structure of alkali-metal diatomic molecules. *Phys. Rev. A* **96**, 042506 (2017).

[290] Will, S. A., Park, J. W., Yan, Z. Z., Loh, H. & Zwierlein, M. W. Coherent microwave control of ultracold ^{23}Na^{40}K molecules. *Phys. Rev. Lett.* **116**, 225306 (2016).

[291] Park, J. W., Will, S. A. & Zwierlein, M. W. Two-photon pathway to ultracold ground state molecules of 23Na40K. *New J. Phys.* **17**, 075016 (2015).

[292] Liu, L. *et al.* Observation of interference between resonant and detuned stirap in the adiabatic creation of ^{23}Na^{40}K molecules. *Phys. Rev. Lett.* **122**, 253201 (2019).

[293] Li, M., Petrov, A., Makrides, C., Tiesinga, E. & Kotochigova, S. Pendular trapping conditions for ultracold polar molecules enforced by external electric fields. *Phys. Rev. A* **95**, 063422 (2017).

[294] Bohn, J. L. & Jin, D. S. Differential scattering and rethermalization in ultracold dipolar gases. *Phys. Rev. A* **89**, 022702 (2014).

[295] Heizenreder, B. *Creation of arbitrary potentials with a digital micromirror device.* Master's thesis, Ludwig-Maximilians-Universität München (2021).

[296] Anderson, B. P. & Kasevich, M. A. Macroscopic Quantum Interference from Atomic Tunnel Arrays. *Science* **282**, 1686–1689 (1998).

[297] Helmerson, K., Phillips, W. D., Burnett, K. & Hutchinson, D. Atom lasers. *Phys. World* **12**, 31 (1999).

[298] Mewes, M.-O. *et al.* Output Coupler for Bose-Einstein Condensed Atoms. *Phys. Rev. Lett.* **78**, 582–585 (1997).

[299] Bloch, I., Hänsch, T. W. & Esslinger, T. Atom Laser with a cw Output Coupler. *Phys. Rev. Lett.* **82**, 3008–3011 (1999).

[300] Bloch, I., Hänsch, T. W. & Esslinger, T. Measurement of the spatial coherence of a trapped Bose gas at the phase transition. *Nature* **403**, 166–170 (2000).

[301] Hagley, E. W. *et al.* A Well-Collimated Quasi-Continuous Atom Laser. *Science* **283**, 1706–1709 (1999).

Acknowledgement

First of all, I would like to thank my supervisor, Immanuel Bloch. His mentorship covered a gamut of topics, from quantum optics to the intricacies of optical lattices. His visions have been essential to our research success. Equally impressive is his enthusiasm for science and his insightful feedback during discussions. His perspective on work ethics — "Scientific research is more of a series of sprints than a continuous long run" — has profoundly resonated with me, providing motivation during challenging moments in the laboratory. I am grateful for being in his group, which is one of the best places to study ultracold atoms and molecules, with knowledgeable people within the group as wells as a large network of international scientists.

Next, my gratitude goes to our PI, Xinyu Luo. Xinyu is a repository of advanced technical expertise. His teachings span from practical skills like tightening a flange to high-level tasks like designing fast PI loops for all kinds of systems. His clear leadership roadmap has enabled us to both lay solid foundations — measuring all loss processes during magnetoassociation — and also progress quickly when opportunities arise — like implementing microwave shielding. On a personal note, he's been a supportive guide, even bringing me food when I worked late.

To Roman and Marcel, you're what I'd call my big brothers in science. We've meshed well, each contributing our unique strengths. Roman has an uncanny ability to juggle multiple projects and prioritize them effectively. His extensive expertise and strong programming abilities greatly facilitate the configuration and control of a variety of instruments. Marcel, on the other hand, is the one I turn to when it comes to the nuts and bolts of our machinery. His is my direct mentor on machine whispering. Together, we've faced challenges but also shared many light-hearted moments.

Andreas, you're the team's eye for detail, always cautioning us against potential pitfalls. When rushing through the preparation phase, you're the one pointing out potential flaws and suggesting further experiments. Your skills in paper writing and concept illustration are indispensable.

I would like to thank the former PhDs — Niko, Zhenkai, and Frauke — as well as to

the previous PI, Christoph, for all the effort they put into the construction of the machine. To the next generation PhDs, Sebb and Shrestha, your diligent work in lab maintenance has turned the space into a productive arena. I can't wait to see how you will advance the experiment. To our next PI Timon, your upcoming contributions with the quantum gas microscope are eagerly awaited.

To our master's students, who have played instrumental roles in improving the setup: Scott for building the horizontal lattice; Benedikt for making the high-voltage PI controller as well as the DMD setup; Akira for implementing the STIRAP system; Renhao for constructing both the box trap and shallow angle lattice. To Leo and Christine, the prospect of your upcoming upgrades fills me with anticipation. Our intern students — Qinxue, Quentin, Benedikt, Garen, and Yunxuan — have sped up our progress through various side projects.

I also convey my thanks to our indispensable technicians: Anton, for your invaluable advice on mechanical designs; Kastern, for your expertise in developing high-precision DAC and high-speed PI controllers; and Olivia, for your practical electronic guidance and repair works. A thanks goes to Christoph Tafelmaier for his assistance with the house water and the air conditioners, as well as to the MPQ workshop team for their mechanical contributions.

To the entire Bloch group, I express my appreciation for the great atmosphere for discussions, for sharing technique, and for the borrowed equipments. Among the shared techniques worth mentioning are the Q-Control timing system, the home-made linear lasers and TAs, ULE-cavity housings, and LEGO optical mounts.

On the administrative front, my sincere thanks to Kristina, Ildiko, Doreen, and Veronika. Your support in navigating the labyrinth of enrollment, visa applications, and other bureaucratic hurdles — especially given my limited German language skills — has been invaluable. I appreciate the social bonds that have been strengthened through the various events you've coordinated, from Christmas parties to group retreats.

Theoretical supports are crucial to our experimental venture, and in this regard. For this I express my gratitude to Nadia Bouloufa-Maafa and Olivia Dulieu for their calculations of the photon scattering rates of the ground state molecules; to Dmitry Petrov for teaching me how to solve the STM equation; to Pierbiagio Pieri for discussions on quantum phase transition in Bose–Fermi mixture; to Axel Pelster and Antun Balaz for their work on Fermi surface deformations; as well as to John Bohn and Rueben Wang for simulations relating to hydrodynamics and evaporative cooling. Additional thanks to our coauthors: Ming Li, Svetlana Kotochigova, Jonas von Milczewski, Richard Schmidt, Goulven Quéméner, Arthur Christianen, Tijs Karman, Fulin Deng, Tao Shi, and Su Yi, for their crucial contributions to our publications.

Special thanks go to Tao Shi for his keen physics intuition, impressive computational

skills, and generous mentorship, all delivered with a sense of humor that I deeply value.

I would also like to acknowledge other molecular experimentalists — Jun Ye, Yicheng Bao, Junyu Lin, and Anbang Yang — for sharing technical knowledge and for simulating discussions. Thanks also to Christian Buchberger, Michael Hani and Erwin Biebl from TUM for their collaborative contributions to the waveguide antenna, and to the experts from Fraunhofer Institut for their early conceptual guidance.

Acknowledgment to the service departments at MPQ and MCQST: IT for network and data support, the purchasing department — especially Carina Steinkrebs — for procurement, and PR — especially Katharina Jarrah — for media outreach. Acknowledgement to Christoph Hohmann for crafting the Nature cover and QPT paper illustrations.

A word of gratitude to my peers at MPQ and TUM, including but not limited to Zhiyuan Wei, Yilun Yang, Sirui Lu, Zongping Gong, Yujie Liu, Xin Chen, and Bingxin Xu. Cheers to Zongping, my Otaku friend, for our aligned interests in ACG.

Thanks must also go to proofreaders of my thesis: Xinyu, Roman, Sebb, Andreas, and Timon.

Last but definitely not least, a special thanks to my parents for their unconditional support. No words can express my deepest gratitude towards them.

Thank you!